

PLANET FORMATION

THE ROLES OF PEBBLE ACCRETION, RADIATIVE AND
CONVECTIVE ENERGY TRANSPORT



ANDRIUS POPOVAS

Dissertation submitted for the degree of

PHILOSOPHIÆ DOCTOR

Centre for Star and Planet Formation
Niels Bohr Institute & Natural History Museum of Denmark
Faculty of Science
University of Copenhagen

This thesis has been submitted to the PhD School of The Faculty of Science, University of Copenhagen

<i>Title</i>	Planet Formation, The Roles of Pebble Accretion, Radiative and Convective Energy Transport
<i>Author</i>	Andrius Popovas
<i>Date of Submission</i>	28 February, 2018
<i>Date of Defence</i>	09 April, 2018
<i>Department</i>	Centre for Star and Planet Formation, Niels Bohr Institute & Natural History Museum of Denmark, Faculty of Science, University of Copenhagen
<i>Academic Advisors</i>	Prof. Åke Nordlund Assoc. Prof. Uffe G. Jørgensen
<i>Informal Advisor</i>	Dr. Jon. P. Ramsey
<i>Assessment Committee</i>	Prof. Anja C. Andersen (chair) Prof. Anders Johansen Prof. Wilhelm Kley

Typeset using the Palatino and Euler type faces by Hermann Zapf
 Layout and typography by the author with L^AT_EX 2_ε using the class “classicthesis”
 developed by André Miede

To you as a reader

ENGLISH ABSTRACT

This thesis deals with the early stages of rocky planet formation, when nascent planets are still embedded in a protoplanetary disk, which consists mostly of hydrogen, helium gas and dust grains. Hydrostatic equilibrium between the gravitating planetary embryo and the surrounding gas forms an envelope. This envelope acts as a buffer between the embryo and the disk. Using our newly developed DISPATCH framework, we construct high resolution nested-grid hydrodynamic simulations to investigate near-planet gas dynamics and how it affects the accretion of pebbles, which are the main building blocks of planets. Only a small fraction of all the pebbles that cross into the planet's region of gravitational influence – the Hill sphere – are accreted. The pebble accretion rates scale linearly with the size of the pebbles and are, due to cancellation effects, nearly independent of disk surface density, if the dust-to-gas surface density ratio is constant. With the measured accretion rates, we estimate accurate growth times for specified particle sizes. For chondrule-size (0.3–1 mm) particles, the growth time from a small seed is ~ 1.5 million years for an Earth mass planet at 1 AU and ~ 1 million years for a Mars mass planet at 1.5 AU. For larger size particles or enhanced ratios of dust-to-gas surface density, the estimates are correspondingly shorter.

Accretion of solids onto the embryo releases a lot of potential energy, which is converted to heat via the friction force. This extra heat drives convective motions, which significantly alter the gas dynamics inside ~ 40 radii of an Earth size embryo. Convective motions do not, however, result in a net change in the transport of mass and the systematic inward drift of already gravitationally-bound pebbles continues as in the non-convective case. To investigate what effect the radiative energy transport has on the local environment of a forming planet, I have implemented a hybrid-characteristics radiative transfer module in the DISPATCH framework. We find that although the envelopes are generally opaque, they are locally optically thin and thus radiative heat transport has significant effects on the near-planet gas thermodynamics. The intensity of the convective motions are increased by radiative cooling of the atmosphere, which tends to increase the super-adiabatic temperature gradient that drives convection. This does not, however, affect the net pebble accretion rates, but smaller pebbles do spend more time in the inner layers of the atmosphere. Here, secondary effects, such as pebble destruction via ablation, which would result in gas enrichment with heavy elements and envelope replenishment with the disk gas rates, may be important. Considering the ongoing efforts to understand planet formation, and the importance of realistically treating all of the relevant physical mechanisms, this thesis provides a good start and a significant stepping stone to build future research upon.

Denne afhandling beskæftiger sig med de tidlige stadier af dannelsen af klippeplaneter, når de fremvoksende planeter stadig er indlejret i den protoplanetare disk, der hovedsagelig består af hydrogen og helium gas. Disken indeholder også ca. 1% fast materiale, i form af støv og "småsten", som måske minder om de "kondruler" man finder i mange slags meteoritter. Hydrostatisk ligevægt mellem planetens tyngdekraft og den omgivende gas fører til dannelsen af en udstrakt, varm atmosfære, som hjælper til med at opsamle støv og småsten, og dermed får planetens masse til at vokse hurtigere. Ved hjælp af vores nyudviklede DISPATCH computerkode kan vi lave hydrodynamiske simuleringer med høj opløsning, og bruge dem til at undersøge hvordan gas- og støv-dynamik påvirker planetens tilvækst. Kun en lille del af de støv og småsten der kommer indenfor planetens såkaldte Hill-sfære, fanges op af dens tyngdekraft, og bidrager til dens tilvækst. Tilvæksthastigheden vokser lineært med størrelsen af støvpartiklerne, men er næsten uafhængig af diskens massetæthed, ved givet forhold mellem mængden af støv og gas. Ved hjælp af computermodellen kan vi beregne nøjagtige tilvæksttider for forskellige partikelstørrelser. For størrelse i omegnen 0,3-1 mm – som for "kondruler" – er tilvæksttiden ca. 1.5 million år for en planet med Jordens masse og afstand fra solen, og ca. 1 million år for en planet med Mars masse og afstand fra solen. For større partikler og for højere forhold mellem massen af støv og gas er tilvæksttiderne tilsvarende kortere.

Planetens tilvækst via opsamling af småsten frigiver potentiel energi, som omdannes til varme via friktionskraften. Den ekstra varme driver energitransport i form af konvektion, som dominerer gasdynamikken inden for ca 40 jordradier. Konvektionen medfører ikke ændring i nettotransporten af masse, og den systematiske drift af allerede bundne småsten forbliver også næsten upåvirket. For at undersøge hvordan forholdene påvirkes af strålingstransport af energi har jeg implementeret en hybrid strålingstransportmetode i DISPATCH. Ved hjælp af den metode finder vi at, selv om disken og planetatmosfæren totalt set er uigennemsigtige, er de lokalt gennemsigtige, og varmetransport via stråling har derfor tydelig indvirkning på gasdynamikken. De konvektive bevægelser og den tilsvarende hastighedsdispersion øges, når strålingsafkøling øger temperaturgradienten i atmosfæren. Generelt har dette ingen nævneværdig indflydelse på tilvæksten af masse, men mindre småsten bruger mere tid i atmosfærens indre lag. Her kan sekundære påvirkninger, såsom fordampning, medføre berigelse af gassen med tunge grundstoffer.

Afhandlingen er et vigtigt skridt hen imod en bedre forståelse af planetdannelsen. Dens mere realistiske behandling end sædvanligt, af alle de vigtigste fysiske mekanismer i planetdannelsen, er et vigtigt grundlag for konstruktionen af endnu mere avancerede modeller i fremtiden.

It should only take a few minutes...

— Anonymous advisor

ACKNOWLEDGMENTS

First and foremost I want to express my deep gratitude to my main advisor, Åke Nordlund, not just for his guidance, but also for being a great mentor while continuously supporting me even when my ideas were diverging from the goals of this work. I want to thank my co-advisor, Uffe G. Jørgensen and an informal advisor, Jon P. Ramsey, for their immense support and countless hours dedicated to advice and support. I want to thank all of them for encouragement to look critically at previously done research and not take it as solid and at the same time reminding me not to veer too much to tangent research. Moreover, I am very grateful to all of them for the invaluable scientific dissemination and not only the already “known” facts, but also new thoughts and ideas. I can honestly say, that I cannot imagine better advisors and without a doubt they had a significant impact to my growth and maturity as a scientist.

My special gratitude goes to Chris W. Ormel for stimulating discussions and sharing intrinsic details about the research of interest as well as continuous support and motivation. My three month stay in Amsterdam (February - May 2017), hosted by Chris and the Anton Pannekoek Institute for Astronomy was very motivating and inspired me to work harder.

Throughout my thesis, thanks to my advisors and the Niels Bohr Institute, I had the opportunity to travel to a number of conferences and PhD schools, where I met and interacted with a number of brilliant leading scientists around the globe. I am grateful to my advisors for letting me participate in the MiNDSTEp collaboration, searching for exoplanets using the gravitational microlensing technique. While a part of this collaboration, I did on-site and remote observations (2 weeks on-site, 2 weeks remote annually) in La Silla, Chile, which lead to co-authorship on 26 publications in peer-reviewed journals. Although not directly related to this thesis, this resulted in a tremendous amount of scientific and technical experience working with telescopes, data and their pipelines.

I also want to thank everybody at StarPlan, which was a fantastic place to work. The warm and collaborative environment made me feel at home and inspired many in-depth, both work-related and unrelated, discussions. I want to express my gratitude to our administrators Marianne Bentsen and Lene Bentzen who helped with numerous inquiries. Special thanks goes to current and previous office mates, Michael Küffmeier, Troels Frostholt, Sigurd Jensen, Mirek Groen and Mattia Tagliavento for fun and pleasant days inside and outside the office.

I am also grateful to both the anonymous referees as well as those who disclosed their names, who greatly improved the quality of the papers through

their detailed reports. All the numerical simulations for this thesis were carried out using local computer resources at the University of Copenhagen HPC center.

I am thankful to Google Translate for translating the thesis abstract to Danish and Inge-Lise Dam for helping to translate the translation.

Last but not least I want to thank my family and friends for their continuous support and understanding in many difficult situations, such as many travels, not socializing for prolonged periods and working instead, as well as sometimes dragging me out to take a break.

CONTENTS

I INTRODUCTION

1	SCIENTIFIC BACKGROUND	3
1.1	Protoplanetary disks	4
1.1.1	Disk Structure	4
1.1.2	Solids in the Disk	6
1.1.3	Instabilities	8
1.2	Star formation and protoplanetary disk environments	10
1.3	Planet Formation	11
1.3.1	Primordial atmospheres	13
1.3.2	Planet – Disk Interaction	14
1.3.3	Gas Retention and Fractionation in the Primordial Atmospheres	16
1.4	The Diversity of Planetary Systems	16
1.4.1	The Regularity of Planetary Systems	17
2	RESEARCH GOALS AND METHODS	19
2.1	Short description and objectives	19
2.2	Publications	20
2.2.1	Paper I: Partition functions. I. Improved partition functions and thermodynamic quantities for normal, equilibrium, and ortho and para molecular hydrogen	21
2.2.2	Paper II: DISPATCH: A Numerical Simulation Framework for the Exa-scale Era. I. Fundamentals	21
2.2.3	Paper III: Pebble dynamics and accretion onto rocky planets. I. Adiabatic and convective models	22
2.2.4	Paper IV: Pebble dynamics and accretion onto rocky planets. II. Radiative models	23
2.3	Own contributions versus contributions of collaborators	23

II THE RESEARCH

3	PAPER I	27
3.1	Introduction	30
3.2	Energy levels and degeneracies	31
3.2.1	Translational partition function	31
3.2.2	Vibrational energies	31
3.2.3	Rotational energies	32
3.2.4	Interaction between vibration and rotation	34
3.2.5	Electronic energies	35
3.2.6	Vibrational and rotational energy cut-offs and the basic concept of quantum numbers	35
3.3	Simplifications used in other studies	39
3.3.1	Case 1.	39
3.3.2	Case 2.	39

3.3.3	Case 3.	40
3.3.4	Case 4.	40
3.3.5	Case 5.	40
3.3.6	Case 6.	40
3.3.7	Case 7.	41
3.3.8	Case 8.	41
3.4	Thermodynamic properties	42
3.5	Orto/para ratio of molecular hydrogen	43
3.6	Results and comparison	44
3.6.1	Determination of Dunham coefficients and evaluation of their accuracy	44
3.6.2	Comparison of cases 1 to 8	48
3.6.3	Polynomial fits	57
3.7	Conclusions	58
3.8	acknowledgements	62
4	PAPER II	73
4.1	Introduction	76
4.2	Object Hierarchy	79
4.2.1	Tasks	79
4.2.2	Task lists	79
4.2.3	Components	80
4.2.4	Scenes	81
4.3	Code Functionality	81
4.3.1	A) Single task view	82
4.3.2	B) Task scheduler view	82
4.3.3	C) MPI process view	84
4.3.4	D) Load balancer view	85
4.3.5	E) Input/Output view	86
4.4	Current code components	87
4.4.1	Internal and external HD, MHD, and PIC solvers	87
4.4.2	Radiative transfer	88
4.4.3	Non-ideal MHD	92
4.4.4	Particle trajectory integration	93
4.4.5	Equation-of-state and opacity tables	94
4.5	Validation	94
4.5.1	Supersonic turbulence	95
4.5.2	Non-ideal MHD: C-shock	101
4.5.3	Radiative transfer: Shadow casting benchmark	101
4.5.4	de Val-Borro disk benchmark	103
4.6	Summary and outlook	104
5	PAPER III	109
5.1	Introduction	112
5.2	Simulation set up	114
5.2.1	Grid set up	114
5.2.2	Initial conditions	115
5.2.3	External forces (accelerations)	118

5.2.4	Boundary conditions	118
5.2.5	Relaxation of initial conditions	120
5.3	Particles	122
5.3.1	Equations of motion	124
5.3.2	Injection of pebbles	127
5.4	Results: gas flows	127
5.4.1	Gas dynamics close to the planetary embryos	132
5.5	Results: particles	138
5.5.1	The distribution of particles	138
5.5.2	Pressure traps	146
5.5.3	Accretion of pebbles	150
5.5.4	Quantitative measurements of accretion rates	154
5.6	Accretion driven convection	156
5.7	Summary and Conclusions	160
5.8	Additional figures	164
6	PAPER IV	175
6.1	Introduction	178
6.2	Methods	179
6.2.1	Initial and boundary conditions	179
6.2.2	Radiative energy transport	180
6.2.3	Particles	182
6.3	Results and Discussion	182
6.3.1	Gas dynamics	182
6.3.2	Solid accretion rates	186
6.4	Conclusions and Outlook	186
7	SUMMARY AND OUTLOOK	189
	BIBLIOGRAPHY	192

ACRONYMS

AD	Ambipolar Diffusion
AU	astronomical unit
ALMA	Atacama Large Millimeter Array
AMR	Adaptive Mesh Refinement
CPU	central processing unit
EMF	Electromotive Force
EOS	equation of state
FLD	flux-limited diffusion
HO	harmonic oscillator
HD	hydrodynamics
HOA	harmonic oscillator approximation
HPC	High Performance Computing
HST	Hubble Space Telescope
JWST	James Webb Space Telescope
LTE	local thermal equilibrium
MHD	magnetohydrodynamics
MMSN	Minimum Mass Solar Nebula
MPI	Message Passing Interface
OPR	ortho-para ratio
OpenMP	Open Multi-Processing
pc	parsec
PIC	Particle-in-Cell
PPD	Protoplanetary disk
RMHD	radiation magnetohydrodynamics
RMSE	root-mean-square error
RRA	rigid rotor approximation

RG	ray geometry
RT	Radiative Energy Transfer
STP	Standard Temperature and Pressure
TESS	Transiting Exoplanet Survey Satellite
WFIRST	Wide-Field Infrared Survey Telescope

Part I

INTRODUCTION

SCIENTIFIC BACKGROUND

It can scarcely be denied that the supreme goal of all theory is to make the irreducible basic elements as simple and as few as possible without having to surrender the adequate representation of a single datum of experience.

— Albert Einstein

The study of star and planet formation has a long history. Initially, it was not well met - the proposal that “stars are other suns with their own planets” in the 16th century lead Giordano Bruno to an unfortunate demise by burning at the stake (Fitzgerald, 2010, p. 239). In the 18th century, Isaac Newton, in the ‘General Scholium’ that concludes his ‘Principia’ wrote “And if the fixed stars are the centres of similar systems, they will all be constructed according to a similar design and subject to the dominion of One”. Indeed, the ‘Nebular Hypothesis’ — the idea that the Solar system has formed from a disk of rotating gas and dust — dates back to Kant, Laplace and others.

Until the last century, however, we had just a single example of a planetary system: our own Solar system. In 1952, Otto Struve wrote that there is no real reason why planets could not be much closer to their parent stars than in our own Solar system and that, even with the technologies of the time, it could be possible to detect close-in giant planets using the radial velocity technique (Struve, 1952). Whereas a first quantitative description of terrestrial planet formation was made by Safronov (1966), a major breakthrough in observations was made only 40 years later, when the first two exoplanets orbiting a pulsar were discovered (Wolszczan & Frail, 1992). A few years later, the first giant exoplanet orbiting a solar-type star, with just a 4.23 day period (Mayor & Queloz, 1995), was discovered. These events marked a remarkable start of discoveries — starting slowly with both ground- and space-based discoveries, first by using the Hubble Space Telescope (HST) and Spitzer space telescopes and then later, with the dedicated Kepler mission (e.g. Borucki et al. 2010), new exoplanets started popping up like mushrooms after a good rain, revealing that planets are extremely abundant in the Universe (Cassan et al., 2012; Tuomi et al., 2014). These discoveries, together with missions to the Moon, Mars, other planets and satellites in our Solar system injected enough fuel that public and scientific interest in the field exploded.

This interest will continue growing with future missions, e.g. Transiting Exoplanet Survey Satellite (TESS), James Webb Space Telescope (JWST), Wide-Field Infrared Survey Telescope (WFIRST), and instead of only detecting exoplanets, such future missions will turn our focus to analyzing their physical and chemical characteristics. These, in turn, might be instrumental to answer one of the ultimate questions — how common are conditions suitable for life as we know it?

This thesis, while not about life in the known Universe, is still rather closely related. In the coming years, we will start to be able to judge whether an exoplanetary atmosphere has any bio-signatures. To judge whether such an atmosphere is altered by any biotic process, we must understand how these atmospheres come to be and later are modified by various abiotic processes (e.g. tectonic activity). The focus of this thesis is the formation of planets and the very early, hot primordial atmospheres. Seeing that planets are present around almost all stars (Cassan et al., 2012; Tuomi et al., 2014), we must conclude that planet formation occurs via a robust and common mechanism, and is not just an accidental or a highly unlikely event.

1.1 PROTOPLANETARY DISKS

Planets form inside protoplanetary disks, which are comprised of gas and dust and surround young stars for the first few million years of their evolution. In this section, I will neglect the outer surroundings of a forming star and the protoplanetary disk. As will be discussed in the next section, this simplification is somewhat erroneous, but it is sufficient for describing the basic dynamics of gas and dust in the disk. It is useful to further assume that pre-stellar cores are initially spherically symmetric and isothermal. In a pressurized medium, such a sphere can maintain hydrostatic equilibrium as long as it's mass is below the Bonnor-Ebert mass (Ebert, 1955; Bonnor, 1956),

$$M_{BE} = \frac{C_{BE} c_{iso}^4}{\sqrt{P_0 G^3}}, \quad (1.1)$$

where $C_{BE} \approx 1.18$ is a dimensionless constant, $c_{iso} = \sqrt{\frac{k_B T}{\mu}}$ is the isothermal sound speed (adiabatic index $\gamma = 1.0$) with μ being the molecular mass, k_B is the Boltzmann constant, T is the temperature, and P_0 is the external gas pressure. If the core exceeds this mass, it will inevitably experience an inside-out gravitational free-fall collapse.

The typical ratio of rotational to gravitational energy in dense cores is (Goodman et al., 1993):

$$\beta \equiv \frac{E_{rot}}{|E_{grav}|} \sim 0.02. \quad (1.2)$$

This small β value still corresponds to a substantial reservoir of angular momentum. The initial angular momentum prevents the gas from collapsing directly onto the protostar, and instead the gas and dust forms an accretion disk around the newborn star. Once gas settles into such a disk, where it rotates with near Keplerian speeds, its specific angular momentum increases with radius (Pringle, 1981), and thus, in order for accretion to proceed angular momentum must be redistributed or lost from the disk gas.

1.1.1 Disk Structure

The equilibrium structure of the protoplanetary disk is generally determined by near rotational balance radially, and by near-hydrostatic equilibrium ver-

tically, with self-gravity usually playing only a minor role. However, in some cases, even if a balance can be found, its dynamical stability is not guaranteed (Papaloizou & Pringle, 1984), especially when considering early, more massive disks, which may be self-gravitating and thus may have local instabilities. In general, disks function as buffers, which both gain and lose mass (Hernández et al., 2008) — mass is accreted from the disk to the central star, while simultaneously matter is accreted from the envelope onto the disk. Except at very early times the total mass of the disk is typically much smaller than the mass of the central star ($M_{\text{disk}} \ll M_*$), which allows us to neglect the gravitational potential of the disk and consider only the stellar gravity.

Disks have a large surface area, which implies they can cool efficiently via radiative heat transport, and therefore the temperature of disks is relatively low, as even a substantial accretion luminosity may be radiated away at relatively low temperatures. Such low temperatures and therefore low pressures are unable to support the gas against gravity except in geometrically very thin configurations $H/r \ll 1$, where H and r are the disk vertical scale-height and the radial coordinate of the disk, respectively. For such a thin disk, the vertical component of the gravitational acceleration may be approximated as $g_z \simeq \Omega_K^2 z$, and the vertical density profile takes the form:

$$\rho(z) = \rho_0 \exp\left(-\frac{\Omega_K^2 z^2}{2p_0/\rho_0}\right), \quad (1.3)$$

where ρ_0 and p_0 are the disk midplane density and pressure, respectively.

The density profile of the disk in the radial direction is more complicated. However, with a given surface density and temperature profile, the orbital velocity of disk gas may be determined. Ignoring viscosity and magnetic effects, the momentum equation is expressed as:

$$\frac{\partial \mathbf{v}}{\partial t} + (\mathbf{v} \cdot \nabla) \mathbf{v} = -\frac{1}{\rho} \nabla p - \nabla \Phi, \quad (1.4)$$

where \mathbf{v} is the velocity, ρ and p are the gas density and pressure respectively, and Φ is the gravitational potential. For a steady-state axisymmetric flow around the central star, the radial component of the momentum equation implies that the orbital velocity of the gas is given by:

$$\frac{v_{\text{gas}}^2}{r} = \frac{GM_*}{r^2} + \frac{1}{\rho} \frac{dp}{dr}. \quad (1.5)$$

Ignoring any local disk sub-structure (e.g. rings, gaps), the pressure near the disk midplane decreases radially outward, so the second term on the right hand side of Eq. 1.5 is negative and the azimuthal velocity of the gas is thus slightly less than the Keplerian velocity,

$$v_K = \sqrt{\frac{GM_*}{r}}. \quad (1.6)$$

The difference in velocities is typically $\sim 0.5\%$ (Armitage, 2013) and although this is small when considering the motion of the gas, it becomes very important for the motion of solids.

1.1.2 Solids in the Disk

Solid particles in protoplanetary disks are subject to gravity and centrifugal (inertial) forces, and they also feel aerodynamic drag from the disk gas. A spherical particle of radius s , moving at a velocity v relative to gas of density ρ_{gas} experiences an aerodynamic drag force which opposes its motion. There are two regimes to consider (Weidenschilling, 1977). In the Epstein regime, when $s \ll \lambda$, where $\lambda = \frac{\mu m_u}{\sqrt{2} \rho_{\text{gas}} \sigma_m}$ is the mean free path of a gas molecule (m_u is the atomic mass unit, $\sigma_m = \pi d_m^2$ is the molecular cross-section, with d_m being the effective molecular diameter), the aerodynamic drag force reads

$$F_D \simeq \frac{4\pi}{3} \rho_{\text{gas}} s^2 v v_{\text{therm}}, \quad (1.7)$$

where $v_{\text{therm}} = \sqrt{\frac{8k_B T}{\pi \mu m_u}}$ is the mean thermal velocity of the gas molecules. When particles are larger than the mean free path of gas molecules ($s \gg \lambda$), the drag force enters the Stokes regime, and reads

$$F_D = \frac{1}{2} C_D \pi s^2 \rho_{\text{gas}} v^2, \quad (1.8)$$

where the first term is the cross-sectional area of the grain, second is the ram pressure exerted on the grain, and the dimensionless drag coefficient C_D , which depends on the Reynolds number $Re = 2s\rho_{\text{gas}}v/\eta$, where η is the gas viscosity. The drag coefficient of a sphere is (Whipple, 1972)

$$C_D \simeq 24Re^{-1} \quad \text{for } Re < 1 \quad (1.9a)$$

$$C_D \simeq 24Re^{-0.6} \quad \text{for } 1 < Re < 800 \quad (1.9b)$$

$$C_D \simeq 0.44 \quad \text{for } Re > 800. \quad (1.9c)$$

It is practical to express the F_D in terms of the stopping time, t_s , which is the timescale on which frictional drag will cause an order-of-unity relative change in the momentum of the dust grain,

$$t_s = \frac{m_{\bullet} v}{F_D}, \quad (1.10)$$

where $m_{\bullet} = \frac{4}{3} \pi s^3 \rho_{\bullet}$ is the mass of the particle and ρ_{\bullet} is the mass density of the particle. In the Epstein regime the stopping time is therefore

$$t_s = \frac{\rho_{\bullet} s}{\rho_{\text{gas}} v_{\text{therm}}}. \quad (1.11)$$

Often a dimensionless Stokes number $St = t_s \Omega_K$, where $\Omega_K = \sqrt{GM_*/r^3}$ is the Keplerian frequency, G is the gravitational constant, M_* and r are the mass of and the distance to the central star, is used as a proxy of the particle size.

As the stopping time scales directly with the particle size the smallest particles are well coupled to the gas, while larger particles partially decouple. Tight coupling means that the particles are carried with the gas, and if the

gas is rotating with sub-Keplerian velocities, particles are unable to move at their preferred, Keplerian velocities and the residual gravity causes them to move inward. Indeed, already [Weidenschilling \(1977\)](#), and others before him ([Whipple, 1972](#)) deduced that particles with $St \sim 1$ (with typical parameters this corresponds to particles with sizes 10 – 100 cm) can drift radially towards the star over very short time scales. For a disk around a $1 M_{\odot}$ star, at 1 astronomical unit (AU) the peak drift velocities for 1 meter boulders can be $\geq 10 \text{ m s}^{-1}$, large enough that the particles would drift all the way to the star in ~ 100 years. This has been and still is one of the major issues in the planetesimal accretion scenario: either boulders have to grow extremely rapidly between 1 m and 1 km to overcome this drift barrier, or planetesimals must form at very large orbital distances and later the planets would migrate inwards. And yet, at large orbital distances, the collisional growth timescales are extremely long, and planets would not be able to form fast enough to have the observed properties.

1.1.2.1 Vertical Settling

Particles away from the midplane experience a vertical component of the force of gravity, which makes them settle towards the midplane. The settling velocity in the Epstein regime is

$$v_z = \frac{\Omega_K^2}{v_{\text{therm}}} \frac{\rho_{\bullet}}{\rho_{\text{gas}}(z)} z S, \quad (1.12)$$

so larger particles settle more rapidly than small ones (settling timescales are ~ 100 yr for 1 mm particle at 1 AU, and $\sim 10^5$ yr for $1 \mu\text{m}$ particle at 1 AU). However, even though settling times differ, particles of all sizes settle towards the midplane. In perfectly laminar disks this would mean that eventually all particles would settle to a razor-thin layer in the midplane.

1.1.2.2 Particle Growth

Small particles can grow in size via collisions with other particles. The mean growth rate of the smallest, sub- μm particles, which are assumed to be spherical, is

$$\frac{ds}{dt} = \frac{\rho_{\text{gas}}}{4\rho_{\bullet}} \sigma Z \varepsilon \quad (1.13)$$

where $\sigma = \sqrt{\frac{m_{\bullet}}{m}} c_s$ is the particle velocity dispersion, which for small particles in the lower limit is that of the Brownian motion, as the particles are very well coupled to the gas. Z in Equation 1.13 is the dust-to-gas ratio and ε is the sticking efficiency, which is assumed to be nearly 100% for the smallest particles and decreases with larger particle size.

As the particles grow, their stopping time increases and the velocity dispersion as well as the rate of radial drift increases. Moreover, cm-size particles simply do not stick together when they collide — they have a tendency to bounce, shatter and compactify instead. Imagine throwing rocks at each other

at high velocities. The last thing to expect would be to see the rocks sticking to each other. More likely such 'experiments' would risk hurting some innocent bystanders, when the rocks would bounce or shatter.

Suggestions have been made that would allow growth to continue. Possibly, as particles grow, they might become porous agglomerates rather than perfectly compactified, and may thus have better chances of sticking (Ormel et al., 2007). Also, experiments show that water-ice coating helps to improve the sticking efficiency. Certainly, collisional growth of particles has been and will continue to be studied extensively, via both numerical simulations and laboratory experiments (c.f. the reviews by Blum & Wurm 2008 and Testi et al. 2014 for detailed discussions of recent results). Many uncertainties remain, but the broad consensus is that collisional growth is only efficient up to sizes in the sub-mm to mm range and that collisional growth essentially stalls at this point. Probably it is not a coincidence that this is the size range of most chondrules we find in meteoritic samples (Friedrich et al., 2015).

1.1.3 *Instabilities*

Pebbles or chondrules are not planetary embryos. It is also clear that growing via collisions from centimeter-size particles all the way to kilometer-size objects is impractical, to say the very least. However, there are several mechanisms that can accelerate this slow and inefficient process.

1.1.3.1 *The Goldreich-Ward Mechanism*

In a perfectly laminar disk, vertical particle settling to the midplane increases the local dust-to-gas ratio until eventually the layer of solids becomes gravitationally unstable and fragments (Safronov, 1960; Goldreich & Ward, 1973). This happens when the Toomre criterion (Toomre, 1964) is satisfied:

$$Q = \frac{\sigma \Omega_K}{\pi G \Sigma_\bullet} \leq 1, \quad (1.14)$$

where Σ_\bullet is the column density of the solids. With canonical dust-to-gas ratio of 0.01, which would translate to 10 g cm^{-2} column density of solids in a 1000 g cm^{-2} gas column density disk, a velocity dispersion of $\sigma \leq 66 \text{ cm s}^{-1}$ at 1 AU is required for gravitational instability to occur. This is much lower than the local speed of sound in the gas (approximately 1 km s^{-1}), thus the solids indeed would have to settle to a razor-thin layer to fragment into bodies of $\sim 10^{16} \text{ g}$ mass (approximately km-size). That is an unlikely scenario, as when local dust-to-gas ratio increases, the feedback from the dust to gas starts to become relevant. In fact, such a razor-thin dust layer would exceed the local gas mass density by a factor of 100, and thus would absolutely dominate the local dynamics, rotating around the central star at Keplerian velocities. The gas above and below this local environment would, however, still be sub-Keplerian. This would create a large velocity shear between the vertical layers, and thus the Kelvin-Helmholtz instability would inevitably oc-

cur. Such an instability would prevent particles from settling to a thin enough layer, by increasing the velocity dispersion of the particles.

1.1.3.2 *Streaming Instability*

The two-fluid streaming instability (Youdin & Goodman, 2005) is driven by the velocity difference between dust and gas. Solid bodies move faster with respect to the gas, and consequently feel a headwind drag force. However, if solids clump together in sufficiently large concentrations, the solids start to shield each other from the headwind and the drag force is reduced. This in turn leads to further concentration of particles, as large clumps decouple from the gas and “trap” more solid bodies. This process can run away and eventually the particle clumps become self-gravitating and can collapse to form planetesimals or planetary embryos (Johansen et al., 2007). However, the development of the streaming instability is very sensitive to the local dust-to-gas ratio, and is most efficient for 10 cm – 1 m size bodies, which, as discussed above, are difficult to make. On the other hand, it may be efficient in turbulent disks, where boulders concentrate in transient high pressure regions in the turbulent gas (Johansen et al., 2006). In addition, the vertical shear instability (Stoll & Kley, 2016) may induce turbulence that can drive the streaming instability.

1.1.3.3 *Snow lines and ionization lines*

The radial drift of pebbles stops if they encounter a zone where the gas is also moving in Keplerian velocities. This can happen e.g. at a local pressure maximum created by a snow-line, where temperatures become low enough that particular molecular species can freeze out (e.g. at a water snow line). Such snow lines may create significant pressure bumps that can stop the radial drift of pebbles (e.g. Schoonenberg & Ormel 2017). Dead-zone inner boundaries, where easily ionized atomic species such as Na and K are ionized is another possible location of pressure maxima (e.g. Tan et al. 2016).

1.1.3.4 *Gravitational Instabilities*

It seems that during the last several decades many scientist were trying to independently “solve” the planet formation problems, since here are so many different variations of the same phenomenon: gravitational instability. And it doesn’t cover just particles—as long as Toomre instability criterion is satisfied, even the gas can become unstable, especially in young, massive disks. This is one of the proposed scenarios for giant planet formation (e.g. Boss 1997; Boley 2009; Galvagni et al. 2012), but local disk instabilities can also occur in vortices (e.g. Barranco & Marcus, 2005; Fuente et al., 2017; Barge et al., 2016), or even in spontaneously occurring large amplitude perturbations (Hopkins & Christiansen, 2013).

1.1.3.5 *Observed disk sub-structures*

As it is now possible to spatially resolve the structure of young protoplanetary disks, e.g., with Atacama Large Millimeter Array (ALMA), it is becoming apparent that the majority of protoplanetary disks have rich sub-structures of rings, gaps, vortices and spirals (e.g. van der Marel et al. 2013; Isella et al. 2013; Casassus et al. 2013; ALMA Partnership et al. 2015; Andrews et al. 2016; Meru et al. 2017). It is still debated whether some of these disk features are caused by embedded planets, or if they are precursors of planet formation (see any of the references above), but it seems likely that they are in one way or another closely related to planet formation. Some of these disk features may originate from internal sources of perturbation (e.g. snow lines), while others may be closely related to the external environment of the forming star and the protoplanetary disk.

1.2 STAR FORMATION AND PROTOPLANETARY DISK ENVIRONMENTS

Investigating completely isolated protoplanetary disks is useful when only the local effects of the main processes involved are considered, but is in principle erroneous, and may give rise to conclusions that work for isolated disks, but might not hold true in reality, where disks are embedded in a larger scale environment.

All stars are born in dense cores inside turbulent giant molecular clouds, with masses ranging up to $\sim 10^7 M_{\odot}$. Local compressions by the turbulence form denser regions, where the gravitational energy starts to dominate over the kinetic energy (Padoan et al., 2012). The turbulence has been proposed to be sustained internally by stellar outflows (Goldbaum et al., 2016) and regions of ionized hydrogen (Walch et al., 2012), or by external mechanisms include accretion flows (Klessen & Hennebelle, 2010) and supernova feedback (Kim & Ostriker, 2015). As shown by Padoan et al. (2016a) the latter is most likely the main source of turbulence in star forming giant molecular clouds.

A typical giant molecular cloud has a diameter of ~ 50 parsec (pc) with internal velocity dispersion of about $8-10 \text{ km s}^{-1}$, which for a cloud with typical temperature of 10 K corresponds to a Mach number of about 40-50 (the sound speed is $\sim 0.2 \text{ km s}^{-1}$). Additionally, giant molecular clouds have magnetic fields with typical strengths between 3 and $10 \mu\text{G}$. Only a small fraction (1 – 10%) of the gas mass in the giant molecular cloud eventually ends up in stars. The typical lifetime of such a giant molecular cloud is 20–30 Myr (Padoan et al., 2016b).

The interaction between the magnetic fields and turbulence lead to formation of filamentary structure inside the giant molecular clouds, as indicated both by observations (e.g. Bally et al. 1987; Mizuno et al. 1995) and numerical simulations (e.g. Padoan et al., 2001; Li et al., 2010). As turbulent motions further compress these filaments, dense cores with masses up to $100 M_{\odot}$ form inside the filaments (Men'shchikov et al., 2010). These cores eventually collapse under their own gravity into the single/binary/multiple pre-

stellar cores. Indeed, a large fraction of all stars form together in binaries or multiples (e.g. [Sadavoy & Stahler 2017](#)). This consequentially means that protoplanetary disks often interact with each other, as indicated by both observations (e.g. [Jensen & Akeson 2014](#)) and simulations (e.g. [Zanazzi & Lai 2017](#)).

Synthetic observations of very high resolution magnetohydrodynamic simulations of star formation show that disks form very early (e.g. [Frimann et al. 2016](#)), also supported by observations (e.g. [Tobin et al. 2015](#)) and are a subset of more general, accretion disks. They act as buffers in between two accretion flows — the external one, onto the disk, and the internal one, onto the star. The two do not need to be identical at any one time, and if they are not it just means that the disk is changing mass. The accretion itself is heterogeneous — there are occasional violent accretion bursts (e.g. [Frimann et al., 2017](#); [Kuffmeier et al., 2017](#)). These outbursts can move the molecular ice lines (and corresponding potential pressure bumps) outwards ([Frimann et al., 2017](#)). The large scale simulations (e.g. [Kuffmeier et al. 2017](#) and references therein) where thousands of stars form show that disks form generically, but with properties that vary very much.

Large scale magnetohydrodynamic simulations of star formation indicate that the majority of angular momentum during the stellar collapse is transported away by large-scale magnetic fields during the formation phase of protoplanetary disks. This mitigates the “angular momentum problem” in standard accretion disk scenarios ([Shakura & Sunyaev, 1973](#); [Lynden-Bell & Pringle, 1974](#)), where completely isolated disks are considered.

1.3 PLANET FORMATION

Any instability in a protoplanetary disk can potentially lead to formation of planetary embryos, which then start growing. To this day there is still several planet growth scenario being advocated for.

The planetesimal accretion hypothesis still have claims to be relevant, but with accumulating new observational and experimental evidence, it is rapidly losing it’s momentum despite numerous attempts to fine-tune and modify the scenario to come in line with the evidence. In this hypothesis, a planetary embryo is impacted by kilometre-size bodies and their mass is added to the embryo (e.g. [Pollack et al., 1996](#); [Hubickyj et al., 2005](#)). At some point the embryo becomes massive enough that gravitational focusing ([Greenberg et al., 1978](#)) becomes important and the embryo enters what is commonly called the ‘runaway growth’ phase. For this part of the hypothesis to happen, we need to assume that all kilometre-size bodies formed at more or less the same time and in large enough numbers to form a planet or even a planetary system. As discussed above, meeting these requirements is rather difficult.

When the embryo grows massive enough to gravitationally stir up nearby planetesimals, enhancing their eccentricities and effectively kicking them out of the feeding zone, the planetesimal accretion ends, as there is no remaining solid material in an embryo’s ‘feeding zone’ ([Ida & Makino, 1993](#)). Now,

the somewhat isolated protoplanet transitions to a much slower, ‘oligarchic growth’ phase (Kokubo & Ida, 1998). In this phase, the few largest mass protoplanets grow oligarchically, while the remaining planetesimals mostly remain small. The critical time scale in this context is the lifetime of the protoplanetary disk, which is of the order of several million years (e.g. Bell et al. 2013). However, numerical simulations of the planetesimal accretion hypothesis have the problem that they predict that it takes much longer than a protoplanetary disk lifetime for cores to grow to observed planetary masses (e.g. Levison et al., 2010; Bitsch et al., 2015b).

This scenario was a natural outcome from observations of the Solar system — here we have small terrestrial planets, giant planets and “planetesimals” — asteroids and comets. Seeing numerous craters on the surfaces of planets and moons, it was a natural stretch to predict that asteroids and comets were the main building blocks.

However, there is a much simpler explanation, according to which planets grow via “pebble accretion” (Ormel & Klahr, 2010; Johansen & Lacerda, 2010; Nordlund, 2011; Lambrechts & Johansen, 2012; Morbidelli & Nesvorny, 2012; Lambrechts & Johansen, 2014; Bitsch et al., 2015b; Chatterjee & Tan, 2014; Visser & Ormel, 2016; Ormel et al., 2017, etc.). “Pebbles”, in the astrophysical context, are millimetre to decimetre-sized particles, similar to small rocks in any garden or the chondrules found in the artefacts from the formation of the Solar system—meteorites. Their stopping times, t_s , are comparable to their orbital period, $t_s \sim \Omega_K^{-1}$. Due to efficient growth to approximately $\mu\text{m} - \text{cm}$ size and highly inefficient growth to larger sizes, pebbles are likely to form a significant part of the solid mass budget in protoplanetary disks. This is also indicated by both dust continuum observations (e.g. Testi et al. 2003; Lommen et al. 2009) and by the mass fraction of chondrules in chondritic meteorites (Johansen et al., 2015; Bollard et al., 2017). Due to the difference in speed between the slightly sub-Keplerian gas (and dust) and the Keplerian embryo (due to its large size, the gas drag is negligible for the embryo), pebbles “rain” down on the embryo as it moves through its orbit. As the mass of the embryo grows, the efficiency of gravitational focusing of pebbles increases, and the effective accretion cross section becomes larger than the embryo itself.

The radius of dominance of the gravitational force of a planet relative to the central star is approximately given by the Hill radius:

$$R_H = a \sqrt[3]{\frac{M_p}{3M_*}}, \quad (1.15)$$

where a is the semi-major axis of the embryo’s orbit, M_p and M_* are the masses of the embryo and the central star, respectively. Pebbles of suitable size, passing the embryo even as far away as the Hill radius may be accreted, as has been shown analytically by Ormel & Klahr (2010), using test particle integrations on top of hydrodynamical simulations by Morbidelli & Nesvorny (2012) and using numerical simulations with particles by Lambrechts & Johansen (2012); Popovas et al. (submitted). These works show that the pebble accretion is very efficient: the planets can grow to the observed masses well

within the lifetime of a protoplanetary disk, even at large orbital distances from the host star.

Of course there could be an occasional planetesimal impact, but the mass fraction in these objects should be negligible, when compared to the mass budget in pebbles and the contribution of direct planetesimal accretion to the growth of planetary embryos is of less importance (Johansen et al., 2015). Forgetting the planetesimal accretion scenario as being an important contributor to the planet formation simplifies things a lot.

1.3.1 *Primordial atmospheres*

When the gravitational energy of the embryo exceeds the thermal energy of nearby gas, the gas becomes bound to the embryo. This condition is satisfied when the escape velocity from the surface of the embryo, v_{esc} , exceeds the local thermal speed of the disk's gas. The nearby gas will always roughly satisfy hydrostatic equilibrium and, as the mass of the core grows, so too does the gas envelope around it. The mass in such an envelope is completely determined (apart from the equation of state) by the pressure and temperature at the outer boundary. This envelope has very important consequences:

First of all, the increased density around the embryo means that the aerodynamic gas drag the pebbles feel in the vicinity of the embryo also increases and thus their stopping time drops. This is the same Weidenschilling effect (Weidenschilling, 1977), which was so dreaded when the planetesimal accretion hypothesis was the main scenario. Here instead of making planet growth very complicated, the mechanism actually helps them grow faster—particle velocities are damped and they feel relatively stronger effects of gravitational attraction. However, this comes with a price—near planet gas dynamic becomes important and is in fact currently a very active research topic (e.g. Ormel et al., 2015b; Cimerman et al., 2017; Masset & Benítez-Llambay, 2016; Xu et al., 2017; Fung et al., 2015; Lambrechts & Lega, 2017).

With typical dust opacities on the order of $0.1 - 1 \text{ cm}^2 \text{ g}^{-1}$, disks with surface densities similar to the Minimum Mass Solar Nebula (MMSN) (Hayashi, 1981) are optically thick in the vertical direction, since the MMSN nominally has 1700 g/cm^2 at 1 AU. This means that the primordial atmosphere is nearly adiabatic and can become very hot close to the surface of the protoplanet, if the protoplanet is massive enough (e.g. 3000–4500 K close to the surface of $1 M_{\oplus}$ embryo, depending on the equation-of-state). This temperature is much higher than the melting point of any solid, thus pebbles can evaporate. Evaporation of solids and the resulting enrichment of the atmosphere with heavy elements (e.g. Alibert 2017; Brouwers et al. 2017) is bound to play an important role in chemical and physical evolution of primordial atmospheres.

The effective, dynamical boundary between the disk and the primordial atmosphere occurs at distances from the surface of the planetary embryo some-

where in the range between the Hill radius and the canonical Bondi radius,

$$R_B = \frac{GM_p}{c_{\text{iso}}^2}, \quad (1.16)$$

In fluid dynamics, the Bondi radius actually has no particular dynamical significance, other than being the radius where the pressure scale height of the atmosphere becomes comparable to the distance from the embryo, and the radius where Mach 1 gas speeds would become unbound.

1.3.2 Planet – Disk Interaction

Forming planets undergo gravitational interactions with their parent disks — angular momentum and energy exchange, which leads to long term orbital evolution of the planets. In 1979 [Goldreich & Tremaine \(1979\)](#); [Lin & Papaloizou \(1979\)](#) laid the groundwork for understanding this planet – disk interaction. Protoplanets exert a gravitational force onto the surrounding material, and the force leads to a net torque at Lindblad resonances. Figure Fig. 1.1 shows a cartoon of the topology of the flow field. The streamlines (black arrows) refer to the corotating frame with the planet (black circle). The corotation region (dashed red circle) effectively splits the disk into two parts — the inner region, where the gas rotates faster and the outer region, where the gas has a lower Keplerian velocity. The corotating region is commonly referred to as the horseshoe region. The Keplerian shear carries away these perturbations in the form of density wakes. These wakes are not symmetric with respect to the line connecting the planet and the central star and gravitational torques are exerted on the planet. This causes the planet to lose or gain angular momentum, depending whether the leading or the trailing arm exerts more force.

Below, I will briefly summarize the effects of the disk – planet interaction. The detailed physics of the gravitational interaction between a planet and a surrounding gas disk is very subtle, and several important details remain poorly understood ([Kley & Crida, 2008](#); [Kley et al., 2009](#); [Paardekooper et al., 2010, 2011](#); [Benítez-Llambay et al., 2015](#)), and to this date this remains an active research field. There are a number comprehensive reviews of planet – disk interaction (e.g. [Kley & Nelson 2012](#); [Baruteau & Masset 2013](#); [Mordasini et al. 2015](#)) and undoubtedly more development will be done in coming years.

TYPE I PLANET MIGRATION occurs for low-mass planets whose interaction with the disk is weak and the disk structure is almost unperturbed with a mild exception to the density wakes. These wakes usually have a few percent difference in density with respect to the unperturbed background density values. The local exchange of angular momentum between the planet and the disk is negligible compared to the redistribution of angular momentum due to disk viscosity. The planet remains fully embedded within the gas disk and material is present at all resonant locations. Depending on a number of local conditions, the planet can migrate either outward or inward. Under certain

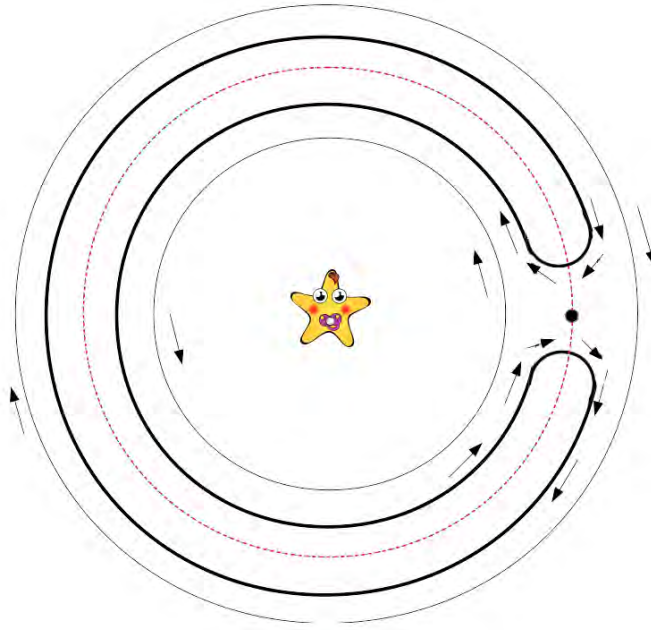


Figure 1.1: A cartoon, depicting the topology of the flow field, where the streamlines refer to the corotating frame. The disk is split into an inner disk with circulating streamlines, a horseshoe corotation region within the thick curves, and an outer disk of circulating gas.

conditions, i.e. when a planet is forming in an isolated and strong pressure trap, it doesn't experience any headwind and torques may cancel out or be very weak. Therefore, under such conditions planets may not experience significant type I migration.

TYPE II PLANET MIGRATION occurs for higher mass planets, whose gravitational torques locally dominate angular momentum transport within the disk. Gravitational torques from the planet repels disk gas away from the orbit of the planet, and eventually the planet opens an annular gap within which the disk surface density is reduced from its unperturbed value. This happens when the Hill radius of the planet becomes larger than the scale height of the disk. Then disk can be regarded as thin compared to the gravitational potential of the planet. Resonances close to the planet are severely depleted of material and contribute little or nothing to the total torque. When the gap is opened two outcomes are possible:

1. If the disk is massive enough, accretion continues and the planet is simply pushed inward. The planet is effectively locked to the disk accretion. This push of the planet is deemed type II migration.
2. If the disk is not massive enough, the planet will not migrate, but the inner disk will deplete.

TYPE III RUNAWAY MIGRATION can occur when the planet is already experiencing the Type II migration. If the planet initially moves inward, some inner disk material enters the horseshoe and consequently gets flung to the outer orbit of the horseshoe by the planet. The planet loses angular momentum. At the same time, some horseshoe material enters the outer disk, but does not get flung back to the inner orbits of the horseshoe. This leads to a one-sided asymmetric angular momentum transport from the planet to the disk, resulting in an inward push. The same thing, but the other way around, happens if the planet initially moves outward.

1.3.3 *Gas Retention and Fractionation in the Primordial Atmospheres*

If the external pressure from the disk to the primordial atmosphere is reduced (e.g. when the protoplanetary disk starts to dissipate), the mass of the atmosphere will also get smaller. This implies that mass must be lost from such atmospheres if / when the disk evolves to lower densities (Nordlund, 2011; Schlichting et al., 2015; Ginzburg et al., 2016; Rubanenko et al., 2017). In the extreme, where the primordial atmosphere remains perfectly adiabatic (i.e. does not cool at all), as the disk dissipates the atmosphere would try to maintain hydrostatic equilibrium, and would dissipate to the extent that nearly all the atmosphere would be stripped away. However, gas can cool radiatively, and as the gas cools the thermal velocity of the gas molecules decreases, and the atmosphere shrinks to a size compatible with the lower temperature, thus effectively shutting down the hydrodynamic escape mechanism (Nordlund, 2011). As the thermal velocity of the gas molecules becomes lower than the thermal escape velocity, the effective Bondi radius (Eq. 1.16) increases. However, the squared thermal velocity of a gas molecule also scales inversely with the mass of the molecule. This leads to two important conclusions:

1. The mass of the retained atmosphere strongly depends on the mass of the core **and** the opacity of the gas and dust.
2. Lighter elements are lost easier than the heavy ones.

The first point means that a planet with a low opacity envelope would retain much heavier atmosphere than an exactly the same mass planet, but with a high opacity envelope. The second point indicates that lower mass planets would preferentially lose lighter elements, while retaining the heavier ones (e.g. Earth-mass planet, if not cooled fast enough, would lose H₂ and He, but a fraction of N₂, CO would be retained), whereas larger mass planets could retain also some of the lighter elements.

1.4 THE DIVERSITY OF PLANETARY SYSTEMS

To date there is 2950 confirmed exoplanets¹ and more than 2300 unconfirmed planet-candidates. Figure 1.2 shows the mass distribution of all detected exo-

¹ Based on exoplanets.org retrieved February 15, 2018

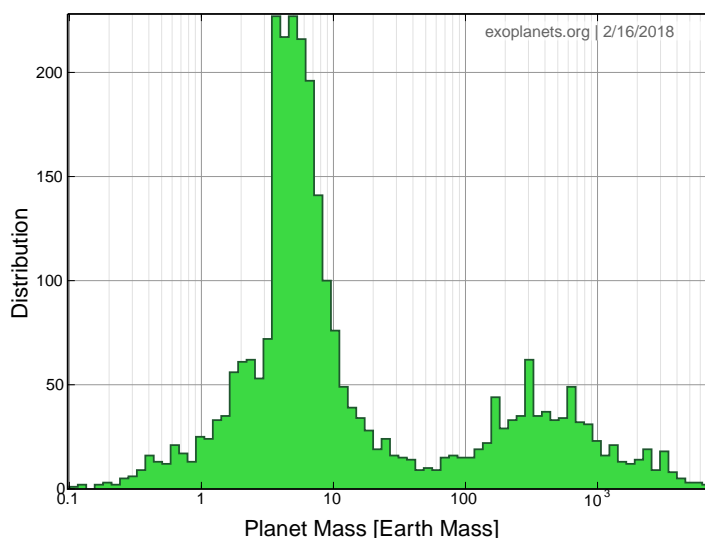


Figure 1.2: Exoplanet mass distribution. Source: exoplanets.org

planets. The masses of confirmed exoplanets to date range from sub-Earth (e.g. [Jontof-Hutter et al. 2015](#); [Gillon et al. 2017](#)) to approximately 30 Jupiter masses (e.g. [Konopacky et al. 2016](#); [Sahlmann et al. 2013](#)), with orbital distances from parent stars ranging from 0.006 AU (e.g. [Charpinet et al. 2011](#); [Smith et al. 2018](#)) to 160 AU (e.g. [Beust et al. 2014](#)). They are found around essentially all types of stars (different mass, metallicity), pulsars, even free-floating — they seem to be everywhere and with a very wide range of physical and chemical qualities. Figure 1.3 demonstrates that even the same mass planets can have a wide range of different radii, which indicates that they have rather different atmospheric content. To our surprise, the majority of detected exoplanets to date are of a type that we don't have here in the Solar system — gaseous, sub-10 M_{\oplus} gas dwarfs, super-Earths, and ice-dwarfs. If we had had such planets in our system, perhaps planet formation theories would have evolved differently.

This diversity of planets is not only natural, but arguably an unavoidable consequence of the very diverse formation environments. First of all, stellar hosts have a large variety of masses and metallicities, and although one can generally expect that stars reflect their birthplaces (e.g. [Andrews et al. 2013](#); [Ribas et al. 2015](#)), even the same mass star can be formed in many different ways, with formation times (and likely protoplanetary disk existence times) that span at least an order of magnitude, and probably more ([Padoan et al., 2014](#); [Kuffmeier et al., 2017](#)).

1.4.1 *The Regularity of Planetary Systems*

Even though systems are so diverse, they display astonishing aspects of regularity: the transition between "types" of planets is smooth, with deviations from different formation environments (2 M_{\oplus} planet can be an ice dwarf with a substantial atmosphere and therefore with an extended radius, and at the

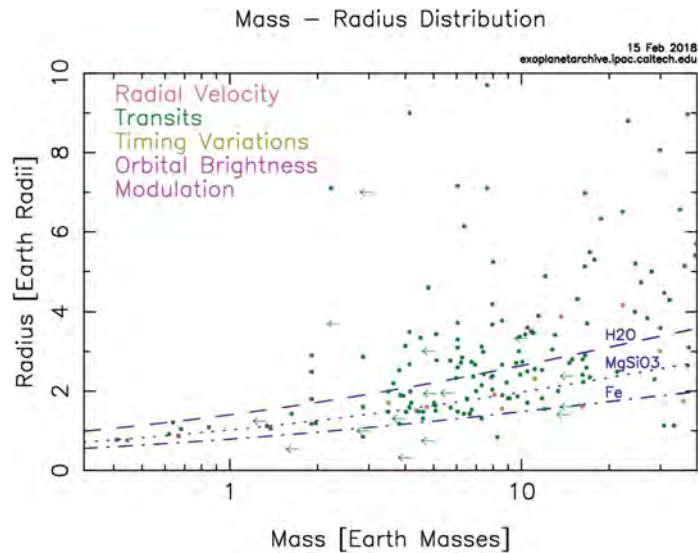


Figure 1.3: Exoplanet mass – radius distribution. Different curves represent different composition, based on models. Source: NASA exoplanet archive, <https://exoplanetarchive.ipac.caltech.edu>

same time $7 M_{\oplus}$ might barely have an atmosphere). Multiple planet systems (e.g. Tuomi 2012; Vogt et al. 2015; Gillon et al. 2017) are usually rather tightly packed, and do not show prominent indications of migration — only about 2% of multi-planet systems show signs of planets being in or near mean motion resonances (Fabrycky et al., 2014; Goldreich & Schlichting, 2014), although there are possible explanations that involve perturbations and destruction of resonances (e.g. Goldreich & Schlichting 2014; Liu et al. 2017).

In any case, the large numbers of exoplanets indicate that the formation of planets takes place via a very robust and simple mechanism — if the formation process would be very complicated and unlikely we would not be able to see so many exoplanets. At the same time, the diversity of physical and chemical properties of exoplanets indicate that many secondary effects exist, which can alter the planet formation pathways, leading to an end “result” that displays both systematic and stochastic properties.

RESEARCH GOALS AND METHODS

2.1 SHORT DESCRIPTION AND OBJECTIVES

The scientific method involves making hypotheses, deriving predictions from them as logical consequences, carrying out experiments based on those predictions and then comparing the results to determine whether the original hypothesis was correct. In astrophysics, relevant processes have an enormous range of spatial and temporal scales — from galaxies, giant molecular clouds, stars and planets to atomic-level processes defining the local thermodynamics. Most, but not all, of these scales influence each other in some way. It is, however, more efficient and sometimes necessary to separate them — an orbit of a moon around a planet is in no way affected by the turbulent motions of a giant molecular cloud in a different part of the galaxy. Although we can conduct experiments with gases and small dust particles here on Earth (e.g., [Blum & Wurm 2000](#); [Güttler et al. 2010](#)), we cannot form a planet in a laboratory. Observations and laboratory measurements provide us with important constraints, but they provide either only a two-dimensional projection of a four dimensional phenomena (time being the 4th dimension) or sample only a very limited environment — meteoritic samples provide a great deal of information about the formation history of the Solar System, but they sample only the Solar System, whereas astronomical observations provide a vast sample of stellar and planetary systems, albeit with limited temporal and spatial resolution. Furthermore, many astrophysical problems simply cannot be solved analytically and instead require numerical solutions, e.g., fluid dynamics. Luckily, in recent decades, the development of computational facilities enables us to simulate physical processes with unprecedented complexity, with conditions moving ever closer to reality.

Many astrophysical problems, due to their intrinsic complexity, are simplified as much as possible, resulting in ‘academic experiments’ and, although they can provide many physical insights, they can also have very little in common with reality. With time, such experiments can be extended to include more complexity and realism. Sometimes, however, when this build-up occurs over a long period of time, an important initial assumption is forgotten. One such example is the way total internal partition functions and resulting thermodynamic quantities are calculated. [Herzberg \(1950\)](#) indicated that, for a particular temperature range (actually — in the vicinity of 1000K) harmonic oscillator and rigid rotor approximations are sufficient to obtain accurate enough partition functions. Somewhere along the way though, the initial assumption of a ‘particular temperature range’ was forgotten and these approximations were used arbitrarily and outside their range of validity. In

some cases, by luck, this did not yield detectable errors, but, in general, the error is indeed significant (Paper I).

As the available computing power has increased exponentially over time, so too has the fidelity and complexity of astrophysical fluid simulations. These simulations have consistently been at the limit of what is computationally possible. The algorithms and techniques used to exploit the available resources have also increased in ingenuity and complexity over the years. As the next step in High Performance Computing (HPC), ‘exa-scale’, is approaching, and as currently available tools reach their limits (e.g. [Dubey et al. 2014](#)), my collaborators and I have developed the new, exa-scale ready DISPATCH framework, which employs novel paradigms and techniques that can fully exploit the upcoming generation of supercomputers (Paper II).

The DISPATCH framework was designed with the efficient simulation of planet formation in mind. By having both very high spatial resolution and dynamic range, we can accurately simulate gas dynamics close to planetary embryos simultaneously with a significant fraction of the protoplanetary disk. Other groups have shown that pebble accretion is a very efficient process ([Ormel & Klahr, 2010](#); [Lambrechts & Johansen, 2012](#); [Morbidelli & Nesvorny, 2012](#); [Lambrechts & Johansen, 2014](#)), but many uncertainties remain — e.g. how pebble accretion rates relate to disk surface densities, particle size and their distribution in the disk. These uncertainties can be understood via hydrodynamical simulations which include particles that feel the effects of gas drag (i.e. not just trace particles), are numerous enough and have a sufficiently large size distribution to reduce the statistical noise significantly (paper III).

It has been clear for some time now that microphysical effects, such as realistic opacities, realistic radiative energy transport or realistic equations of state, contribute significantly to the uncertainties in planet formation described above (e.g. [Ormel 2014](#); [Venturini et al. 2016](#)). Unfortunately, including even several of these effects was previously highly computationally expensive. Now many groups start including them with a varying degree of complexity and see the dramatic effects they make (e.g. [D’Angelo & Bodenheimer 2013](#); [Piso et al. 2015](#); [Szulágyi et al. 2016](#) and Paper IV).

2.2 PUBLICATIONS

This thesis consists of three papers, published (or submitted) in refereed journals:

1. [Popovas & Jørgensen \(2016\)](#): Partition functions. I. Improved partition functions and thermodynamic quantities for normal, equilibrium, and ortho and para molecular hydrogen
2. [Nordlund et al. \(2018\)](#): DISPATCH: A Numerical Simulation Framework for the Exa-scale Era. I. Fundamentals
3. [Popovas et al. \(submitted\)](#): Pebble dynamics and accretion onto rocky planets. I. Adiabatic and convective models

The final and fourth paper consists of research which is ready to be submitted, but is intentionally being held back until the third paper is close to being accepted for publication because it is a direct sequel to the third paper. I have devoted a chapter in the second part of this thesis to each of the above mentioned papers in the order by which they were published. The papers are redacted to conform with the thesis layout — to enhance the readability of figures and sub-figures, they are split and enlarged. The only modifications to the text are related to the splitting of figures. Here, I briefly summarize the main messages and outcomes of the papers.

2.2.1 *Paper I: Partition functions. I. Improved partition functions and thermodynamic quantities for normal, equilibrium, and ortho and para molecular hydrogen*

The roots of this study lie in my Master’s thesis, “Stellar model atmospheres of late stellar type stars”, where we accidentally noticed large discrepancies in the total internal partition functions of various molecules found in the literature. Since molecular hydrogen is by far the most abundant molecule in the Universe and plays a key role in most astrophysical processes, we conducted an in-depth analysis of the errors. After investigating the reasons for the discrepancies, we described the various simplifications used to calculate partition functions and what error (not uncertainty) they introduce. Together with a prescription for the currently most accurate way to calculate the partition functions, we presented the total internal partition functions and thermodynamic quantities for normal, equilibrium, ortho- and para-molecular hydrogen in the temperature range 1–20000K. In this work, we concluded that, for most of the relevant astrophysical cases, it is strongly advised to not use simplifications, such as the harmonic oscillator or rigid rotor approximations to estimate accurate partition functions.

2.2.2 *Paper II: DISPATCH: A Numerical Simulation Framework for the Exascale Era. I. Fundamentals*

This paper presents a new, highly efficient computational framework that employs existing solvers adapted from other codes, but with a significant increase in computational speed. It uses a *dispatcher* (hence one source for the name) for task-based scheduling, local asynchronous time-stepping and DISconnected PATCHes (hence the other source for the name) and continuous load balancing of tasks between nodes. The definition of a task is flexible, and current possibilities include the solution of the equations of ideal magnetohydrodynamics, radiative transfer, particle motion, or even implementation of particle-in-cell methods. Tasks are not required to be grid-based, but tasks that are may use either Cartesian or orthogonal curvilinear meshes. Åke Nordlund and Jon P. Ramsey are the main developers of the framework, whereas I developed the radiative energy transport module. This framework was designed with efficient simulations of planet formation in mind, but with its efficient

asynchronous time-stepping and parallel scalability, the dynamic range can be extended to global disks, giant molecular clouds or even galaxies (while still including planets at the highest level of refinement). DISPATCH is the main tool I utilized for the research presented in this thesis.

2.2.3 *Paper III: Pebble dynamics and accretion onto rocky planets. I. Adiabatic and convective models*

This paper presents a series of nested-grid, high-resolution hydrodynamic computer simulations of gas and particle dynamics in the vicinity of Mars- to Earth-mass planetary embryos. The simulations extend from the surface of the embryos to a few vertical disk scale heights with a highest resolution close to the embryo of $\sim 3\%$ of the embryo radius. Instead of using an unrealistic ‘softening’ of the gravitational potential, we used a ‘solid’ spherical boundary. Using test simulations, we have ensured that our boundary conditions remain stable over long periods of integration time and under rather extreme conditions whilst remaining physically accurate.

In the simulations, we used up to 56 million particles with sizes ranging from $10\ \mu\text{m}$ to $1\ \text{cm}$ (i.e. dust to pebbles) and with a flat size distribution in logarithmic size. The initial spatial distribution of macro-particles is chosen to be proportional to the local gas density. Rather than having to make assumptions about the particle settling, we instead analyse sub-populations of our initial distribution, tagging and following, for example, only the particles that initially reside within a given distance from the midplane. The motion of the particles was followed, taking into account drag forces relative to the gas, while feedback from the particle ensemble on the gas was neglected. We confirm that only a small fraction of all the pebbles that cross the Hill sphere are accreted. The pebble accretion rates scale linearly with the size of the pebbles and are, due to cancellation effects, nearly independent of disk surface density if the dust-to-gas surface density ratio is constant. With the determined accretion rates we estimated planet growth times for specified particle sizes. For chondrule-size ($0.3\text{--}1\ \text{mm}$) particles, the growth time from a small seed is ~ 1.5 million years for an Earth mass planet at $1\ \text{AU}$ and ~ 1 million years for a Mars mass planet at $1.5\ \text{AU}$. For larger size particles and for enhanced ratios of dust-to-gas surface density, the estimates are correspondingly shorter. This is an important finding, as it indicates that rocky planets in the Solar System could have formed from an essentially chondrule-like particle distribution.

In some of the simulations, we accounted for the heating arising from the accretion of solids onto the embryo, which releases a lot of potential energy and is converted to heat via the friction force. The resolution of our simulations was sufficient to resolve the convective motions of the gas. Although convection significantly modifies the gas thermodynamics within ~ 40 radii of the planet, it does not affect the particle accretion rates in any significant manner.

2.2.4 *Paper IV: Pebble dynamics and accretion onto rocky planets. II. Radiative models*

In this letter, we continue to investigate the gas and pebble dynamics close to planetary embryos. Unlike in paper III, here we consider only a single mass embryo — $0.95 M_{\oplus}$, but instead consider the radiative energy transport including realistic, albeit schematic, scattering. We find that radiative cooling effects do not penetrate down to the very bottom of the atmosphere, where convection is the dominant mechanism of energy transport. However, in response to the tendency of cooling to increase the radial temperature gradient, the amplitude of convective motions increase by nearly an order of a magnitude near the embryo surface. This implies that planetary embryos embedded in a protoplanetary disk can retain hot and hence relatively light atmospheres throughout much of the evolution of the protoplanetary disk.

2.3 OWN CONTRIBUTIONS VERSUS CONTRIBUTIONS OF COLLABORATORS

This section states my own contribution to the papers and the contributions of the co-authors, respectively.

PAPER I All data collection from the literature and analysis was carried out by myself. I made all of the figures and tables in the paper. The initial draft of the paper was written by myself and then all the aspects of the text as well as formulation of conclusions were discussed in detail and edited by both authors.

PAPER II The paper was primarily written by Åke Nordlund and Jon P. Ramsey. I was the main developer of the radiative energy transport package and I wrote the corresponding sections in the paper including the presented “shadow” benchmark. The “shadow” benchmark itself was set up and run together with Jon P. Ramsey.

PAPER III All the simulations were carried out by myself. The initial and boundary conditions were set up through close collaboration of all of the authors. The data post-processing and analysis, which included writing the data analysis tools from scratch, was performed by all of the authors. I enabled the reading of DISPATCHoutput by the YT project for analysis and visualisation (Turk et al., 2011). I made all the figures and tables, except for the Hammer projection plots, which were created by Jon P. Ramsey. I wrote the initial draft of the manuscript, which was later was edited by all authors.

PAPER IV All the simulations were carried out by myself. The formulae for the radiative energy transport were set up together with Åke Nordlund. The data post-processing and analysis was done by all the authors. I made the

figures and wrote a large fraction of the text, which was later edited by all authors.

Part II

THE RESEARCH

PAPER I: PARTITION FUNCTIONS 1: IMPROVED
PARTITION FUNCTIONS AND THERMODYNAMIC
QUANTITIES FOR NORMAL, EQUILIBRIUM, AND
ORTHO AND PARA MOLECULAR HYDROGEN

Andrius Popovas¹ and U. G. Jørgensen¹

¹ Centre for Star and Planet Formation, Niels Bohr Institute and Natural History Museum of Denmark, University of Copenhagen, Øster Voldgade 5-7, DK-1350 Copenhagen K, Denmark

Appeared in *Astronomy & Astrophysics*, vol. 595, article no. A130, November 2016

Hydrogen is the most abundant molecule in the Universe. Its thermodynamic quantities dominate the physical conditions in molecular clouds, protoplanetary disks, etc. It is also of high interest in plasma physics. Therefore thermodynamic data for molecular hydrogen have to be as accurate as possible in a wide temperature range. We here rigorously show the shortcomings of various simplifications that are used to calculate the total internal partition function. These shortcomings can lead to errors of up to 40 percent or more in the estimated partition function. These errors carry on to calculations of thermodynamic quantities. Therefore a more complicated approach has to be taken. Seven possible simplifications of various complexity are described, together with advantages and disadvantages of direct summation of experimental values. These were compared to what we consider the most accurate and most complete treatment (case 8). Dunham coefficients were determined from experimental and theoretical energy levels of a number of electronically excited states of H_2 . Both equilibrium and normal hydrogen was taken into consideration. Various shortcomings in existing calculations are demonstrated, and the reasons for them are explained. New partition functions for equilibrium, normal, and ortho and para hydrogen are calculated and thermodynamic quantities are reported for the temperature range 1 - 20000 K. Our results are compared to previous estimates in the literature. The calculations are not limited to the ground electronic state, but include all bound and quasi-bound levels of excited electronic states. Dunham coefficients of these states of H_2 are also reported. For most of the relevant astrophysical cases it is strongly advised to avoid using simplifications, such as a harmonic oscillator and rigid rotor or ad hoc summation limits of the eigenstates to estimate accurate partition functions and to be particularly careful when using polynomial fits to the computed values. Reported internal partition functions and thermodynamic quantities in the present work are shown to be more accurate than previously available data.

3.1 INTRODUCTION

The total internal partition function, $Q_{tot}(T)$, is used to determine how atoms and molecules in thermodynamic equilibrium are distributed among the various energy states at particular temperatures. It is the statistical sum over all the Boltzmann factors for all the bound levels. If the particle is not isolated, there is an occupation probability between 0 and 1 for each level depending on interactions with its neighbours. Together with other thermodynamic quantities, partition functions are used in many astrophysical problems, including equation of state, radiative transfer, dissociation equilibrium, evaluating line intensities from spectra, and correction of line intensities to temperatures other than given in standard atlases. Owing to the importance of $Q_{tot}(T)$, a number of studies were conducted throughout the past several decades to obtain more accurate values and present them in a convenient way. It is essential that a standard coherent set of $Q_{tot}(T)$ is being used for any meaningful astrophysical conclusions from calculations of different atmospheric models and their comparisons.

Unfortunately, today we face a completely different situation. We have noted that most studies give more or less different results, sometimes the differences are small, but sometimes they are quite dramatic, for instance when different studies used different conventions to treat nuclear spin states (and later do not strictly specify these) or different approximations, cut-offs, etc. Furthermore, different methods of calculating the $Q_{tot}(T)$ are implemented in different codes, and it is not always clear which methods in particular are used. Naturally, differences in $Q_{tot}(T)$ values and hence in their derivatives (internal energy, specific heat, entropy, free energy) result in differences in the physical structure of computed model atmosphere even when line lists and input physical quantities (e.g. T_{eff} , $\log g$, and metallicities) are identical.

In the subsequent sections we review how $Q_{tot}(T)$ is calculated, comment on which simplifications, approximations, and constraints are used in a number of studies, and show how they compare to each other. We also argue against using molecular constants to calculate the partition functions. The molecular constants are rooted in the semi-classical idea that the vibrational-rotational eigenvalues can be expressed in terms of a modified classical oscillator-rotor analogue. This erroneous concept has severe challenges at the highest energy levels that are not avoided by instead making a simple summation of experimentally determined energy levels, simply due to the necessity of naming the experimental levels by use of assigned quantum numbers. Instead, we report [Dunham \(1932\)](#) coefficients for the ground electronic state and a number of excited electronic states, as well as resulting partition functions and thermodynamic quantities. The Dunham coefficients are not rooted in the classical picture, but still use quantum number assignments of the energy levels, and this approach is also bound to the same challenges of defining the upper energy levels in the summation, as is the summation using molecular constants (and/or pure experimental data). No published studies have solved

this challenge yet, but we quantify the uncertainty it implies on the resulting values of the chemical equilibrium partition function.

3.2 ENERGY LEVELS AND DEGENERACIES

In the Born-Oppenheimer approximation (Born & Oppenheimer, 1927) it is assumed that the rotational energies are independent of the vibrational energies, and the latter are independent of the electronic energies. Then the partition function can be written as the product of separate contributors - the external (i.e. translational) partition function, and the rotational, vibrational, and electronic partition functions.

3.2.1 Translational partition function

The Q_{tr} can be expressed analytically as

$$Q_{tr} = \frac{Nk_B T}{\lambda^3 P}, \quad (3.1)$$

where

$$\lambda = \sqrt{\frac{2\pi\hbar^2}{mk_B T}}, \quad (3.2)$$

and N is the number of particles, k_B is Boltzmann's constant, P is the pressure, and m the mass of the particle. The rest of this section considers the internal part, Q_{int} .

3.2.2 Vibrational energies

The energy levels of the harmonic oscillator (HO)

$$E(v) = \left(v + \frac{1}{2}\right) h\omega \quad (3.3)$$

depend on the integer vibrational quantum number $v = 0, 1, 2, \dots$. These energy levels are equally spaced by

$$\Delta E = h\omega. \quad (3.4)$$

The frequency $\omega = \frac{1}{2\pi} \sqrt{k/\mu}$ depends on the constant k , which is the force constant of the oscillator, and μ , the reduced mass of the molecule. The lowest vibrational level is $E = \frac{1}{2} \hbar\omega$. The harmonic oscillator potential approximates a real diatomic molecule potential well enough in the vicinity of the potential minimum at $R = R_e$, where R is the internuclear distance and R_e is the equilibrium bond distance, but it deviates increasingly for larger $|R - R_e|$. A better approximation is a Morse potential,

$$E_{pot}(R) = E_D \left[1 - e^{-a(R-R_e)}\right]^2, \quad (3.5)$$

where E_D is the dissociation energy of the rigid molecule. The experimentally determined dissociation energy E_D^{exp} , where the molecule is dissociated from its lowest vibration level, has to be distinguished from the binding energy E_B of the potential well, which is measured from the minimum of the potential. The difference is $E_D^{exp} = E_B - \frac{1}{2}\hbar\omega$. The energy eigenvalues are

$$E(v) = h\omega \left(v + \frac{1}{2} \right) - \frac{h^2\omega^2}{4E_D} \left(v + \frac{1}{2} \right)^2 \quad (3.6)$$

with energy separations

$$\Delta E(v) = E(v+1) - E(v) = h\omega \left[1 - \frac{h\omega}{2E_D}(v+1) \right]. \quad (3.7)$$

When using a Morse potential, the vibrational levels are clearly no longer equidistant: the separations between the adjacent levels decrease with increasing vibrational quantum number v , in agreement with experimental observations. In astrophysical applications these energies are commonly expressed in term-values $G(v) = E(v)/hc$, and the vibrational energies in the harmonic case are then given as

$$G(v) = \omega_e \left(v + \frac{1}{2} \right), \quad (3.8)$$

and in the anharmonic case are given (when second-order truncation is assumed) as

$$G(v) = \omega_e \left(v + \frac{1}{2} \right) - \omega_e x_e \left(v + \frac{1}{2} \right)^2, \quad (3.9)$$

where $\omega_e = \frac{\omega}{c}$ is the harmonic wave number, $\omega_e x_e = \frac{h\omega^2}{4cE_D} = \omega_e^2 \frac{hc}{4E_D}$ is the anharmonicity term, and $\omega = a\sqrt{2E_D/\mu}$ is the vibrational frequency. We remark that literally, only ω is a frequency (measured in s^{-1}), while ω_e is a wave number (measured in cm^{-1}), but in the literature ω_e is commonly erroneously called a frequency any way. In the harmonic approximation, the Boltzmann factor (i.e. the relative population of the energy levels) can be summed analytically from $v = 0$ to $v = \infty$ (Herzberg, 1945),

$$Q_v \approx \sum_{v=0}^{\infty} e^{-hc\omega_e(v+\frac{1}{2})/k_B T} = (1 - e^{-hc\omega_e/k_B T})^{-1}. \quad (3.10)$$

3.2.3 Rotational energies

In the rigid rotor approximation (RRA), a diatomic molecule can rotate around any axis through the centre of mass with an angular velocity ω_{\perp} . Its rotation energy is

$$E(J) = \frac{1}{2}I\omega_{\perp}^2 = \frac{J^2}{2I}, \quad (3.11)$$

here $I = \mu R^2$ is the moment of inertia of the molecule with respect to the rotational axis and $|J| = I\omega_z$ is its rotational angular momentum. In the simplest quantum mechanical approximation, the square of the classical angular momentum is substituted by $J(J+1)$,

$$|J|^2 \rightarrow J(J+1)\hbar^2 \quad (3.12)$$

and the rotational quantum number J can take only discrete values. The rotational energies of a molecule in its equilibrium position are therefore represented by a series of discrete values

$$E(J) = \frac{J(J+1)\hbar^2}{2I}, \quad (3.13)$$

and the energy separation between adjacent rotational levels

$$\Delta E(J) = E(J+1) - E(J) = \frac{(J+1)\hbar^2}{2I} \quad (3.14)$$

is increasing linearly with J . Rotational term-values are

$$F(J) = \frac{J(J+1)\hbar^2}{8\pi^2 I} = B_e J(J+1), \quad (3.15)$$

where

$$B_e = \frac{\hbar^2}{8\pi^2 c I} \quad (3.16)$$

is the main rotational molecular constant and $F(J)$ is measured in the same units as $G(v)$, that is, cm^{-1} . A mathematical advantage (but physically erroneous) of Eq. 3.15 is that the rotational partition function Q_{rot} can be calculated analytically,

$$Q_{rot} \approx \int (2J+1) e^{-hcB_e J(J+1)/kT} dJ = \frac{kT}{hcB_e}. \quad (3.17)$$

A slightly more general approximation would be a non-rigid rotor. In this case, when the molecule rotates, the centrifugal force, $F_c = \mu\omega_z^2 R \approx \mu\omega_z^2 R_e$, acts on the atoms and the internuclear distance widens to a value R that is longer than R_e , and then the rotation energies are expressed as

$$E(J) \approx \frac{J(J+1)\hbar^2}{2I} - \frac{J^2(J+1)^2\hbar^4}{2k\mu^2 R_e^6}, \quad (3.18)$$

where $k = 4\pi^2\omega_z^2 c^2 \mu$ is the restoring force constant in a harmonic oscillator approximation, introduced above.

For a given value of the rotational quantum number J the centrifugal widening makes the moment of inertia larger and therefore the rotational energy lower, as expressed in Eq. (3.18). This effect compensates for the increase in potential energy. Using term-values, a centrifugal distortion constant D_e is introduced into Eq. (3.15), yielding

$$F(J) = B_e J(J+1) - D_e J^2(J+1)^2. \quad (3.19)$$

It is often assumed that two terms are enough to have a good approximation and that more terms only give a negligible effect on the partition function. Unfortunately, this is rarely the case. When higher vibrational and rotational states are taken into consideration, as we show in the subsequent sections, higher order terms must be used. The rotational partition function Q_{rot} can be computed in the same way as the vibrational partition function. However, there are $2J + 1$ independent ways the rotational axis can orient itself in space with the same given energy. Furthermore, a symmetry factor, σ , has to be added as well if no full treatment of the nuclear spin degeneracy is included. In this case, oppositely oriented homonuclear molecules are indistinguishable, and half of their $2J + 1$ states are absent. Hence σ is 2 for homonuclear molecules and unity for heteronuclear molecules, and this leads to half as many states in homonuclear molecules as in corresponding heteronuclear molecules, such that Eq. (3.17) becomes

$$Q_{rot} = \frac{kT}{\sigma hcB_e}. \quad (3.20)$$

In the full spin-split degeneracy treatment for homonuclear molecules, the degeneracy factor is given by

$$g_n = (2S_1 + 1)(2S_2 + 1) \quad (3.21)$$

for the possible orientations of the nuclear spins S_1 and S_2 . For the two nuclei, each with spin S , there are $S(2S + 1)$ antisymmetric spin states and $(S + 1)(2S + 1)$ symmetric ones. For diatomic molecules, composed of identical Fermi nuclei¹, the spin-split degeneracy for even and odd J states are

$$g_{n,even} = [(2S + 1)^2 + (2S + 1)]/2, \quad (3.22)$$

$$g_{n,odd} = [(2S + 1)^2 - (2S + 1)]/2$$

respectively. The normalisation factor for g_n is $1/(2S + 1)^2$. For identical Bose nuclei², the spin-split degeneracy for even and odd J states are opposite to what they are for Fermi systems.

3.2.4 Interaction between vibration and rotation

Interaction between vibrational and rotational motion can be allowed by using a different value of B_v for each vibrational level:

$$B_v = B_e - \alpha_e \left(v + \frac{1}{2} \right), \quad (3.23)$$

where α_e is the rotation-vibration interaction constant.

¹ $S=1/2, 3/2, 5/2, \dots$

² $S=0, 1, 2, \dots$

3.2.5 Electronic energies

The excited electronic energy levels typically are at much higher energies than the pure vibrational and rotational energy levels. For molecules they therefore contribute only a fraction to the partition function. [Bohn & Wolf \(1984\)](#) points out that for molecules the electronic state typically is non-degenerate because the electronic energy is typically higher than the dissociation energy, so that $Q_{el} = 1$. Although this is the case for most molecules, others do have degenerate states, therefore Q_{el} is sometimes fully calculated nonetheless. Naturally, molecules can and do occupy excited electronic states, as many experiments show. The electronic partition function is expressed as

$$Q_{el} = \sum \tilde{\omega}_e e^{-T_e/k_B T}, \quad (3.24)$$

where $\tilde{\omega}_e = (2 - \delta_{0,\Lambda})(2S + 1)$ is the electronic statistical weight, where $\delta_{i,j}$ is the Kronecker delta symbol, which is 1 if $\Lambda = 0$ and 0 otherwise.

3.2.6 Vibrational and rotational energy cut-offs and the basic concept of quantum numbers

If the semi-classical approach to the very high eigenstates (where this approximation has already lost its validity) is maintained by assigning v and J quantum numbers either as reached from the Morse potential (Eq. (3.7)) or from introducing second-order terms (as is most common), then the absurdity in the approach becomes more and more obvious. In Herzberg's pragmatic interpretation ([Herzberg, 1950](#), p. 99-102) the classical theory is applied until the dissociation energy is reached (which for H_2 corresponds to $v = 14$), and then v values are disregarded above this. Other authors have not always been happy with this interpretation, however, and insisted on including v values well above the dissociation energy to a somewhat arbitrary maximum level, which affects the value of the partition function substantially at high temperatures. In the Morse potential (Eq. (3.7)) the vibrational eigenstates can in principle be counted up to v quantum numbers corresponding to approximately twice the dissociation energy, and for even higher v quantum numbers, the vibrational energy becomes a decreasing function of the increasing v number:

$$\Delta E(v) = h\omega \left[1 - \frac{h\omega}{2E_D}(v+1) \right] < 0, \quad (3.25)$$

solving for v where $\Delta E(v)$ first becomes lower than or equal to 0, we obtain

$$v_{max} = \frac{2E_D - h\omega}{h\omega}. \quad (3.26)$$

The next level, $v_{max} + 1$, would produce zero or even negative energy addition. To solve this failure, more terms are needed to better approximate the real potential. Expressing v_{max} in vibrational term molecular constants, we obtain

$$v_{max} = \frac{2E_D - h\omega}{h\omega} = \frac{\omega}{c} \frac{8cE_D}{2h\omega^2} = \frac{\omega_e}{2\omega_e x_e} - 1. \quad (3.27)$$

v_{max} is sometimes used as a cut-off level for summation of vibrational energies (e.g. Irwin 1987).

The classical non-rigid rotor approximation, Eq. (3.19) also shows that the energy between adjacent levels decreases with increasing J , thus writing Eq. (3.19) for J and $J + 1$ states and making the difference between eigenstates equal to zero,

$$B_e(J+1)(J+2) - D_e(J+1)^2(J+2)^2 - B_eJ(J+1) + D_eJ^2(J+1)^2 = 0, \quad (3.28)$$

and solving for J , we obtain the maximum rotational number,

$$J_{max} = \frac{\sqrt{2}\sqrt{B_e} - 2\sqrt{D_e}}{2\sqrt{D_e}}. \quad (3.29)$$

The summation over rotational energies is commonly cut-off at some arbitrary rotational level or is approximated by an integral from 0 to ∞ . When examining the literature, we did not note this J_{max} expression. As with the non-harmonic oscillator, adding more terms to the non-rigid rotor approximation would give a better approximation. Now it is possible to measure more terms ($\omega_y e_y, \omega_z e_z, \dots$ for vibrational levels, H_e for rotational levels). Although they are important for high-temperature molecular line lists and partition functions, they are often calculated only from energy levels measured in the vicinity of the bottom of the potential well. For higher v and J values, the resulting energies can therefore still deviate from experimentally determined energy term values. Furthermore, the whole concept of quantum numbers v and J and associated degeneracies etc. of course relates to the classical approximations in quantum theory, which breaks down at energies far from the validity of a description of the molecule as a rotating system of some kind of isolated atoms bound to one another by some kind of virtual spring. This shows that there is an unclear limit beyond which it is no longer meaningful to continue adding higher order terms to expand the simple quantum number concept to fit the highest measured energy levels. At these highest levels there is nothing other than the mathematical wavefunction itself that represent reality in a meaningful way.

Given these limitations in defining the uppermost levels in a meaningful way within the semi-classical quantum mechanics, the question is whether in the end it is not more accurate to use only experimental energy levels in the construction of the partition function. However, exactly for the uppermost levels there is no such concept as experimentally determined energy levels summed to a partition function. The first problem is the practical one that for no molecule all the levels have been measured. For any missing level an assumption has to be applied, which could be to exclude the level in the summation, to make a linear fit of its energy between the surrounding measured energy levels, or to construct some type of polynomial fit from which to determine the missing levels, which would then be based on a choice of harmonic or anharmonic and rigid or non-rigid rotor or other polynomial fits. Another

practical limitation is that experimentally, energy levels beyond the molecular dissociation energy would be seen. These levels can either give rise to a photo-dissociation of the molecule or relax back into a bound state, each with a certain probability. To construct a meaningful partition function, it would therefore at best have to be both temperature and pressure dependent, taking into account the timescales for molecular dissociation and recombination. An even more fundamental problem in defining a partition function based on experimental data is that each observed energy level has to be “named”. This naming is done by assigning a quantum number, which associates the measurements to a chosen semi-classical theory, however, and the quantum numbers associated with the state determines the degeneracy that the summation in the partition function will be multiplied with. This dilemma becomes perhaps more clear for slightly larger molecules than H_2 where the degeneracy of the bending mode is multiplied directly into the partition function, but is a non-trivial function of the assigned vibrational quantum number of the state (Sørensen & Jørgensen, 1993), while at the same time quantum mechanical ab initio calculations show that the wavefunction of the uppermost states can only be expressed as a superposition of several wavefunctions that are expressed by each their set of quantum numbers (Jørgensen et al., 1985), such that there is no “correct” assignment of the degeneracy factor that goes into the “experimental” partition function. There have been various ways in the literature to circumvent this problem. The most common is to ignore it. In some cases (e.g. Irwin 1987 and Kurucz 1987) it was chosen to first complement the “experimental” values with interpolation between the measured values and then add extrapolated values above the dissociation energy (ignoring the pressure dependence) based on polynomial fits to the lower levels, with a cut-off of the added levels determined by where the order of the fit caused energy increments of further states to become negative (determined e.g. from Eqs. (3.26) and (3.29)). For low temperatures these inconsistencies have no practical implication because the somewhat arbitrarily added eigenstates do not contribute to the final partition function within the noise level. For higher temperatures, however, the uncertainty due to the inconsistency of how to add energy levels above the dissociation energy becomes larger than the uncertainty in using a polynomial fit, rather than the actually computed values, as illustrated in Fig. 3.1. Realising that strictly speaking there is no such concept as an experimentally summed partition function, and there is no “correct” upper level, we decided for a hybrid model, where the uppermost energy level in our summations are the minimum of the last level before the dissociation energy and the level where the energy increments become negative according to Eqs. (3.39) and (3.40), see case 8 in the next section for more details. For high temperatures this approach will give results in between the results that would be obtained by a cut at the dissociation energy of the ground electronic state and an upper level determined by Eqs. (3.39) and (3.40), or a more experimentally inspired upper level (black curve), as is illustrated in Fig. 3.1. The difference between the three methods (upper cuts) is an illustration of the unavoidable uncertainty in the way the partition functions can be

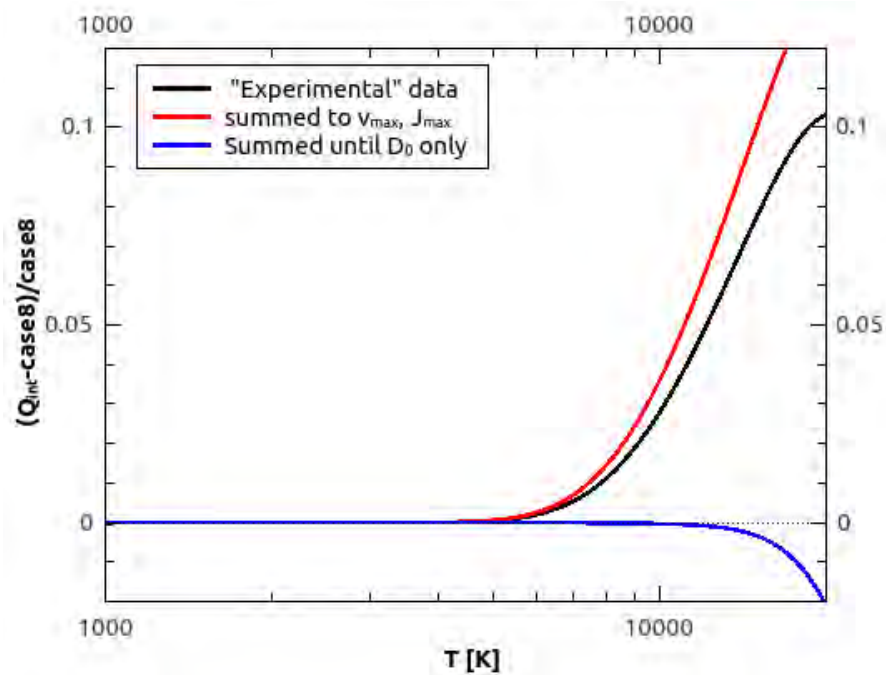


Figure 3.1: Difference between different methods used to stop the summation (upper cuts) of the partition function. Different cut-offs are compared to the partition function obtained from case 8 (see text for more details), which is the zero line. The curve marked “experimental “ data is derived by summing the Boltzmann factor of experimental data for the ground state used in Kurucz (1987)³. The blue curve is the summation for the ground electronic state summed to D_0 only. The red curve is the corresponding summation of energy levels of the three lowest electronic states based on Dunham coefficients and with a cut-off according to Eqs. (3.39) and (3.40).

calculated today. In the future, computers may be powerful enough to make sufficiently accurate ab initio calculations of these uppermost energy levels (but today the upper part of the ab initio energy surface is most often fitted to the experiments rather than representing numerical results).

There are no restrictions on the number of energy eigenstates available for an isolated molecule before dissociation. However, the physical conditions of a thermodynamic system impose restrictions on the number of possible energy levels through the mean internal energy Cardona et al. (2005); Vardya (1965). A molecule in a thermodynamic system is subjected to the interaction with other molecules through collisions and with the background energy that permeates the system, making the number of energy states available dependent on the physical conditions of the system. From a geometric point of view, in a thermodynamic system with total number density of particles N , the volume occupied by each molecule considering that the volume is cubic and of side L , is $L^3 = 1/N$. This imposes a maximum size that the molecule may have without invading the space of other molecules, and therefore the number

³ listed at <http://kurucz.harvard.edu/molecules/h2/eleroyh2.dat>

of states becomes finite. From a physical point of view, the number of energy states of the molecules is delimited by the interactions with the rest of the system since the energy state above the last one becomes dissociated by the mean background thermal energy of the system under study. Hence the maximum number of states available for a particle is dependent on the properties of the surrounding system. Cardona & Corona-Galindo (2013) have shown that in a dense medium ($N \geq 10^{21} \text{ cm}^{-3}$) interaction between molecules and their surroundings starts to become important and that the physical approach dominates the geometrical one. They also derived equations for the maximum vibrational and rotational levels in such conditions, assuming the rigid rotor approximation.

3.3 SIMPLIFICATIONS USED IN OTHER STUDIES

In this section we briefly review the simplifications in calculating Q_{int} that have been used and how they compare to each other.

3.3.1 Case 1.

This is the simplest case that is often given in textbooks: a simple product of harmonic oscillator approximation (HOA) and RRA, respectively summed and integrated to infinity, assuming Born-Oppenheimer approximation without interaction between vibration and rotation, and assuming that only the ground electronic state is present. Q_{int} then becomes a simple product of Eqs. (3.10) and (3.27):

$$Q_{int} = \frac{T}{c_2 \sigma B_e} \frac{1}{1 - \exp(-c_2 \omega_e / T)}, \quad (3.30)$$

where $c_2 = hc/k_B$ is the second radiation constant.

3.3.2 Case 2.

This time, HOA is dropped. v_{\max} is evaluated by Eq. (3.26)⁴, only ground electronic state and no upper energy limit are assumed:

$$Q_{int} = \exp \left[\frac{c_2}{T} \left(\frac{\omega_{e,1}}{2} - \frac{\omega_e x_{e,1}}{4} \right) \right] \frac{T}{\sigma c_2 B_e} \sum_{v=0}^{v_{\max}} \exp \left[\frac{c_2}{T} \omega_e \left(v + \frac{1}{2} \right) - \omega_e x_e \left(v + \frac{1}{2} \right)^2 \right], \quad (3.31)$$

where the first term refers to the lowest vibrational level of the ground state instead of the bottom of the potential well.

⁴ Which has no physical meaning

3.3.3 Case 3.

This is the same as case 2, but this time B_e in Eq. 3.31 is replaced by B_v , obtained by Eq. (3.23) (i.e. the Born-Oppenheimer approximation is abandoned):

$$Q_{int} = \exp \left[\frac{c_2}{T} \left(\frac{\omega_{e,1}}{2} - \frac{\omega_e x_{e,1}}{4} \right) \right] \sum_{v=0}^{v_{max}} \frac{T}{\sigma c_2 B_v} \exp \left[\frac{c_2}{T} \omega_e \left(v + \frac{1}{2} \right) - \omega_e x_e \left(v + \frac{1}{2} \right)^2 \right]. \quad (3.32)$$

3.3.4 Case 4.

This is the same as case 3, but this time an arbitrary energy truncation for the vibrational energy is added. The most commonly used (Tatum, 1966; Sauval & Tatum, 1984; Rossi et al., 1985; Gamache et al., 1990; Goorvitch, 1994; Gamache et al., 2000; Fischer et al., 2003) value is 40000 cm^{-1} :

$$Q_{int} = \exp \left[\frac{c_2}{T} \left(\frac{\omega_{e,1}}{2} - \frac{\omega_e x_{e,1}}{4} \right) \right] \sum_{v=0}^{v_{max}=40000 \text{ cm}^{-1}} \frac{T}{\sigma c_2 B_v} \exp \left[\frac{c_2}{T} \omega_e \left(v + \frac{1}{2} \right) - \omega_e x_e \left(v + \frac{1}{2} \right)^2 \right]. \quad (3.33)$$

3.3.5 Case 5.

In this case, excited electronic states are added,

$$Q_{int} = \exp \left[\frac{c_2}{T} \left(\frac{\omega_{e,1}}{2} - \frac{\omega_e x_{e,1}}{4} \right) \right] \sum_e^{T_{e,max}} \sum_{v=0}^{v_{max}} \frac{\tilde{\omega}_e T}{\sigma c_2 B_v} \exp \left[\frac{c_2}{T} \omega_e \left(v + \frac{1}{2} \right) - \omega_e x_e \left(v + \frac{1}{2} \right)^2 + T_e \right], \quad (3.34)$$

where $T_{e,max} = 40000 \text{ cm}^{-1}$.

3.3.6 Case 6.

This case provides the full treatment: we finally drop the RRA. As in cases 3 - 5, this case also fully abandons the Born-Oppenheimer approximation because electronic and vibrational and rotational states are interacting and depend on one another. Different vibrational and rotational molecular constants are used for the different electronic levels. Furthermore, the arbitrary truncation is dropped and the real molecular dissociation energy, D_0 , is used for the ground state. In principle, molecules can occupy eigenstates above the dissociation energy, but they are not stable and dissociate almost instantly or relax to lower states below the dissociation level. Since the timescale for dissociation is usually shorter than for relaxation, molecules tend to dissociate rather than relax. Furthermore, a pre-dissociation state is usually present

for molecules, where no eigenstates can be distinguished and a continuum of energies is present. This regime is beyond the scope of this work. For excited electronic states the ionisation energy is used instead of the dissociation energy. The equation for the full treatment takes the form

$$Q_{int} = \exp \left[\frac{c_2}{T} \left(\frac{\omega_{e,1}}{2} - \frac{\omega_e x_{e,1}}{4} \right) \right] \sum_{e=0}^{T_{e,max}} \sum_{v=0}^{v_{max}} \sum_{J=0}^{J_{max}} \tilde{\omega}_e (2J+1) \exp \left[\frac{-c_2}{T} (T_e + G_v + F_J) \right], \quad (3.35)$$

where G_v is calculated as in Eq. (3.9), $F_J = B_v J(J+1) - D_v J^2(J+1)^2$, where B_v is calculated as in Eq. (3.23), and $D_v = D_e - \beta_e(v + \frac{1}{2})$. $T_{e,max}$ is the term energy of the highest excited electronic state and is taken into account. For each electronic state the v and J quantum numbers are summed to a maximum value that corresponds to the dissociation energy of that particular electronic state.

3.3.7 Case 7.

For homonuclear molecules, nuclear spin-split degeneracy must also be taken into account. In this case, the form of the equation is

$$Q_{int} = \exp \left[\frac{c_2}{T} \left(\frac{\omega_{e,1}}{2} - \frac{\omega_e x_{e,1}}{4} \right) \right] \sum_{e=0}^{e_{max}} \sum_{v=0}^{v_{max}} \sum_{J=0}^{J_{max}} \tilde{\omega}_e g_n (2J+1) \exp \left[\frac{-c_2}{T} (T_e + G_v + F_J) \right], \quad (3.36)$$

where g_n is calculated as in Eq. (3.22).

3.3.8 Case 8.

This is the most accurate model we present here. Although cases 6 and 7 give reasonable results, they are still not sufficient at high temperatures. Molecular constants are conceptually rooted in classical mechanics (such as force constants of a spring and centrifugal distortion), and most often they are evaluated only from lower parts of the potential well and represent higher states poorly. For this reason it is more accurate to use a Dunham polynomial (Dunham, 1932) to evaluate energy levels,

$$T_{Dun} = \sum_{i,k=0}^{i_{max},k_{max}} Y_{ik} \left(v + \frac{1}{2} \right)^i (J(J+1))^k, \quad (3.37)$$

where Y_{ik} are Dunham polynomial fitting constants. These constants are not exactly related to classical mechanical concepts, such as bond lengths and force constants, and as such represent one step further into modern quantum mechanics. The lower order constants have values very close to the corresponding classical mechanics analogue constants used in cases 1-7, with the largest deviations occurring for H_2 and hydrides (Herzberg, 1950, p. 109). For

example, the differences between the molecular constants of $H_2 X$ $1s \sigma$ state (taken from [Pagano et al. 2009](#)) and the corresponding Dunham coefficients, obtained in this work, are 0.12% for ω_e and Y_{10} , 3% for $\omega_e x_e$ and Y_{20} , 72% for $\omega_e y_e$ and Y_{30} , 0.015% for B_e and Y_{01} , 1.8% for α_e and Y_{11} , 5.9% for γ_e and Y_{21} , 0.25% for D_e and Y_{02} , 40% for β_e and Y_{12} , etc. Dunham polynomial constants used together as a whole represent all experimental data more accurate than the classical picture in cases 1-7⁵. Results from Eq. (3.37) are then summed to obtain Q_{int} :

$$Q_{int} = \sum_{e,v,J}^{e_{max},v_{max},J_{max}} \omega_e (2J+1) \frac{1}{8} [(2S+1)^2 - (-1)^J (2S+1)] \exp \left[\frac{-c_2}{T} T_{Dun} \right]. \quad (3.38)$$

In this case, v_{max} and J_{max} are evaluated numerically, defined as the first v or J , where $\Delta E \leq 0$ (as in case 2, but now based on less biased coefficients), with ΔE given as

$$\Delta E(v) = \sum_{i=1}^{i_{max}} Y_{i,0} \left[\left(v + \frac{3}{2} \right)^i - \left(v + \frac{1}{2} \right)^i \right] \leq 0, \quad (3.39)$$

for v_{max} , and

$$\Delta E(J) = \sum_{i=0,k=1}^{i_{max},k_{max}} Y_{i,k} \left(v + \frac{1}{2} \right)^i \left[(J+1)^k (J+2)^k - J^k (J+1)^k \right] \leq 0 \quad (3.40)$$

for J_{max} .

3.4 THERMODYNAMIC PROPERTIES

From Q_{tot} and its first and second derivatives we calculate thermodynamic properties. For Q_{tr} (Eq. 3.1) we assume 1 mol of ideal-gas molecules, $N = N_A$, Avogadro's number. The ideal-gas standard-state pressure (SSP) is taken to be $p^\circ = 1$ bar and the molecular mass is given in amu. The internal contribution E_{int} to the thermodynamic energy, the internal energy $U - H(0)$, the enthalpy $H - H(0)$, the entropy S , the constant-pressure specific heat C_p , the constant-volume specific heat C_v , the Gibbs free energy $G - H(0)$, and the adiabatic index γ are obtained respectively from

$$E_{int} = RT^2 \frac{\partial \ln Q_{int}}{\partial T} \quad (3.41)$$

$$U - H(0) = E_{int} + \frac{3}{2} RT \quad (3.42)$$

⁵ In most cases the estimated energies from Dunham polynomials differ by less than 1 cm^{-1} from experimentally determined energies. For high energies they can, however, sometimes differ by up to 20 cm^{-1} .

$$H - H(0) = E_{int} + \frac{5}{2}RT \quad (3.43)$$

$$S = R \ln Q_{tot} + \frac{RT}{Q_{tot}} \left(\frac{\partial Q_{tot}}{\partial T} \right) \quad (3.44)$$

$$C_p = R \left[2T \left(\frac{\partial \ln Q_{int}}{\partial T} \right) + T^2 \left(\frac{\partial^2 \ln Q_{int}}{\partial T^2} \right) \right] + \frac{5}{2}R \quad (3.45)$$

$$C_v = \frac{\partial E_{int}}{\partial T} + \frac{3}{2}R \quad (3.46)$$

$$G - H(0) = -RT \ln Q_{tot} + RT \quad (3.47)$$

$$\gamma = \frac{H - H(0)}{U - H(0)}. \quad (3.48)$$

3.5 ORTO/PARA RATIO OF MOLECULAR HYDROGEN

In addition to equilibrium hydrogen, we also calculate the normal hydrogen following the paradigm of [Colonna et al. \(2012\)](#). In this case, ortho-hydrogen and para-hydrogen are not in equilibrium, but act as separate species. This aspect is particularly important for simulations of protoplanetary disks. The equilibrium timescale is short enough (300 yr) that the ortho/para ratio (OPR) can thermalise in the lifetime of a disk, but the equilibrium timescale is longer than the dynamical timescale inside about 40 AU ([Boley et al., 2007](#)). In case of normal hydrogen, ortho and para states have to be treated separately. Then Eq. (3.38) is split into two, one for para states:

$$Q_{para} = \sum_{e,v,J_{even}}^{e_{max},v_{max},J_{max}} \omega_e(2J+1) \exp \left[\frac{-c_2}{T} T_{Dun} \right], \quad (3.49)$$

and one for ortho states:

$$Q_{ortho} = \sum_{e,v,J_{odd}}^{e_{max},v_{max},J_{max}} \omega_e(2J+1) \exp \left[\frac{-c_2}{T} (T_{Dun} - \epsilon_{001}) \right]. \quad (3.50)$$

We note that weights for nuclear spin-split are omitted. The partition function for ortho-hydrogen is (as opposed to Q_{para}) referred to the first excited rotational level ($J = 1$) of the ground electronic state in its ground vibrational level. ϵ_{001} can be considered as the formation energy of the ortho-hydrogen ([Colonna et al., 2012](#)). Q_{int} is then ([Colonna et al., 2012](#))

$$Q_{int}^{norm} = (Q_{para})^{g_p} (Q_{ortho})^{g_o}, \quad (3.51)$$

where g_p and g_o are the statistical weights of the ortho and para configurations, 0.25 and 0.75, respectively. Moreover, the OPR is not necessarily either 3 or in equilibrium, but can be a time-dependant variable. The last consideration is beyond the scope of this work, therefore we do not discuss different ratios and assume that there are only two possibilities: either H_2 is in equilibrium or not.

3.6 RESULTS AND COMPARISON

We finally are ready to compare these different approaches. We here focus on H_2 , but we plan to apply the theory given above to other molecules in a forthcoming paper. Since Q_{int} varies with several orders of magnitude as a function of temperature, we normalised the differences to case 8 : $\frac{Q_{tot,X}-Q_{tot,8}}{Q_{tot,8}}$, where X is the case number.

Molecular constants for cases 1-7 were taken from the NIST⁶ database, summarised in [Pagano et al. \(2009\)](#). $D_0 = 36118.0696 \text{ cm}^{-1}$ ([Piszcztowski et al., 2009](#)). Experimental and theoretical data for molecular hydrogen for case 8 was taken from a number of sources that are summarised in [Table 3.1](#). Theoretical calculations were used only when observational data were incomplete. For every electronic state, coefficients were fitted to all $v - J$ configurations simultaneously using a weighted Levenberg-Marquardt ([Transtrum & Sethna, 2012](#)) algorithm and giving lower weights to theoretical data.

3.6.1 Determination of Dunham coefficients and evaluation of their accuracy

In this subsection we show how estimated energies from our Dunham coefficients for particular e, v, J configurations compare to those estimated from molecular constants and to experimental data. For simplicity we will here discuss only two electronic ($X 1s \sigma, D 3p\pi$)⁷ and vibrational ($v=0$ and 10) configurations of molecular hydrogen. Additionally, for the $X 1s \sigma$ state we show Dunham coefficients from [Dabrowski \(1984\)](#) and [Irwin \(1987\)](#). For [Dabrowski \(1984\)](#) signs had to be inverted for the $Y_{02}, Y_{04}, Y_{12}, Y_{14}$, and Y_{22} coefficients so that they would correctly follow the convention presented in [Eq. \(3.37\)](#). The comparison for $X 1s \sigma$ state is shown in [Fig. 3.2](#) and for $D 3p\pi$ state in [Fig. 3.3](#). The top panels show vibrational energies of both states, middle panels show energy levels of the $v = 0$ vibrational state, and bottom panels show energy levels of the $v = 10$ vibrational state. Experimental data are shown as black dots, red curves represent calculations of this work, green curves calculations from molecular constants, blue and cyan calculations using Dunham

⁶ K.P. Huber and G. Herzberg, "Constants of Diatomic Molecules" (data prepared by J.W. Gallagher and R.D. Johnson, III) in NIST Chemistry WebBook, NIST Standard Reference Database Number 69, Eds. P.J. Linstrom and W.G. Mallard, National Institute of Standards and Technology, Gaithersburg MD, 20899, <http://webbook.nist.gov>, (retrieved July 19, 2014).

⁷ These states have a sufficiently large amount of molecular constants determined. Most other states have only few to no molecular constants determined, thus comparing them would be ungentlemanly.

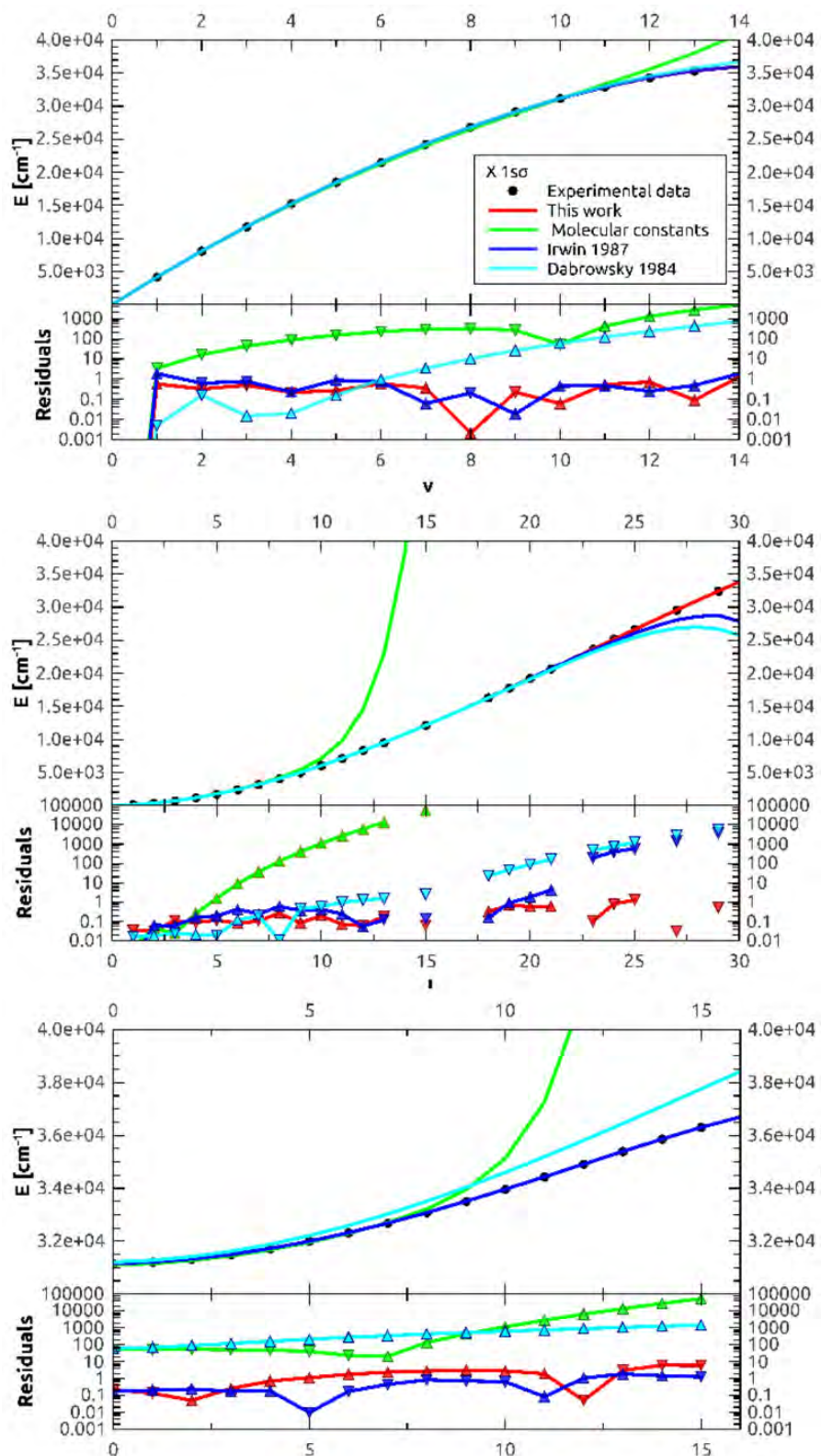


Figure 3.2: Energy levels for the $X\ 1s\ \sigma$ state of H_2 . Top: $X\ 1s\ \sigma$ vibrational energies. Middle: $X\ 1s\ \sigma$ ($v = 0$) energy levels. Bottom: $X\ 1s\ \sigma$ ($v = 10$) energy levels. See text for more details.

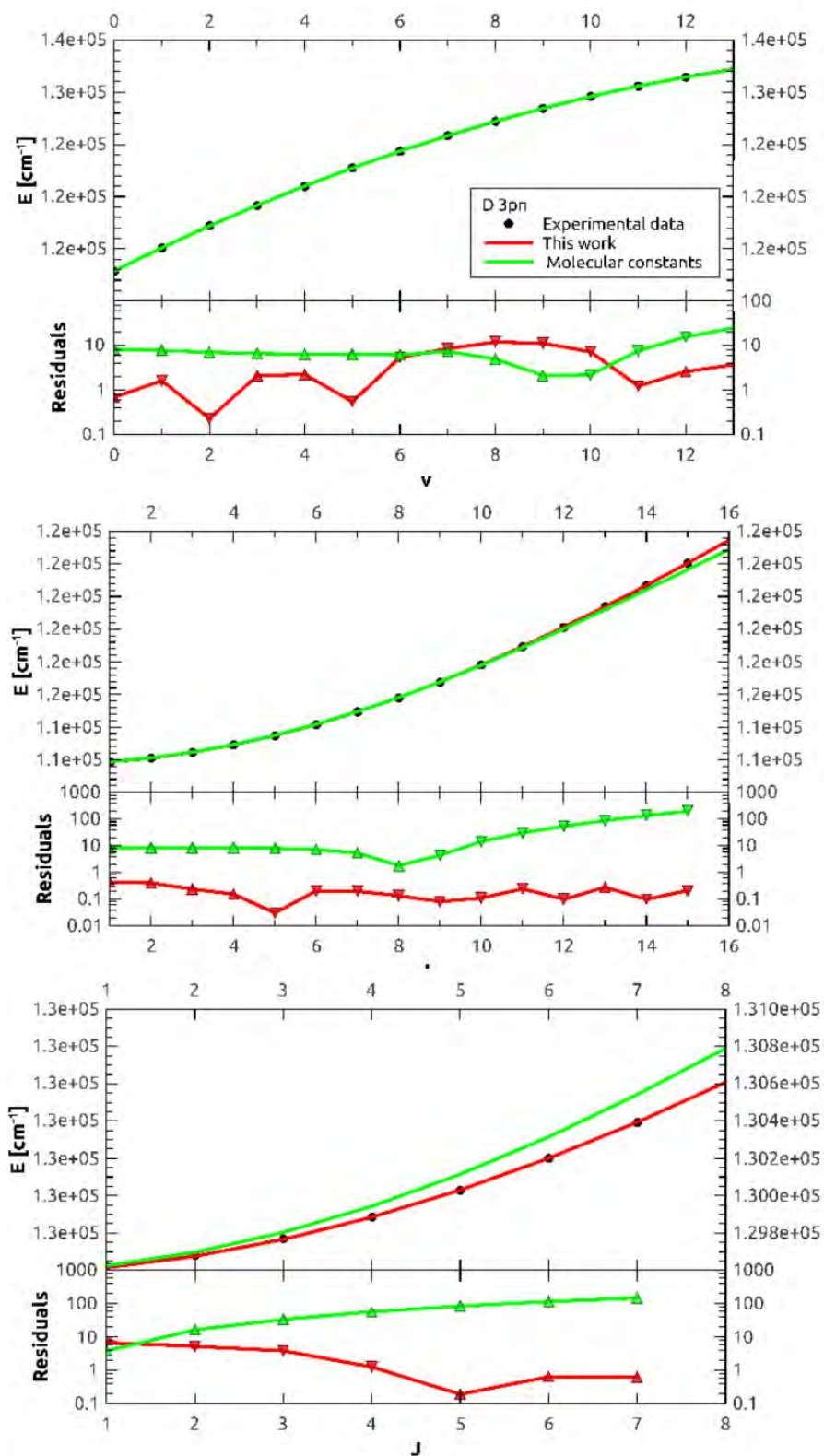


Figure 3.3: Energy levels for the $D 3p\pi$ state of H_2 . Top: $D 3p\pi$ vibrational energies. Middle: $D 3p\pi$ ($v = 0$) energy levels. Bottom: $D 3p\pi$ ($v = 10$) energy levels. See text for more details.

coefficients from [Irwin \(1987\)](#) and [Dabrowski \(1984\)](#), respectively. The top subpanels in both figures show the resulting energies, the bottom subpanels the residuals (calculated - experimental) in logarithmic scale. Triangles, facing down, indicate that the calculated energy is lower than observed, upward facing triangles that it is higher. These figures show that energies calculated from molecular constants can diverge substantially, especially in the $X\ 1s\ \sigma$ state, which contributes most to Q_{int} . For most of the states the results of [Irwin \(1987\)](#) are of similar quality as ours (but we used fewer coefficients, which speeds up the Q_{int} calculation), while for the lower vibrational levels of the $X\ 1s\ \sigma$ state our results are much more accurate (especially at high J).

A complete set of Dunham coefficients is given in [Tables 3.2 to 3.23](#) (available online). The number of coefficients for all cases was chosen separately from examining the root-mean-square error (RMSE), compared to experimental/theoretical data, to determine those with the lowest number of coefficients and lowest RMSE. In some cases as little as a 5x5 matrix is enough (e.g. $EF\ 2p\ \sigma\ 2p\ \sigma^2$), whereas in other cases up to a 11x11 matrix is needed. These differences depend on the complexity of the shape of the potential well. In all the tables the limiting energies are given up to which particular matrices should be used. All the limitations have to be employed (maximum energy as well as [Eqs. 3.39 and 3.40](#)) for every electronic configuration, since all the coefficients are only valid under these limitations.

Table 3.1: Summary of data sources for H_2 energy levels

State	Experimental (levels)	Theoretical (levels)
$X\ 1s\ \sigma$	Dabrowski (1984) , ($v = 0 - 14, J = 0 - 29$)	
$B\ 2p\ \sigma$	Dabrowski (1984) , ($v = 0 - 17, J = 0 - 30$) Abgrall et al. (1993) , ($v = 0 - 33, J = 0 - 28$) Bailey et al. (2010) , ($v = 0 - 13, J = 0 - 13$)	Wolniewicz et al. (2006) , ($v = 0 - 38, J = 0 - 10$)
$C\ 2p\ \pi$	Dabrowski (1984) , ($v = 0 - 13, J = 1 - 13$) Abgrall et al. (1993) , ($v = 0 - 13, J = 1 - 24$) Bailey et al. (2010) , ($v = 0 - 3, J = 0 - 7$)	Wolniewicz et al. (2006) , ($v = 0 - 13, J = 1 - 10$)
$EF^{[a]}\ 2p\ \sigma\ 2p\ \sigma^2$	Senn & Dressler (1987) , ($v = 0 - 20, J = 0 - 5$) Bailey et al. (2010) , ($v = 0 - 28, J = 0 - 13$)	Ross & Jungen (1994) , ($v = 0 - 28, J = 0 - 5$)
$B'\ 3p\ \sigma$	Abgrall et al. (1994) , ($v = 0 - 7, J = 0 - 12$) Bailey et al. (2010) , ($v = 0 - 3, J = 0 - 7$)	Wolniewicz et al. (2006) , ($v = 0 - 9, J = 0 - 10$)
$D\ 3p\ \pi$	Abgrall et al. (1994) , ($v = 0 - 14, J = 1 - 17$) Bailey et al. (2010) , ($v = 0 - 2, J = 1 - 7$)	Wolniewicz et al. (2006) , ($v = 0 - 17, J = 1 - 10$)
$GK^{[a]}\ 3d\ \sigma$	Bailey et al. (2010) , ($v = 0 - 6, J = 0 - 9$)	Ross & Jungen (1994) , ($v = 0 - 5, J = 0 - 5$) Yu & Dressler (1994) ($v = 0 - 8, J = 0 - 5$)
$H\bar{H}^{[a]}\ 3s\ \sigma$	Bailey et al. (2010) , ($v = 0 - 2, J = 0 - 6$)	
$I\ 3d\ \pi$	Bailey et al. (2010) , ($v = 0 - 3, J = 1 - 10$)	
$J\ 3d\ \delta$	Bailey et al. (2010) , ($v = 0 - 2, J = 2 - 6$)	
$B''\ Bbar^{[a]}\ 4p\ \sigma$	Glass-Maujean et al. (2007) , ($v = 4 - 11, J = 0 - 2$)	Wolniewicz et al. (2006) , ($v = 0 - 56^{[b]}, J = 0 - 10$) Glass-Maujean et al. (2007) , ($v = 4 - 11, J = 0 - 2$)
$D'\ 4p\ \pi$	Takezawa (1970) , ($v = 0 - 5, J = 1 - 5$)	Wolniewicz et al. (2006) , ($v = 0 - 9, J = 1 - 10$) Glass-Maujean & Jungen (2009) , ($v = 0 - 17, J = 1 - 4$)
$5p\ \sigma$	Takezawa (1970) , ($v = 0 - 2, J = 0 - 4$)	Wolniewicz et al. (2006) , ($v = 0 - 9, J = 0 - 10$) Glass-Maujean et al. (2013b) , ($v = 0 - 8, J = 0 - 4$)
$D''\ 5p\ \pi$	Takezawa (1970) , ($v = 0 - 2, J = 1 - 3$) Glass-Maujean et al. (2013c) , ($v = 0 - 12, J = 1 - 4$)	Glass-Maujean et al. (2013c) , ($v = 0 - 12, J = 1 - 4$)
$6p\ \sigma$	Takezawa (1970) , ($v = 0 - 2, J = 0 - 4$)	Wolniewicz et al. (2006) , ($v = 0 - 9, J = 0 - 10$) Glass-Maujean et al. (2013b) , ($v = 0 - 7, J = 0 - 4$)
$6p\ \pi$	Glass-Maujean et al. (2013a) , ($v = 0 - 9, J = 1 - 4$)	
$7p\ \sigma$	Takezawa (1970) , ($v = 0 - 2, J = 0 - 3$)	Glass-Maujean et al. (2013b) , ($v = 0 - 6, J = 0 - 4$)
$7p\ \pi$	Glass-Maujean et al. (2013a) , ($v = 0 - 7, J = 1 - 4$)	

Notes. ^[a]Double potential well state. ^[b]32 lowest v levels are used in this study.

Table 3.2: $Y_{i,j}$ for X $1s$ σ state. $E_{max} = E_D = 36118.0696$.

$i \setminus j$	0	1	2	3	4	5	6
0	0.0	60.8994	-0.0464547	4.6066e-5	-4.44761e-8	2.89037e-11	-8.51258e-15
1	4408.97	-3.22767	0.00251022	-2.85502e-6	2.15163e-9	-7.60784e-13	
2	-127.648	0.165697	-0.000458971	5.036e-7	-2.1465e-10		
3	2.90163	-0.031327	6.61024e-5	-4.15522e-8			
4	-0.302736	0.00278106	-3.45438e-6				
5	0.0175198	-0.000105554					
6	-0.000606749						

Table 3.3: $Y_{i,j}$ for B $2p$ σ state. $E_{max} = 118376.981$.

$i \setminus j$	0	1	2	3	4	5	6	7
0	89540.7	20.3249	-0.0244189	6.10056e-5	-1.18524e-7	1.20211e-10	-4.73402e-14	2.11275e-20
1	1323.2	-1.09933	0.00881566	-4.47483e-5	1.02297e-7	-1.06706e-10	4.16538e-14	-1.58919e-19
2	1.11679	-0.153064	-0.000546492	6.67274e-6	-1.75266e-8	1.8647e-11	-7.16464e-15	4.0682e-20
3	-4.13726	0.063354	-0.000205483	7.37966e-8	4.55652e-10	-6.51076e-13	2.62926e-16	-2.00198e-21
4	0.394415	-0.0062084	2.25521e-5	-2.5732e-8	1.48268e-12	2.0649e-14	-1.16798e-17	
5	-0.0155583	0.000194542	-5.03613e-7	1.07722e-10	4.69293e-13	-4.60339e-16		
6	8.69305e-5	3.59161e-6	-2.00997e-8	3.79657e-11	-1.75735e-14			
7	1.09635e-5	-3.72309e-7	9.95017e-10	-7.35739e-13				
8	-2.49984e-7	8.41556e-9	-1.11877e-11					
9	-6.45466e-11	-6.35193e-11						
10	3.13732e-11							

$i \setminus j$	8	9	10
0	-2.50566e-19	-2.92577e-19	1.61127e-19
1	7.7568e-20	2.10342e-20	
2	-2.63039e-21		

Table 3.4: $Y_{i,j}$ for C $2p\pi$ state. $E_{max} = 118376.981$.

$i \setminus j$	0	1	2	3	4	5	6	7
0	97882.0	32.5557	-0.0399421	0.000132418	-3.34989e-7	4.2892e-10	-2.12309e-13	3.53673e-19
1	2446.06	-3.09621	0.0222126	-0.000114815	2.84875e-7	-3.3416e-10	1.48677e-13	-1.64883e-19
2	-68.1303	0.685829	-0.00833825	3.73323e-5	-7.62593e-8	7.06128e-11	-2.30836e-14	
3	-0.0313063	-0.150771	0.00152702	-5.22981e-6	7.37665e-9	-3.65104e-12		
4	0.0746035	0.019201	-0.000146625	3.3335e-7	-2.36923e-10			
5	0.00144141	-0.00146403	7.19968e-6	-8.04132e-9				
6	-0.00185288	6.26612e-5	-1.45669e-7					
7	0.000162238	-1.20807e-6						
8	-4.75062e-6							

$i \setminus j$	8
0	-1.42451e-20

3.6.2 Comparison of cases 1 to 8

First, we consider only the equilibrium H_2 . The comparison of cases 1-7 to case 8 is shown in Fig. 3.4. The main differences between all cases come from whether or not rigid-rotor approximation is used. The simplest case, case 1, underestimates Q_{int} throughout the complete temperature range. The underestimation in the high-temperature range is easily explained by the equidistant separation (or linear increase with increasing J) between eigenstates (Eqs. 3.4 and 3.14, respectively): in HOA/RRA the eigenstate energies are higher for a

Table 3.5: $Y_{i,j}$ for $EF\ 2p\ \sigma\ 2p\ \sigma^2$ state, inner well. $E_{max} = 105000.0$.

$i \setminus j$	0	1	2	3	4
0	98068.8	23.2211	2.25688	-0.149909	0.00273895
1	2136.55	-8.10192	0.679069	-0.00863188	
2	140.173	-1.30784	-0.14758		
3	9.85717	1.4317			
4	-22.7252				

Table 3.6: $Y_{i,j}$ for $EF\ 2p\ \sigma\ 2p\ \sigma^2$ state, outer well. $E_{max} = 118376.981$.

$i \setminus j$	0	1	2	3	4	5	6
0	98606.2	5.74637	1.37059	-0.17094	0.00474712	0.000128489	-4.8543e-6
1	1454.02	-2.7411	-0.180194	0.022727	-0.00104196	1.65094e-5	
2	-80.3398	1.01425	0.00144103	-0.000222756	5.37232e-7		
3	1.77242	-0.101008	0.000235334	5.67045e-6			
4	0.191269	0.00388008	-9.85281e-6				
5	-0.0119227	-5.07168e-5					
6	0.000188356						

given set of v, J values than when less strict approximations are used (Eq. 3.7). This effect is particularly strong for H_2 , since the rotational distortion constant D_e (see Eq. 3.19) is so large ($D_{e,H_2} = 0.0471$ for the $X^1\Sigma_g$ state, whereas it is only $D_{e,CO} = 6.1215 \times 10^{-6}$ in the case of CO). The higher energy levels are therefore less populated in the HOA/RRA than in a more realistic computation, and these levels play a relatively larger role the higher the temperature. At the lowest temperatures the few lowest eigenstates dominate the value of Q_{int} , and these levels have slightly too high energies in HOA/RRA and therefore also cause Q_{int} from HOA/RRA to be substantially underestimated for low temperatures. Numerical differences are small, but the percentage difference is substantial: between 80 K and 1200 K the difference is 10 to 20 percent. Anharmonicity (difference between cases 1 and 2) for H_2 is only relevant above 1000 K. Interaction between rotation and vibration gives only 2 percent difference (between cases 2 and 3) below 2000 K and becomes substantial thereafter. Since $D_0 = 36118.0696\text{ cm}^{-1}$, and $T_e = 91700\text{ cm}^{-1}$ for the $B^1\Sigma_u^+$ state, for H_2 it makes no difference whether excited electronic states are taken into account or not for low temperatures or if arbitrary truncation (e.g. 40000 cm^{-1}) is below the first excited state. On the other hand, summing above the dissociation energy, at temperatures above 10000 K gives larger Q_{int} than it should be, assuming only the ground electronic state is available. On the other hand, if the RRA is used, Q_{int} is still somewhat too low even if erroneously, it is summed to infinity. Case 6 shows how large the difference is when nuclear spin-split degeneracy is omitted from the full calculations and $\sigma = 1/2$ is used. For temperatures below 200 K, case 6 overestimates the partition function by up to a factor of 2 compared to case 8. For T between 200 K and 2000 K, cases 6 and 7 are indistinguishable from case 8. Above 2000 K even case 7 (and 6) gives different results. The latter is due to poor predictions of the higher rotational energy states at higher vibrational levels.

Naturally, using different approaches (cases 1-8) leads to different estimates of thermodynamic quantities. In Fig. 3.5 the adiabatic index γ , Fig. 3.6

Table 3.7: $Y_{i,j}$ for $B' 3p \sigma$ state. $E_{max} = 133610.273$

$i \setminus j$	0	1	2	3	4	5	6	7
0	109640.0	28.872	0.836305	-0.0136974	4.01261e-5	1.23323e-6	-1.6454e-8	8.27886e-11
1	1427.0	-15.3274	-2.85783	0.0525351	-0.000479745	2.55235e-6	-7.52893e-9	1.07135e-11
2	689.282	27.9589	2.41683	-0.0353017	0.000231187	-7.70384e-7	8.98726e-10	
3	-449.987	-22.3981	-0.880946	0.00944058	-3.7779e-5	6.29088e-8		
4	136.699	8.40707	0.160582	-0.00115863	2.0487e-6			
5	-21.732	-1.6006	-0.0142388	5.45786e-5				
6	1.61573	0.149031	0.000481531					
7	-0.0356702	-0.00537226						
8	-0.00077895							
$i \setminus j$	8							
0	-1.55865e-13							

Table 3.8: $Y_{i,j}$ for $D 3p\pi$ state. $E_{max} = 133610.273$.

$i \setminus j$	0	1	2	3	4	5	6	7
0	111713.0	30.0272	-0.0142088	-2.07092e-5	-5.35965e-8	1.77885e-9	-8.13272e-12	1.15704e-14
1	2354.63	-0.771873	-0.0151207	0.000144998	-7.04225e-7	1.31303e-9	1.27466e-12	-5.18074e-15
2	-68.7361	-0.431929	0.00809662	-6.33383e-5	2.90083e-7	-7.21926e-10	6.91788e-13	
3	2.91624	0.0927337	-0.00152849	8.35883e-6	-2.25164e-8	2.73782e-11		
4	-0.743664	-0.0073304	0.000130395	-4.7786e-7	5.34873e-10			
5	0.103972	8.18834e-5	-4.89806e-6	1.01828e-8				
6	-0.00749572	1.39201e-5	6.07114e-8					
7	0.000262281	-4.49286e-7						
8	-3.56422e-6							
$i \setminus j$	8							
0	4.25363e-20							

the normalised internal energy (E_{int}/RT), and in Fig. 3.7 the entropy S are shown for all the cases. Constant adiabatic indexes (5/3 or 7/5) clearly completely misrepresent reality for a wide range of temperatures when local thermal equilibrium (LTE) is assumed. When considering the simplest cases (case 1 to 5), they follow the 7/5 simplification well until 1000 K, but are far from the most realistic estimate (case 8). Case 6 gives results almost identical to case 7 above 300 K. Case 7 is indistinguishable from case 8 up until 2000 K. The same trends can be seen for internal energy. From a first glance, the entropy seems to be very similar in all the cases, but this is because the dominating factor comes from Q_{tr} . Keeping that in mind, variability throughout all the temperature range is substantial. Entropy in case 7 is accurate until 3000 K.

Now we compare equilibrium and normal hydrogen. Equilibrium, normal, and one, neglecting OPR, partition functions are shown in Fig. 3.8. At low temperature, the three models show large differences, while in the high temperature range ($T > 2000$ K) the results coalesce. The same trends can be seen for the calculated thermodynamic quantities, shown in Figures 3.9, 3.10, 3.11 and 3.12. Both internal energy and specific heat at constant pressure are lower for normal hydrogen, whereas equilibrium hydrogen has higher values. The adiabatic index is dramatically different for both cases. Normal hydrogen does not have a depression at low temperatures. This depression can lead to accelerated gravitational instability and collapse in molecular clouds to form pre-stellar cores and protoplanetary cores in protoplanetary disks. Large differences in entropy are only present at temperatures below 300 K. Neglecting

Table 3.9: $Y_{i,j}$ for GK $3d$ σ state, inner well. $E_{max} = 116900.0$.

$i \setminus j$	0	1	2	3	4
0	109217.0	23.8085	-0.253881	-0.00473545	1.98913e-5
1	970.614	-7.78821	0.412418	4.68762e-5	
2	24.2579	-1.06924	-0.0590925		
3	1.64268	0.369018			
4	-0.465966				

Table 3.10: $Y_{i,j}$ for GK $3d$ σ state, outer well.

$i \setminus j$	0	1	2	3	4
0	110177.0	14.5226	0.387782	-0.0137014	0.000137787
1	1009.41	-7.16505	-0.0941763	0.00148123	
2	-25.2145	2.75273	0.00636093		
3	-1.88729	-0.245496			
4	0.489779				

OPR would lead to intermediate values between normal and equilibrium hydrogen.

3.6.2.1 Other studies.

There are a number of commonly used studies of Q_{int} . Here we give a brief summary of how other studies were performed, which simplifications they used, which molecular constants were adopted, and for which temperature range they were recommended. We stress that although it is commonly done, data must not be extrapolated beyond the recommended values under any circumstances. The resulting partition functions as well as their derivatives often diverge from the true values remarkably fast outside the range of the data they are based on. In our present study we took care to validate our data and formulas, such that they can be used in a wider temperature range than those of any previous study. Our data and formulas can be safely applied in the full temperature range from 1 K to 20000 K and easily extended beyond 20000 K in extreme cases, such as shocks, by use of the listed Dunham coefficients.

TATUM 1966 (TATUM, 1966, T1966) presented partition functions and dissociation equilibrium constants for 14 diatomic molecules in the temperature range $T = 1000 - 8000$ K with 100 K steps. Calculations were made using case 5. The upper energy cut-off was chosen to be at 40000 cm^{-1} . Only the first few molecular constants were used ($\omega_e, \omega_e x_e, B_e, \alpha_e$).

IRWIN 1981 (IRWIN, 1981, I1981) presented partition function approximations for 344 atomic and molecular species, valid for the temperature range $T = 1000 - 16000$ K. Data for molecular partition functions were taken from Tatum (1966); McBride et al. (1963); Stull et al. (1971). Irwin (1981) gave partition function data in the form of polynomials,

$$\ln Q = \sum_{i=0}^5 a_i (\ln T)^i, \quad (3.52)$$

Table 3.11: $Y_{i,j}$ for $H\bar{H}$ $3s \sigma$ state, inner well. $E_{max} = 118000.0$.

$i \setminus j$	0	1	2	3	4
0	111909.0	33.4756	-0.0628269	-0.00674187	8.95921e-5
1	2003.13	-12.1054	0.479189	0.00472823	
2	199.147	2.47998	-0.246944		
3	1.52825	0.64834			
4	-22.8763				

Table 3.12: $Y_{i,j}$ for $H\bar{H}$ $3s \sigma$ state, outer well.

$i \setminus j$	0	1	2	3	4	5	6
0	122617.0	2.85838	-0.452462	0.0496827	-0.00129124	-3.65898e-5	1.30097e-6
1	600.772	-2.03478	0.165172	-0.0186535	0.000900787	-1.33774e-5	
2	-178.292	0.705169	-0.0128	8.90067e-5	-7.25588e-6		
3	48.1293	-0.0969926	0.00148014	1.46566e-5			
4	-5.82021	0.00514187	-6.94023e-5				
5	0.319828	-8.17859e-5					
6	-0.00657088						

which is very convenient to use. For each species, the coefficients of Eq. (3.52) were found by the method of least-squares fitting. Some molecular data were linearly extrapolated before fitting the coefficients. For the extrapolated data the weight was reduced by a factor of 10^6 . Irwin stated that these least-squares fits have internally only small errors. However, a linear extrapolation to strongly non-linear data results in large errors even before fitting the polynomial, and the size of the errors due to this effect was not estimated.

BOHN AND WOLF 1984 (BOHN & WOLF, 1984, BW1984) derived partition functions for H_2 and CO that are valid for the temperature range $T = 1000 - 6000$ K. In principle, this paper aimed to show a new approximate way of calculating partition functions, specific heat c_V , and internal energy E_{int} . Calculations were made using case 5 for "exact" partition functions and using assumptions of case 3 for approximations. Only the ground electronic state was included, and only the first few molecular constants were used ($\omega_e, \omega_e x_e, B_e, \alpha_e$).

SAUVAL AND TATUM 1984 (SAUVAL & TATUM, 1984, ST1984) presented total internal partition functions for 300 diatomic molecules, 69 neutral atoms, and 19 positive ions. Molecular constants ($\omega_e, \omega_e x_e, B_e, \alpha_e$) were taken from Huber & Herzberg (1979). The partition function polynomial approximations are valid for the temperature range $T = 1000 - 9000$ K. The authors adopted the previously used equation, [T1966] (case 5) for all the species. A polynomial expression

$$\log Q = \sum_{n=0}^4 a_n (\log \theta)^n \quad (3.53)$$

was used for both atoms and molecules. Here $\theta = 5040/T$.

ROSSI ET AL. 1985 (ROSSI ET AL., 1985, R1985) presented total internal partition functions for 53 molecular species in the temperature range

Table 3.13: $Y_{i,j}$ for I $3d\pi$ state.

$i \setminus j$	0	1	2	3	4
0	110177.0	14.5226	0.387782	-0.0137014	0.000137787
1	1009.41	-7.16505	-0.0941763	0.00148123	
2	-25.2145	2.75273	0.00636093		
3	-1.88729	-0.245496			
4	0.489779				

Table 3.14: $Y_{i,j}$ for J $3d\delta$ state.

$i \setminus j$	0	1	2	3
0	111260.0	41.8057	0.0950125	-0.00450042
1	2006.46	-6.68957	-0.0253833	
2	195.159	0.807222		
3	-56.9367			

$T = 1000 - 5000$ K. Molecular constants ($\omega_e, \omega_e x_e, B_e, \alpha_e$) were taken from [Huber & Herzberg \(1979\)](#). For diatomic molecules the authors followed Tatum's ([Tatum, 1966](#)) paradigm, case 5. The authors claimed that Q_J was evaluated with a non-rigid approximation ([Rossi et al., 1985](#)), but upon a simple inspection it is clear that they used rigid-rotor approximation. They did, however, allow interaction between vibration and rotation. An arbitrary truncation in the summation over the electronic states is at 40000 cm^{-1} . For polynomial approximations the authors considered the "exact" specific heat, whose behaviour near the origin is more amenable to approximation schemes. The partition functions were then obtained by integration ([Rossi et al., 1985](#)). Their specific heat approximation is

$$\frac{C_v}{k} = \sum_{m=0}^4 a_m Z^m, \quad (3.54)$$

where $Z = T/1000$ and a_m are coefficients. The partition function they obtained is listed as the seven fitting constants a_0 to a_6 to the polynomial:

$$\ln Q = a_0 \ln Z + \sum_{m=1}^4 \frac{a_m}{m(m+1)} Z^m - \frac{a_5}{Z} + a_6. \quad (3.55)$$

KURUCZ 1985 ([KURUCZ, 1987](#), K1985) commented on the situation regarding the partition functions of H_2 and CO . Approximate expressions for the molecular partition functions in previous studies were considered not rigorous enough because they did not include coefficients of sufficiently high order and did not keep proper track of the number of bound levels. K1985 used experimentally determined energy levels, when available, and supplemented them with fitted values, presumably extended to a higher cut-off energy as discussed in Sect. 2.6 and Fig. 1 above. The author explicitly summed over the energies of the three lowest electronic states (data for H_2 were derived from [Dabrowski 1984](#)) and gave polynomial fits for the partition functions between 1000 K and 9000 K and also tabulated the exact results with steps of 100 K.

Table 3.15: $Y_{i,j}$ for $B''Bbar$ $4p$ σ state, inner well. $E_{max} = 130265.0$.

$i \setminus j$	0	1	2	3	4	5	6
0	115722.0	116.926	-4.45735	0.188078	-0.00440882	4.63197e-5	-1.71816e-7
1	5867.53	-52.4159	-0.493037	0.0487225	-0.000747071	3.25362e-6	
2	-4015.06	44.4104	-0.526875	0.00647721	-2.37322e-5		
3	1961.35	-13.9427	0.00852245	-9.78352e-5			
4	-482.848	2.58965	0.000454106				
5	56.5459	-0.17409					
6	-2.50753						

Table 3.16: $Y_{i,j}$ for $B''Bbar$ $4p$ σ state, outer well. $E_{max} = 138941.911$.

$i \setminus j$	0	1	2	3	4	5	6
0	122624.0	0.95644	0.000305579	-3.2579e-6	-4.94167e-8	1.00874e-9	-4.52608e-12
1	360.513	0.00827397	-6.93853e-5	1.30952e-6	-1.07964e-8	3.57405e-11	
2	-4.41936	-0.00140404	1.00237e-6	-2.28296e-8	5.20907e-11		
3	0.0202615	6.54562e-5	5.32386e-8	2.54713e-10			
4	0.000542329	-1.81073e-6	-1.7598e-9				
5	-1.29422e-5	2.24736e-8					
6	8.5522e-8						

IRWIN1987 (IRWIN, 1987, I1987) presented refined total internal partition functions for H_2 and CO. The partition function polynomial approximations are valid for the temperature range $T = 1000 - 9000$ K. Estimated errors at 4000 K are 2% for H_2 and 0.004% for CO. $Y_{i,j}$ for H_2 were determined by using an equally weighted simultaneous least-squares fit of Dunham series using energy data obtained from Dabrowski (1984). This was done for the ground H_2 electronic state only.

I1987 compared his results with those of Kurucz (1987); Sauval & Tatum (1984) and found slightly higher values of Q , which he attributed to a combination of the number of included electronic states and a difference in the treatments of the highest rotational levels. Our results indicate that the main difference between the results of I1987 (Irwin, 1987) and K1985 (Kurucz, 1987) is the use of slightly too low energies in I1987 of the highest rotational levels, and we conclude that the value trend by K1985 is slightly closer to the values obtained by a full treatment (our case 8) than are those of I1987. A main difference between our method and those of I1987, K1985, and older works is, however, that our method is applicable in a higher temperature range and can treat ortho and para states separately. It can therefore be used in a wider range of physical conditions, including shocks, non-equilibrium gasses, etc.

PAGANO ET AL. 2009 (PAGANO ET AL., 2009, P2009) presented internal partition functions and thermodynamic properties of high-temperature (50 - 50000 K) Jupiter-atmosphere species. The authors used case 7 to calculate the partition functions with more than the first few (e.g. ω_e and $\omega_e x_e$, B_e and D_e) molecular constants for the ground and first few electronically excited states. The calculations are completely self-consistent in terms of maximum rotational states for the individual vibrational levels, presumably such that $E(v, J_{max}) \approx D_0$ for each v .

Table 3.17: $Y_{i,j}$ for D' $4p\pi$ state. $E_{max} = 138941.911$.

$i \setminus j$	0	1	2	3	4	5	6
0	116682.0	30.2145	-0.0194539	-0.000248291	8.12785e-6	-8.99861e-8	3.37172e-10
1	2343.11	-1.70002	0.00414816	-8.34473e-5	9.02456e-7	-3.67685e-9	
2	-71.7393	0.0665521	0.000201895	-1.68829e-6	1.27848e-8		
3	2.55445	-0.0143264	-3.77337e-5	1.03224e-8			
4	-0.348338	0.00198268	2.02175e-6				
5	0.0287842	-0.000102487					
6	-0.000981186						

Table 3.18: $Y_{i,j}$ for $5p\sigma$ state. $E_{max} = 143570.0$.

$i \setminus j$	0	1	2	3	4	5	6
0	118948.0	12.553	-0.458717	-0.0753537	-0.00159359	9.37272e-5	9.54153e-6
1	1192.64	36.5609	3.12137	0.00958014	-0.00304086	-0.00015569	
2	956.798	-40.5327	-0.987989	0.015968	0.00140718		
3	-419.015	13.7138	0.0387677	-0.00421793			
4	83.7293	-1.72833	0.00539521				
5	-7.99491	0.072457					
6	0.288787						

LARAIA ET AL. 2011 (LARAIA ET AL., 2011, L2011) presented total internal partition functions for a number of molecules and their isotopes for the temperature range 70 – 3000 K. The methods used in this study are based on Gamache et al. (2000); Fischer et al. (2003). Rotational partition functions were determined using the formulae in McDowell (1988, 1990). Vibrational partition functions were calculated using the harmonic oscillator approximation of Herzberg (1945). All state-dependent and state-independent degeneracy factors were taken into account in this study. The H_2 partition function was calculated as a direct sum using ab initio energies. A four-point Lagrange interpolation was used for the temperature range with intervals of 25 K. Data are presented in an easily retrievable FORTRAN program (Laraia et al., 2011).

COLONNA ET AL. 2012 (COLONNA ET AL., 2012, C2012) gave a statistical thermodynamic description of H_2 molecules in normal ortho/para mixture. The authors determined the internal partition function for normal hydrogen on a rigorous basis, solving the existing ambiguity in the definition of those quantities directly related to partition functions rather than on its derivatives (Colonna et al., 2012). The authors used case 7 with more molecular constants for the ground and first few electronically excited states than shown with equations 3.36. Internal partition function as well as thermodynamic properties for 5 - 10000 K are also given.

COMPARISON. Figure 3.13 shows the normalised value of Q_{int} for molecular hydrogen from the ten different studies we have described here, in their respective temperature ranges listed in the respective studies. The normalisation is made with respect to the results of this work (case 8). For C2012 normal hydrogen Q_{int} is used, whereas equilibrium hydrogen Q_{int} is used for all the other studies. The main frame of Fig. 3.13 is for the 1000-20000K

Table 3.19: $Y_{i,j}$ for $5p\pi$ state. $E_{max} = 143570.0$.

$i \setminus j$	0	1	2	3	4	5	6
0	118995.0	36.0716	-0.319741	-0.014872	-0.000238203	1.99987e-5	2.23272e-6
1	2415.58	2.15448	0.505586	0.0148412	-0.000399269	-6.86912e-5	
2	-147.992	-7.47147	-0.160739	0.000242203	0.000546545		
3	36.0906	2.80197	0.00598473	-0.00176365			
4	-7.57518	-0.384299	0.0030262				
5	0.760411	0.016345					
6	-0.0284743						

Table 3.20: $Y_{i,j}$ for $6p\sigma$ state. $E_{max} = 148240.0$.

$i \setminus j$	0	1	2	3	4	5	6
0	120709.0	27.2762	-0.142997	0.00648973	0.000194723	-2.7412e-6	-6.47774e-7
1	61.5226	-15.6536	0.324584	0.00741685	-9.39748e-5	-1.86748e-5	
2	2379.78	7.34398	-0.0986585	0.00318703	-2.58488e-5		
3	-1170.3	-1.19031	-0.0159069	1.37776e-5			
4	269.026	0.074286	0.00197083				
5	-29.2007	-0.000671958					
6	1.20284						

temperature range. The inset shows the low-temperature (10 - 1000 K) range. In the low-temperature range our results clearly differ only marginally from the three studies (P2009, L2011, C2012) that listed values of Q_{int} for low temperatures (the percentage difference is smaller than 0.1 percent in most of the temperature range). Since L2011 did not normalise the spin-split degeneracy, their results had to be divided by a factor of 4 before the comparison, shown in Fig. 3.13. In the high-temperature range, all studies using cases 1-5 have large errors (also seen from our case comparison in Fig. 3.4). Since K1985 explicitly derived his partition functions from experimental energy data, his results are in very good agreement with our results (from case 8) for his given temperature range (1000 - 9000 K). I1987 is also in great agreement with both K1985 and our results for the same temperature range. Using the values of Y_{ij} determined by I1987 gives results that perfectly agree with our work, as expected. At the higher end of the I1987 recommended temperature range, however, the polynomial approximation starts to have larger errors (the estimated 2 percent). At the highest temperature range, P2009 and C2012 also start to show considerable errors. These two studies are the only ones based on summation of energy levels, calculated based on molecular constants, and the comparison of our work with P2009 and C2012 therefore illustrates approximately how large errors in Q_{int} are obtained from methods based on molecular constants. The reason is, as mentioned before, that molecular constants are commonly fitted to the bottom of the potential well and poorly represent higher vibrational and rotational states energies. Finally, the I1981 results follow the T1966 results perfectly until 8000 K, which is the latter's high temperature limit. Then, since I1981 extrapolated data, the corresponding Q_{int} begin to show exponentially larger errors and is completely unreliable, which illustrates both how poor the HOA + RRA approximation represents reality (T1966 and I1981), and, in particular, *how unreliable it can*

Table 3.21: $Y_{i,j}$ for $6p\pi$ state. $E_{max} = 148240.0$.

$i \setminus j$	0	1	2	3	4	5	6
0	120320.0	58.0291	-0.686311	-0.0354304	-0.00063191	3.08385e-5	3.85789e-6
1	2264.49	-53.1853	1.41237	0.0776417	-1.83826e-5	-0.000191495	
2	15.0754	28.5592	-0.725983	-0.027318	0.00157845		
3	-37.0221	-6.48257	0.162007	-0.00265325			
4	7.77546	0.602542	-0.00483593				
5	-0.725696	-0.0217911					
6	0.0252225						

Table 3.22: $Y_{i,j}$ for $7p\sigma$ state. $E_{max} = 150000.0$.

$i \setminus j$	0	1	2	3	4	5	6
0	120984.0	14.4145	-0.206167	0.0189087	0.000577862	9.43236e-7	-1.05878e-6
1	2253.23	9.04999	0.299251	0.00127009	-0.000479448	-4.18786e-5	
2	-32.7638	-6.58075	-0.230493	0.00195881	0.000781566		
3	-8.66359	2.25858	0.021996	-0.00369885			
4	1.34773	-0.280184	0.00674419				
5	-0.16511	0.00597372					
6	0.0113496						

be to extrapolate beyond the calculated or measured data (as was done in the work of I1981), as seen clearly in Fig 3.13.

In Fig. 3.14 our results for H_2 specific heat at constant pressure are compared to (Stull et al., 1971, JANAF), (Le Roy et al., 1990, LeRoy), (Pagano et al., 2009, P2009) and (Colonna et al., 2012, C2012). The latter is compared to our results for normal hydrogen, and the others are compared to our equilibrium hydrogen calculations. All calculations agree very well until 10000 K. Figure 3.15 depicts our results for entropy calculations for H_2 . Once again, the agreement is very good (except with C2012 below 100 K), especially between our results and the JANAF data. However, there is a systematic offset between LeRoy and our results (and those of JANAF) of $11.52 \text{ J K}^{-1} \text{ mol}^{-1}$. This might be due to slightly different Standard Temperature and Pressure (STP) values, used by Le Roy et al. (1990), resulting in slightly different Q_{tr} . We note that the JANAF data represent equilibrium H_2 , while we computed equilibrium as well as normal and ortho and para H_2 (and span a much wider temperature range), which makes our data more generally applicable.

3.6.3 Polynomial fits

Following the common practice, we present polynomial fits to our results. All partition function data were fit to a fifth-order polynomial of the form

$$Q_{int}(T) = \sum_{i=0}^5 a_i T^i. \quad (3.56)$$

The data for the partition function were spliced into three intervals to reach better accuracy. Polynomial constants are given in Table 3.24, and the fitting accuracy is shown in Fig. 3.16. Combining the three intervals, we reach an error smaller than 2 percent for all the temperature range. The decision for

Table 3.23: $Y_{i,j}$ for $7p\pi$ state. $E_{max} = 150000.0$.

$i \setminus j$	0	1	2	3	4	5	6
0	121025.0	54.6852	-0.657303	-0.0278393	-0.000517054	1.93446e-5	2.61651e-6
1	2526.84	-33.3826	0.975964	0.0535573	0.000185217	-0.000113024	
2	-237.926	18.9794	-0.678591	-0.0232719	0.00118664		
3	63.6492	-4.60154	0.1826	-0.00237026			
4	-11.6711	0.422664	-0.00727658				
5	1.08902	-0.0152207					
6	-0.040398						

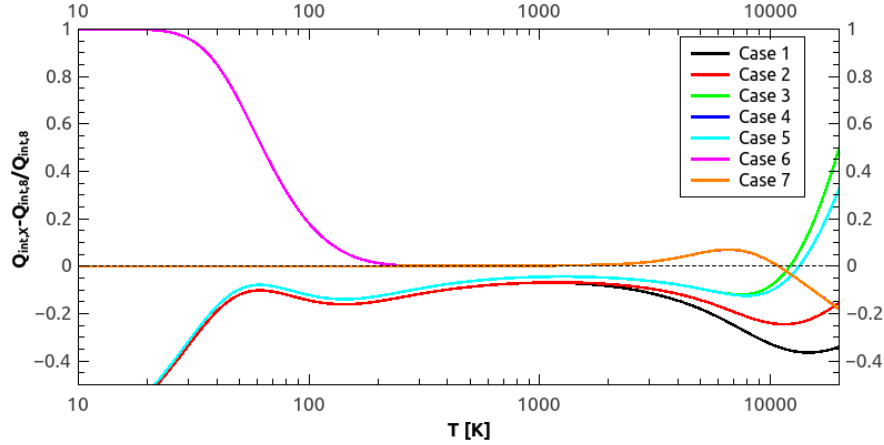


Figure 3.4: Comparison of different approaches for calculating Q_{int} for the H_2 molecule. Case 1 is identical to case 2 below 1500 K; case 4 is completely identical to case 5 for H_2 . All of the methods (i.e. cases 1-7) diverge substantially from our most accurate computation (case 8) for low as well as high temperatures.

using lookup tables with significantly larger accuracy or the faster polynomial fits with increased errors needs to be made on an individual basis.

3.7 CONCLUSIONS

We have investigated the shortcomings of various simplifications that are used to calculate Q_{int} and applied our analyses to calculate the time-independent partition function of normal, ortho and para, and equilibrium molecular hydrogen. We also calculated E_{int}/RT , $H - H(0)$, S , C_p , C_v , $-[G - H(0)]/T$, and γ . Our calculated values of thermodynamic properties for ortho and para, equilibrium, and normal H_2 are presented in Tables 3.26, 3.25, 3.27, and 3.28, rounded to three significant digits. Full datasets in 1 K temperature steps⁸ can be retrieved online. The partition functions and thermodynamic data presented in this work are more accurate than previously available data from the literature and cover a more complete temperature range than any previous study in the literature. Determined Dunham coefficients for a number of electronic states of H_2 are also reported.

⁸ Data with smaller temperature steps or beyond the given temperature range can be requested personally from the corresponding author

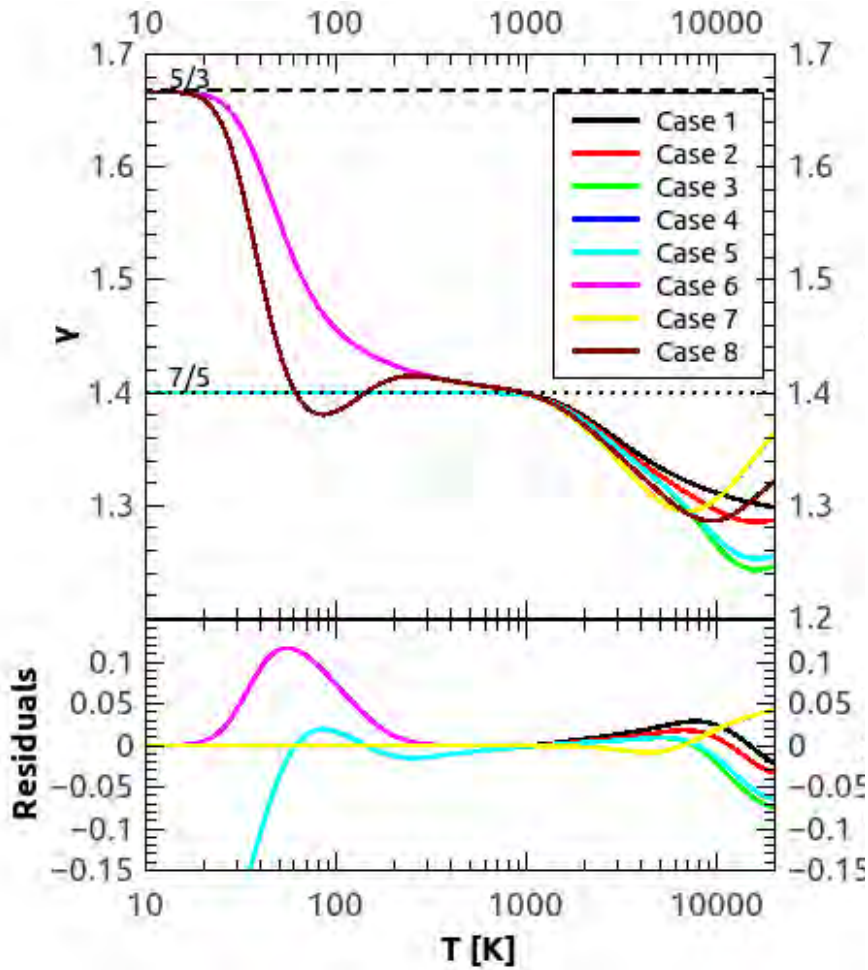


Figure 3.5: Adiabatic index for the H_2 molecule. We also show the constants $\gamma = 5/3$ and $\gamma = 7/5$. Residuals are for cases 1-7 with respect to case 8. Cases 1-5 are equal to $\gamma = 7/5$ below 1000 K, case 6 is identical to case 7 after 300 K, and case 7 is identical to case 8 until 6000 K.

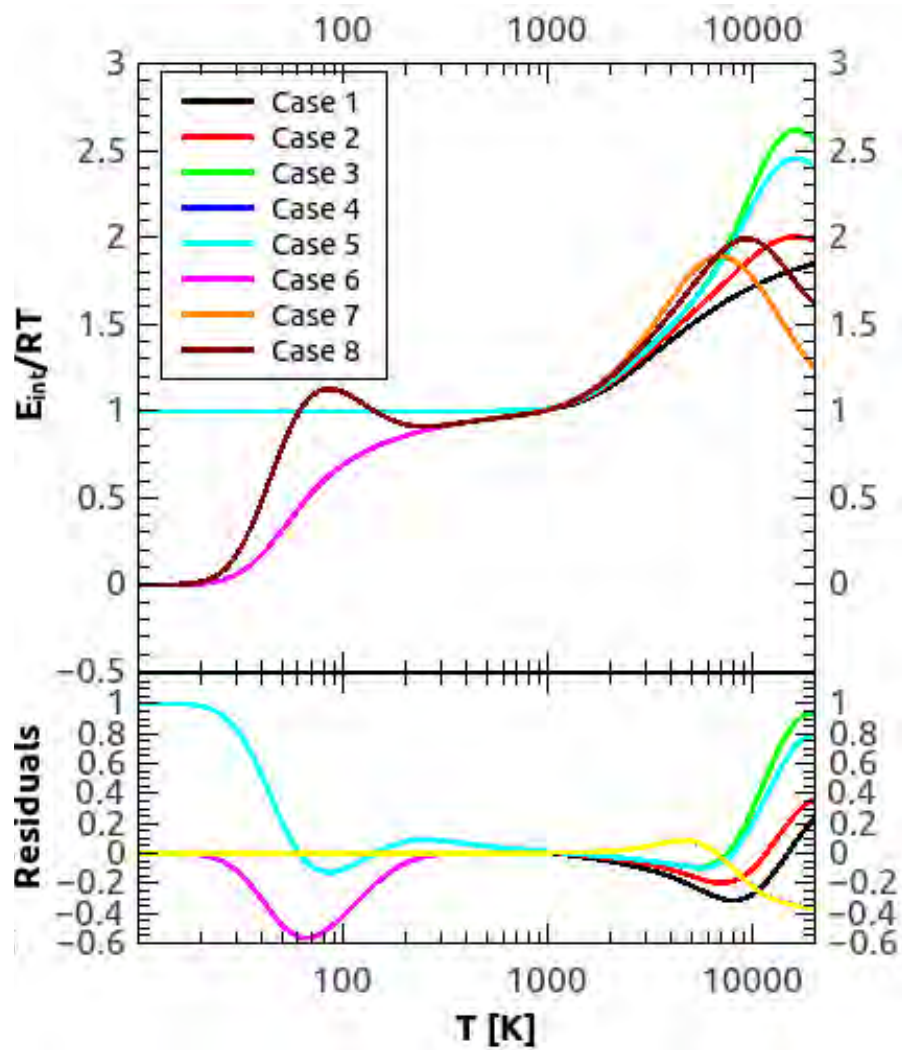


Figure 3.6: Normalised internal energy for the H_2 molecule. Cases 1 to 5 are identical until 1000 K, and case 7 is almost identical to case 8 until 2000 K.

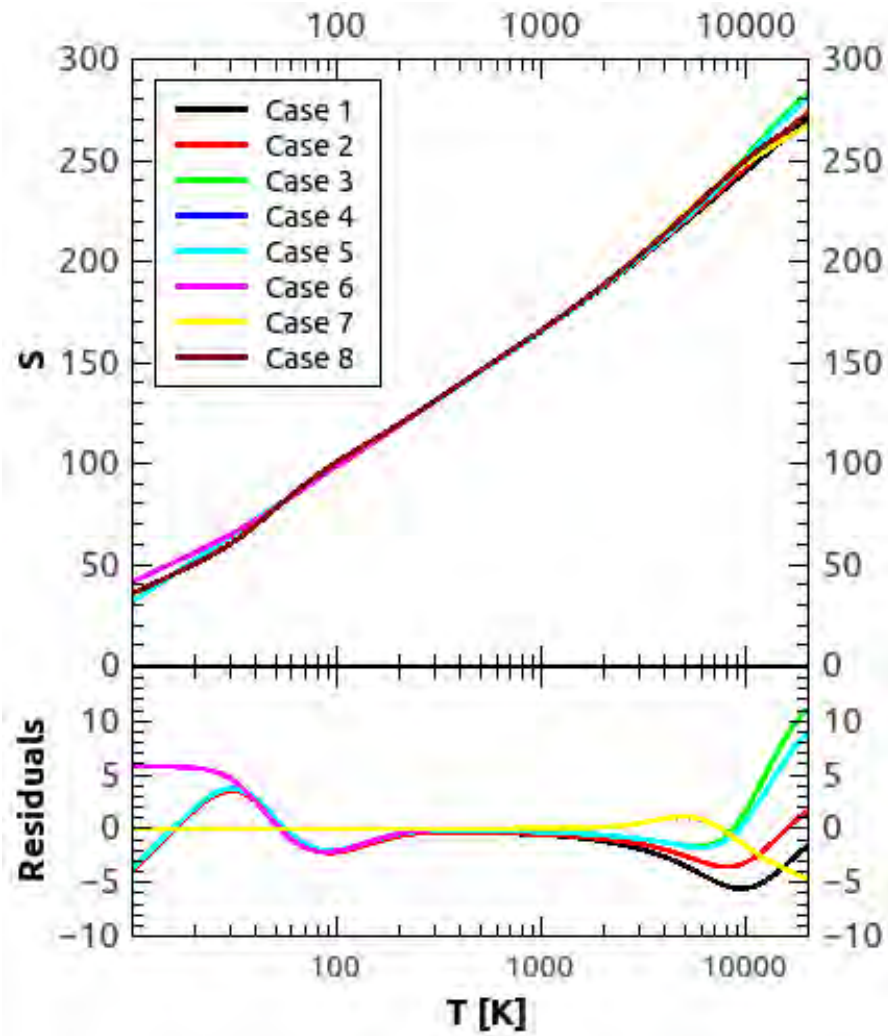


Figure 3.7: Entropy for the H₂ molecule.

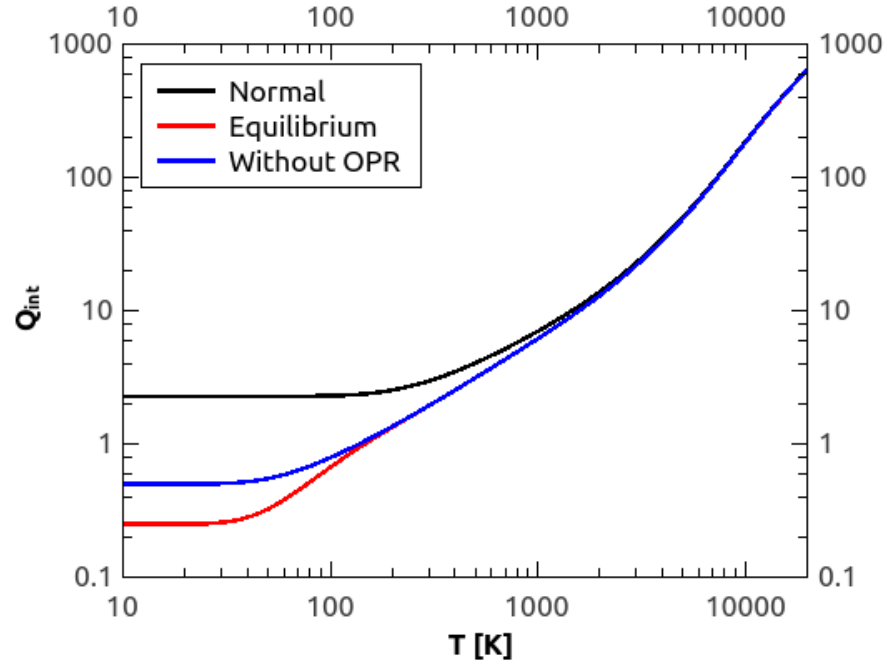


Figure 3.8: Q_{int} for equilibrium, normal, and one (i.e. neglecting OPR) hydrogen.

In future work we plan to use the method we described here to calculate partition functions and thermodynamic quantities for other astrophysically important molecular species as well.

3.8 ACKNOWLEDGEMENTS

We thank Åke Nordlund and Tommaso Grassi for a critical reading of this manuscript and all the very valuable discussions. We are also grateful to the referee, Robert Kurucz, for valuable comments and suggestions. AP work is supported by grant number 1323-00199A from the Danish Council for Independent Research (FNU).

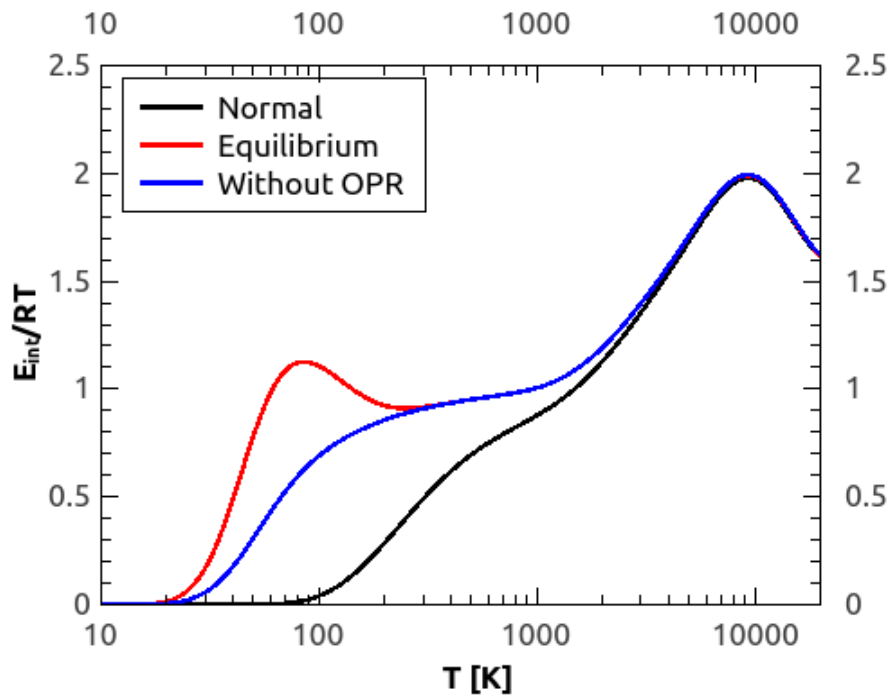


Figure 3.9: Normalised internal energy, calculated for equilibrium, normal, and with neglected OPR hydrogen.

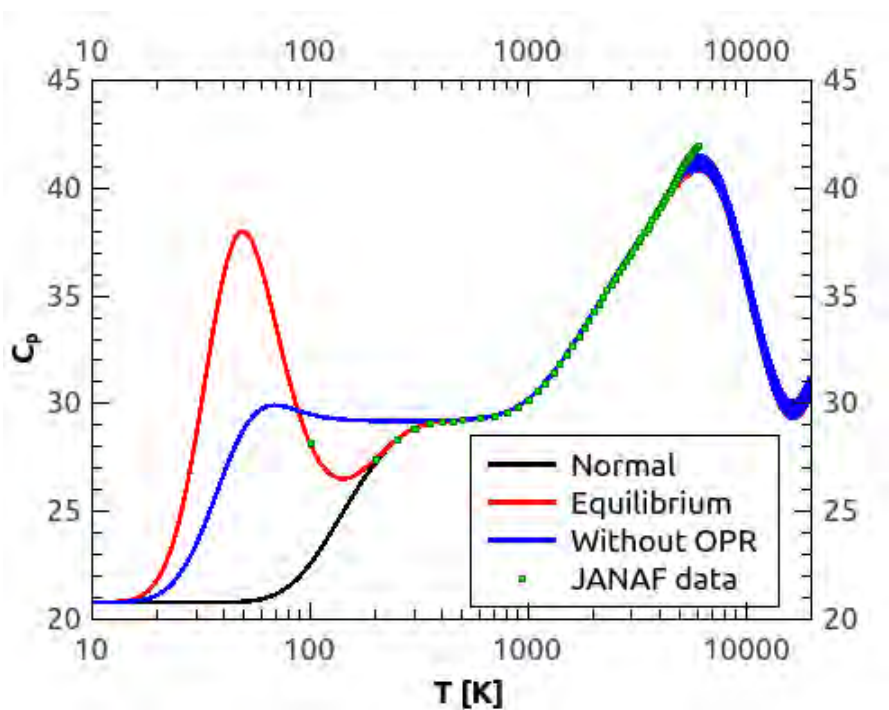


Figure 3.10: C_p , calculated for equilibrium, normal, and with neglected OPR hydrogen. JANAF data are also shown.

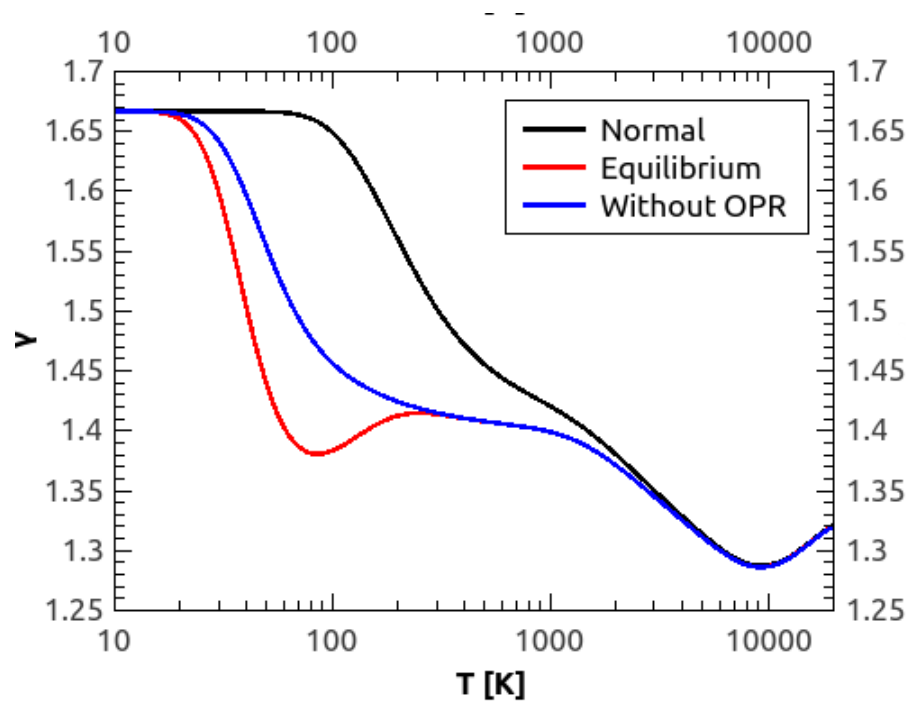


Figure 3.11: Adiabatic index, calculated for equilibrium, normal, and with neglected OPR hydrogen.

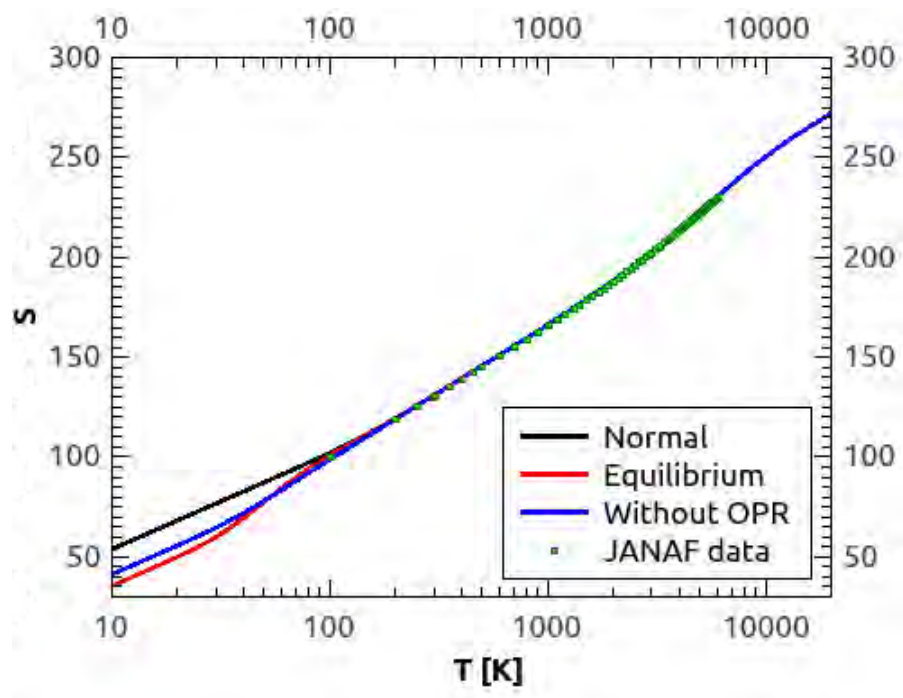


Figure 3.12: Entropy, calculated for equilibrium, normal, and with neglected OPR hydrogen. JANAF data are also shown.

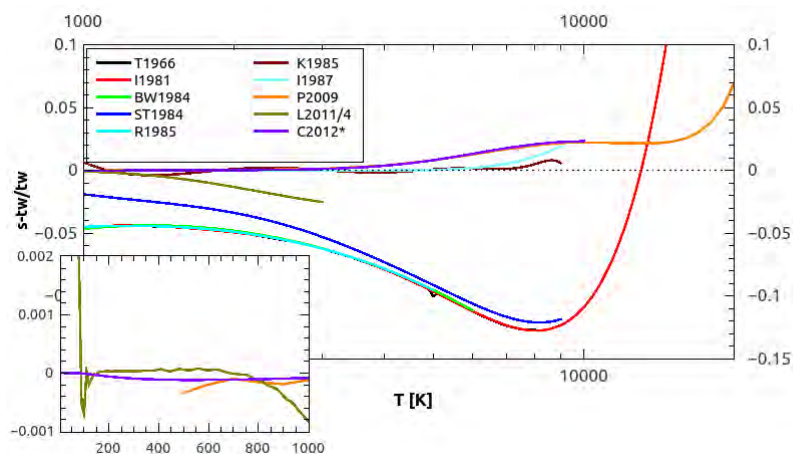


Figure 3.13: Normalised Q_{int} from other studies in their respective temperature ranges. Normalisation is made with respect to the results of this work, $([study - this\ work]/this\ work)$. C2012 is normalised to normal hydrogen, all other studies to equilibrium hydrogen. The inset shows the low-temperature range.

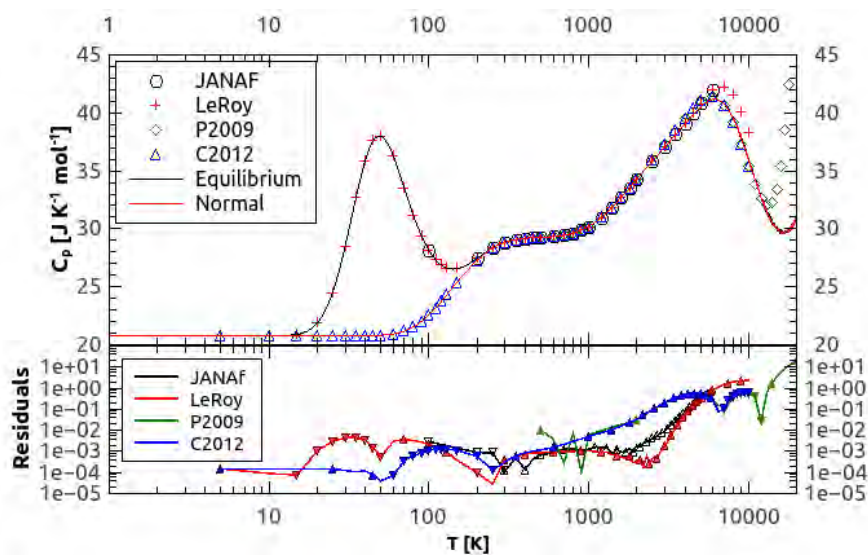
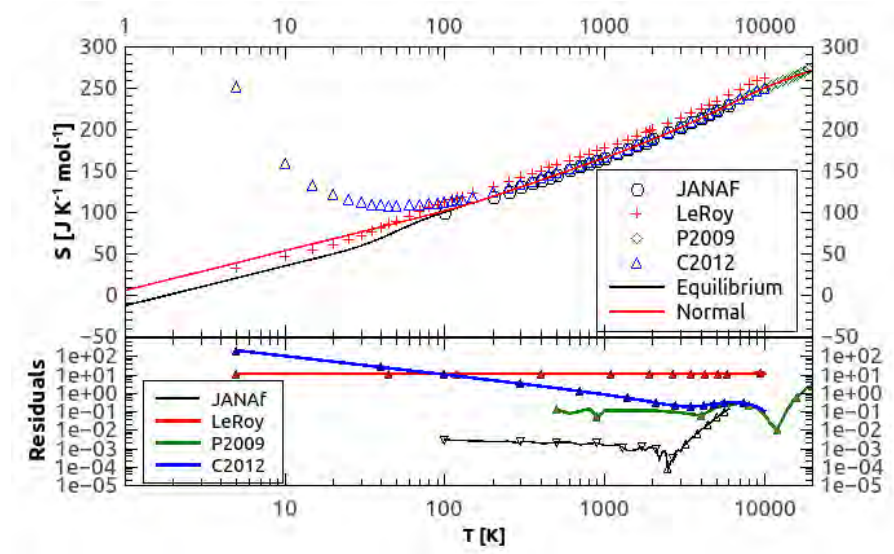


Figure 3.14: Calculated C_p comparison to other studies. The top panel shows resulting C_p values, the bottom panel residuals (other - ours) on a logarithmic scale. Facing down triangles indicate that other results have lower values than ours, facing up triangles indicate that the values are higher.

Figure 3.15: Same as in Fig. 3.14, but for S .Table 3.24: Polynomial fit constants for partition functions of equilibrium, normal, and ortho and para H_2

Low temperature (T = 10 - 250 K)							
Flavor	a_0	a_1	a_2	a_3	a_4	RMS	
Equilibrium	2.673e-01	-3.4956e-03	1.2279e-04	-5.77644e-07	9.2512e-10	0.00516	
Normal	2.277	3.1155e-04	-1.1992e-05	1.3483e-07	-2.4935e-10	0.00091	
Ortho	2.9964	3.80786e-04	-8.6597e-06	5.779e-08	-5.4077e-11	0.00107	
Para	9.994e-01	3.1354e-04	-1.5994e-05	2.032e-07	-4.09e-10	0.00186	
Medium temperature (T = 200 - 1100 K)							
Flavor	a_0	a_1	a_2	a_3	a_4	RMS	
Equilibrium	1.41e-01	6.0857e-03	-4.097e-07	4.22e-10	-8.79e-14	0.0007	
Normal	1.9198	1.7462e-03	7.6932e-06	-6.5043e-09	2.132e-12	0.00247	
Ortho	2.89	-1.24e-03	1.31e-05	-1.1051e-08	3.56265e-12	0.00402	
Para	3.31288e-01	4.871e-03	2.3399e-06	-2.214e-09	8.2108e-13	0.00164	
High temperature (T = 1000 - 20000 K)							
Flavor	a_0	a_1	a_2	a_3	a_4	a_5	RMS
Equilibrium	-9.6618e-01	7.3021e-03	-6.76089e-07	3.1287e-10	-1.6452e-14	2.7886e-19	0.099
Normal	-1.1428e-01	7.2454e-03	-6.4045e-07	3.11097e-10	-1.6428e-14	2.79e-19	0.10151
Ortho	2.2317e-01	7.190413e-03	-6.192077e-07	3.096e-10	-1.64e-14	2.79e-19	0.10242
Para	-1.019e+00	7.36e-03	-6.93579e-07	3.14527e-10	-1.64658e-14	2.78e-19	0.10004

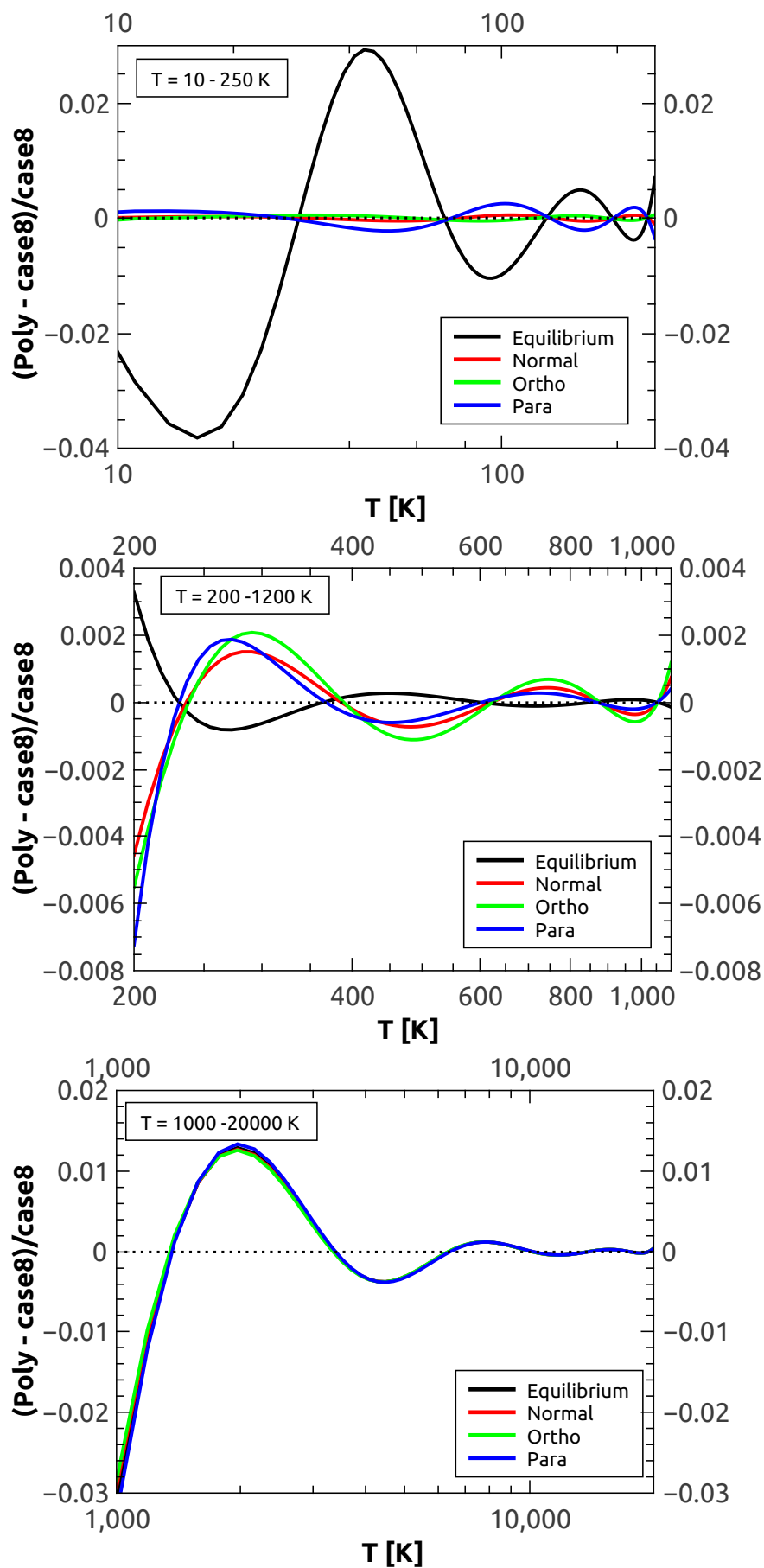


Figure 3.16: Accuracies of polynomial fits for the partition functions of H_2 .

Table 3.25: Thermodynamic properties of equilibrium H₂.

T [K]	Q_{int}	E_{int}/RT [J]	$H - H(0)$ [J mol ⁻¹]	S [J K ⁻¹ mol ⁻¹]	C_p [J K ⁻¹ mol ⁻¹]	C_v [J K ⁻¹ mol ⁻¹]	$-(G - H(0))/T$ [J K ⁻¹ mol ⁻¹]	γ
5.0	0.25	0.0	103.931	21.095	20.786	0.0	-40.026	1.667
10.0	0.25	0.0	207.862	35.503	20.787	0.001	64.026	1.667
15.0	0.25	0.001	311.94	43.942	20.898	0.112	222.473	1.666
20.0	0.25	0.015	418.257	50.053	21.864	1.078	416.507	1.66
25.0	0.252	0.066	533.473	55.184	24.518	3.732	638.256	1.638
30.0	0.258	0.169	665.765	59.996	28.537	7.751	884.693	1.599
35.0	0.267	0.315	819.085	64.715	32.706	11.92	1154.933	1.551
40.0	0.282	0.48	991.15	69.305	35.893	15.107	1448.489	1.505
45.0	0.301	0.642	1175.533	73.647	37.61	16.824	1764.426	1.467
50.0	0.324	0.783	1364.975	77.638	37.97	17.184	2101.227	1.438
60.0	0.382	0.984	1737.824	84.441	36.242	15.456	2829.782	1.403
70.0	0.448	1.085	2086.766	89.826	33.537	12.75	3619.013	1.387
80.0	0.519	1.123	2409.737	94.142	31.153	10.367	4456.451	1.381
90.0	0.593	1.124	2711.881	97.703	29.377	8.591	5333.052	1.381
100.0	0.667	1.107	2999.115	100.73	28.151	7.365	6242.444	1.384
110.0	0.74	1.082	3276.322	103.373	27.351	6.565	7180.087	1.387
120.0	0.813	1.055	3547.19	105.73	26.867	6.081	8142.661	1.391
130.0	0.883	1.029	3814.429	107.869	26.613	5.827	9127.671	1.395
140.0	0.952	1.005	4080.006	109.837	26.526	5.739	10133.185	1.399
150.0	1.02	0.984	4345.331	111.668	26.556	5.77	11157.669	1.403
200.0	1.341	0.923	5692.821	119.414	27.448	6.662	16527.172	1.413
150.0	1.02	0.984	4345.331	111.668	26.556	5.77	11157.669	1.403
298.15	1.931	0.916	8467.176	130.682	28.836	8.05	28016.705	1.414
300.0	1.942	0.916	8520.534	130.86	28.849	8.063	28243.25	1.414
350.0	2.238	0.926	9969.563	135.327	29.081	8.294	34484.941	1.412
400.0	2.534	0.936	11426.436	139.218	29.181	8.395	40934.958	1.411
450.0	2.831	0.944	12886.795	142.658	29.229	8.442	47567.798	1.409
500.0	3.128	0.952	14349.02	145.739	29.259	8.473	54363.344	1.408
600.0	3.725	0.963	17278.057	151.079	29.326	8.54	68380.83	1.406
700.0	4.324	0.973	20215.836	155.608	29.44	8.654	82889.4	1.404
800.0	4.928	0.983	23168.335	159.55	29.623	8.837	97820.014	1.403
900.0	5.536	0.994	26142.864	163.053	29.88	9.094	113121.903	1.401
1000.0	6.151	1.006	29146.545	166.217	30.204	9.418	128756.479	1.399
1100.0	6.774	1.019	32185.337	169.113	30.579	9.793	144693.583	1.397
1200.0	7.406	1.034	35263.602	171.792	30.991	10.204	160909.037	1.395
1300.0	8.051	1.051	38384.094	174.289	31.421	10.635	177383.01	1.392
1400.0	8.709	1.069	41548.164	176.634	31.86	11.074	194098.888	1.389
1500.0	9.382	1.089	44756.054	178.847	32.297	11.511	211042.494	1.386
2000.0	13.015	1.193	61416.861	188.419	34.278	13.492	298792.538	1.371
2500.0	17.181	1.299	78962.143	196.243	35.838	15.052	390859.016	1.357
3000.0	21.964	1.397	97201.242	202.89	37.077	16.291	486526.148	1.345
3500.0	27.428	1.486	116007.0	208.686	38.121	17.335	585293.496	1.335
4000.0	33.632	1.568	135302.809	213.838	39.043	18.257	686790.762	1.326
4500.0	40.634	1.644	155031.8	218.484	39.852	19.066	790732.925	1.318
5000.0	48.492	1.713	175128.639	222.719	40.508	19.721	896892.151	1.311
6000.0	66.988	1.831	216042.905	230.176	41.156	20.37	1.115128382e6	1.3
7000.0	89.448	1.917	257096.393	236.506	40.779	19.993	1.340240895e6	1.293
8000.0	115.989	1.97	297322.673	241.879	39.553	18.767	1.571192049e6	1.288
9000.0	146.498	1.991	336046.785	246.442	37.836	17.049	1.807099542e6	1.286
10000.0	180.675	1.986	372961.362	250.333	35.979	15.193	2.047222929e6	1.287
11000.0	218.099	1.962	408052.021	253.679	34.211	13.425	2.29095485e6	1.289
12000.0	258.301	1.925	441490.549	256.589	32.676	11.89	2.537806546e6	1.292
13000.0	300.818	1.881	473549.464	259.156	31.484	10.698	2.787389971e6	1.296
14000.0	345.231	1.834	504545.723	261.453	30.59	9.804	3.039399948e6	1.3
15000.0	391.19	1.788	534806.189	263.541	29.996	9.21	3.293598228e6	1.304
16000.0	438.423	1.744	564646.464	265.467	29.722	8.936	3.549799968e6	1.308
17000.0	486.741	1.705	594357.51	267.269	29.744	8.958	3.80786255e6	1.312
18000.0	536.03	1.671	624196.974	268.974	29.964	9.178	4.067676383e6	1.315
19000.0	586.244	1.642	654383.656	270.606	30.448	9.662	4.329157371e6	1.318
20000.0	637.389	1.62	685094.498	272.181	39.3	18.514	4.59224074e6	1.321

Table 3.26: Thermodynamic properties of normal H₂.

T [K]	Q_{int}	E_{int}/RT [J]	$H - H(0)$ [J mol ⁻¹]	S [J K ⁻¹ mol ⁻¹]	C_p [J K ⁻¹ mol ⁻¹]	C_v [J K ⁻¹ mol ⁻¹]	$-[G - H(0)]/T$ [J K ⁻¹ mol ⁻¹]	γ
5.0	2.28	0.0	103.931	39.472	20.786	0.0	51.859	1.667
10.0	2.28	0.0	207.861	53.88	20.786	0.0	247.797	1.667
15.0	2.28	0.0	311.792	62.308	20.786	-0.0	498.116	1.667
20.0	2.28	0.0	415.723	68.288	20.786	0.0	783.751	1.667
25.0	2.28	0.0	519.654	72.926	20.786	0.0	1095.646	1.667
30.0	2.28	0.0	623.585	76.716	20.786	0.0	1428.468	1.667
35.0	2.28	0.0	727.518	79.92	20.787	0.001	1778.693	1.667
40.0	2.28	0.0	831.461	82.696	20.791	0.005	2143.818	1.667
45.0	2.28	0.0	935.441	85.146	20.802	0.016	2521.971	1.667
50.0	2.28	0.0	1039.506	87.339	20.827	0.041	2911.705	1.666
60.0	2.28	0.002	1248.259	91.144	20.941	0.155	3721.536	1.666
70.0	2.281	0.006	1458.731	94.388	21.175	0.389	4566.442	1.664
80.0	2.284	0.014	1672.186	97.238	21.537	0.751	5441.706	1.661
90.0	2.29	0.026	1889.847	99.801	22.011	1.225	6343.964	1.656
100.0	2.298	0.041	2112.669	102.148	22.563	1.777	7270.725	1.649
110.0	2.309	0.06	2341.243	104.326	23.155	2.369	8220.08	1.641
120.0	2.323	0.082	2575.795	106.367	23.754	2.968	9190.508	1.632
130.0	2.34	0.106	2816.26	108.291	24.334	3.548	10180.745	1.623
140.0	2.361	0.131	3062.367	110.115	24.881	4.094	11189.711	1.613
150.0	2.384	0.157	3313.73	111.849	25.385	4.599	12216.458	1.603
200.0	2.54	0.287	4634.245	119.434	27.269	6.483	17589.625	1.56
150.0	2.384	0.157	3313.73	111.849	25.385	4.599	12216.458	1.603
298.15	2.964	0.487	7404.367	130.682	28.834	8.047	29079.567	1.503
300.0	2.973	0.49	7457.721	130.861	28.846	8.06	29306.112	1.503
350.0	3.224	0.561	8906.702	135.327	29.08	8.294	35547.806	1.485
400.0	3.488	0.616	10363.571	139.218	29.181	8.395	41997.824	1.473
450.0	3.761	0.66	11823.929	142.658	29.229	8.442	48630.664	1.463
500.0	4.039	0.696	13286.154	145.739	29.259	8.473	55426.21	1.455
600.0	4.609	0.75	16215.191	151.079	29.326	8.54	69443.696	1.444
700.0	5.191	0.791	19152.97	155.608	29.44	8.654	83952.266	1.437
800.0	5.782	0.823	22105.469	159.55	29.623	8.837	98882.88	1.43
900.0	6.381	0.852	25079.998	163.053	29.88	9.094	114184.769	1.425
1000.0	6.989	0.878	28083.68	166.217	30.204	9.418	129819.345	1.421
1100.0	7.608	0.903	31122.471	169.113	30.579	9.793	145756.449	1.416
1200.0	8.239	0.928	34200.737	171.792	30.99	10.204	161971.903	1.412
1300.0	8.883	0.953	37321.228	174.289	31.422	10.635	178445.876	1.408
1400.0	9.542	0.978	40485.298	176.634	31.86	11.074	195161.754	1.404
1500.0	10.217	1.003	43693.188	178.847	32.297	11.51	212105.359	1.399
2000.0	13.874	1.129	60353.995	188.419	34.278	13.492	299855.404	1.38
2500.0	18.083	1.248	77899.277	196.243	35.838	15.052	391921.882	1.364
3000.0	22.92	1.354	96138.376	202.89	37.077	16.291	487589.013	1.35
3500.0	28.448	1.45	114944.134	208.686	38.122	17.336	586356.362	1.339
4000.0	34.724	1.536	134239.943	213.838	39.043	18.257	687853.627	1.329
4500.0	41.805	1.615	153968.934	218.484	39.852	19.065	791795.791	1.321
5000.0	49.748	1.687	174065.773	222.719	40.508	19.722	897955.017	1.314
6000.0	68.431	1.809	214980.038	230.176	41.156	20.37	1.116191248e6	1.302
7000.0	91.097	1.899	256033.52	236.505	40.784	19.998	1.34130376e6	1.294
8000.0	117.857	1.954	296259.779	241.879	39.56	18.774	1.572254912e6	1.29
9000.0	148.594	1.977	334983.848	246.442	37.84	17.054	1.808162398e6	1.288
10000.0	182.999	1.973	371898.356	250.333	35.983	15.197	2.048285773e6	1.288
11000.0	220.648	1.95	406988.917	253.679	34.219	13.432	2.292017674e6	1.29
12000.0	261.068	1.914	440427.327	256.589	32.717	11.931	2.538869339e6	1.293
13000.0	303.791	1.871	472486.104	259.156	31.482	10.696	2.788452722e6	1.297
14000.0	348.397	1.825	503482.216	261.453	30.569	9.782	3.040462648e6	1.301
15000.0	394.537	1.78	533742.527	263.541	30.004	9.217	3.294660864e6	1.305
16000.0	441.939	1.736	563582.645	265.467	29.741	8.955	3.550862531e6	1.309
17000.0	490.413	1.697	593293.539	267.268	29.736	8.95	3.808925029e6	1.313
18000.0	539.849	1.664	623132.856	268.974	29.995	9.209	4.06873877e6	1.316
19000.0	590.199	1.636	653319.399	270.606	30.443	9.657	4.330219658e6	1.319
20000.0	641.473	1.613	684030.114	272.181	30.297	18.511	4.593302921e6	1.321

Table 3.27: Thermodynamic properties of ortho H₂.

T [K]	Q_{int}	E_{int}/RT [J]	$H - H(0)$ [J mol ⁻¹]	S [J K ⁻¹ mol ⁻¹]	C_p [J K ⁻¹ mol ⁻¹]	C_v [J K ⁻¹ mol ⁻¹]	$-(G - H(0))/T$ [J K ⁻¹ mol ⁻¹]	γ
5.0	3.0	0.0	103.931	41.756	20.786	0.0	63.277	1.667
10.0	3.0	0.0	207.861	56.164	20.786	0.0	270.633	1.667
15.0	3.0	0.0	311.792	64.592	20.786	0.0	532.37	1.667
20.0	3.0	0.0	415.723	70.572	20.786	0.0	829.423	1.667
25.0	3.0	0.0	519.654	75.21	20.786	0.0	1152.736	1.667
30.0	3.0	0.0	623.584	79.0	20.786	0.0	1496.976	1.667
35.0	3.0	0.0	727.515	82.204	20.786	0.0	1858.619	1.667
40.0	3.0	0.0	831.446	84.98	20.786	0.0	2235.16	1.667
45.0	3.0	0.0	935.377	87.428	20.786	0.0	2624.727	1.667
50.0	3.0	0.0	1039.308	89.618	20.786	0.0	3025.865	1.667
60.0	3.0	0.0	1247.182	93.408	20.789	0.003	3858.425	1.667
70.0	3.0	0.0	1455.125	96.613	20.802	0.016	4725.796	1.667
80.0	3.0	0.001	1663.318	99.393	20.842	0.056	5622.99	1.666
90.0	3.001	0.002	1872.131	101.853	20.93	0.144	6546.308	1.666
100.0	3.002	0.004	2082.135	104.065	21.083	0.297	7492.933	1.665
110.0	3.003	0.008	2294.057	106.085	21.315	0.529	8460.68	1.663
120.0	3.006	0.014	2508.698	107.952	21.627	0.84	9447.833	1.66
130.0	3.011	0.023	2726.839	109.698	22.013	1.227	10453.031	1.657
140.0	3.017	0.034	2949.171	111.346	22.462	1.676	11475.178	1.652
150.0	3.025	0.047	3176.238	112.912	22.958	2.171	12513.382	1.647
200.0	3.103	0.14	4390.077	119.878	25.561	4.775	17922.591	1.61
150.0	3.025	0.047	3176.238	112.912	22.958	2.171	12513.382	1.647
298.15	3.416	0.352	7069.282	130.738	28.461	7.675	29431.377	1.54
300.0	3.424	0.355	7121.959	130.914	28.486	7.7	29658.024	1.539
350.0	3.641	0.441	8559.265	135.345	28.941	8.155	35901.334	1.515
400.0	3.88	0.51	10011.739	139.223	29.13	8.344	42351.87	1.497
450.0	4.134	0.566	11470.509	142.66	29.21	8.424	48984.875	1.484
500.0	4.399	0.611	12932.172	145.74	29.253	8.467	55780.474	1.474
600.0	4.948	0.679	15860.941	151.079	29.325	8.539	69797.982	1.459
700.0	5.517	0.73	18798.687	155.608	29.44	8.653	84306.554	1.448
800.0	6.098	0.77	21751.181	159.55	29.623	8.837	99237.169	1.441
900.0	6.69	0.804	24725.709	163.053	29.88	9.094	114539.057	1.434
1000.0	7.294	0.835	27729.391	166.217	30.204	9.418	130173.634	1.428
1100.0	7.909	0.864	30768.183	169.113	30.579	9.793	146110.737	1.423
1200.0	8.537	0.892	33846.448	171.792	30.99	10.204	162326.192	1.418
1300.0	9.179	0.92	36966.94	174.289	31.422	10.635	178800.165	1.413
1400.0	9.836	0.948	40131.01	176.634	31.86	11.074	195516.042	1.409
1500.0	10.511	0.975	43338.899	178.847	32.297	11.51	212459.648	1.404
2000.0	14.173	1.108	59999.706	188.419	34.278	13.492	300209.693	1.383
2500.0	18.393	1.231	77544.988	196.243	35.838	15.052	392276.17	1.366
3000.0	23.248	1.34	95784.081	202.89	37.077	16.291	487943.302	1.352
3500.0	28.797	1.438	114589.782	208.686	38.122	17.335	586710.645	1.34
4000.0	35.096	1.526	133885.328	213.838	39.042	18.256	688207.888	1.331
4500.0	42.202	1.606	153613.51	218.484	39.849	19.063	792149.966	1.322
5000.0	50.173	1.678	173708.508	222.718	40.503	19.717	898308.966	1.315
6000.0	68.916	1.802	214614.043	230.174	41.144	20.357	1.116543844e6	1.303
7000.0	91.645	1.893	255650.45	236.501	40.76	19.974	1.34165289e6	1.295
8000.0	118.466	1.948	295852.244	241.871	39.533	18.746	1.572597596e6	1.29
9000.0	149.256	1.971	334547.337	246.43	37.81	17.024	1.808495266e6	1.288
10000.0	183.704	1.967	371431.338	250.318	35.952	15.166	2.048605493e6	1.288
11000.0	221.382	1.945	406492.024	253.661	34.191	13.405	2.292321206e6	1.29
12000.0	261.814	1.909	439902.437	256.569	32.688	11.902	2.53915404e6	1.293
13000.0	304.533	1.866	471935.664	259.134	31.454	10.668	2.788716353e6	1.297
14000.0	349.119	1.82	502908.834	261.43	30.545	9.758	3.040703339e6	1.301
15000.0	395.221	1.775	533148.787	263.516	29.974	9.188	3.294877066e6	1.305
16000.0	442.572	1.732	562971.041	265.441	29.735	8.949	3.551052967e6	1.309
17000.0	490.982	1.693	592666.488	267.241	29.721	8.935	3.809088657e6	1.313
18000.0	540.34	1.659	622492.742	268.946	29.99	9.204	4.068874749e6	1.317
19000.0	590.602	1.631	652668.607	270.577	30.434	9.648	4.330327328e6	1.319
20000.0	641.778	1.61	683371.061	272.152	39.29	18.504	4.59338178e6	1.322

Table 3.28: Thermodynamic properties of para H₂.

T [K]	Q_{int}	E_{int}/RT [J]	$H - H(0)$ [J mol ⁻¹]	S [J K ⁻¹ mol ⁻¹]	C_p [J K ⁻¹ mol ⁻¹]	C_v [J K ⁻¹ mol ⁻¹]	$-[G - H(0)]/T$ [J K ⁻¹ mol ⁻¹]	γ
5.0	1.0	0.0	103.931	32.622	20.786	0.0	17.605	1.667
10.0	1.0	0.0	207.861	47.03	20.786	0.0	179.289	1.667
15.0	1.0	0.0	311.792	55.458	20.786	0.0	395.355	1.667
20.0	1.0	0.0	415.723	61.437	20.786	0.0	646.735	1.667
25.0	1.0	0.0	519.654	66.076	20.786	0.0	924.377	1.667
30.0	1.0	0.0	623.585	69.865	20.787	0.001	1222.945	1.667
35.0	1.0	0.0	727.525	73.07	20.79	0.004	1538.917	1.667
40.0	1.0	0.0	831.508	75.847	20.806	0.02	1869.79	1.667
45.0	1.0	0.001	935.632	78.3	20.85	0.064	2213.703	1.666
50.0	1.0	0.002	1040.099	80.501	20.947	0.161	2569.224	1.666
60.0	1.001	0.009	1251.492	84.354	21.398	0.612	3310.871	1.663
70.0	1.003	0.025	1469.549	87.713	22.291	1.505	4088.379	1.656
80.0	1.009	0.054	1698.789	90.773	23.621	2.835	4897.857	1.644
90.0	1.017	0.097	1942.994	93.647	25.255	4.469	5736.931	1.626
100.0	1.031	0.151	2204.272	96.398	27.003	6.217	6604.1	1.606
110.0	1.049	0.215	2482.799	99.052	28.677	7.891	7498.282	1.583
120.0	1.071	0.283	2777.086	101.611	30.136	9.35	8418.531	1.561
130.0	1.099	0.354	3084.521	104.071	31.298	10.511	9363.887	1.539
140.0	1.131	0.423	3401.955	106.423	32.136	11.349	10333.31	1.52
150.0	1.167	0.488	3726.206	108.66	32.666	11.88	11325.683	1.503
200.0	1.393	0.727	5366.75	118.102	32.393	11.607	16590.726	1.449
150.0	1.167	0.488	3726.206	108.66	32.666	11.88	11325.683	1.503
298.15	1.937	0.892	8409.623	130.514	29.951	9.165	28024.137	1.418
300.0	1.947	0.894	8465.01	130.699	29.927	9.141	28250.377	1.418
350.0	2.24	0.919	9949.013	135.275	29.497	8.711	34487.222	1.413
400.0	2.535	0.933	11419.066	139.201	29.333	8.547	40935.684	1.411
450.0	2.831	0.944	12884.19	142.653	29.283	8.497	47568.031	1.409
500.0	3.128	0.951	14348.103	145.738	29.278	8.492	54363.419	1.408
600.0	3.725	0.963	17277.941	151.079	29.329	8.542	68380.839	1.406
700.0	4.324	0.973	20215.82	155.608	29.44	8.654	82889.401	1.404
800.0	4.928	0.983	23168.333	159.55	29.623	8.837	97820.014	1.403
900.0	5.536	0.994	26142.863	163.053	29.88	9.094	113121.903	1.401
1000.0	6.151	1.006	29146.545	166.217	30.204	9.418	128756.479	1.399
1100.0	6.774	1.019	32185.337	169.113	30.579	9.793	144693.583	1.397
1200.0	7.406	1.034	35263.602	171.792	30.99	10.204	160909.037	1.395
1300.0	8.051	1.051	38384.094	174.289	31.422	10.635	177383.01	1.392
1400.0	8.709	1.069	41548.164	176.634	31.86	11.074	194098.888	1.389
1500.0	9.382	1.089	44756.054	178.847	32.297	11.511	211042.494	1.386
2000.0	13.015	1.193	61416.861	188.419	34.278	13.492	298792.538	1.371
2500.0	17.181	1.299	78962.144	196.243	35.838	15.051	390859.016	1.357
3000.0	21.964	1.397	97201.262	202.89	37.077	16.291	486526.149	1.345
3500.0	27.428	1.486	116007.188	208.686	38.122	17.336	585293.51	1.335
4000.0	33.632	1.568	135303.791	213.838	39.047	18.26	686790.847	1.326
4500.0	40.634	1.644	155035.207	218.485	39.859	19.073	790733.265	1.318
5000.0	48.493	1.713	175137.568	222.721	40.522	19.736	896893.167	1.311
6000.0	66.995	1.831	216078.024	230.183	41.192	20.405	1.11513346e6	1.3
7000.0	89.472	1.919	257182.729	236.52	40.847	20.061	1.340256372e6	1.292
8000.0	116.05	1.972	297482.384	241.903	39.641	18.855	1.57122686e6	1.288
9000.0	146.624	1.994	336293.379	246.476	37.931	17.145	1.807163794e6	1.286
10000.0	180.9	1.99	373299.41	250.377	36.071	15.285	2.047326615e6	1.287
11000.0	218.462	1.966	408479.598	253.731	34.302	13.516	2.29110708e6	1.288
12000.0	258.842	1.93	442001.997	256.649	32.799	12.012	2.538015238e6	1.292
13000.0	301.576	1.887	474137.426	259.222	31.549	10.763	2.787661831e6	1.295
14000.0	346.243	1.84	505202.36	261.525	30.652	9.865	3.039740575e6	1.299
15000.0	392.49	1.794	535523.749	263.617	30.079	9.293	3.294012259e6	1.304
16000.0	440.045	1.75	565417.46	265.546	29.776	8.99	3.550291223e6	1.308
17000.0	488.713	1.711	595174.689	267.35	29.787	9.0	3.808434146e6	1.311
18000.0	538.38	1.676	625053.198	269.058	30.023	9.237	4.068330833e6	1.315
19000.0	588.994	1.648	655271.777	270.692	30.442	9.656	4.329896651e6	1.318
20000.0	640.561	1.625	686007.275	272.268	30.406	18.62	4.593066343e6	1.32

PAPER II: DISPATCH: A NUMERICAL SIMULATION
FRAMEWORK FOR THE EXA-SCALE ERA. I.
FUNDAMENTALS

Å. Nordlund, J. P. Ramsey, A. Popovas, M. Küffmeier

¹ Centre for Star and Planet Formation, Niels Bohr Institute and Natural History Museum of
Denmark, University of Copenhagen, Øster Voldgade 5-7, DK-1350 Copenhagen K, Denmark

Submitted to *Monthly Notices of the Royal Astronomical Society (MNRAS)*

We introduce a high-performance simulation framework that permits the semi-independent, task-based solution of sets of partial differential equations, typically manifesting as updates to a collection of ‘patches’ in space-time. A hybrid Message Passing Interface (MPI)/Open Multi-Processing (OpenMP) execution model is adopted, where work tasks are controlled by a rank-local ‘dispatcher’ which selects, from a set of tasks generally much larger than the number of physical cores (or hardware threads), tasks that are ready for updating. The definition of a task can vary, for example, with some solving the equations of ideal magnetohydrodynamics (MHD), others non-ideal MHD, radiative transfer, or particle motion, and yet others applying Particle-in-Cell (PIC) methods. Tasks do not have to be grid-based, while tasks that are, may use either Cartesian or orthogonal curvilinear meshes. Patches may be stationary or moving. Mesh refinement can be static or dynamic. A feature of decisive importance for the overall performance of the framework is that time steps are determined and applied locally; this allows potentially large reductions in the total number of updates required in cases when the signal speed varies greatly across the computational domain, and therefore a corresponding reduction in computing time. Another feature is a load balancing algorithm that operates ‘locally’ and aims to simultaneously minimise load and communication imbalance. The framework generally relies on already existing solvers, whose performance is augmented when run under the framework, due to more efficient cache usage, vectorisation, local time stepping, plus near-linear and, in principle, unlimited OpenMP and MPI scaling.

4.1 INTRODUCTION

Numerical simulations of astrophysical phenomena are indispensable in furthering our understanding of the Universe. A particularly successful example is the many applications of the equations of MHD in the contexts of cosmology, galaxy evolution, star formation, stellar evolution, solar and stellar activity, and planet formation. As the available computer power has increased over time, so too has the fidelity and complexity of astrophysical fluid simulations; more precisely, one could say these simulations have consistently been at the limit of what is computationally possible. The algorithms and techniques used to exploit the available resources have also increased in ingenuity and complexity over the years; from block-based Adaptive Mesh Refinement (AMR) (Berger & Olinger 1984; Berger & Colella 1989) to space-filling curves (e.g. Peano-Hilbert) to non-blocking distributed communication (e.g. Message Passing Interface version 3; MPI). The next evolution in HPC, ‘exa-scale’¹, is approaching and, as currently available tools are quickly reaching their limits (see, e.g., Dubey et al. 2014), new paradigms and techniques must be developed to fully exploit the upcoming generation of supercomputers.

However, since exa-scale supercomputers do not yet exist, we instead choose to limit our definition of ‘exa-scale ready’ to software that has intra- and inter-node scaling expected to continue to the number of cores required to reach exa-scales. Here, we present an intra-node task scheduling algorithm that has no practical limit, and we demonstrate that MPI-communications are only needed between a limited number of ‘nearby’ nodes. The first property guarantees that we will always be able to utilize the full capacity inside nodes, limited mainly by the memory bandwidth. The second property means that, as long as cluster network capacity continues to grow in proportion to compute capacity, inter-node communication will never become a bottleneck. Load and communication balancing is only indirectly involved, in the sense that, for problems where static load balancing is sufficient, the scaling properties can be measured for arbitrary size problems. In what follows, we point out that balancing the compute load is essentially trivial when tasks can be freely traded between compute nodes, and that the most important aspect of load balancing then shifts to minimizing inter-node communications. We indicate how this can be accomplished using only communications with nearest neighbour nodes, leaving the details to a forthcoming paper.

There are many astrophysical fluid simulation codes currently available within the scientific community. The most commonly used techniques include single grids (e.g. ZEUS; Stone & Norman 1992; Clarke 1996, FARGO3D; Benítez-Llambay & Masset 2016, PLUTO; Mignone et al. 2007, ATHENA; Stone et al. 2008, PENCIL; Brandenburg & Dobler 2002, Stagger; Nordlund et al. 1994; Kritsuk et al. 2011, BIFROST; Gudiksen et al. 2011), adaptively refined grids (e.g. ART; Kravtsov et al. 1997, NIRVANA; Ziegler 1998, ORION; Klein 1999, FLASH; Fryxell et al. 2000, RAMSES; Teyssier 2002; Fro-

¹ Exa-scale computing is defined as the use of computer systems capable of 10^{18} floating point operations (FLOPs) per second.

mang et al. 2006, AstroBEAR; Cunningham et al. 2009, CASTRO; Almgren et al. 2010, CRASH; van der Holst et al. 2011, AZEuS; Ramsey et al. 2012, ENZO; Bryan et al. 2014, AMRVAC; Porth et al. 2014) and smoothed particle hydrodynamics (e.g. GADGET; Springel 2005, PHANTOM; Lodato & Price 2010). More recently, moving mesh and mesh-less methods have begun to emerge (e.g. AREPO; Springel 2010, TESS; Duffell & MacFadyen 2011, GIZMO; Hopkins 2015, GANDALF; Hubber et al. 2018). The range of physics available from one code to the next is very broad, and includes (but is not limited to) radiative transport, heating and cooling, conduction, non-ideal MHD, cosmological expansion, special and general relativity, multiple fluids, and self-gravity.

There also exists a growing collection of frameworks which are solver- and physics-agnostic, but instead manage the parallelism, communication, scheduling, input/output and even resolution of a simulation (e.g. BoxLib², Charm++; Kale et al. 2008, Chombo; Adams et al. 2015, Overture; Brown et al. 1997, Uintah; Berzins et al. 2010, PATCHWORK; Shiokawa et al. 2017). Indeed, a few of these frameworks already couple to some of the aforementioned simulation codes (e.g. PLUTO+Chombo, CASTRO+BoxLib, ENZO-P/CELLO+Charm++).

Nearly all of the codes and frameworks mentioned above have fundamental weaknesses which limit their ability to scale indefinitely. In the survey of block-based adaptive mesh refinement codes and frameworks by Dubey et al. (2014), the authors conclude that “future architectures dictate the need to eliminate the bulk synchronous model that most codes currently employ”. Traditional grid-based codes must advance using time steps that obey the worst possible condition throughout the simulation volume, advancing at some fraction of a time step $\Delta t = \min(\Delta x/v_{\text{signal}})$. The time step may be determined locally, but it is applied globally. For AMR codes with sub-cycling, where larger meshes can take longer time steps, these must generally be a multiple of the finer mesh time steps, resulting again in a global coupling of time steps. A global time step which is controlled by the globally worst single cell is problematic, and the problem unavoidably becomes exasperated as supercomputers grow larger and the physical complexity of models correspondingly increases. Dubey et al. (2014) also discuss challenges related to both static load balancing, where difficulties arise when multi-physics simulations employ physics modules with very different update costs, and dynamic load balancing, wherein the load per MPI process needs to be adjusted, for example, because of time-dependent adaptive mesh refinement.

Parallelism in both specific codes and frameworks is almost always implemented using (distributed-memory) MPI, shared-memory thread-based parallelism (e.g. OpenMP, pthreads), or a combination of the two. Although MPI has its limitations (e.g. fault tolerance support), and new approaches are beginning to emerge (e.g. partitioned global address space; PGAS), it is the de facto standard for distributed-computing and will likely remain so leading up to the exa-scale era. Therefore, efficient and clever use of MPI is neces-

² <https://ccse.lbl.gov/BoxLib/index.html>

sary to ensure that performance and scaling do not degrade as we attempt to use the ever-growing resources enabled by ever-larger supercomputers (e.g. [Mendygral et al. 2017](#)). An important aspect of this is efficient load balancing, whereby a simulation redistributes the work dynamically in an attempt to maintain an even workload across resources.

Herein, we put forward and explore novel techniques that not only enable better utilisation and scaling for the forthcoming exa-scale era, but immediately offers distinct advantages for existing tools. Key to this, among other features, are: The concept of locally determined time steps, which, in realistic situations, can lead to dramatic savings of computing time. Next, the closely related concept of task-based execution, wherein each task depends on only a finite number of ‘neighbouring’ tasks. These tasks are often, but not necessarily, geometrically close. For example, sets of neighbouring tasks which solve a system of partial differential equations in space and time (which we denote as *patches*) need to supply guard zone values of density, momentum, etc., to one another, but neighbouring *tasks* can also encompass radiative transfer tasks with rays passing through the patch, or particle-based tasks, where particles travel through and interact with gas in a grid-based task. The neighbour concept can thus be described as a ‘dependency’ concept. By relying on this concept, we can ensure that **MPI** processes only need to communicate with a finite number of other **MPI** processes and, thus, we can, to a large (and often complete) extent, avoid the use of **MPI** global communications. In this regard, the neighbour concept provides the potential for essentially unlimited **MPI** scalability. The avoidance of global operations and the neighbour concept also applies to intra-node shared-memory parallelism: First, we keep the number of **OpenMP** ‘critical regions’ to an absolute minimum and instead rely on ‘atomic’ constructs. Second, we employ many more tasks per **MPI** rank than there are hardware threads, ensuring there are many more executable tasks than neighbour dependencies. Intra-node scalability is therefore, in general, limited only by memory bandwidth and cache usage.

These features are the foundation of the DISPATCH simulation framework. In what follows, we first describe the overall structure of the framework, outlining its constituent components and their interaction (Section 4.2). In Section 4.3, we then review the code structure in the context of execution of an experiment. In Section 4.4, we describe the major code components of the DISPATCH framework in detail. In Section 4.5, we validate the concepts and components by using four different numerical experiments to demonstrate the advantages of the DISPATCH framework and confirm that the solvers employed produce the same results as when used separately. To emphasise the framework aspect, each of the experiments uses a different solver; two internal solvers (a hydrodynamical Riemann solver and a staggered-mesh radiation magnetohydrodynamics (**RMHD**) solver) and one external solver (**ZEUS-3D**, implemented as an external library). Finally, in Section 4.6, we summarise the properties and advantages of the DISPATCH framework, relative to using conventional codes such as **RAMSES**, **Stagger**, and **AZEUS**. In follow-up work ([Popovas et al.](#); [Ramsey et al.](#), in prep.), we will extend our description of the

DISPATCH framework to include dynamic refinement, moving patches and patches of mixed coordinate types.

4.2 OBJECT HIERARCHY

DISPATCH is written in object-oriented Fortran and relies heavily on the concept of inheritance³. Certainly, the ideas and concepts within DISPATCH could easily be carried over to another object-oriented language, such as C++, but conversely, Fortran does not impose any serious language-related limitations on their implementation.

The framework is built on two main classes of objects: *tasks* and *task lists*.

4.2.1 *Tasks*

The task class hierarchy has, as its defining member, a

1. *task* data type, which carries fundamental state information such as task position, times, time steps, the number of time slices stored, status flags, rank, and so on. The *task* data type also includes methods⁴ for acquiring a task ID, setting and inquiring about status flags, plus ‘deferred methods’ that extending objects must implement. All mesh-based tasks extend the *task* data type to a
2. *patch* data type, which adds spatial properties, such as size, resolution, number of guard zones, coordinate system (Cartesian or curvilinear), number of physical variables, etc. Patches also contain methods for measuring intersections between different patches in space and time, as well as for writing and reading snapshots. These are generic properties and methods, and are shared by all mesh-based
3. *solver* data types, which specify the physical variables to be advanced, adds methods to initialise and advance the patch data forward in time, plus any parameters that are specific to the solver in question. The specific solver data type is then extended to an
4. *experiment* data type, which adds experiment-specific functionality, such as initial and boundary conditions, in addition to the specific update procedure for the experiment. The *experiment* data type also serves as a generic wrapper that is accessed from the *task list* class hierarchy, effectively hiding the choice of solver, thus making it possible to execute the same experiment with different solvers.

4.2.2 *Task lists*

The task list class hierarchy has as its base member a

³ In Fortran, ‘objects’ are called ‘derived types’, and inheritance is implemented by ‘extending’ a derived type.

⁴ ‘Type-bound procedures’ in Fortran speak.

1. *node* data type, which defines a single node in a doubly-linked list that points to, and carries information about, individual tasks. In addition to pointers to the previous and next nodes, nodes have a pointer to the head of a linked list of *nbors*, a concept that generalises neighbours beyond spatial proximity to include tasks that in one way or another depend on the current task, or because the current task depends on them. The *node* data type also includes methods to initialise and maintain its own neighbour list. Individual nodes are used by the
2. *list* data type, which defines a doubly-linked list of nodes and keeps track of its properties. The *list* data type also contains the generic methods necessary to manipulate linked lists, such as appending, removing and sorting of nodes. It is, however, the
3. *task list* data type that extends the *list* data type with methods that are specific to the execution of tasks and the handling of task relations. In particular, the *task list* data type contains the *update* method, which is a key procedure in DISPATCH and responsible for selecting a task for updating. The complete execution of a DISPATCH experiment essentially consists of calling the task list *execute* procedure, which calls the task list *update* procedure repeatedly until all tasks are finished; this is typically defined as having advanced to a task's final time.

4.2.3 Components

The primary means of generating task lists in DISPATCH is via a set of *components*, each of which produces a subset of tasks, organised in some systematic fashion. For example, one of the most frequently-used components is the *cartesian* component, which generates and organises tasks in a non-overlapping, regular and Cartesian-like spatial decomposition; in this case, each task initially has, in general, $3^3 - 1 = 26$ spatial *nbors*. The corresponding mesh-based tasks/patches may, in turn, use Cartesian or orthogonal curvilinear coordinates; in the latter case, the Cartesian-like partitioning of tasks is performed in curvilinear space.

Another commonly-used component creates nested sets of 'Rubik's Cube' (3x3x3) or 'Rubik's Revenge' (4x4x4) patches. For example, one can arrange 27 patches into a 3x3x3 cube, and then repeat the arrangement recursively by splitting the central patch into 3x3x3 child patches, each with a cell size that is three times smaller than its parent patch. A 'Rubik's Revenge' set up is analogous, except that it uses 4x4x4 patches and the central 2x2x2 patches are each split into a new 2x2x2 arrangement, leading to a resolution hierarchy with a factor of two decrease in patch and cell size with each additional level. The nested set can furthermore be complemented by repeating the coarsest level configuration in one or more directions.

The Rubik's-type component is useful, for example, to represent the environment near a planetary embryo embedded in an accretion disk, making it possible to cover the dynamic range from a small fraction of the planet radius

to the scale height of the accretion disk with a relatively limited number of patches (e.g. [no. levels + no. extra sets] \times 27). The set of patches produced by a Rubik’s component can then be placed in the reference frame co-moving with the planetary embryo, with corresponding Coriolis and net inertial (centrifugal) forces added to the solver, thus gaining a time step advantage relative to the stationary lab frame.

Another kind of component available in DISPATCH, exemplified by sets of tasks that solve radiative transfer (Sect. 4.4.2), may overlap spatially with patches, but there is additionally an important *causal* dependency present. For example, patches which solve the equations of MHD provide densities and temperatures to sets of radiative transfer tasks in order to calculate the radiation field. In return, the radiative transfer tasks provide heating or cooling rates to be applied to the MHD patches prior to the next update. This kind of ‘causally-linked’ component can operate either as an extension on top of another task, or as a semi-independent set of tasks coupled only by pointers. In the former, the task presents as only a single task and is therefore updated in step with its causal *nbor*. In the latter, there is substantial freedom in choosing when to update the component. A good example of this in practice in BIFROST (Gudiksen et al., 2011) solar simulations, where the radiative transfer problem is solved with a slower cadence than the one used to evolve the MHD (Hayek et al., 2010).

4.2.4 Scenes

Components, such as those described in the previous subsection, are used as building blocks to create a *scene* hierarchy, where one could have, for example, a top level that is a galaxy model, which, in its spiral arms, contain a number of instances of giant molecular cloud components, each of which contains any number of protostellar system components, where a protostellar system component contains an accretion disk component, with a collection of moving patches representing the gas in the accretion disk. These patches would be orbiting a central star, whose evolution could be followed by, for example, a MESA (Paxton et al. 2010) model, which takes the accretion rate directly from a sink particle component that represents the star. In addition, the protostellar system component could contain Rubik’s Cube components, co-moving with planetary embryos, which could, in turn, be coupled to particle transport tasks representing dust in the accretion disk. Indeed, scenes are the way to build up simulations, complex or otherwise, from one or more individual components in DISPATCH; in the end, a scene need only provide a task list that is ready for execution, i.e., with the *nbor* relations already determined.

4.3 CODE FUNCTIONALITY

The overall structure and functionality of the code framework is best understood by combining several possible perspectives on the activities that take place as an experiment is executed. Below we adopt, one-by-one, perspect-

ives that take A) the point of view of a single task, and the steps it goes through cyclically, B) the point of view of the task scheduler/dispatcher, as it first selects tasks for execution/updating and then later checks on these tasks to evaluate the consequences of the updates. Then C) we take the point of view of the ensemble of MPI processes, and their means of communicating. Next, D) we take the point of view of the load balancer, and look at how, in addition to keeping the load balanced between the MPI processes, it tries to minimise the actual need to communicate. Finally, E) we take the point of view of the input/output (I/O) sub-system, and examine how, within the ensemble of MPI processes, snapshots can be written to disk for post-processing and/or experiment continuation.

4.3.1 A) *Single task view*

For simplicity, we consider the phases that a mesh-based *experiment* task goes through; the sequence that a different type of task experiences does not differ substantially. An *experiment* task, an extension of a *solver* task, itself an extension of a *patch* task, relies on having guard zone values that are up-to-date before it can be advanced to the next time step. In general, guard zone values have to be interpolated in time and space, since patches use local time stepping (and are therefore generally not synchronised in time) and can have differing resolutions. To enable interpolation in time, values of the field variables (e.g. density, momentum, etc.) in each patch are saved in a number of time slices (typically 5–7) using a circular buffer. Interpolation in space, prolongation, and its inverse process, restriction, are meanwhile accomplished using conservative interpolation and averaging operators.

The ‘dispatcher’ (see below) checks if neighbouring patches have advanced sufficiently enough in time to supply guard zone values to the current patch before moving it to a (time-sorted) ‘ready queue’. After having been selected by the dispatcher for update, patches are then switched to a ‘busy’ state, in which both the internal state variables (e.g. the MHD variables) and the patch time is updated. The new state overwrites the oldest state in the circular buffer, and since guard zone values corresponding to the next time step are not yet available, the task is put back in to the ‘not ready’ state. Occasionally, when the patch time exceeds its next scheduled output time, an output method (which can be generic to the *patch* data type or overloaded by a *solver* or *experiment*-specific method) is called (see below).

4.3.2 B) *Task scheduler view*

In the series of states and events discussed above, the selection and preparation of the task for update is the responsibility of the task scheduler *update* method, which is a central functionality (in practice, spread over several methods) in the DISPATCH code – this is essentially the *dispatcher* functionality that has given the code framework one of the inspirations for its name (the other one derived from its use of partially DISconnected PATCHes).

The task list update procedure can operate in two modes. It can either

1. let threads pick the oldest task from a linked list of tasks (the ready queue) that have been cleared for update. This linked list is sorted by time (oldest first), so a thread only has to pick off the head from the queue and execute its update method. In this scheme, after updating the task, the thread immediately checks the neighbours of the updated task to see if perhaps one of those tasks became ‘ready’, e.g. because the newly updated task is able to provide the last piece of missing guard zone data. If any ‘ready’ tasks are found, they are inserted into the ‘ready queue’ in ascending time order. Alternatively,
2. the task list update procedure runs on a single `OpenMP` thread, picks off the oldest task from the ready queue and subsequently spawns a thread to update it. As before, it then searches the neighbour list for tasks that possibly became executable, and adds these tasks to the ready queue.

Note that, regardless of the operational mode, the task scheduler is rank-local.

The first operational mode is the simpler one; indeed, thread-parallelism in this mode is implemented using a single `$omp parallel` construct placed around the task list update method. This mode, however, has the drawback that two of the linked list operations – picking off the head and adding new tasks to the ready queue – are continuously being performed by a large number of threads in parallel. These two operations must therefore be protected with `OpenMP` critical regions to ensure that only one thread at a time is allowed to manipulate the ready queue. This is not a problem as long as the number of threads per `MPI` process is limited; even on a 68-core Intel Xeon Phi processor, there is hardly any measurable impact.

However, in order to obtain truly unlimited `OpenMP` scalability, it is necessary to operate entirely without `OpenMP` critical regions, which is possible with the second mode of operation. In this mode, a single (master) thread is responsible for both removing tasks from the ready queue, as well as adding new tasks to it. In this mode, the actual task updates are performed by `OpenMP` threads initiated by `$omp task` constructs, with the task list update method running on the master thread being responsible (only) for spawning tasks and handling linked list operations. Therefore, no critical regions are needed, and one can reach much larger numbers of threads per `MPI` process. The load on the master thread is expected to be ignorable, and if it ever tended to become noticeable, it can easily spawn sub-tasks that would take care of most of the actual work. Note also, that the default behaviour of `OpenMP` task constructs is that the spawning task can also participate in the actual work (possibly encouraged to do so by suitably placed `$omp taskyield` constructs).

4.3.2.1 *Defining task ‘readiness’*

The definition of when a task is considered ready for updating is intentionally flexible. By default, it is implemented via a logical function `is_ahead_of`

which examines the difference between the time of a task and its neighbours. A particular task (“self”) is deemed ready to be updated if the condition,

$$t_{\text{self}} \leq t_{\text{nbr}} + g\Delta t_{\text{nbr}}, \quad (4.1)$$

is true for all tasks in the neighbour list of self. Here, g is a ‘grace’ parameter which specifies the amount of extrapolation permitted relative to the neighbour time step, Δt_{nbr} . Note that, since the actual update will take place later and other tasks are constantly being updated by other threads, even though an extrapolation is allowed, it is not necessarily required when the actual update happens. From experience, setting $g = 0.05$ already generally increases the number of tasks in the ready queue at any given time significantly, while, on the other hand, setting g as high as 0.3 has not been found to produce visible glitches in results.

The `is_ahead_of` function may be overloaded at any level of the task hierarchy. This may be used, e.g., where the tasks of a particular experiment are defined. One might decide, as is done routinely in the BIFROST code, that the radiative transfer solution should be calculated less frequently than the dynamics, and thus `is_ahead_of` should be overloaded to return true when the causal neighbours of self satisfy an appropriate criterion.

When extrapolation in time is actually used, as well as when interpolating in time to fill guard zone values, the default action is to use linear inter- and extrapolation in time. However, since several time slices are available, one may choose to use higher order time inter- and extrapolation. Second-order extrapolation in time has, e.g., turned out to be optimal for the gravitational potential when solving the Poisson equation under certain circumstances (Ramsey et al., submitted).

4.3.3 C) MPI process view

In DISPATCH, there is typically one MPI process per compute node or per physical central processing unit (CPU) ‘socket’. Each MPI process also typically engages a number of OpenMP threads that matches or exceeds (if ‘hyper-threading’ is supported and favourable) the number of physical cores. Since the number of tasks that are executable at any given time may be a small fraction of the total number of tasks, each MPI process typically ‘owns’ a number of tasks that significantly exceeds the number of available OpenMP threads. Some of these tasks are naturally located near the geometrical edge of a rank (henceforth ‘boundary tasks’), and they therefore could have neighbour tasks that belong to a different MPI process (henceforth ‘virtual tasks’); the remaining ‘internal’ tasks have, by definition, neighbours that are entirely owned by the same MPI process.

As soon as a task marked as a boundary task has been updated by an OpenMP thread, the thread prepares an MPI package and sends it to all MPI processes that need information from that task (i.e. its ‘nbors’). Conversely, each time a thread receives a package from a nbor, it immediately issues a new MPI_IRecv to initiate receipt of the next package. Threads that become

available for new work start by checking a share of the outstanding message requests using a thread private list, which eliminates the need for `OpenMP` critical regions when receiving and unpacking `MPI` packages.

The `MPI` packages are typically used for supplying guard zone values. By sending this information pro-actively (using `MPI_ISEND`), rather than having other `MPI` processes ask for it, the latency can be greatly reduced, and chances improve that the boundary patches of other processes will have up-to-date data available in their virtual neighbours to supply guard zone data when their neighbour lists are checked.

The `MPI` packaging for patches contains both a copy of the most relevant task parameters and the state variables in the interior of the patch. There are essentially two reasons to ship data for all interior zones, rather than limiting the package content only to layers that will be needed for guard zone data. First, this simplifies package creation and handling, and network capacity is generally large enough to allow this for moderately-sized patches without any noticeable slowdown. Second, this simplifies load balancing (see below), since it allows changing the owner of a patch by simply ‘giving’ a patch to a neighbour `MPI` process. The patch then needs only change its status, from ‘virtual’ to ‘boundary’ on the receiver side, and from ‘boundary’ to ‘virtual’ on the sender side.

Should memory bandwidth actually become a problem one can reduce the network traffic significantly by only sending guard zone values, at the cost of added complexity in the package pack and unpack methods and in the load balancing methods.

4.3.4 D) Load balancer view

Given the ownership swap protocol outlined above, the actual balancing of workload is a nearly trivial task, since any `MPI` process that finds itself with a surplus of work, relative to a neighbouring `MPI` process, can easily ‘sell’ some of its boundary tasks to its less-loaded neighbour `MPI` processes. However, doing so indiscriminately risks creating ragged geometric boundaries between neighbouring `MPI` processes. In this sense, the load balancer should also function as a ‘communication balancer’ which attempts to keep the number of `MPI` communications per rank and per unit simulation time near some minimum value.

Load balancing follows each task update, and can be performed after every update, after a given number of updates of each task, or after a given wall clock time has passed since the previous load balance. Load balancing is entirely local, with each task evaluating (in an `OpenMP` critical region) if the number of communications, or the load imbalance, can be reduced by passing ownership of the task to one of its rank neighbours. A minimum threshold for imbalance is implemented to prevent frequent passing of tasks that only marginally improves the imbalance. Only boundary tasks, i.e., tasks that have neighbours on other ranks are candidates for ownership transfer. If the transfer is beneficial, the task indicates to the rank neighbour that ownership should

be changed. The rank that takes over ownership then changes the task status from ‘virtual’ to ‘boundary’, while the previous owner changes the status from ‘boundary’ to ‘virtual’. All affected tasks then refresh their neighbour lists to reflect the new situation.

By using emulation of an initially and severely fragmented patch distribution via software prototyping, we find that it is more efficient to address the load imbalance and the communication reduction in two separate steps while, within each step, the other aspect of the balancing is more or less ignored.

The procedure is essentially as follows:

1. Count the number of **MPI** neighbours for each rank by enumerating the number of different ranks recorded in the neighbour lists of a rank’s boundary tasks;
2. Evaluate, for each boundary task, if the total number of **MPI** neighbours on the involved ranks would be reduced if ownership of a task is swapped. In this step, one carries out the most advantageous swaps, even if a swap would tend to introduce a load imbalance.
3. In a separate step, evaluate if any task swaps can be made that restore load balance, without increasing the number of **MPI** neighbours.

The reason this two step procedure is advantageous, relative to trying to reduce communications under the simultaneous constraint to avoid causing imbalance, is that it is relatively difficult to find good swaps in step (ii), and the process is made easier if load (im)balance is temporarily ignored. It is, meanwhile, relatively easy in step (iii) to find swaps that improve load balance without changing the total number of of **MPI** neighbours.

4.3.5 E) Input/Output view

After a task has been updated, its current time in code units is compared to the `task%out_next` parameter and, upon passage of that `out_next`, the *task* output method is called and a snapshot is written. The actual method invoked depends on where in the task hierarchy the generic output method has been overridden. For example, if an *experiment*-specific method has not been implemented, then a *solver*-specific method will be invoked if implemented, otherwise a generic *patch* output method is used. Currently, `DISPATCH` snapshots use one of two output formats: One that writes patch data as raw binary data to one file, and patch information as text to another file. An alternative output format uses the packing procedure used to communicate task data between **MPI** ranks, and collects the data for all tasks on a **MPI** rank into a single file. In either case, these snapshots are suitable not only for visualisation but also for restarting a simulation. Finally, for reasons of portability and performance, parallel HDF5 support is currently being explored.

4.4 CURRENT CODE COMPONENTS

4.4.1 *Internal and external HD, MHD, and PIC solvers*

The solvers from a few well-used and well-documented astrophysical fluid codes have been ported to the DISPATCH framework and validated using experiments carried out with both the original code and the DISPATCH implementation. As a first representative of Godunov-type Riemann solvers, the HLLC solver from the public domain RAMSES code (Teyssier, 2002) has been incorporated. To take advantage of the DISPATCH speed advantages in stellar atmosphere and similar work (e.g. Baumann et al. 2013), several versions of the Stagger Code (Nordlund et al., 1994; Kritsuk et al., 2011) class of solvers have also been ported. As an example of connecting to an external solver, the ZEUS-3D solver (Clarke, 1996, 2010) used in the AZEuS adaptive mesh refinement code (Ramsey et al., 2012) is available; the ZEUS-3D solver is also the only currently-included solver that can leverage the advantage of orthogonal, curvilinear coordinate systems (e.g. cylindrical, spherical).

Incorporating an external solver as a library call in DISPATCH is straightforward, but requires some modification of the external code. An explicit interface must be defined by the external solver. One must also ensure that the external solver is ‘thread-safe’, i.e., it can safely be invoked by many threads at once. Initialisation and updating procedures are meanwhile defined in the DISPATCH *solver* module; these procedures exist for all solvers in DISPATCH, external or otherwise. As part of the update procedure, conversion procedures may be required to ensure the physical variables are in a format suitable for the solver. For example, in ZEUS-3D, velocity is a primary variable while, in DISPATCH, we store the momentum. After the external solver is called, the data must be converted back to DISPATCH variables. At this point, the developer decides whether DISPATCH or the external solver determines the next time step. In the case of ZEUS-3D, it determines the next Courant-limited time step internally and returns the value to DISPATCH. Calling an external solver occurs at the same point in DISPATCH as any other solver, as part of a *task* update procedure. Memory management within the external solver is, meanwhile, not controlled by DISPATCH.

In ongoing work, we are also incorporating the public domain version of the photon-plasma particle-in-cell code, PPcode⁵ (Haugbølle et al., 2013), and the BIFROST MHD code (Gudiksen et al., 2011), including its modules related to chromospheric and coronal physics. We intend to use these solvers for multiple-domain-multiple-physics experiments in the context of modelling solar and stellar atmospheric dynamics driven by sub-surface magneto-convection, expanding on the type of work exemplified in Baumann et al. (2013).

⁵ <https://bitbucket.org/taugboelle/ppcode>

4.4.2 Radiative transfer

Radiative processes are undeniably important in most astrophysical applications (e.g. planetary atmospheres, protoplanetary disk structure, HII regions, and solar physics, to name a few). Being a 7-dimensional problem (three space + time + wavelength + unit position vector), it can be a daunting physical process to solve. A number of approaches have been developed over the last several decades in an attempt to tackle the problem, including flux-limited diffusion (FLD) (Levermore & Pomraning, 1981), Fourier transforms (e.g. Cen 2002), Monte Carlo techniques (e.g. Robitaille 2011), variable tensor Edington factors (Dullemond & Turlola, 2000), short (e.g. Stone et al. 1992), long (e.g. Nordlund 1982; Heinemann et al. 2006) and hybrid (Rijkhorst et al., 2006) characteristics ray-tracing.

DISPATCH currently implements a hybrid-characteristics ray-tracing Radiative Energy Transfer (RT) scheme: long rays inside patches and short rays in-between, albeit with a few exceptions as described below. The RT module consists of a ray geometry component, an initialisation component, and run time schemes; each component needs to know very little about how the others work, even though they rely heavily on each other. In addition, since the RT module depends on the values of, for example, density and temperature, it also relies on the co-existence of instances of a *solver* data type that can provide these quantities. Below, we briefly explain the purpose of each of the RT components; a detailed description of the RT module, together with implementation details for refined meshes and additional validation tests, will appear in a subsequent paper of this series (Popovas et al., in prep.).

Current solver implementations include Feautrier and integral method formal solvers (e.g. Nordlund 1984), multi-frequency bin opacities, and source function formulations with either pure thermal emission, or with a scattering component⁶. Scattering is handled in a similar way as in the BIFROST code (Hayek et al., 2010). For cases with low to moderate albedos, the method is essentially lambda-iteration. The specific intensities from previous time steps are stored in DISPATCH time slices and can be used as starting values for the next time steps, which makes this approach effective. Extreme scattering cases could be handled by implementing more sophisticated methods, such as accelerated lambda iteration (Hubeny, 2003).

4.4.2.1 Ray geometry

When the RT module is initialised, it first creates a ray geometry (RG) for existing patches. The only information the RG component needs is the simulation geometry type (Cartesian/cylindrical/spherical), dimensions of a patch (number of cells per direction), the desired number of ray-directions, and their angular separation. The RG component then proceeds to spawn rays: Each ray starts at one patch boundary and ends at another boundary (face, edge, or corner) of the same patch. Spacing of rays is set to the patch cell size

⁶ Although the Feautrier method conserves energy by construction, the integral method does not. As such, the choice of RT solver should be made with this in mind.

along the direction that forms the largest angle with the ray. The ray points are, ideally, co-centred with patch cell centres along the direction of the ray. In this case, the required hydrodynamic quantities (e.g. density and internal energy) do not need to be interpolated to the **RG**, and neither do the resulting intensities need to be interpolated back to the mesh; this saves a significant amount of computational time. If angular resolution surpassing that provided by rays along axes, face diagonals and space diagonals is required, this can be accomplished via rays in arbitrary directions but with an extra cost resulting from interpolating temperature and density to ray points and then interpolating the resulting net heating or cooling back to the patch mesh. In this case, as with the **MHD** variables, interpolation to ray points and of the subsequent heating rate back to the mesh are done using conservative operators.

Once all rays have been created, they are organised into a fast look-up tree hierarchy. The primary access to this tree is through the ray geometry type. Within a *ray geometry* object, the rays are further sub-divided into

1. *ray directions* - in principle, as long as scattering is not considered, rays in one direction do not care about rays with another direction, so they can be separated and updated as independent tasks by different threads. To solve for **RT** inside a patch, boundary conditions from the patch walls (i.e. boundary face) that the rays originate from are required. Not all slanted rays with one direction originate and terminate at the same wall (see Figure 4.1). To avoid waiting time originating from sets of *ray directions* that end on more than one patch wall, the complete set is further sub-divided into
2. *ray bundles*; these are defined as sets of rays that originate and terminate on the same pair of patch walls. **RT** is a highly repetitive task, where a large numbers of rays is typically considered. It is thus highly advantageous to use schemes that maximise hardware vectorisation in order to reduce the computation time. Therefore, all rays should, preferably, be of the same length. This is a natural feature of rays that are parallel to a patch coordinate axis; slanted ones, meanwhile, are further rearranged into
3. *ray packets*; these are the sets of rays in one *ray bundle* that have the same length. To promote faster data lookup (e.g. interpolating ray coordinates to patch coordinates, origin/termination points, etc.), they are organised as data arrays.

Note that axis-oriented rays, as well as rays with specific spatial angles (e.g. 45°), will generally terminate at locations that coincide with the origins of rays in a ‘downstream’ (with respect to **RT**) patch. This is exploited in the current implementation by introducing the concept of *ray bundle chains*.

4.4.2.2 *Ray bundle chains*

To obtain the correct heating/cooling rates inside a patch, one needs boundary values/incoming intensities from ‘upstream’ patches. By reorganising rays

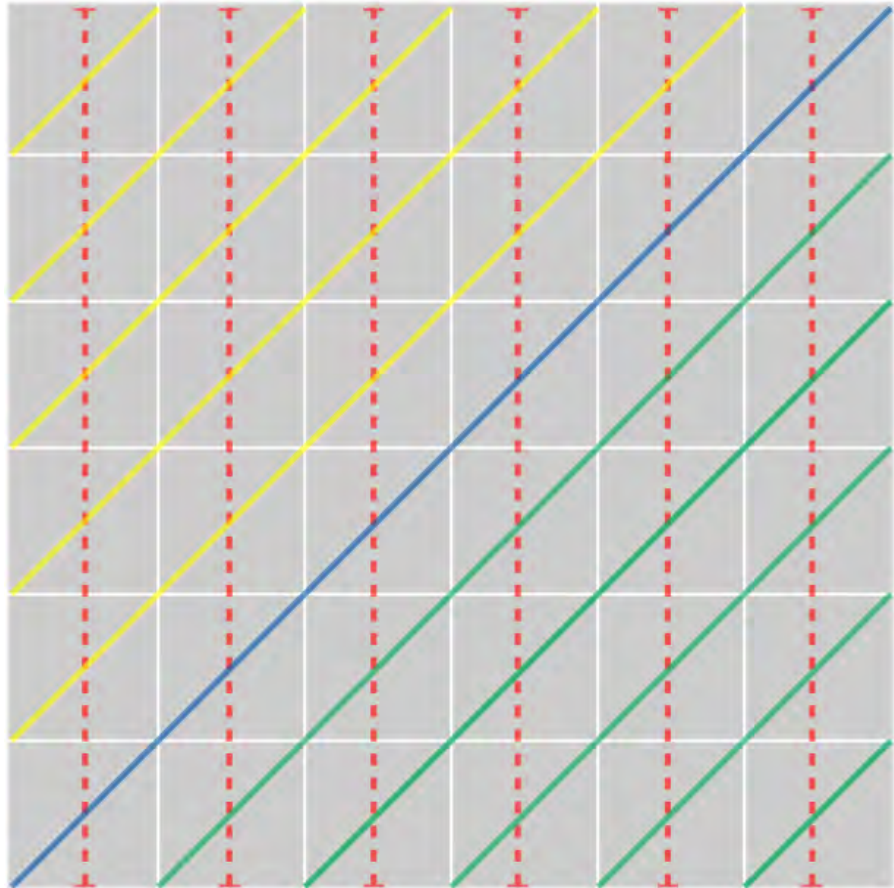


Figure 4.1: Ray geometry representation in 2-D. (M)HD grid cells are represented by grey squares, coloured lines represent rays. Different line styles represent different directions. Different colours represent different bundles.

into bundles (see above), one minimises the number of walls needed per particular bundle down to a single pair: one at the origin and one at the termination. Such an arrangement allows the connection of one ray bundle to a similar ray bundle in a neighbour patch, resulting in a *bundle chain*. If we continue the analogy with actual chains, then the first, or master, chain ‘link’ is connected to an outer boundary, and all the other links, by virtue of the chain, obtain their boundary values from their upstream link immediately after the RT is solved on the upstream link. If the upstream surface of a link is a physical boundary or a change in spatial resolution, this particular link is defined as being the first link in the chain, i.e., the one from which execution of the chain starts. Bundle chains effectively transform the short-characteristic ray scheme inside patches into long-characteristic rays over many patches along the ray bundle direction.

4.4.2.3 RT initialisation and execution

After the ray geometry has been generated, the RT initialisation component steps through all of the patches in the task list and creates an overlapping RT patch. The RT patch keeps track of all the ray-directions and sets up bundle chains by searching for upstream patches in a patch’s neighbour list.

When an MHD patch, and subsequently the internal state variables, is updated, a corresponding RT patch is ready to be executed. Initially, it may not have wall/boundary data available, but it can still prepare the internal part by evaluating the source function and opacities for the internal cells. The RT patch then steps through its list of bundles and ‘nudges’ the master links of any bundle chains. The master link could belong to this patch, or it could belong to a very distant patch along a particular ray direction. In most cases, chain links along an arbitrary ray direction are not yet ready for execution (e.g. the internal data for an RT patch is not prepared yet), so the master link simply records which links in the chain are ready. As soon as a last nudge indicates that all links are ready, the chain can be executed recursively, as follows:

1. The first bundle in the chain gets boundary values either from physical boundary conditions, or retrieves them from an upstream patch; in the latter case, the upstream source is either a virtual patch on another MPI rank or has a different spatial resolution (and therefore requires interpolation);
2. Simultaneously, the source function and opacities are mapped from internal patch data onto the ray bundle coordinates;
3. The boundary values and mapped internal data are sent to an RT solver. The solver returns the heating/cooling rates for internal cells in addition to wall intensities, which, in turn, are sent to the next, downstream link in the bundle chain.

Once a bundle chain has executed, the chain and its individual links are placed in a ‘not ready’ state while the chain waits for the corresponding MHD

patches to be updated again. In practice, it may not be necessary (or practical) to solve **RT** after every **MHD** update. Thus, one can instead specify the number of **MHD** updates or time interval after which the next **RT** update will be scheduled.

4.4.3 Non-ideal MHD

The importance of magnetic fields in astrophysics is well-established, as is the application of **MHD** to problems involving magnetised fluids. However, non-ideal **MHD** effects (Ohmic dissipation, ambipolar diffusion, and the Hall effect) can be important in various astrophysical contexts, for instance, in protoplanetary disks and the interstellar medium. Here, we account for the additional physical effects of Ohmic dissipation and ambipolar diffusion in **DISPATCH** by extending the already implemented **MHD** solvers. We illustrate the process using the staggered-mesh solvers based on the Stagger Code (Nordlund et al., 1994; Kritsuk et al., 2011); the implementation in other solvers would differ mainly in details related to the centring of variables. In the Stagger and **ZEUS-3D** solvers, for example, components of momentum are face-centred, while in the **RAMSESMHD** solver, momentum is cell-centred. In all of the currently implemented **MHD** solvers, electric currents and electric fields are edge-centred, following the constrained transport method (Evans & Hawley, 1988) to conserve $\nabla \cdot \mathbf{B} = 0$.

4.4.3.1 Ohmic dissipation

Ohmic dissipation results from the additional Electromotive Force (**EMF**) induced by imperfect conduction (non-zero resistivity) in a magnetised fluid. For simplicity, we assume an isotropic resistivity that can be described by a scalar parameter, η_{Ohm} , and write the additional electric field as:

$$\mathbf{E}_{Ohm} = \eta_{Ohm} \mathbf{J}, \quad (4.2)$$

where $\mathbf{J} = \nabla \times \mathbf{B}$ is the current density and \mathbf{B} is the magnetic field; \mathbf{E}_{Ohm} is added to the ideal **EMF** ($\mathbf{E} = -\mathbf{v} \times \mathbf{B}$) prior to invoking the induction equation. Meanwhile, a non-zero resistivity also results in an additional heating term:

$$Q_{Ohm} = \mathbf{J} \cdot \mathbf{E}_{Ohm} = \eta_{Ohm} J^2. \quad (4.3)$$

Since the current density is edge-centred, we must appropriately average its components to compute the cell-centred heating rate.

Additionally, we use the following expression for the Ohmic time step:

$$\Delta t_{Ohm} = C_{Ohm} \cdot \min \left(\frac{\Delta x^2}{\eta_{Ohm}} \right), \quad (4.4)$$

where Δx is the cell size and C_{Ohm} is a Courant-like parameter, conservatively chosen to be 0.1 following Masson et al. (2012). The Courant time step is subsequently modified to select the minimum of Δt_{Ohm} and the usual Δt_{MHD} .

4.4.3.2 Ambipolar diffusion

In the case of a gas that is only partially ionised, magnetic fields directly affect the ionised gas but not the neutral gas; the neutral gas is instead coupled to the ions via an ion-neutral drag term. In general, therefore, the ionised gas moves with a different speed than the neutral gas. If the speed difference is small enough to neglect inertial effects, the drag term can be represented by estimating the speed difference (i.e. the ‘drift speed’) between the ionised and neutral gas. We implement this so-called single-fluid approach along the lines of previous works (cf. [Mac Low et al. 1995](#); [Padoan et al. 2000](#); [Duffin & Pudritz 2008](#); [Masson et al. 2012](#)).

Specifically, we add an additional ambipolar diffusion [EMF](#),

$$\mathbf{E}_{AD} = -\mathbf{v}_D \times \mathbf{B}, \quad (4.5)$$

to the induction equation, where

$$\mathbf{v}_D = \frac{1}{\gamma_{AD}\rho\rho_i} \mathbf{J} \times \mathbf{B} \quad (4.6)$$

is the drift velocity, ρ is the total mass density, ρ_i is the ion mass density and γ_{AD} is the ambipolar drift coefficient.

Like Ohmic dissipation, ambipolar diffusion also results in an additional heating term:

$$Q_{AD} = \rho\rho_i\gamma_{AD}(\mathbf{v}_D)^2. \quad (4.7)$$

As before, we appropriately average the components of $\mathbf{J} \times \mathbf{B}$ to cell-centre in order to compute the cell-centred Q_{AD} .

Similar to the implementation of Ohmic dissipation, we add a constraint on the time step such that (cf. [Masson et al. 2012](#)):

$$\begin{aligned} \Delta t \leq \Delta t_{AD} &= C_{AD} \min \left(\frac{\gamma_{AD}\rho_i}{v_A^2} (\Delta x)^2 \right) \\ &= C_{AD} \min \left(\frac{\gamma_{AD}\rho_i\rho}{B^2} (\Delta x)^2 \right), \end{aligned} \quad (4.8)$$

with C_{AD} again conservatively chosen to be 0.1.

4.4.4 Particle trajectory integration

Particles in DISPATCH can be treated as both massive and massless. Massless particles may be used for diagnostic tracing of Lagrangian evolution histories, while particles with mass may be used to model the interaction of gas and dust, which is an important process, particularly in protoplanetary disks.

To be able to represent a wide distribution of dust particle sizes without major impact on the cost the particle solver must be fast, and the particle integration methods have been chosen with that in mind. Trajectories are integrated using a symplectic, kick-drift-kick leap-frog integrator, similar to the one in GADGET2 ([Springel, 2005](#)). In the case of massive particles we use

forward-time-centring of the drag force, which maintains stability in the stiff limit when drag dominates in the equation of motion. Back-reaction of the drag force on the gas is currently neglected – this will be included in a future version.

4.4.5 *Equation-of-state and opacity tables*

DISPATCH is designed from the ground up to include several options and look-up tables for both idealised and realistic equation of state (EOS) and opacities. To look-up tables as efficient as possible, binary data files with fine grained tables are generated ahead of time using utilities written in Python and included with the code. These utilities read data from various sources and convert it to look-up tables in the logarithm of density and an energy variable; which type energy is used depends on the solver. For example, the HLLC and ZEUS-3D solvers use thermal energy in the EOS, as do most of the Stagger Code solvers, while one version of the Stagger Code instead uses entropy as the ‘energy’ variable. Naturally, for simple EOSs such as constant gamma ideal gas, a look-up table is not necessary and calls to the EOS component instead end in a function appropriate for the current solver.

The table look-up is heavily optimised, first by using spline interpolations in the Python utilities to produce tables with sufficient resolution to enable bi-linear interpolation in log-space in DISPATCH. The table address calculations and interpolations are vectorised, while a small fraction of the procedure (data access) remains non-vectorised because of indirect addressing.

4.5 VALIDATION

Since the solver components of DISPATCH are taken from existing, well-documented codes, validation in the current context requires only verification that the DISPATCH results agree with those from the standalone codes and, furthermore, verification that the partitioning into patches with independent time steps does not significantly affect the results. In this section, we document validation tests for the main hydrodynamics (HD) and MHD solvers, for the non-ideal MHD extension to these solvers, and for the radiative transfer code component. We concentrate on the validation aspect, mentioning performance and scaling only in passing; more details on these aspects will appear in a subsequent paper (Ramsey et al., in prep.).

For any particular experiment, all solvers use the same ‘generator’ to set the initial conditions, which makes it easy to validate the solvers against each other, and to check functionality and reproducibility after changes to the code. A simple regression testing mechanism has been implemented in the form of a shell script, permitting each experiment to be validated against previous or fiducial results. By also making use of the ‘pipelines’ feature on `bitbucket.org`, selected validations are automatically triggered whenever an update is pushed to the code’s git repository.

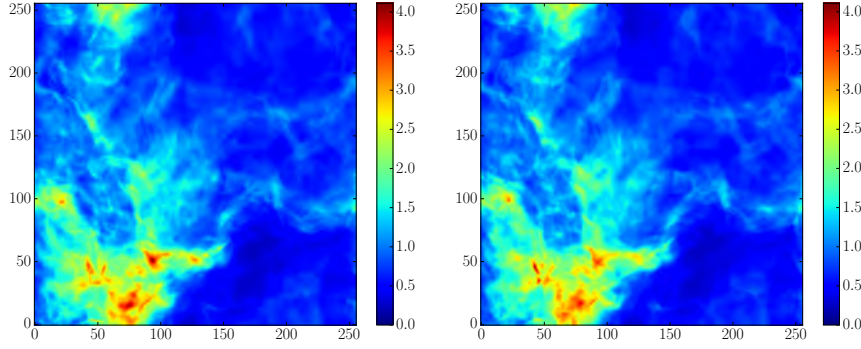


Figure 4.2: *Left*: Projected density in code units at time $t = 0.2$ for the KITP decaying turbulence experiment when using a single patch with 256^3 cells. *Right*: The same, but using 512 patches, each with 32^3 cells. Note that the density has been raised to a power of 0.5 to enhance the contrast. The cell indices are denoted on the axes.

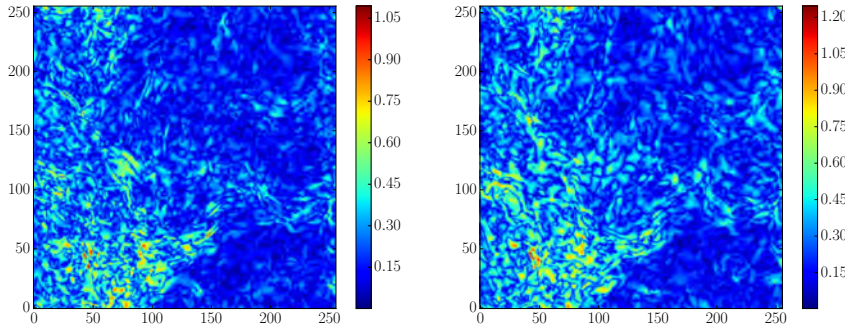


Figure 4.3: *Left*: The absolute difference between the left and right panels of Figure 4.2 (i.e. in projected density). *Right*: The difference between two runs, obtained with Courant numbers 0.6 and 0.8, respectively.

4.5.1 Supersonic turbulence

For the first demonstration that the solvers implemented in the DISPATCH framework reproduce results from the stand-alone versions of existing codes, we use the decaying turbulence experiment from the KITP code comparison (Kritsuk et al., 2011). The experiment follows the decay of supersonic turbulence, starting from an archived snapshot with 256^3 cells at time $t = 0.02$, until time $t = 0.2$.

In Figure 4.2, we display the projected mass density at the end of the experiment, carried out using the HLLC solver from RAMSES. On the one hand, a single patch (left panel) reproduces results obtained with RAMSES, while, on the other hand, using 512 (right panel) patches with 32^3 cells each, evolving with local time steps determined by the same Courant conditions as in the RAMSEScode (but locally, for each patch), still demonstrates good agreement with the RAMSES results. The solutions are visually nearly indistinguishable, even after roughly two dynamical times. The root-mean-square velocities are

practically identical, with a relative difference of only $6 \cdot 10^{-4}$ at the end of the experiments.

Figure 4.3 shows two difference images, displaying the absolute value of the differences in the projected density (raised to the power of 0.5 to enhance visibility). The left panel shows the difference between the runs with 1 and 512 patches, while the right panel shows the difference between two otherwise identical cases with 512 patches, but with slightly different Courant numbers (0.6 and 0.8). This illustrates that a turbulence experiment can never be reproduced identically, except when all conditions are exactly the same; small differences due to truncation errors grow with time, according to some Lyapunov exponent.

Figures 4.2 and 4.3 validate the use of our patch-based local time stepping in two different ways: First, through the absence of any trace of patch boundaries in the difference image and, second, by demonstrating that the differences are consistent with differences expected simply from the use of different Courant numbers. In the single patch case (as well as in RAMSES and other traditional codes), local regions with relatively low flow speeds are effectively evolved with very low local Courant numbers (i.e., time steps are locally much smaller than that permitted by the local Courant condition), while the patch-based evolution takes advantage of the lower speeds by using locally larger time steps.

The local time step advantage can be quantified by the number of cell-updates needed. The single patch case needs about $2 \cdot 10^{10}$ cell updates (as does RAMSES), while the experiment using 512 patches with local time steps needs only about $1.4 \cdot 10^{10}$ cell-updates. Using 20-core Intel Xeon Ivy Bridge CPUs, the 512 patch experiment takes only 6.5 minutes when run on 30 hardware threads (and 7.0 minutes with 20 threads). The cost per cell update is 0.61 core microseconds in the single patch case, 0.56 core-microseconds in the 20 thread case, and 0.53 core-microseconds in the 30 thread case. The super-linear scaling from 1 to 20 cores is mainly due to better cache utilisation when using 32^3 cells per patch, while the additional improvement when using 30 hardware threads on 20 cores illustrates a hyper-threading advantage; with more hardware threads than cores, the CPU has a better chance to find executable threads.

4.5.1.1 *Weak and strong scaling*

We now switch to driven isothermal turbulence experiments to explore the weak and strong scaling properties of DISPATCH; the decaying turbulence experiment relies on the 256^3 code comparison snapshot, and is therefore not suitable for weak scaling tests. In brief, we drive purely solenoidal, supersonic turbulence in a box with wave numbers $kL/2\pi \leq 3.2$, where $L = 1$ is the box size, until $t = 0.2$. The density is initially uniform and equal to 1.0, while the velocities are initially zero. There are nominally 512 patches per MPI rank, each with $32^3 - 64^3$ cells per patch. The optimal number of cells per patch is problem and hardware dependent; a substantially reduced number of cells

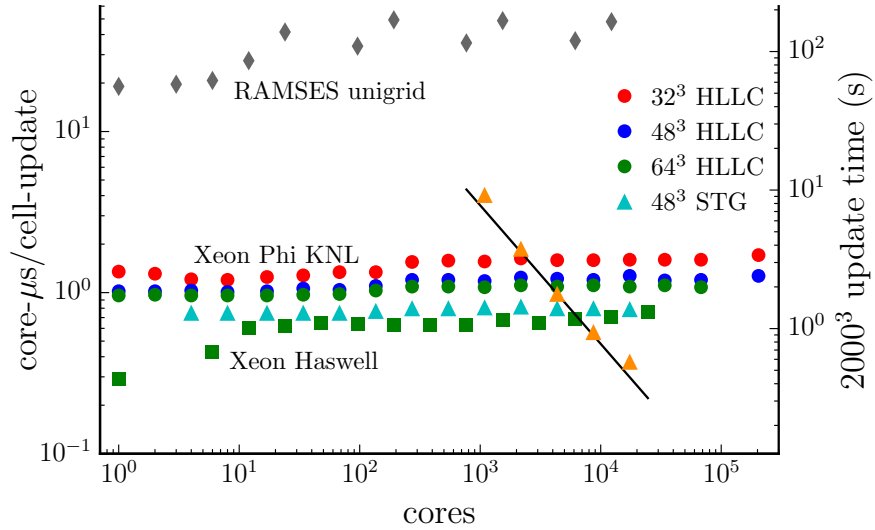


Figure 4.4: Strong and weak scaling for DISPATCH with the RAMSESHLLC and STAGGER ("STG") code solvers, as applied to a driven turbulence experiment. The performance of the framework is demonstrated using the cost to update one cell as a function of the number of cores. The bottom set of squares denote scaling on Intel Xeon Haswell nodes at HLRS Stuttgart/HazelHen, while the top set of circles (HLLC) and triangles (STAGGER) denote scaling on Intel Xeon Phi Knights Landing (KNL) nodes at CINECA/Marconi (in both cases, with generally two MPI ranks per node). The grey diamonds denote the performance of RAMSES(HLLD) in uniform resolution mode on Intel Xeon Haswell nodes for the same driven turbulence set up. The orange triangles shows strong scaling with 16, 32, 64, 128, and 256 KNL nodes on a 2048^3 fixed size case, using the STAGGER solver with 32^3 patches; the straight line indicates ideal strong scaling.

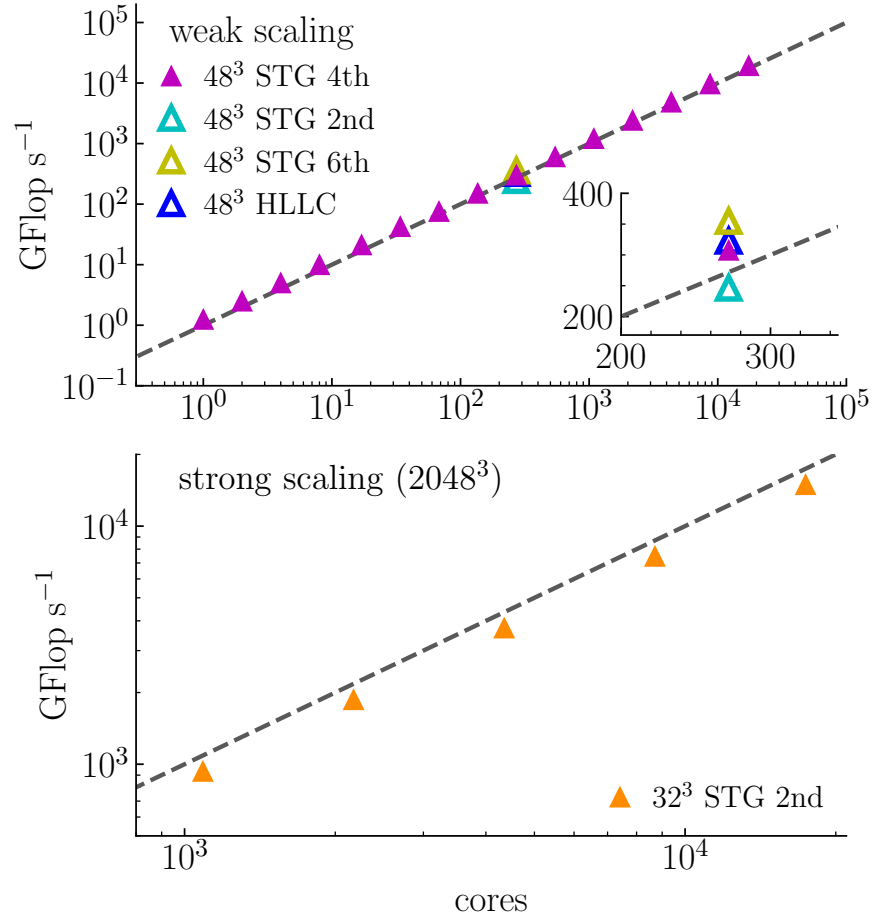


Figure 4.5: Weak (*top*) and strong (*bottom*) scaling for the driven turbulence experiment expressed in units of GFlop s⁻¹ as a function of the number of cores. Dashed lines indicate ideal scaling. The inset zooms in on the differences in GFlop s⁻¹ between solvers. All data was collected on CINECA/Marconi. Weak scaling tests were conducted with 48³ cells per patch. The strong scaling was conducted with a fixed total 2048³ cells and 32³ cells per patch.

per patch results in a degradation in performance (cf. [Mendygral et al. 2017](#)), but also allows a potentially larger local time step advantage.

On Intel Xeon (Haswell) CPUs, we find that, as in the decaying turbulence case, the typical cell-update cost on a single node is on the order of 0.5 – 0.6 core-microseconds, while on the somewhat slower Intel Xeon Phi (Knights Landing; KNL) cores, the update cost is approximately 0.8 – 1.1 core-microseconds. As with traditional Xeon CPUs, we find that using $2\times$ hyper-threading on Xeon Phi CPUs reduces the run time by $\sim 20\%$. Figure 4.4 demonstrates that DISPATCH has excellent strong scaling properties, subject to the conditions that there needs to be enough work to keep the threads busy, and sufficient memory to hold the time slices. Figure 4.4 also demonstrates that, even with MPI overhead (visible at higher core counts), DISPATCH weak scaling on Intel Xeon and Xeon Phi CPUs is virtually flat up to 1024 (corresponding to 24,576 cores) and 3000 MPI ranks (corresponding to 204,000 cores), respectively. For comparison, we also include performance measurements for RAMSES (using the HLLD solver) operating in uniform resolution mode for the same driven turbulence experiment. After adjusting for the cost difference between HLLD and HLLC solvers (the former is $\sim 5\times$ more expensive than the latter), evidently, DISPATCH is up to $16\times$ faster than RAMSES at large core counts.

Figure 4.5 presents another metric of the performance of the DISPATCH framework and integrated solvers: the gigaflops per second (GFlop s^{-1}) as a function of the number of cores for the driven turbulence experiment. The theoretical single precision peak performance of one Intel Xeon Phi 7250 (KNL) CPU (i.e. the ones that constitute CINECA/Marconi-KNL) is ~ 78 GFlop s^{-1} per core. The solvers currently implemented in DISPATCH only reach $\sim 2 - 3\%$ of this theoretical peak. This is not uncommon for astrophysical fluid codes, which are typically memory bandwidth limited. Note that these values characterize the solvers even in single core execution; the DISPATCH framework controls the scaling of the performance, while the performance per core is determined by the particular solver.

However, while the time per cell update and its scalings (Figure 4.4) are the main factors determining the ‘time-to-solution’ for a simulation, the number of Flops used per second remains an important complementary indicator; not only is it the measure that *defines* exa-scale, its consideration is also important when trying to minimise the time-to-solution. Modern CPUs can do many Flops per memory load/store, and for essentially all MHD solvers, the Flops per second is limited by memory bandwidth rather than by theoretical peak performance. Added complexity per update step thus potentially carries very low extra cost, especially if it does not incur any extra loads/stores. We illustrate this in Figure 4.5 by showing the number of GFlop s^{-1} when employing 2nd, 4th, and 6th order operators in the Stagger solver. Although the 4th order operators use five Flops per point, vis-a-vis two Flops per point for the 2nd order operators, the total number of Flops per cell update increases only by a factor of ~ 1.3 (due to Flops not related to differential operators). Meanwhile, the time per cell update/number of cell updates per core-second

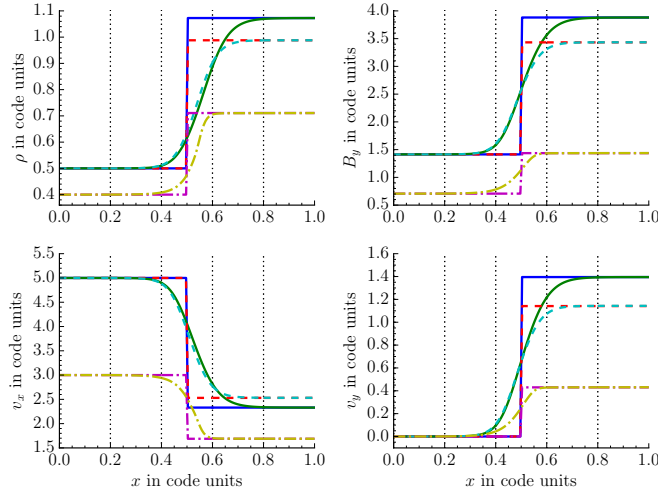


Figure 4.6: Density (upper left), B_y (upper right), v_x (lower left) and v_y (lower right) for the C-shock experiments. The solid lines correspond to the initial (blue) and evolved (green) states of the isothermal run with AD, the dashed lines correspond to the initial (red) and evolved (cyan) states of the non-isothermal run with AD, the dash-dotted lines correspond to the initial (magenta) and evolved (yellow) states of the non-isothermal run with Ohmic dissipation. Vertical dotted lines denote patch boundaries.

Table 4.1: Initial conditions for the non-ideal C-shock experiments. Pre-shock (upstream) values refer to the left hand side of panels in Figure 4.6.

Variable	ρ	v_x	v_y	B_x	B_y	P
Pre-shock (AD)	0.5	5	0	$\sqrt{2}$	$\sqrt{2}$	0.125
Post-shock (AD; isothermal)	1.0727	2.3305	1.3953	$\sqrt{2}$	3.8809	0.2681
Post-shock (AD; non-isothermal)	0.9880	2.5303	1.1415	$\sqrt{2}$	3.4327	1.4075
Pre-shock (Ohm)	0.4	3	0	$\frac{1}{\sqrt{2}}$	$\frac{1}{\sqrt{2}}$	0.4
Post-shock (Ohm)	0.71084	1.68814	0.4299	$\frac{1}{\sqrt{2}}$	1.43667	1.19222

remains essentially unchanged, consistent with memory bandwidth being the bottleneck. Since higher order operators reduce the numerical dispersion of the scheme, they potentially allow for a reduction in the number of cells at constant solution quality, and since, in 3-D, the time-to-solution generally scales as the 4th power of the number of cells per dimension, using 4th order operators is a virtually certain advantage. Using 6th order operators further increases the number of flops per core-second while affecting the time per cell update only marginally, potentially offering yet more advantage. However, the increased number of guard zones necessary for higher order operators is another factor that enters the cost balance analysis, and the most optimal choice is thus problem dependent. In current (and future) applications of the framework, we (will) base the choice of solver and order of operators on the quality of the, and the time to, solution using pilot simulations to compare outcomes and to choose measures of ‘quality’ most relevant for each application.

4.5.2 Non-ideal MHD: C-shock

To validate the non-ideal MHD extensions, we carry out C-shock experiments following Masson et al. (2012) for both Ohmic dissipation and ambipolar diffusion. Table ?? shows the initial (left and right) states. In the isothermal case, we set the adiabatic index $\gamma = 1 + 10^{-7}$, while we use $\gamma = 5/3$ for the non-isothermal and Ohmic dissipation runs. In the ambipolar diffusion runs, we set $\gamma_{AD} = 75$, and in the Ohmic dissipation run we use $\eta_{Ohm} = 0.1$, where we assumed an ion density of $\rho_i = 1$ in all three cases. We test the implementations using five patches, each with dimensions $30 \times 1 \times 1$, and plot the results in Figure 4.6. Our results are in good agreement with Masson et al. (2012). Like Masson et al. (2012) and Duffin & Pudritz (2008), we find that the shock undergoes a brief period of adjustment before reaching a steady state solution in all cases. We have confirmed that, for a moving C-shock, the solution quality is not affected by crossing patch boundaries.

Even for a simple benchmark like the non-ideal C-shock, the DISPATCH local time stepping advantage is already beginning to show: In the ambipolar diffusion experiments, there is a factor of ~ 2 difference in the time steps between patches⁷. As the complexity of the problem and the number of patches increases, the advantage for non-ideal MHD experiments is expected to increase. Indeed, we are currently exploring if DISPATCH can compete with super-time-stepping algorithms (e.g. Alexiades et al. 1996; Meyer et al. 2014) for ambipolar diffusion, or even if there is a greater benefit by combining them.

4.5.3 Radiative transfer: Shadow casting benchmark

To test our radiative transfer implementation, we apply the so-called ‘shadow’ casting benchmark (e.g. Hayes & Norman 2003; Jiang et al. 2012; Ramsey & Dullemond 2015). We consider a 3-D Cartesian domain of size $-0.5 \leq [x, y, z] \leq 0.5$ cm. An overdense ellipsoid is placed at the origin, with a density profile prescribed by:

$$\rho(x, y, z) = \rho_0 + \frac{\rho_1 - \rho_0}{1 + e^{10(r-1)}}, \quad (4.9)$$

where $r = (x/a)^2 + (y/b)^2 + (z/b)^2$, $a = 0.10$ cm, $b = 0.06$ cm, and $\rho_1 = 10\rho_0$. The ambient medium is initialised with a gas temperature $T_0 = 290$ K and a density $\rho_0 = 1$ g cm⁻³. The entire domain is in pressure equilibrium. The gas opacity is given by:

$$\alpha = \rho \kappa = \alpha_0 \left(\frac{T}{T_0} \right)^{-3.5} \left(\frac{\rho}{\rho_0} \right)^2, \quad (4.10)$$

where $\alpha_0 = 1$. We apply a constant and uniform irradiation source across the left boundary (at $x = -0.5$ cm), characterised by blackbody emission with

⁷ In the Ohmic dissipation experiment, since the Ohmic time step depends only on (a constant) η_{Ohm} and the grid spacing, the time step is the same in every patch.

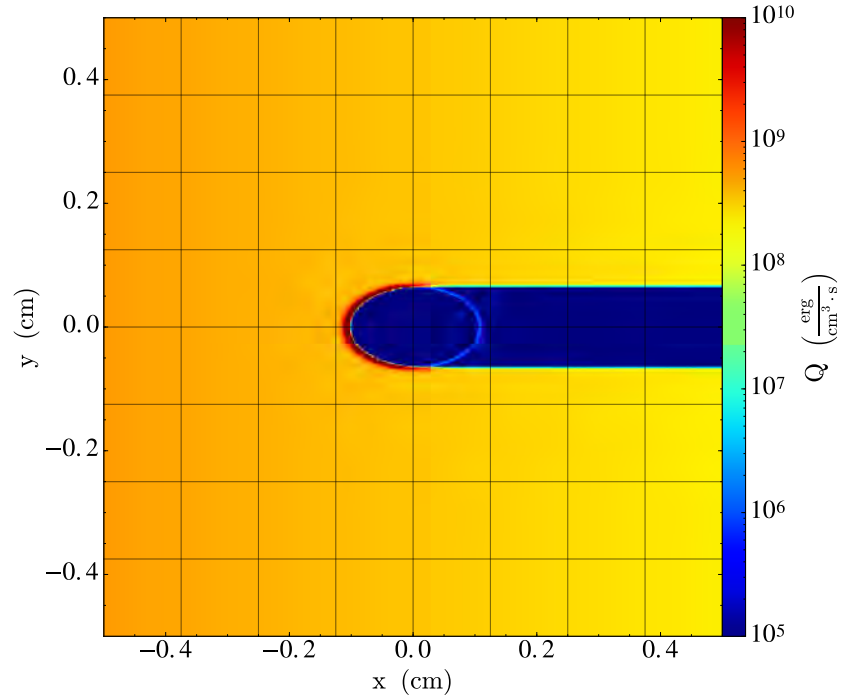


Figure 4.7: Results for the shadow casting benchmark. The irradiation source is located at the left boundary. The heating rate per unit volume, Q (Eq. 4.11), is shown, with levels indicated by the colour bar to the right.

an effective temperature $T_{irr} = 6 T_0$ K. The other boundaries are assumed to be blackbodies with effective temperature T_0 . For the experiment, we use 8^3 patches, each containing 64^3 cells. The ray geometry contains 13 directions with 45° space-angle separation.

In this set up, the ambient medium is optically thin and the photon mean free path parallel to a coordinate axis is equal to the length of the domain. The clump is, meanwhile, optically thick and has an interior mean free path of $\approx 3.2 \cdot 10^{-6}$ cm. The clump thus absorbs the incident irradiation, and subsequently casts a shadow behind it. Figure 4.7 shows the resulting heating rate per unit volume, which is given by:

$$Q = \rho \kappa (J - S), \quad (4.11)$$

where J is the mean intensity and S is the source function. The solution displays, qualitatively and quantitatively, all the expected features: the shadow is sharp, it has a finite-size border, the front of the clump is strongly heated due to the incident radiation, and the back side of the clump experiences a very mild heating due to the incident thermal radiation from the ambient medium. The heating rates, meanwhile, compare well with the results of Ramsey & Dullemond (2015).

For this experiment, the update cost is ~ 0.6 core-microseconds per cell on Intel Xeon Ivy Bridge CPUs, including RT. Running the same experiment with RT disabled instead results in a cost of ~ 0.5 core-microseconds per cell. Thus,

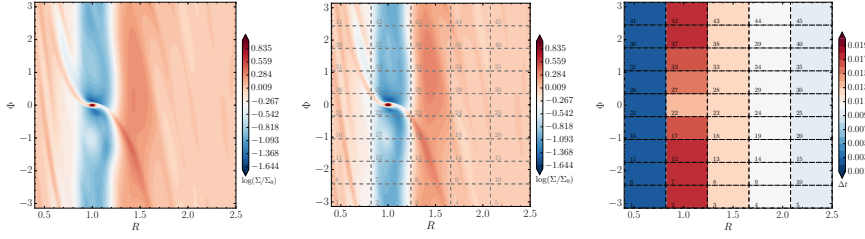


Figure 4.8: *Left*: A $1M_J$ planet simulated for 100 orbits using a single patch with $n_R \times n_\Phi = 160 \times 450$ uniformly-spaced zones. *Middle*: The same but subdividing the domain into 45 equally-sized patches. *Right*: The time step in each patch after 100 orbits.

even with 13 spatial directions, and even with solving for RT after every MHD update, the RT algorithm only adds approximately 20% to the experiment cost. Although using a more realistic EOS (i.e. look-up table) will increase the cost slightly, clearly, the DISPATCH RT algorithm can provide accurate RT solutions at a very low cost. In a subsequent paper of this series (Popovas et al., in prep.), additional details and benchmarks, including further documentation on the accuracy and speed of RT in DISPATCH, will be provided.

4.5.4 *de Val-Borro disk benchmark*

One of the current and primary science goals of DISPATCH is to model planet formation processes in global and realistic settings. As such, we now apply DISPATCH to the global disk benchmark of [de Val-Borro et al. \(2006\)](#). More specifically, we embed a Jupiter-like planet in an initially uniform surface density protoplanetary accretion disk and then allow the disk to evolve for 100 orbits at the semi-major axis of the planet. Following [de Val-Borro et al. \(2006\)](#), we initialise a two-dimensional, geometrically thin disk with a constant surface density given by $\Sigma_0 = 0.002M_*/\pi a^2$, where M_* is the mass of the central star and a is the semi-major axis of the planet. We use an aspect ratio of $H/R = 0.05$, where H is the canonical disk scale height, an effectively isothermal EOS ($\gamma = 1.0001$), and an initially Keplerian orbital velocity.

In scaled units, the mass of the central star is set to 1.0, while the planet is assigned a mass of 10^{-3} and a semi-major axis of 1.0. The simulation is performed in the reference frame co-rotating with the planet and centred on the central star. Therefore, the gravitational potential of the system is comprised of one term each for the star and planet, plus an additional ‘indirect’ term to account for the fact that the centre-of-mass of the system does not correspond to the origin (cf. [D’Angelo & Bodenheimer 2013](#)):

$$\Phi = -\frac{GM_*}{R} - \frac{GM_p}{\sqrt{|R - R_p|^2 + \epsilon^2}} + \frac{GM_p}{R_p^3} R \cdot R_p, \quad (4.12)$$

where G is the gravitational constant, M_p is the mass of the planet, R is the cylindrical radius, R_p is the position of the planet in cylindrical coordinates, and ϵ is the gravitational softening length. Still following [de Val-Borro et al.](#)

(2006), we set $\varepsilon = 0.6H$, and a planetary position of $(Z, R, \Phi) = (0.0, 1.0, 0.0)$. In the co-rotating frame, the planet’s position is fixed, i.e., the planet is not permitted to migrate.

The computational domain has dimensions $[0.4a, 2.5a]$ in radius and $[-\pi, \pi]$ in azimuth; we use polar cylindrical coordinates and the ZEUS-3D solver. When using curvilinear coordinates with ZEUS-3D, it is the angular rather than the linear momentum that is solved, thus guaranteeing the conservation of angular momentum (Kley, 1998). Code parameters of note are the Courant factor, which is set to 0.5, and the artificial viscosity parameters (Clarke, 2010), q_{con} and q_{lin} , are set to 2.0 and 0.1, respectively. In the results presented below, a kinematic viscosity of 10^{-5} (in units where $GM_* = 1$ and $a = 1$) is used.

We adopt periodic boundary conditions in the azimuthal direction, and the ‘wave-killing’ conditions of de Val-Borro et al. (2006) in the radial direction, with damping activated in the ranges $[0.4a, 0.5a]$ and $[2.1a, 2.5a]$. It is worth noting that we do not gradually grow the planet mass over the first few orbits (cf. de Val-Borro et al. 2006; Sect. 3.1), but instead begin with the full planetary mass in place.

The left panel of Figure 4.8 shows the benchmark results for a single patch at a resolution of $n_R \times n_\Phi = 160 \times 450$ cells after 100 orbits. These results can be directly and favourably compared with Figure 10 of de Val-Borro et al. (2006). The middle panel, meanwhile, shows the results from sub-dividing the domain into 45 equally-sized patches. As can be seen, the model with 45 individual patches is nearly identical to the model with a single patch. Finally, the right panel illustrates the time step in each patch after 100 orbits; there is a factor of ~ 8.2 difference between the largest and smallest time steps. This local time-stepping advantage, over the course of 100 orbits, reduces the CPU time required by the multiple-patch version by a factor of roughly two relative to the single-patch version (~ 6 hr vs. ~ 12 hr).

4.6 SUMMARY AND OUTLOOK

We have introduced a hybrid MPI/OpenMP code framework that permits semi-independent task-based execution of code, e.g., for the purpose of updating a collection of semi-independent patches in space-time. OpenMP parallelism is handled entirely by the code framework – already existing code need not (and should not) contain OpenMP parallel constructs beyond declaring appropriate variables as `threadprivate`. OpenMP tasks are generated by a rank-local *dispatcher*, which also selects the tasks that are ready for (and most in need of) updating. This typically implies having valid guard zone data imported from neighbours, but can take the form of any type of inter-task dependency. The type of tasks can vary, with HD, ideal MHD, radiative transfer and non-ideal MHD demonstrated here; PIC methods coupled to MHD methods on neighbouring patches are currently in development. Tasks do not necessarily have to be grid-based (allowing, e.g., particle-based tasks), while tasks that are may use either Cartesian or curvilinear meshes. The code framework supports both sta-

tionary and moving patches, as well as both static and dynamic mesh refinement; the implementation details for moving patches and dynamic refinement will be featured in a forthcoming paper (Ramsey et al., in prep.).

As DISPATCH is targeting exa-scale computing, a feature of great importance for the performance of the framework is that time steps are determined by local conditions (e.g. the Courant condition in the case of mesh-based tasks/patches); this can lead to potentially significant reductions in computing time in cases where the signal speed varies greatly within the computational domain. Patches, in particular, are surrounded by a sufficient number of guard zones to allow interior cells to be updated independently of other patches within a single time step; the guard zone data is retrieved or interpolated from neighbouring patches. Since patches evolve with different time steps, it is necessary to save a number of time slices for interpolation (and possibly extrapolation) to the time whence guard zone values are required. Performance, even for existing codes, improves when running under the DISPATCH framework for several reasons: First, patches are small enough to utilise cache memory efficiently, while simultaneously being large enough to obtain good vectorisation efficiency. Secondly, task overloading ensures all OpenMP threads remain constantly busy, which results in nearly linear OpenMP speed-up, even for a very large numbers of cores (e.g. Intel Xeon Phi). Third, load imbalance caused by multi-physics modules with significantly different update costs per unit time is automatically compensated for, since the task scheduling automatically favours tasks that tend to lag behind. Fourth, each MPI process (typically one per socket per node) only communicates with its nearest neighbours – here interpreted broadly as those MPI processes that are either geometrically close, or else causally coupled via, for example, radiative transfer. Finally, load balancing is designed to minimise work imbalance while simultaneously keeping the number of communications links near a minimum. As demonstrated in Figures 4.4 and 4.5, these features result in a code framework with excellent OpenMP and MPI scaling properties.

When combined with co-moving patches in, for example, a protoplanetary disk, the advantages of DISPATCH relative to a conventional adaptive mesh refinement code such as RAMSES are, first of all, a gain from the co-moving patches and, second, an additional advantage due to local time stepping. Beyond that, the implementation of the RAMSES solver in DISPATCH exhibits a substantial raw speed improvement per cell update by up to a factor of 16 relative to the standalone version – in large part due to the much smaller guard zone overhead (the 2x2x2 octs used in RAMSES need 6x6x6 cells for updates), but also due to contributions from better vectorisation and cache utilisation. In fact, comparisons to recent zoom-in simulations performed with RAMSES (Nordlund et al., 2014; Kuffmeier et al., 2016, 2017) demonstrate that cost reductions of up to a factor of 40 are possible.

In DISPATCH the number of tasks per MPI rank (typically one per compute node or CPU socket) is kept sufficiently high to ensure all of the cores within a rank stay busy at all times. As the capacity (i.e. the number of cores) of compute nodes is growing with time, in the future, each rank will be able to

handle more tasks, and hence an increasing fraction of tasks will be ‘internal’, i.e., their neighbour tasks will reside on the same `MPI` rank, and thus will not require communication with neighbouring ranks. By construction then, as the capacity grows, each node remains fully occupied, and inter-node communication needs decrease rather than increase with growing problem size. Combined with the fact that, in `DISPATCH` each rank only communicates with its nearest neighbours, the `OpenMP` and `MPI` scaling characteristics of `DISPATCH` therefore satisfy our definition of being exa-scale ready.

Planned and ongoing applications of the `DISPATCH` code framework include pebble accretion via hierarchically resolved Hill spheres around planetary embryos (Popovas et al., submitted), solar and stellar magneto-convection with chromospheric and coronal activity, with further extensions applying a combined `MHD-PIC` multiple-domain-multiple-physics method to particle acceleration in model coronae. Solar and stellar magneto-convection is a context where the local time step advantage can become very large. Analysis of snapshots from Stein & Nordlund (2012) shows a gain of a factor ~ 30 , caused by the contrast between the extremely short time steps required in the low density atmosphere above sunspots, and the generally much longer time steps allowed at other locations on the surface, as well as essentially everywhere below the surface.

Part of the motivation for developing `DISPATCH` was to create a framework that is suitable for studying planet formation. Recall, for example, the scene including a protostellar system modelled by using a sink particle component plus `MESA` stellar evolution model for the central star, plus a collection of moving, orbiting patches to represent the gas in the protostellar accretion disk (Sect. 4.2.4). Likewise, particle tasks could be operating to represent the dust, either as sub-tasks inside other tasks, or as semi-independent separate tasks. These would then be able to use data on gas and dust properties from accretion disk patches to estimate the production rate of thermally processed components – representing, for example, chondrules and high-temperature-condensates (calcium-aluminium inclusions, amoeboid olivine aggregates, hibonites, etc.; cf. Haugboelle et al. 2017), and would be able to model the subsequent transport of thermally processed components by disk winds and jet outflows (e.g. Bizzarro et al. 2017b).

The `DISPATCH` framework will be made open-source and publicly available in a not too distant future.

ACKNOWLEDGEMENTS

The work of ÅN, MK, and AP was supported by a grant from the Danish Council for Independent Research (DFF). The Centre for Star and Planet Formation is funded by the Danish National Research Foundation (DNRF97). Storage and computing resources at the University of Copenhagen HPC centre, funded in part by Villum Fonden (VKR023406), were used to carry out some of the simulations presented here. We also acknowledge PRACE for awarding us preparatory access (2010PA3402) to Hazel Hen at HLRS Stuttgart to

obtain scaling data. We further acknowledge Klaus Galsgaard for allowing us to obtain KNL scaling data on CINECA/Marconi under his PRACE grant 2016143286 and CINECA support staff for helping us obtain scaling measurements at 204,000 cores.

PAPER III: PEBBLE DYNAMICS AND ACCRETION
ONTO ROCKY PLANETS. I. ADIABATIC AND
CONVECTIVE MODELS

Andrius Popovas¹, Åke Nordlund,¹ Jon P. Ramsey,¹ and Chris W. Ormel,²

¹ Centre for Star and Planet Formation, Niels Bohr Institute and Natural History Museum of Denmark, University of Copenhagen, Øster Voldgade 5-7, DK-1350 Copenhagen K, Denmark

²Anton Pannekoek Institute, University of Amsterdam, Science Park 904, C4.149, 1098 XH Amsterdam, The Netherlands

Submitted to *Monthly Notices of the Royal Astronomical Society (MNRAS)*

We present nested-grid, high-resolution hydrodynamic simulations of gas and particle dynamics in the vicinity of Mars- to Earth-mass planetary embryos. The simulations extend from the surface of the embryos to a few vertical disk scale heights, with dynamic ranges $L_z/\Delta z \sim 1.4 \times 10^5$. Our results confirm that “pebble”-sized particles are readily accreted, with accretion rates continuing to increase up to metre-size “boulders” for a 10% MMSN surface density model. The gas mass flux in and out of the Hill sphere is consistent with the Hill rate, $\Sigma \Omega R_H^2 = 4 \cdot 10^{-3} M_\oplus \text{ yr}^{-1}$. While smaller size particles mainly track the gas, a net accretion rate of $\approx 2 \cdot 10^{-5} M_\oplus \text{ yr}^{-1}$ is reached for 0.3–1 cm particles, even though a significant fraction leaves the Hill sphere again. Effectively all pebble-sized particles that cross the Bondi sphere are accreted. The resolution of these simulations is sufficient to resolve accretion-driven convection. Convection driven by a nominal accretion rate of $10^{-6} M_\oplus \text{ yr}^{-1}$ does not significantly alter the pebble accretion rate. We find that, due to cancellation effects, accretion rates of pebble-sized particles are nearly independent of disk surface density. As a result, we can estimate accurate growth times for specified particle sizes. For 0.3–1 cm size particles, the growth time from a small seed is ~ 0.15 million years for an Earth mass planet at 1 AU and ~ 0.1 million years for a Mars mass planet at 1.5 AU.

5.1 INTRODUCTION

We now know that the majority of stars in our galaxy host at least one planet (Cassan et al., 2012). We also know that planets form inside the gaseous and dusty Protoplanetary disk (PPD)s that orbit stars during their youth. As it is now possible to spatially resolve the structure of young PPDs (e.g., with the Atacama Large Millimetre/sub-millimetre Array; ALMA), it is becoming apparent that the majority of PPDs have a rich sub-structure of rings, gaps, vortices and spirals (e.g. van der Marel et al. 2013; Isella et al. 2013; Casassus et al. 2013; ALMA Partnership et al. 2015; Andrews et al. 2016; Meru et al. 2017). Recent, spatially resolved observations of young disks with ALMA (ALMA Partnership et al., 2015; Andrews et al., 2016), as well as meteoritic evidence (Bizzarro et al., 2017a), furthermore indicate that planet formation starts early. What remains to be answered, however, is how planets grow efficiently enough under realistic conditions to agree with the astronomical observations and meteoritic evidence.

There are currently two scenarios for planet growth which are popular in the literature: First, the planetesimal accretion scenario, in which a planetary embryo is impacted by kilometre-size bodies and their mass is added to the embryo (e.g. Pollack et al. 1996; Hubickyj et al. 2005). Eventually, the embryo becomes massive enough that gravitational focusing (Greenberg et al., 1978) becomes important and the embryo enters what is commonly called the ‘runaway growth’ phase. Planetesimal accretion ends when there is no remaining solid material in an embryo’s ‘feeding zone’, e.g., when the embryo grows massive enough to gravitationally stir up nearby planetesimals, enhancing their eccentricities and effectively kicking them out of the feeding zone (Ida & Makino, 1993). The growth of the, now somewhat isolated, protoplanet transitions to the much slower ‘oligarchic growth’ phase (Kokubo & Ida, 1998). In this phase, the few, largest mass protoplanets grow oligarchically, while the remaining planetesimals mostly remain small. The critical time scale in this context is the lifetime of the PPD, which is of the order of several million years (e.g. Bell et al. 2013). However, numerical simulations of the planetesimal accretion hypothesis have the problem that they predict that it takes much longer than a PPD lifetime for cores to grow to observed planetary masses (e.g. Levison et al. 2010; Bitsch et al. 2015b).

The “pebble accretion” scenario has, meanwhile, demonstrated promise in being able to accelerate the protoplanet growth process significantly (Ormel & Klahr, 2010; Johansen & Lacerda, 2010; Nordlund, 2011; Lambrechts & Johansen, 2012; Morbidelli & Nesvorny, 2012; Lambrechts & Johansen, 2014; Bitsch et al., 2015b; Chatterjee & Tan, 2014; Visser & Ormel, 2016; Ormel et al., 2017, etc.). “Pebbles”, in the astrophysical context, are millimetre to centimetre-sized particles with stopping times, t_s , comparable to their orbital period, $t_s \sim \Omega_K^{-1}$, where $\Omega_K = \sqrt{GM_*/r^3}$ is the Keplerian frequency, G is the gravitational constant, M_* and r are the mass of and the distance to the central star. Pebbles are likely to form a significant part of the solid mass budget in PPDs, as indicated by both dust continuum observations (e.g. Testi

et al. 2003; Lommen et al. 2009) and by the mass fraction of chondrules in chondritic meteorites (Johansen et al., 2015; Bollard et al., 2017). Due to the difference in speed between the slightly sub-Keplerian dust (and gas) and the Keplerian embryo, in this scenario, pebbles “rain” down on the embryo as it moves through its orbit. As the embryo grows, the efficiency of gravitational focusing of pebbles increases, and the effective accretion cross section becomes larger than the embryo itself.

The radius of dominance of the gravitational force of a planet relative to the central star is approximately given by the Hill radius:

$$R_H = a \sqrt[3]{\frac{M_p}{3M_*}}, \quad (5.1)$$

where a is the semi-major axis of the embryo’s orbit, M_p and M_* are the masses of the embryo and the central star, respectively. Particles of suitable size, passing the embryo even as far away as the Hill radius may be accreted, as has been shown analytically by Ormel & Klahr (2010), using test particle integrations on top of hydrodynamical simulations by Morbidelli & Nesvorný (2012) and using numerical simulations with particles by Lambrechts & Johansen (2012). According to these works, pebble accretion is so efficient that it can reduce planet growth time scales to well within the lifetime of a PPD, even at large orbital distances from the host star.

Herein, we present the first-ever high resolution simulations of gas and pebble dynamics in the vicinity of low-mass, “rocky” planetary embryos (for simplicity, often referred to only as ‘embryos’ in what follows) and report on the measured accretion efficiency of pebbles. We consider three embryo masses: $0.95 M_\oplus$, $0.5 M_\oplus$, and $0.096 M_\oplus$, and we specifically choose to study conditions expected for pressure traps associated with inside-out-scenarios of planet formation (e.g. Tan et al., 2016). The embryos are thus assumed to be embedded in disks that have a local pressure maximum at the orbital radius of the embryo. The presence of a local pressure maximum has two important effects on the particle dynamics: It eliminates the head wind otherwise associated with the slightly sub-Keplerian motion of the gas and it helps to trap particles drifting inwards from larger orbital radii (Whipple, 1972; Paardekooper & Mellema, 2006).

The structure of the paper is as follows. In Section 5.2 we describe the simulation set up, including initial conditions and their dynamic relaxation to a quasi-stationary state. We then describe, in Section 5.3, our treatment of particles, their equations of motion and how they are injected into the simulation domain. In Section 5.4 we describe the gas dynamics that develops in our simulations and compare our results to other studies. In Section 5.5 we present our main results regarding particle dynamics and accretion efficiency onto planetary embryos. In Section 5.6 we present the first results of simulations of accretion-driven convection in the primordial atmospheres of rocky planets. Finally, in Section 5.7, we summarize our main results, discuss their implications and indicate future work.

5.2 SIMULATION SET UP

This study is carried out using the new DISPATCH framework (Nordlund et al., 2018) in a three-dimensional, Cartesian (shearing box) domain, with a set of static, nested patches. We employ a variation of the finite-difference STAGGER solver (Nordlund et al., 1994; Kritsuk et al., 2011) that, in principle (apart from the effects of transformation to a rotating coordinate system detailed below), solves the following set of partial differential equations:

$$\frac{\partial \rho}{\partial t} = -\nabla \cdot (\rho \mathbf{u}); \quad (5.2)$$

$$\frac{\partial \rho \mathbf{u}}{\partial t} = -\nabla \cdot (\rho \mathbf{u} \mathbf{u} + \underline{\underline{\tau}}) - \nabla (p + p_a) - \rho \nabla \Phi; \quad (5.3)$$

$$\frac{\partial s}{\partial t} = -\nabla \cdot (s \mathbf{u}), \quad (5.4)$$

on a staggered mesh, where ρ is the gas density, \mathbf{u} is the gas velocity, p is the gas pressure, p_a is a stabilising artificial pressure term, $\underline{\underline{\tau}}$ is a viscous stress tensor, $s = \rho \log(p/\rho^\gamma)/(\gamma - 1)$ is the entropy density per unit volume, γ is the ratio of specific heats and Φ is the gravitational potential. The viscous stress tensor is taken to be

$$\underline{\underline{\tau}} = \tau_{i,j} = v_1 \Delta x (c_s + u) \rho \left(\frac{\partial u_i}{\partial x_j} + \frac{\partial u_j}{\partial x_i} \right), \quad (5.5)$$

where Δx is the grid resolution, c_s is the sound speed, and the coefficient v_1 is a small fraction of unity. The artificial pressure is computed as:

$$p_a = v_2 \rho \min(0, \Delta x (\nabla \cdot \mathbf{u}))^2, \quad (5.6)$$

where v_2 is a coefficient ~ 1 .

This allows a discretisation that explicitly conserves mass, momentum and entropy. The viscous stress tensor stabilizes the code in general, while the artificial pressure term ensures that shocks are marginally resolved.

The EOS considered herein is that of an ideal gas with adiabatic index $\gamma = 1.4$ and molecular weight $\mu = 2$. Although not considered here, in a forthcoming paper we include radiative energy transfer and adopt a more realistic, table-based EOS (Popovas et al., in prep.).

We use code units where length is measured in Earth radii, mass is measured in Earth masses, and velocity is measured in units of 1 km s^{-1} .

Partly because the time step is determined locally in each patch, and partly because of the small number of cells per patch (33^3 in this case), the hydro solver operates near its optimal speed—updating on the order of 1.4 million cells per core per second—we performed these simulations using only a single, 20-core Intel Ivy Bridge node for each experiment.

5.2.1 Grid set up

We use nested sets of Cartesian patches centred on the embryo. With the embryo as the origin of our coordinate system, the x -axis is parallel to the

cylindrical radial direction and points away from the central star, while the y - and z - axes are oriented along the azimuthal and vertical directions, respectively. The $+y$ -axis lies along the direction of orbital rotation. The embryo is assumed to move in a circular orbit. Patches are arranged in a nested, hierarchical ‘Rubik’s Cube’ arrangement, with 216 patches arranged into a $6 \times 6 \times 6$ cube. The central 8 patches are then split recursively into $6 \times 6 \times 6$ child patches, which have a three times finer resolution than the previous level. This is repeated for up to 7 levels of refinement (8 levels for the smallest embryo mass), while the coarsest set is duplicated 5 times in the y -direction. The size of the innermost, central, patch, exceeds the embryo radius R_p by 10-30%. With 7 levels in the hierarchy, the outer scale in the vertical and radial directions is then $\sim 5000R_p$, which is about 4 times a typical disk scale height for an Earth-mass planet, and $\sim 20x$ larger than the Hill radius. In the y -direction, the model extends to $\sim 25000R_p$. Each patch contains $33 \times 33 \times 33$ cells, leading to a maximum resolution in our simulations, near the embryo’s surface, of $\approx 3\%R_p$.

5.2.2 Initial conditions

We consider a local shearing flow in the reference frame that co-moves with the embryo at the local Keplerian frequency, Ω_K . We ignore the slight curvature of the partial orbit but include the Coriolis force resulting from the orbital motion. The origin of the co-moving frame is, depending on the simulation run, placed at either 1 or 1.5 astronomical units (AU). The initial gas velocity is then given by:

$$\mathbf{u}(t=0) = -\left(\frac{3}{2} + \zeta_p\right) \Omega_K x \hat{\mathbf{y}}, \quad (5.7)$$

where ζ_p is a pressure trap parameter, defined below. In this study, we do not consider a systematic accretion flow towards the central star, nor the headwind that an embryo experiences when the gas is slightly sub-Keplerian. In analytically constructed accretion disks, with pressure decreasing systematically with radius, the headwind is typically on the order of one percent of the Keplerian velocity, but when an embryo is embedded in a local pressure bump there is no headwind. A systematic accretion flow would allow the smallest size particles to escape the pressure trap, and would thus tend to increase the fraction of large size particles, but since we are mainly concerned with measuring the accretion *efficiency* of different size particles, the possible evolution of the grain size distribution is not of direct importance for our study.

The background vertical density stratification is set by the balance between the stellar gravity and the gradient of the gas pressure:

$$\rho(z) = \rho_0 \exp\left(-\frac{\Omega_K^2 z^2 + 2\zeta_p x^2}{2p_0/\rho_0}\right), \quad (5.8)$$

where ρ_0 and p_0 are the disk midplane density and pressure, respectively, and are estimated from the 2D radiative disk models of [Bitsch et al. \(2015a\)](#).

The ζ_p term gives rise to a pressure gradient that balances the extra shear introduced in Eq. 5.7 above.

With typical dust opacities¹ on the order of $0.1 - 1 \text{ cm}^2 \text{ g}^{-1}$, disks with surface densities similar to the Minimum Mass Solar Nebula (MMSN; Hayashi, 1981) are optically thick in the vertical direction, since the MMSN nominally has 1700 g/cm^2 at 1 AU. If early hydrostatic atmospheres that surround planetary embryos are assumed to be nearly adiabatic one can predict their approximate vertical structure from knowledge of only the density, ρ_0 , and temperature, T_0 , at the outer boundary. The pressure at the outer boundary of the atmosphere is assumed to match the local pressure of the surrounding disk. Therefore, for reasonable initial conditions, we approximate an adiabatic atmosphere profile outside-in to the embryo. From the EOS we have the pressure at the outer boundary:

$$P_0 = \frac{\rho_0 k_B T_0}{\mu m_u}, \quad (5.9)$$

where k_B is the Boltzmann constant and m_u is the atomic mass unit. For each layer of the atmosphere, r_i , we iterate over the set of equations:

$$\rho_i = \frac{P_i \mu m_u}{k_B T_i}; \quad (5.10)$$

$$\Delta \ln P_i = \Delta \ln r_i \frac{GM_p}{2} \left(\frac{\rho_{i+1}}{P_{i+1} r_{i+1}} + \frac{\rho_i}{P_i r_i} \right); \quad (5.11)$$

$$\Delta \ln T_i = \Delta \ln P_i \frac{\gamma - 1}{\gamma}, \quad (5.12)$$

where $\Delta \ln r_i = 2(r_{i+1} - r_i)/(r_{i+1} + r_i)$. The temperature and pressure for each layer are then simply $T_i = T_{i+1} e^{\Delta \ln T_i}$ and $P_i = P_{i+1} e^{\Delta \ln P_i}$, respectively. We use 500 logarithmically-spaced layers between half the embryo radius and the Hill radius. We then do a polynomial interpolation between these layers to map the density, pressure and temperature to each cell in the simulation box in order to construct the initial conditions in the vicinity of the embryo.

For the purposes of this study, an ideal gas EOS ($\gamma = 1.4$) is sufficient. As demonstrated by Fig. 5.1, the thermal profiles of the atmosphere surrounding an $M = 0.95 M_\oplus$ embryo given by an ideal gas EOS and a realistic, tabular EOS (Tomida et al. 2013, updated by Tomida & Hori 2016) are only significantly different close to the surface of the embryo. Gas flows in the vicinity of the Hill sphere, as well as embryo particle accretion rates, are insensitive to these differences.

With constant opacities and an internal heating source (due to the accretion of solids) such an atmosphere is convective, and hence has a nearly adiabatic structure (Stevenson, 1982). The atmosphere might have a radiative outer shell — cf. the works by Piso et al. (2015) on giant planets and by Inaba & Ikoma (2003) for a terrestrial mass planet — but this shell would not substantially change the physical structure of the atmosphere, and ignoring

¹ Chondritic meteorites typically have a fair fraction of “matrix”, which corresponds to essentially unprocessed dust. This demonstrates that, at least during the epoch when chondritic parent bodies formed, dust provided substantial opacity per unit mass in the proto-Solar disk.

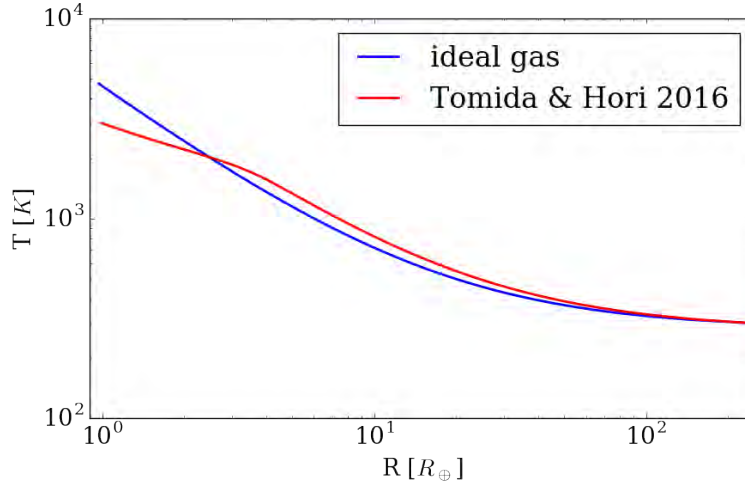


Figure 5.1: Radial temperature profile for a planetary embryo atmosphere using an ideal gas EOS ($\gamma = 1.4$, blue curve) and a realistic, tabular EOS (red curve).

it is a reasonable approximation when constructing the initial conditions. In forthcoming work, however, we include radiative energy transfer in our simulations, and there the initial conditions take this radiative shell into account.

The effective, dynamical boundary between the disk and the embryo atmosphere occurs at distances from the planetary embryo somewhere in the range between the Hill radius and the Bondi radius,

$$R_B = \frac{GM_p}{c_{\text{iso}}^2}, \quad (5.13)$$

where c_{iso}^2 is the isothermal sound speed. In fluid dynamics, the Bondi radius has no particular dynamical significance, other than being the radius where the pressure scale height of the atmosphere becomes comparable to the distance from the embryo, and the radius where trans-sonic bulk gas speeds would become unbound.

Note that the mass in such an adiabatic atmosphere is completely determined (apart from the equation of state) by the pressure and temperature at the outer boundary, and that if the external pressure is reduced the resulting mass is smaller. This implies that mass must be lost from such atmospheres if / when the disk evolves to lower densities (Nordlund, 2011; Schlichting et al., 2015; Ginzburg et al., 2016; Rubanenko et al., 2017).

5.2.2.1 Parameter space

In this study, we consider 8 cases: 3 different embryo masses ($M_p = \{0.95, 0.5, 0.096\} M_{\oplus}$) at 2 distances from the central star ($a = \{1.0, 1.5\}$ AU), with different disk midplane densities ($\rho_0 = \{1 \cdot 10^{-10}, 4 \cdot 10^{-11}\}$ g cm $^{-3}$) and temperatures ($T_0 = \{230, 300\}$ K), as well as with/without a pressure bump ($\zeta_p = \{0.0, 0.05, 0.1\}$). The basic parameters for all cases are summarised in Table 5.1.

Table 5.1: Basic parameters for the different simulation runs. See the text for more details.

Run	$M_p [M_\oplus]$	$R_p [R_\oplus]$	$a [AU]$	$T_0 [K]$	$\rho_0 [g\text{ cm}^{-3}]$	$\frac{\Omega_K}{2\pi} [yr^{-1}]$	ζ_p	x_{damp}	$\Delta x_{min} [R_\oplus]$	box $[R_\oplus]$
m095t00	0.95	0.988	1.0	300	$1\ 10^{-10}$	1.0	0.0	700	0.037	5186 x 5186 x 25930
m095t05	0.95	0.988	1.0	300	$1\ 10^{-10}$	1.0	0.05	700	0.037	5186 x 5186 x 25930
m095t10	0.95	0.988	1.0	300	$1\ 10^{-10}$	1.0	0.1	700	0.037	5186 x 5186 x 25930
m05t00	0.5	0.83	1.0	300	$1\ 10^{-10}$	1.0	0.0	500	0.031	4360 x 4360 x 21801
m05t05	0.5	0.83	1.0	300	$1\ 10^{-10}$	1.0	0.05	500	0.031	4360 x 4360 x 21801
m05t10	0.5	0.83	1.0	300	$1\ 10^{-10}$	1.0	0.1	500	0.031	4360 x 4360 x 21801
m01t00	0.096	0.532	1.5	230	$4\ 10^{-11}$	0.5433	0.0	400	0.023	9773 x 9773 x 48866
m01t10	0.096	0.532	1.5	230	$4\ 10^{-11}$	0.5433	0.1	400	0.023	9773 x 9773 x 48866
m095t10-conv	0.95	0.988	1.0	300	$1\ 10^{-10}$	1.0	0.1	700	0.037	5186 x 5186 x 25930

The radii of the embryos are estimated using the mass-radius formula from [Zeng et al. \(2016\)](#):

$$\left(\frac{R_p}{R_\oplus}\right) = (1.07 - 0.21\ CMF) \left(\frac{M}{M_\oplus}\right)^{1/3.7}, \quad (5.14)$$

where CMF stands for core mass fraction. We take $CMF = 0.325$, although the exact value is not important; taking $CMF = 0.0$ only changes the radius of the embryo on the order of 5%.

5.2.3 External forces (accelerations)

External forces, arising from the transformation to a rotating coordinate system, and from linearising the force of gravity due to the central star, are added to the hydrodynamics as source terms:

$$\frac{\partial \mathbf{u}}{\partial t} = -\frac{GM_p(x\hat{\mathbf{x}} + y\hat{\mathbf{y}} + z\hat{\mathbf{z}})}{r^3} + 3\Omega_K^2 x\hat{\mathbf{x}} - \Omega_K^2 z\hat{\mathbf{z}} - 2\Omega_K \times \mathbf{u}, \quad (5.15)$$

where r is the distance from the embryo. The first term in Eq. 5.15 is the two-body force from the embryo. The second term is the tidal force and has two contributions: the centrifugal force and the differential change of the stellar gravity with radius. Vertically, there is a contribution from the projection of the force of gravity onto the z -axis (the third term). The last term is the classical Coriolis force.

To avoid the singularity of the two-body force, rather than using a ‘softening’ of the potential (e.g. [Ormel et al. 2015a](#); [Lambrechts & Lega 2017](#); [Xu et al. 2017](#)), we truncate it via $r = \max(r, 0.1R_p)$. Truncation is better than softening, since the gas outside the radius of the embryo feels the correct force, and the spherical boundary conditions (described below) negates the effect of truncation for the innermost cells, well within the radius of the spherical boundary condition/embryo.

5.2.4 Boundary conditions

Using test simulations, we have ensured that our boundary conditions remain stable over long periods of integration time and under rather extreme

conditions (e.g. highly supersonic flows, low densities). The ‘‘azimuthal’’ y -boundaries are set to be periodic, whereas the vertical z - and ‘‘radial’’ x -boundaries are set as follows:

- Zero-gradient conditions for the entropy per unit mass.
- The x - and z -velocity components are set symmetric with respect to the boundaries, while the y -component is extrapolated in the x -direction and z directions.
- The density boundary condition in the x -direction is constructed from assuming hydrostatic balance:

$$\rho_x = \rho_{x_i} \exp\left(-\frac{\Omega_K^2 \zeta_p}{T_0}(x^2 - x_i^2)\right), \quad (5.16)$$

where ρ_x is the density in the boundary at location x and ρ_{x_i} is the density at location x_i , which corresponds to the last cell inside a patch’s active domain.

- If a pressure trap is not present we assume a vanishing derivative of the density in the x -direction.
- In the vertical direction, we apply a similar condition:

$$\rho_z = \rho_{z_0} \exp\left(-\frac{\Omega_K^2}{2T_0}(z^2 - z_0^2)\right), \quad (5.17)$$

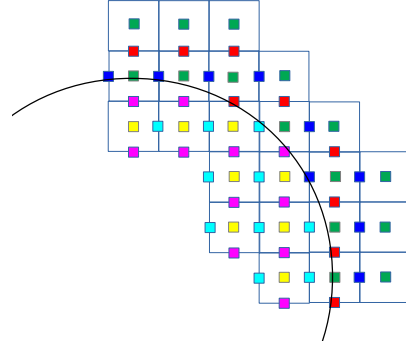
where ρ_z is the density in the boundary at location z and ρ_{z_0} is the density at location z_0 , which again corresponds to the last cell inside the active domain.

We additionally apply the ‘‘wave-killing’’ prescription of [de Val-Borro et al. \(2006\)](#) to reduce reflections at the x -boundaries. It is only applied over a specific range, given by x_{damp} (column 9 in Table 5.1).

5.2.4.1 Spherical boundaries

In these simulations we use ‘‘jagged’’, no-slip boundaries to approximate the embryo surface. Fig. 5.2 shows a 2D representation of these boundary conditions on a staggered mesh. Density and entropy are allowed to evolve freely everywhere; only the mass flux is constrained. We deem a set of cell faces that approximate the spherical surface to belong to the boundary. If the cell face is inside the spherical boundary, the mass flux is set to zero, otherwise it is allowed to evolve freely. Hence, density cannot change inside the boundary and cells that have faces belonging to the boundary react exactly as they should: inflows towards the boundary produce a positive $\partial\rho/\partial t$ at the boundary. The corresponding increase in pressure causes an increase in the outward directed pressure gradient at the last ‘live’ mass flux point, as expected at a solid boundary. This permits the system to find an equilibrium and react to perturbations from it, and since there are never any inflows and outflows through the boundary, mass is conserved.

Figure 5.2: Treatment of spherical boundary conditions on a staggered mesh. Blue and red squares represent horizontal and vertical mass fluxes outside the boundary, which evolve freely, whereas turquoise and magenta squares represent mass fluxes inside the boundary, which are set to zero. Green squares represent density points that are subject to change, while yellow squares show density points that remain constant throughout the simulation.

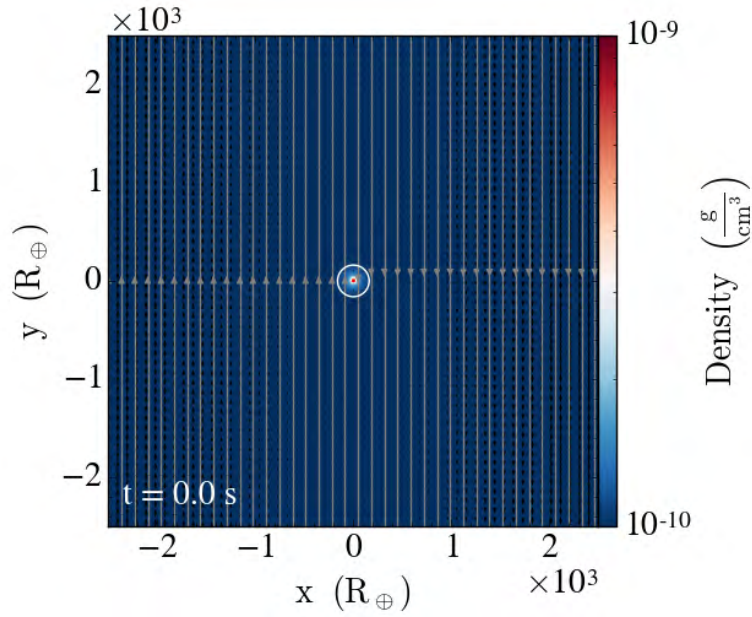


5.2.5 Relaxation of initial conditions

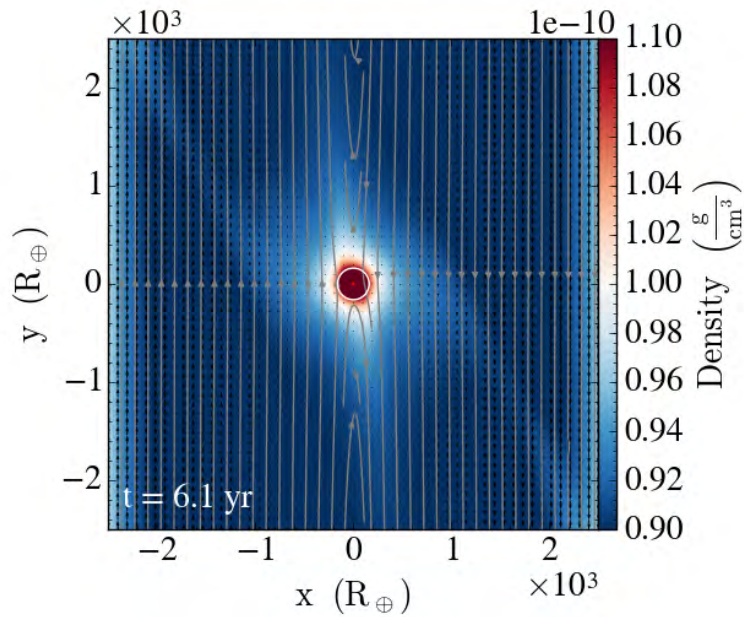
We allow the system to relax for 30 000 time units, which corresponds to about 6 years (given a code time unit $\tilde{t} = R_{\oplus} / (1 \text{ km s}^{-1}) = 6371$ seconds) in order to ensure that dynamically consistent conditions are attained. Indeed, as discussed below, tests demonstrate that it takes on the order of only one orbit for the initial conditions to relax.

The density stratification well inside the Hill sphere is almost hydrostatic, but with deviations and fluctuations on short time scales, and it is thus not necessary to include the detailed dynamics of this region while larger structures are relaxing. Therefore, we begin our experiments by fixing the hydrostatic structure there, and set the spherical boundary to a radius of 27 embryo radii. We then ‘release’ layers (add an extra level of refinement, reduce the radius of the spherical boundary, turn on the dynamics outside of the new spherical boundary) at successively smaller radii (9, 3 and finally, 1 embryo radii). The ‘releases’ are typically done at times = 10 000, 20 000 and 26 000 in code units. Successive releases are increasingly more expensive due to the smaller cell size and larger sound speeds, but need less time in code units to adjust to the surrounding environment (for essentially the same reasons, i.e., smaller scales and larger sound speeds). This procedure saves significant amounts of computing time during the initial relaxation phase.

After the last release, the simulations are allowed to relax for an additional 4000 time units before they are deemed ready for the next phase. Figures 5.3 and 5.4 show large-scale and zoomed-in density slices at the midplane for run m095t00 at $t = 0$ and after a relaxed state is reached at $t = 30\,000$. Panels on the right show the relaxed state with well established horseshoe orbits, density wakes, and slight density perturbations ahead/behind of the embryo at the same orbital distance (discussed in more detailed below).



(a) Initial conditions at time = 0.



(b) Relaxed simulation at time = 30 000

Figure 5.3: Relaxation of initial conditions for the $m095t00$ run. The panels show density slices and velocity streamlines at the midplane, with almost the entire extent of the simulation box in the x -direction and $1/5$ of the way in the y -direction. Horseshoe orbits are clearly visible in panel (b). Panel (b) is plotted with a highly enhanced contrast (the colour scale spans only 20% in density) to show the wakes and density increase at the orbital radius in the y -direction. The white and red circles (barely visible in these figures) denote the Hill radius and the isothermal Bondi radius of the embryo, respectively. The embryo itself is smaller than a pixel.

Fig. 5.4 is a zoom-in of the same run with the Bondi radius more clearly visible (largest red circle); the Rubik’s cube nesting of grids is also visible. The dashed lines indicate the successive releases of the radius of the embryo (green - 27, yellow - 9, light red - 3 embryo radii). The tiny black circle corresponds to one embryo radii. The right panel shows the simulation when fully relaxed and, via streamlines, demonstrates that the disk gas penetrates deeply into R_B , down to $\approx 20R_p$. At even smaller radii the atmosphere is nearly static, with motions that have a weak rotational tendency (see below).

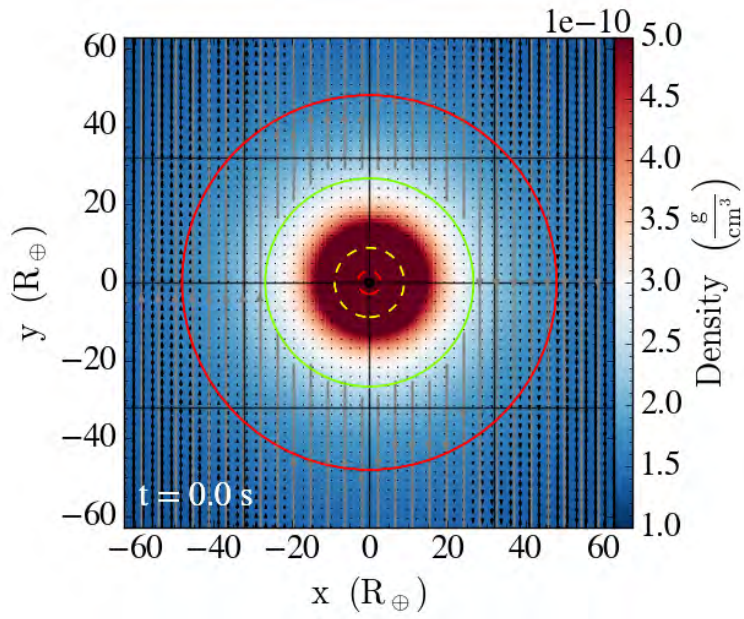
Fig. 5.5 shows the physical structure of the primordial atmosphere at both time = 0 and 30 000. The cuts are done along the x -axis in the midplane and along the z -axis at $x = y = 0$. As can be seen, the initial state is very close to the final state of the atmosphere, and there are only negligible variations for different cuts. Although the density and temperature profiles have changed slightly, the changes are minimal and the use of these initial conditions thus saves a lot of relaxation time (compared to, e.g., a sudden insertion of the planet’s gravitational potential, which would require waiting tens of orbits with the maximum level of refinement for the dynamics to relax). Although the innermost parts of the atmosphere still retain some weak random motions, by time = 30 000, the run has nearly reached a steady-state, when injection of particles can commence. Note that, as has been pointed out by Ormel et al. (2015b), a completely steady, static state will likely never be reached in the vicinity of the embryo.

5.3 PARTICLES

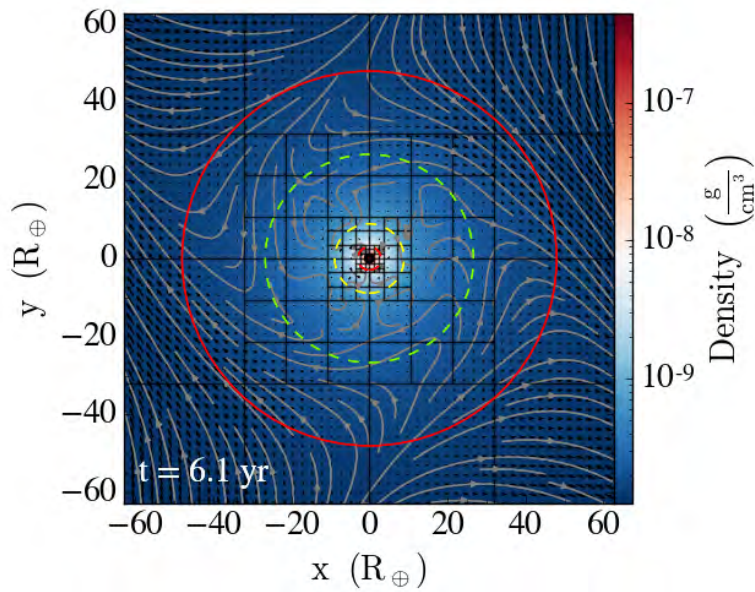
The initial spatial distribution of macro-particles is chosen to be proportional to the local gas density. The actual dust-to-gas ratio is likely characterized by a strong settling towards the midplane, while the dust-to-gas surface density ratio should be essentially constant in the upstream flow entering the Hill sphere. However, rather than having to make assumptions about the settling, we instead analyse sub-populations of our initial distribution, tagging and following for example only the particles that initially reside within a given distance from the midplane.

We use particle sizes normally ranging from 10^{-6} m to 1 cm (i.e. dust to pebbles), with a flat size distribution in logarithmic size. We include 1 cm particles for completeness, even though such large particles are typically found only in CB chondrites (Friedrich et al., 2015, with the exception of macro-chondrules), partly because there is no guarantee that the size distribution of chondrules in chondrites spans the entire size range that was available at the time of pebble accretion onto planet embryos. We also made complementary experiments with even larger size particles (up to 1 m), to explore saturation of accretion rates with size.

The shape of the distribution will be modified near the embryo, because large particles accrete more rapidly onto the embryo, while being replenished at the same rate as smaller size particles. The resulting change of the relative



(a) Initial conditions at time = 0.



(b) Relaxed simulation at time = 30 000

Figure 5.4: Relaxation of initial conditions for the m095t00 run. Intermediate scale density slices at the midplane. The large red circle is the Bondi radius. The solid green circle in panel (a) shows the current ‘active’ radius, while subsequent dashed circles show where future ‘releases’ will place a temporary embryo surface. The tiny black circle shows the actual radius of the embryo, which is reached after the final release.

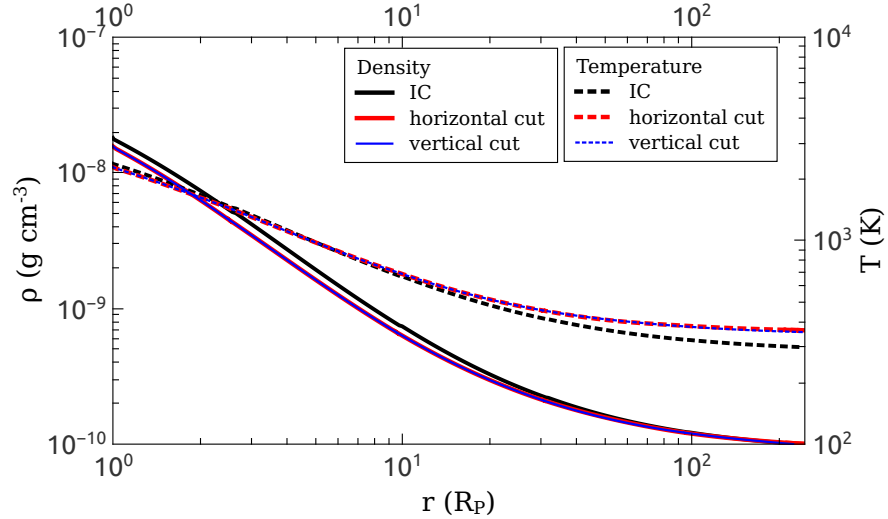


Figure 5.5: Physical structure of the primordial atmosphere for run m095t00 at $t = 0$ (initial conditions; IC) and $t = 30\,000 = 6.1$ years (fully relaxed). The horizontal and vertical cuts overlay each other nearly perfectly.

size distribution is a result of this study, and does not need to be anticipated in the initial conditions.

Note that, since we do not consider particle growth and destruction in this study, nor the back reaction of the particles on the gas, we are free to renormalise the size distribution *a posteriori* by changing the interpretation of the statistical weight factors of the macro-particles. We can thus match any given initial size distribution, and derive what the final distribution would be. We also note that since the span in space and time of our models is very limited (relative to disk extents and lifetimes), ignoring coagulation and shattering is an excellent approximation; such effects may instead be taken into account by modifying – *a posteriori* as per the remarks above – the assumed initial size distribution.

5.3.1 Equations of motion

In these simulations, we consider macro-particles (sometimes called super-particles; Rein et al. 2010; Ebisuzaki & Imaeda 2017), each of which represents a swarm of real, identical particles. The acceleration of the macro-particles:

$$\frac{d\mathbf{u}_p}{dt} = \mathbf{a}_G + \mathbf{a}_d, \quad (5.18)$$

is governed by \mathbf{a}_G , the differential forces originating from the planet, the star and the Coriolis force, which, in analogy with Eq. 5.15, are

$$\mathbf{a}_G = -\frac{GM_p(x\hat{\mathbf{x}} + y\hat{\mathbf{y}} + z\hat{\mathbf{z}})}{r^3} + 3\Omega_K^2 x\hat{\mathbf{x}} - \Omega_K^2 z\hat{\mathbf{z}} - 2\Omega_K \times \mathbf{u}, \quad (5.19)$$

and the acceleration from the gas drag,

$$\mathbf{a}_d = \frac{\mathbf{u}_{\text{gas}} - \mathbf{u}_{\text{part}}}{t_s}, \quad (5.20)$$

which is a product of the relative velocity of the particle, \mathbf{u}_{part} , with respect to that of the gas, \mathbf{u}_{gas} , and the inverse of the stopping time, t_s , which, in the Epstein regime is:

$$t_s = \frac{\rho_{\bullet} s}{\rho v_{\text{th}}}, \quad (5.21)$$

where ρ_{\bullet} is the solid density (taken to be 3 g cm^{-3}), s is the size of the particle, and v_{th} is the mean thermal velocity of the gas. We further assume that particles are spherical.

For simplicity and speed, we parametrise the inverse stopping time as:

$$\left(\frac{1 \text{ yr}}{t_s}\right) = \left(\frac{s}{1 \text{ cm}}\right) \left(\frac{c_d}{\rho}\right), \quad (5.22)$$

where $c_d = 10^{-12} \text{ g cm}^{-3}$ is a normalisation constant, defined such that in the sub-sonic Epstein regime, the stopping time is 1 year for a 1 cm particle in a gas density of $10^{-12} \text{ g cm}^{-3}$. This estimates the stopping time in the disk and outer parts of the Hill sphere sufficiently well, while ignoring the additional decrease of the stopping time due to the higher temperature near the surface of the embryo. Particles that reach such depths of the potential well are in any case doomed to accrete, so nothing is lost by ignoring the temperature dependence, and doing so reduces the cost to compute the stopping time.

Although this approximation may overestimate the stopping time slightly, the precise value is not critical, since there is in any case an uncertain factor that depends on the shape and porosity of the particles, and a different value can be compensated for by a corresponding shift of the assumed particle distribution.

In a similar vein, there is no need to expand the parameter space with different assumed disk densities, since that too corresponds to a rescaling of the particle stopping time, and a corresponding rescaling of the disk and adiabatic atmospheric structures with a constant factor in density.

Because of its dependence on gas density and particle size, the stopping time can vary over many orders of magnitude. Given the time step, Δt , that is necessary based on the velocity and acceleration of gravity, \mathbf{a}_G , one can thus have both $\Delta t \ll t_s$ and $\Delta t \gg t_s$. The latter case means that the differential equation governing the particle path becomes *stiff*.

To handle this, particle positions and velocities are updated with a modified kick-drift-kick leapfrog scheme (e.g. [Dehnen & Read 2011](#)), reformulated to give the correct relative speed also in the asymptotic limit when the time step is much larger than the stopping time. Instead of sub-cycling, which is computationally expensive, we use the method that is commonly referred to as “forward time differencing”, which ensures that the solution has the correct asymptotic behaviour, both when the stopping time is very long and

very short, and that the behaviour is also nearly the correct one in intermediate cases.

With forward time differencing, the velocity update, assuming for now only an acceleration due to the drag force, \mathbf{a}_d , may be written:

$$\mathbf{v}(t + \Delta t) = \mathbf{v}(t) + \Delta \mathbf{v} = \mathbf{v}(t) + \Delta t \mathbf{a}_d(t + \Delta t), \quad (5.23)$$

where the acceleration is time-centred at $t + \Delta t$. The resulting update relation is:

$$\Delta \mathbf{v} = \Delta t \mathbf{a}_d(t + \Delta t) = -(\Delta t / t_s) (\mathbf{v} + \Delta \mathbf{v} - \mathbf{v}_g(t + \Delta t)), \quad (5.24)$$

with solution:

$$\Delta \mathbf{v} = -\frac{\Delta t / t_s}{(1 + \Delta t / t_s)} (\mathbf{v} - \mathbf{v}_g(t + \Delta t)). \quad (5.25)$$

In the limit $\Delta t / t_s \gg 1$, the velocity ends up very close to the gas velocity (as it should), but without the need to take very short time steps, resulting in a much more efficient time integration. In the limit $\Delta t / t_s \ll 1$, one recovers the normal kick-drift-kick behaviour.

We thus advance the velocity in the first (kick) step with:

$$\mathbf{v}_1 = \mathbf{v}_0 + \frac{\Delta t}{(1 + \Delta t / t_s)} (\mathbf{a}_G(\mathbf{r}_0, t_0) + \mathbf{a}_d(\mathbf{r}_0 + \mathbf{v}_0 \Delta t, t_0 + \Delta t)). \quad (5.26)$$

The particle position and time are then updated (drift step) with:

$$\mathbf{r}_2 = \mathbf{r}_0 + \mathbf{v}_1 2\Delta t, \quad (5.27)$$

and

$$t_2 = t_0 + 2\Delta t. \quad (5.28)$$

Finally, the third step (kick) advances the velocity using the acceleration at the end of the full time step, with

$$\mathbf{v}_2 = \mathbf{v}_1 + \frac{\Delta t}{(1 + \Delta t / t_s)} [\mathbf{a}_G(\mathbf{r}_2, t_2) + \mathbf{a}_d(t_2)]. \quad (5.29)$$

We have tested this formulation on particle drift in disks with known solutions (Weidenschilling, 1977), recovering behaviour sufficiently accurate for our purposes for arbitrary values of Stokes numbers $St = \Omega t_s$.

The particle update procedure is computationally efficient, with the average update cost per cell on an Intel Ivy Bridge core increasing from $0.65 \mu\text{s}$ without particles to $0.72 \mu\text{s}$ with one particle per cell, indicating an average update cost of about 70 nanoseconds per particle. Most of that time is spend looking up properties needed to calculate the particle-gas drag force.

5.3.2 Injection of pebbles

Once the simulations are considered to be fully relaxed, pebbles are injected into the system. The probability that a particular cell in a particular patch will spawn a macro-particle is proportional to N_{ppc} , the number of particles per cell (which need not be an integer). We set N_{ppc} to 0.05 in most runs, but increase it to 1.0 in a few runs to improve the statistics when studying the distribution of particle sizes in small volumes.

The mass carried by a macro-particle is encoded in a ‘weight factor’, $w = \rho \Delta V / N_{\text{ppc}}$, where ΔV is the cell volume. The weight factor is thus proportional to the mass of gas in the cell where the macro-particle originates divided by N_{ppc} . An advantage of this approach is that the sum over all particles (or a subset defined by particle size or initial particle location) results in the total mass of those particles (to be renormalized by a preferred initial dust-to-gas ratio).

However, because the mass contained in any given cell can vary substantially, particles may need to be split to avoid the situation where the particle mass in a patch is represented by too few particles. For purposes of efficiency, the need for splitting is only checked when a particle passes from one patch to another. If an inbound particle carries more weight than, e.g., five times the initial average in the patch, it is split into a number of “child particles”. The child particles continue to carry, also after any additional splits, a memory of their initial identity, which is needed for identifying sub-populations based on initial physical location.

When a macro-particle is created, it is assigned a random position inside a cell and a randomly chosen size:

$$s = 10^{-3\mathfrak{R}} \text{ cm}, \quad (5.30)$$

where $\mathfrak{R} \subseteq [0,1]$ is a random number. The spawned macro-particles are initially given the gas velocity of the cell. We spawn ≈ 2.6 million macro-particles in most runs, with 53 million in a few runs with $N_{\text{ppc}} = 1$. We save a complete set of particle data when a snapshot of the gas dynamics is taken, but, for visualization purposes, we also separately save trajectory information for a smaller subset of macro-particles ($\sim 15\,000$) at every particle time step. These ‘tracer particles’ are used to accurately track the trajectories of accreting particles and correspondingly to show the escape routes of particles that enter the Hill sphere and then leave again.

5.4 RESULTS: GAS FLOWS

We begin by investigating the gas flow patterns around the different mass cores. In the last several years, a number of authors have studied the hydrodynamics in the vicinity of embedded planetary embryos (e.g. [D’Angelo & Bodenheimer 2013](#); [Ormel et al. 2015b](#); [Fung et al. 2015](#); [Masset & Benítez-Llambay 2016](#); [Cimerman et al. 2017](#); [Lambrechts & Lega 2017](#); [Xu et al. 2017](#), etc.) across a broad range of different conditions (e.g. different core

masses, orbital distances from the parent star, disk structures), physical processes (isothermal/adiabatic/realistic EOS, with/without radiative energy transfer, magnetic fields, etc.). As illustrated below, our simulations are consistent with these previous studies, while offering both a higher resolution and a larger domain around the embryo.

Figures 5.6 to 5.11 shows the details of the gas flow in the m095t00 run for the $M = 0.95 M_{\oplus}$ planetary embryo. For clarity, we zoom-in to the Hill radius (234 embryo radii, white circle). The red circle denotes the nominal Bondi radius, R_B , which is $\approx 49R_p$. The embryo is marked by a black circle, but it is too small to be visible in these figures. The four Figures, 5.6, 5.7, 5.8 and 5.9 show the velocity magnitude in the disk midplane ($z=0$), and at $z = 10, 25,$ and $75 R_p$ respectively. As expected, the perturbation of the gas due to the embryo decreases with increasing height above the midplane, as indicated by the streamlines². The velocity magnitude is nearly uniform along the y -direction, indicating that there are no substantial perturbations close to $y=0$ where the embryo is located, and is consistent with Ormel et al. (2015b). We also observe that the width of the horseshoe orbits decrease with increasing height above the midplane, which agrees with the results of Fung et al. (2015), but contradicts the isothermal results of Masset & Benítez-Llambay (2016). This might be attributed to the fact that we use a non-isothermal EOS, but further analysis of the horseshoe orbits is beyond the scope of this work. Figure 5.10 shows the vertical component of the vorticity measured relative to the rotating coordinate system. A clear vorticity pattern can be seen, with separators splitting the flow into regions that pass the embryo on the left and right sides. The flows passing on the “wrong” side contribute directly to positive (prograde, counter-clockwise) vorticity, which adds to the rotation of the flow.

Figure 5.11 shows the vertical velocity, v_z , in an xz plane at $y = 0$. A vertical gas flow pattern can be distinguished: gas flows towards the embryo from the poles and moves away at the midplane. Zonal flow patterns are visible as closed streamline loops. Vertical velocities inside R_B are of the order of a few cm s^{-1} , which agrees well with previous works (e.g. Ormel et al. 2015b; Lambrechts & Lega 2017).

Qualitatively, the $M = 0.5 M_{\oplus}$ case is very similar, thus the figures for this mass are presented in Appendix 5.8; Fig. 5.47 to 5.52. The similarity with the higher mass case is apparently because embryos of such masses have well established primordial atmospheres, which are very close to being hydrostatic, leading to very similar flows in the vicinity of the Hill sphere.

In contrast, the gas flows around the $M = 0.096 M_{\oplus}$ embryo (m01t00 run) behave differently, as illustrated in Figures 5.12 to 5.19. The horseshoe orbits reach in towards the embryo surface and the core is not massive enough to form a substantial pseudo-hydrostatic atmosphere, even though a marginally stable region is seen very close to the surface (extending to about two embryo radii). There are no consistent vorticity patterns, and the gas flow pat-

² Note, however, that the streamlines does not give an entirely accurate impression of the flow pattern because they only consider the velocity in the plane of the slice.

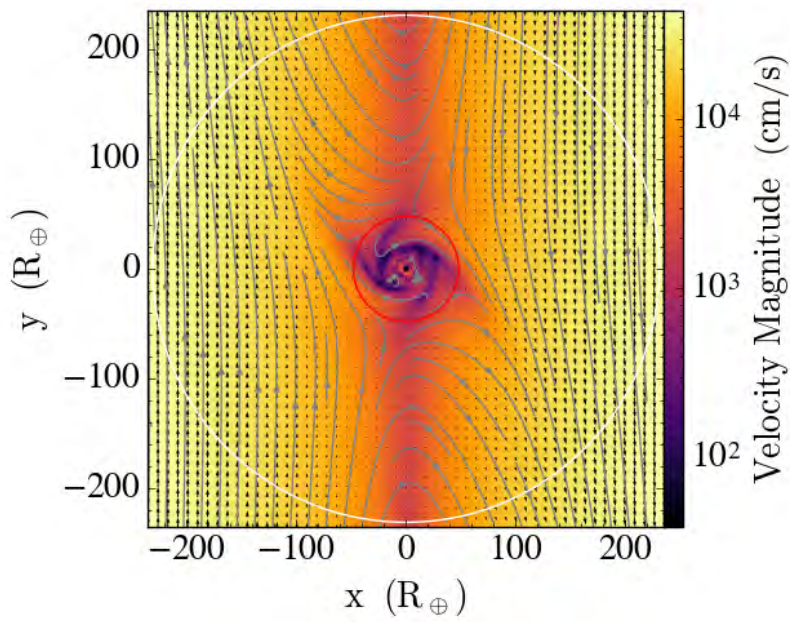


Figure 5.6: Velocity magnitude in the midplane around the $M = 0.95 M_{\oplus}$ embryo in the m095t00 run. Velocity streamlines are also shown.

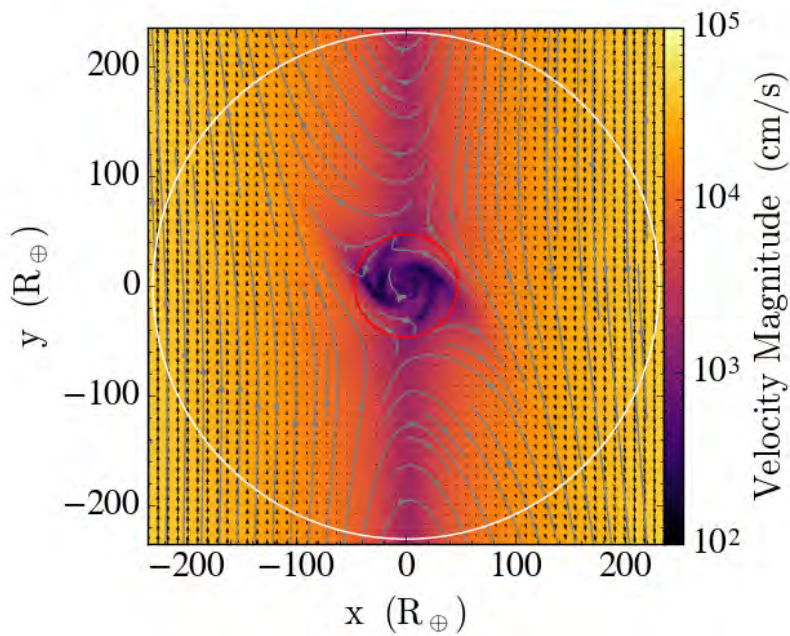


Figure 5.7: Same as 5.6, but at $z = 10 R_p$ above the midplane. The scale of the colour bar is deliberately held constant.

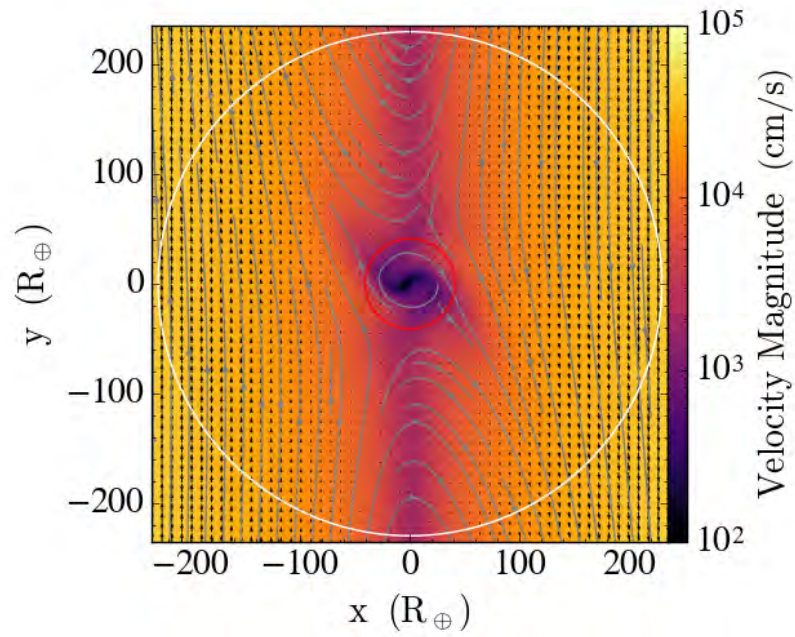


Figure 5.8: Same as 5.6, but at $z = 25 R_p$ above the midplane. The scale of the colour bar is deliberately held constant.

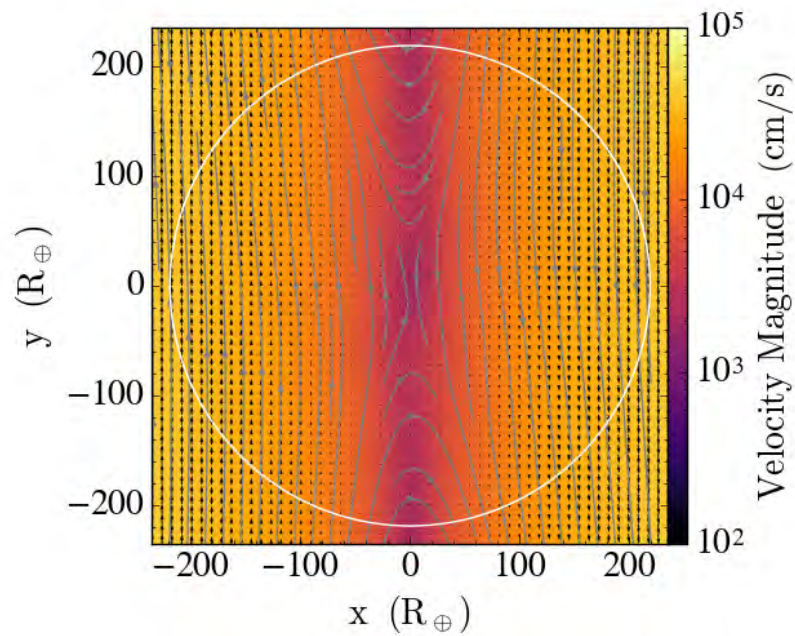


Figure 5.9: Same as 5.6, but at $z = 75 R_p$ above the midplane. The scale of the colour bar is deliberately held constant.

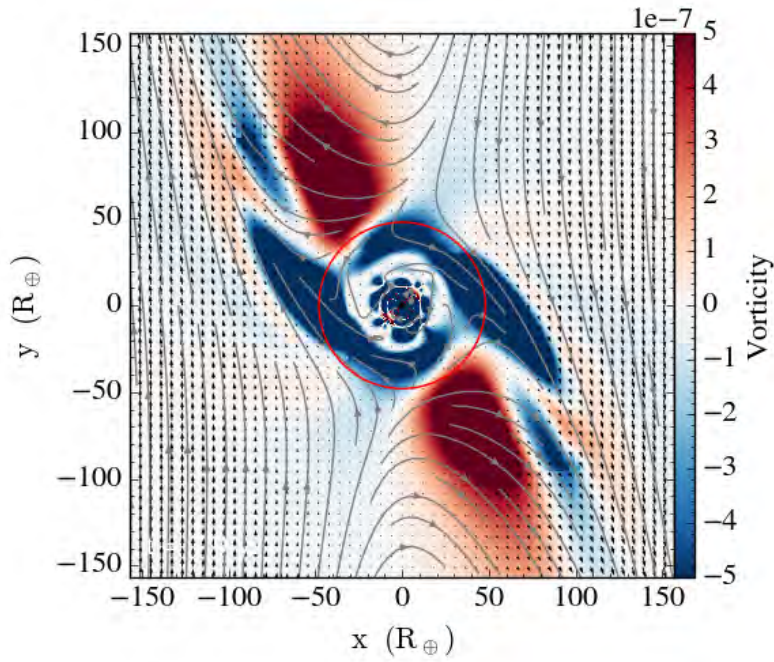


Figure 5.10: Vertical component of the vorticity in the midplane around the $M = 0.95 M_{\oplus}$ embryo in the m095t00 run. Velocity streamlines are also shown.

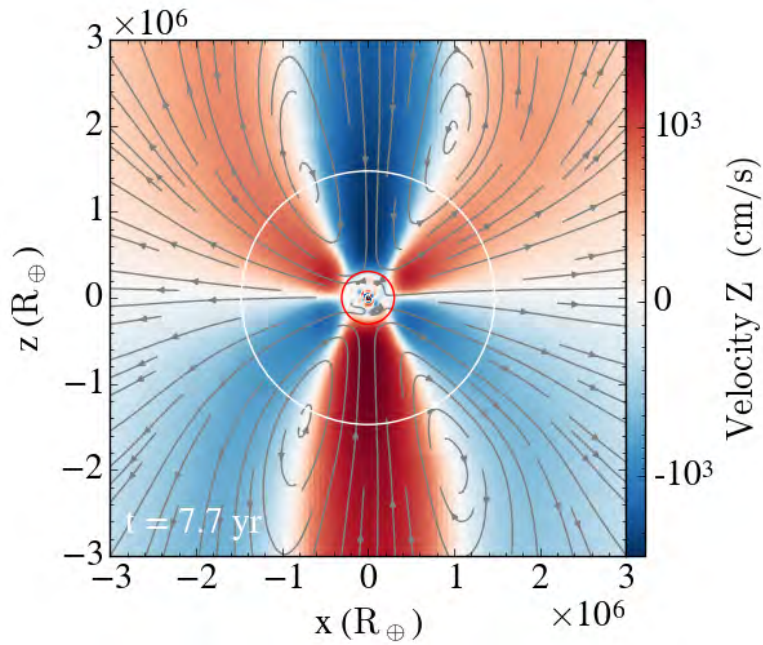


Figure 5.11: xz slice of u_z at $y = 0$ around the $M = 0.95 M_{\oplus}$ embryo in the m095t00 run. Velocity streamlines are also shown.

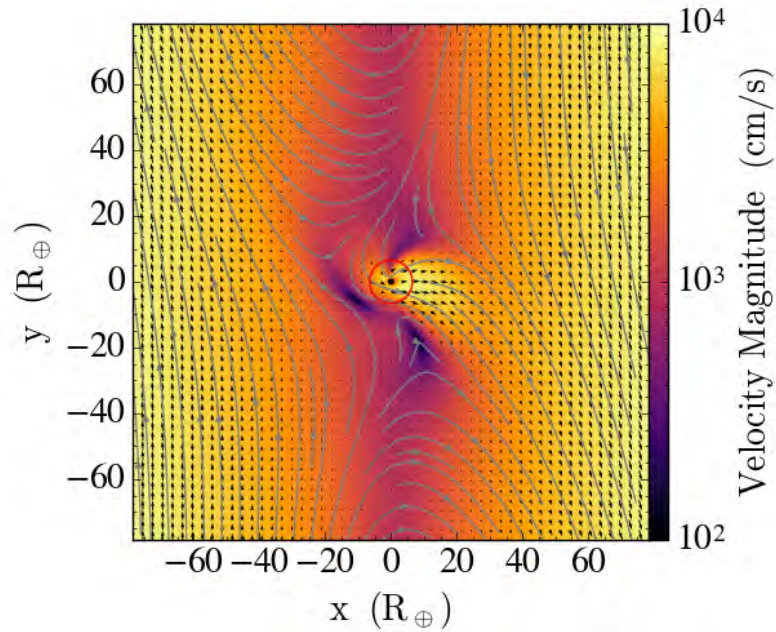


Figure 5.12: Same as Fig. 5.6, but for the $M=0.096 M_{\oplus}$ embryo in the m01t00 run.

terns change with time, alternating between dominating gas inflows from the leading/outer horseshoe flow and the trailing/inner one. The locations of the stagnation points also vary with time. The vertical flows of the gas, meanwhile, approach the embryo without substantially slowing down before being deflected to the sides.

5.4.1 Gas dynamics close to the planetary embryos

One reason why this work stands out relative to previous studies is that we are able to resolve the detailed gas dynamics (and hence accurate particle paths) in the close vicinity of the planetary embryos. Figures 5.20 to 5.22 shows the gas velocity magnitude in the vicinity of R_B for the $M = 0.096 M_{\oplus}$ (Fig. 5.20), $M = 0.5 M_{\oplus}$ (Fig. 5.21) and $M = 0.95 M_{\oplus}$ (Fig. 5.22) embryo masses. The $M = 0.096 M_{\oplus}$ core is not massive enough to form a hydrostatic atmosphere – the horseshoe flows constantly flush the atmosphere and only a tiny part of it ($\approx 2 R_p$ from the embryo) is nearly static. With increasing embryo mass, more gas becomes bound and the velocity magnitude decreases. Nevertheless, there are always slow gas movements inside R_B due to both gas from the disk that reaches deeper interior layers and from small scale turbulence. Therefore, the primordial atmospheres are never fully isolated and always interact with the surrounding disk.

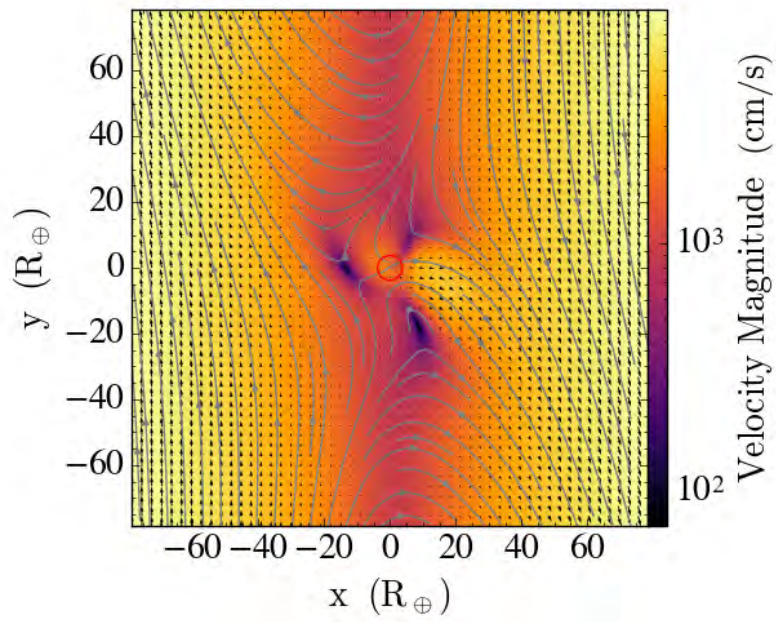


Figure 5.13: Same as Fig. 5.7, but for the $M=0.096 M_{\oplus}$ embryo in the m01t00 run.

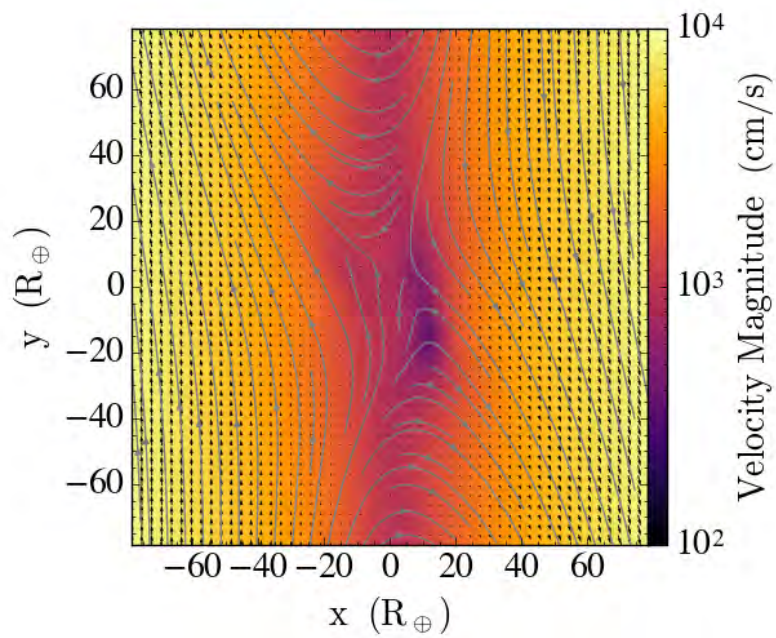


Figure 5.14: Same as Fig. 5.8, but for the $M=0.096 M_{\oplus}$ embryo in the m01t00 run.

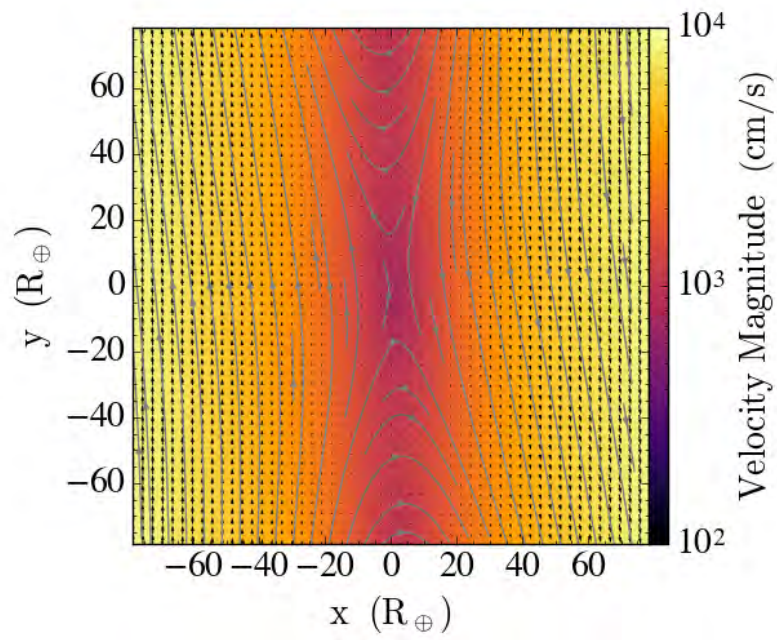


Figure 5.15: Same as Fig. 5.9, but for the $M=0.096 M_{\oplus}$ embryo in the m01t00 run.

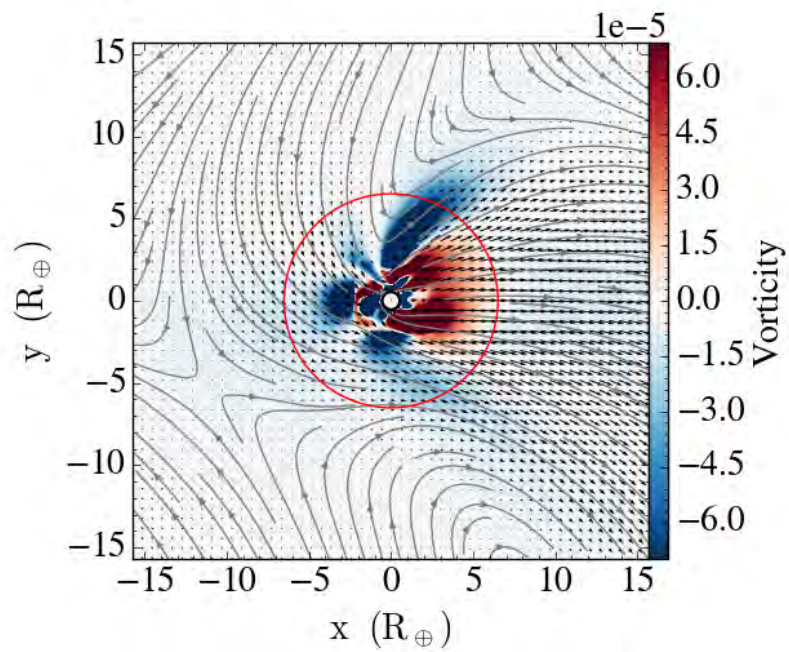


Figure 5.16: Same as Fig. 5.10, but for the $M=0.096 M_{\oplus}$ embryo in the m01t00 run.

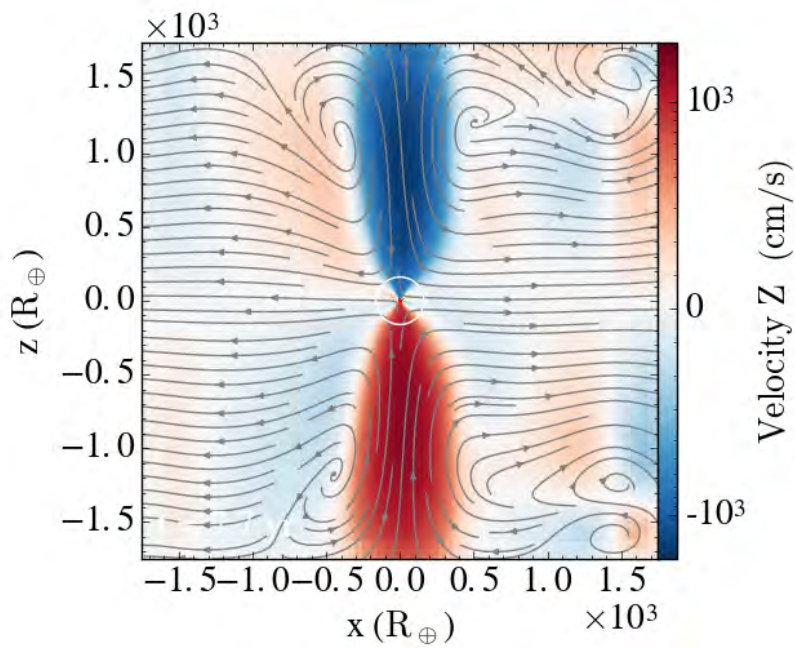


Figure 5.17: Same as Fig. 5.11, but for the $M=0.096 M_{\oplus}$ embryo in the m01t00 run.

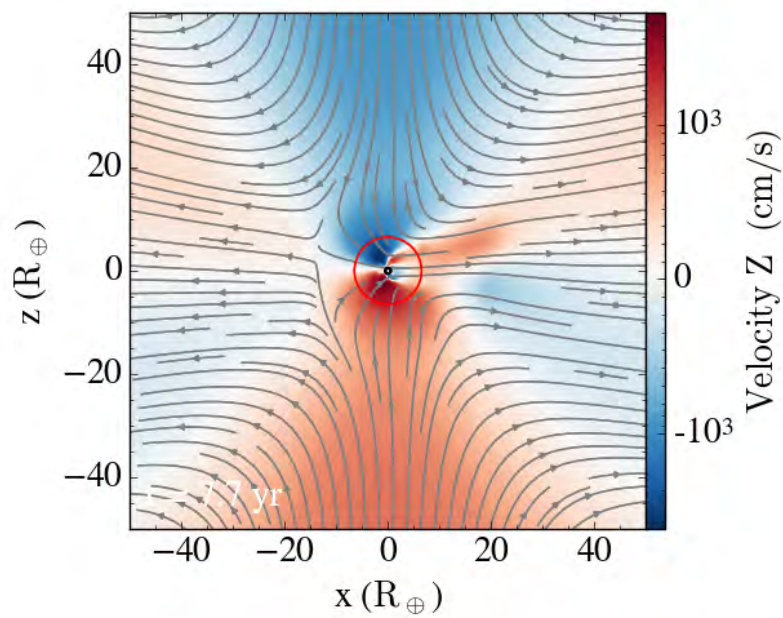


Figure 5.18: Zoom-in of u_z in the xz plane of Figure 5.17.

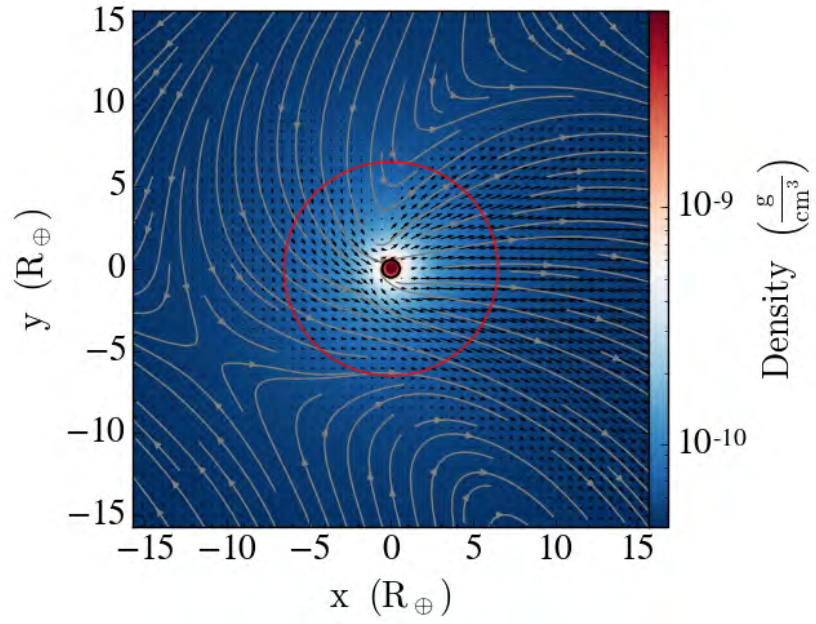


Figure 5.19: Density slice in the midplane for the $M=0.096 M_{\oplus}$ embryo in the m01t00 run.

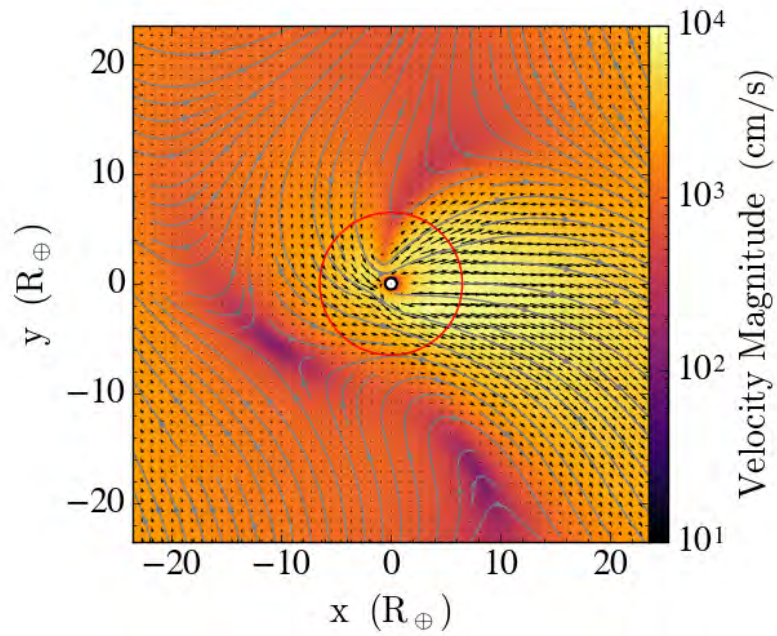


Figure 5.20: Velocity magnitude in the midplane in the vicinity of the embryo of the m01t00 run.

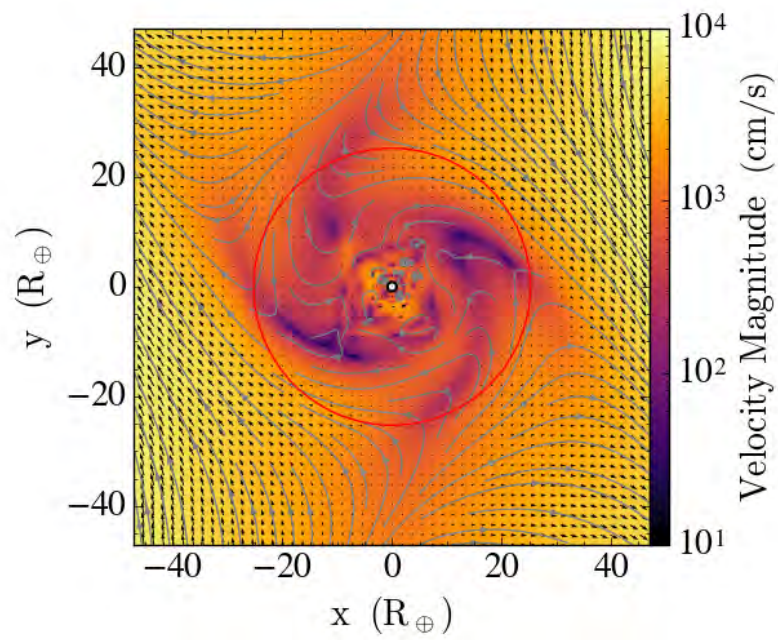


Figure 5.21: Velocity magnitude in the midplane in the vicinity of the embryo of them05t00 run.

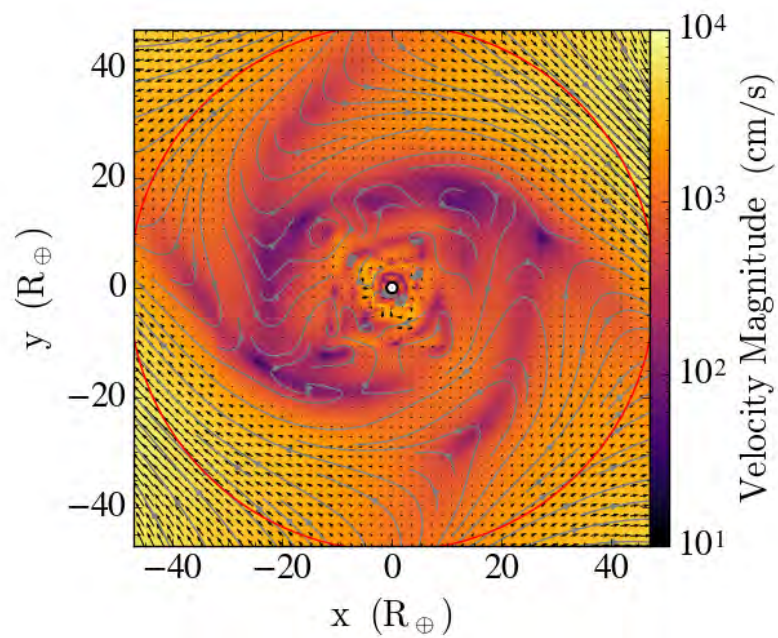


Figure 5.22: Velocity magnitude in the midplane in the vicinity of the embryo of them095t00 run.

5.5 RESULTS: PARTICLES

An obvious advantage of our large simulation box is the large particle reservoir. Smaller simulation boxes, especially with non-periodic x -boundaries, often experience a depletion of macro-particles. This makes the accurate evaluation of accretion rates more difficult, and additional injections of particles may be needed (e.g. Xu et al. 2017).

In Figures 5.23 to 5.26, we show time-series of particle mass density from run m095t10 across a range of integrated radial layers (shells) from the embryo surface to twice the Hill radius. The bin width dr is $4.66R_p$. For clarity, we subdivide our macro-particles into 3 size bins: particles with size between 0.001 and 0.01 cm (Fig. 5.23), particles between 0.01 and 0.1 cm (Fig. 5.24), and particles between 0.1 and 1 cm (Fig. 5.25). Fig. 5.26 shows the total density of all the solids. Additionally, Fig. 5.26 shows the integrated density of the gas, divided by 100 (the canonical gas-to-dust ratio), in cyan for the same radial bins. In each panel, black denotes the first snapshot after the injection of the pebbles (after 40 time units) while the other lines are plotted at 4 000 time unit intervals (which corresponds to ≈ 0.8 of an orbital period). The bottom part of each panel shows the number of macro-particles in each radial bin. Here, the initial dips on the black curves stem from changes in the level of refinement. As time goes on, the number of macro-particles decreases due to accretion and transport, but new particles are continuously coming from further out. These new particles originate in patches with lower numerical resolution (i.e. larger cell sizes), and thus carry larger representative weights.

Even after 2.4 orbits, there is no indication of depletion of solids – the mass influx through a given shell is sufficient to replace any accreted or lost particles. The increasing noise level and the decrease in the number of macro-particles with time are, meanwhile, due to an increasing contribution from (a smaller number of) higher statistical weight macro-particles. Similar trends are seen for the other embryo masses; as the solid density is proportional to the gas density, we choose to not show separate figures for them.

5.5.1 *The distribution of particles*

We initialize particles uniformly in the dust-to-gas ratio, and we therefore assume the initial vertical stratification of particles is the same as that of the gas. Particles then settle towards the midplane due to the vertical force of gravity, with settling time scales of the order of $1/(t_s \Omega_K^2)$. In panel (a) of Fig. 5.27 we show the local e-folding time of particle settling in our simulations, assuming there are no net vertical gas flows. The figure shows that the settling time scale for particles is long relative to the duration of our experiments for small and intermediate size particles, while it is comparable to our run times for the largest particles. Lacking proper turbulence in the disk, the settling of particles is anyway not very realistic—turbulence stirs up the particles and controls their scale height. Additionally, zonal gas flows (e.g. Fig. 5.11) close to the Hill sphere are capable of stirring up well-coupled particles.

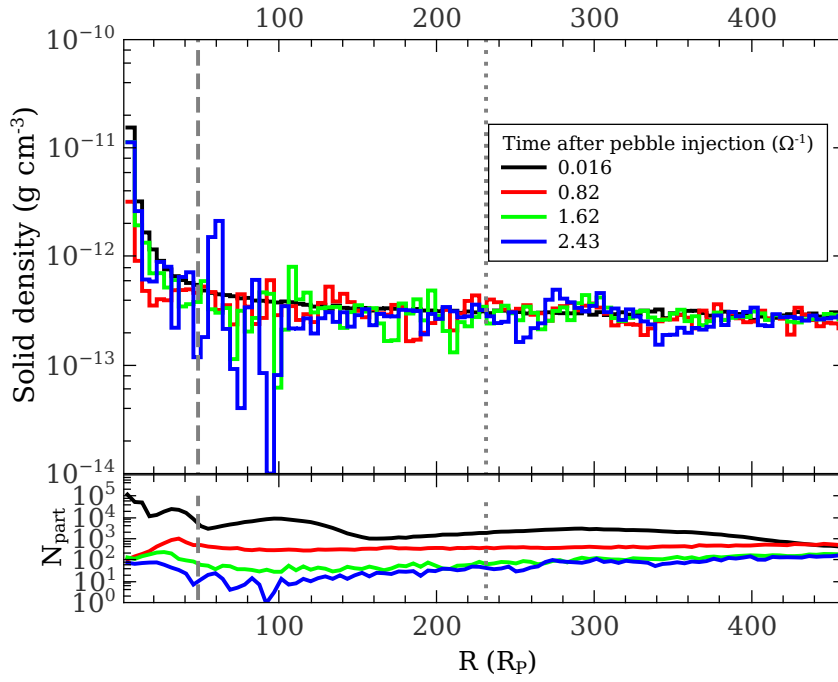


Figure 5.23: Solid mass distribution close to the embryo at different times for the $m095t10$ run for $s < 0.01$ cm size particle bin. The vertical dashed and dotted lines show the Bondi and Hill radii, respectively. The lower panel shows the number of macro-particles as a function of radius. As initially local macro-particles with low weights are replaced by macro-particles with larger weights from larger distances, the statistical noise increases.

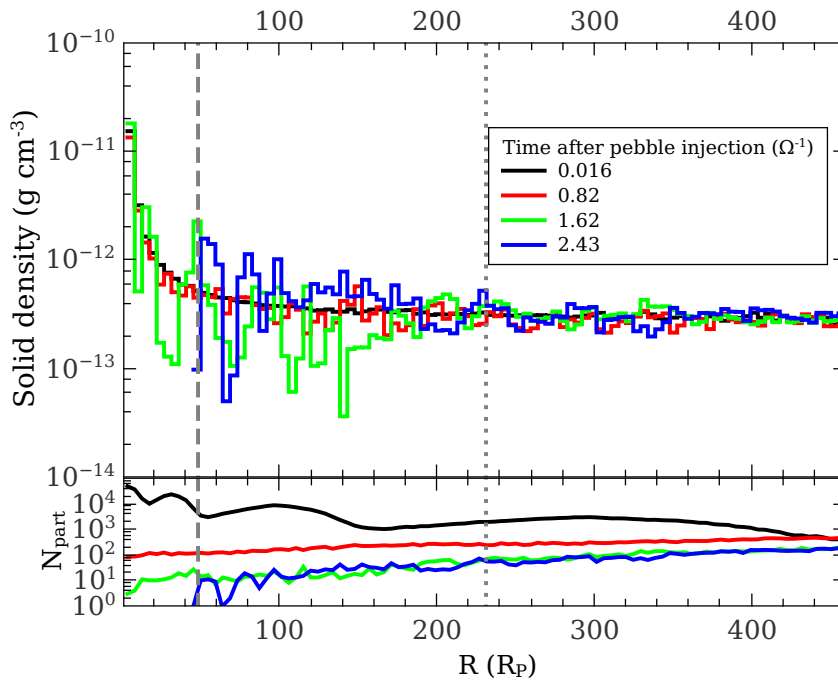


Figure 5.24: Same as Fig. 5.23, but for $0.01 < s < 0.1$ cm size particle bin.

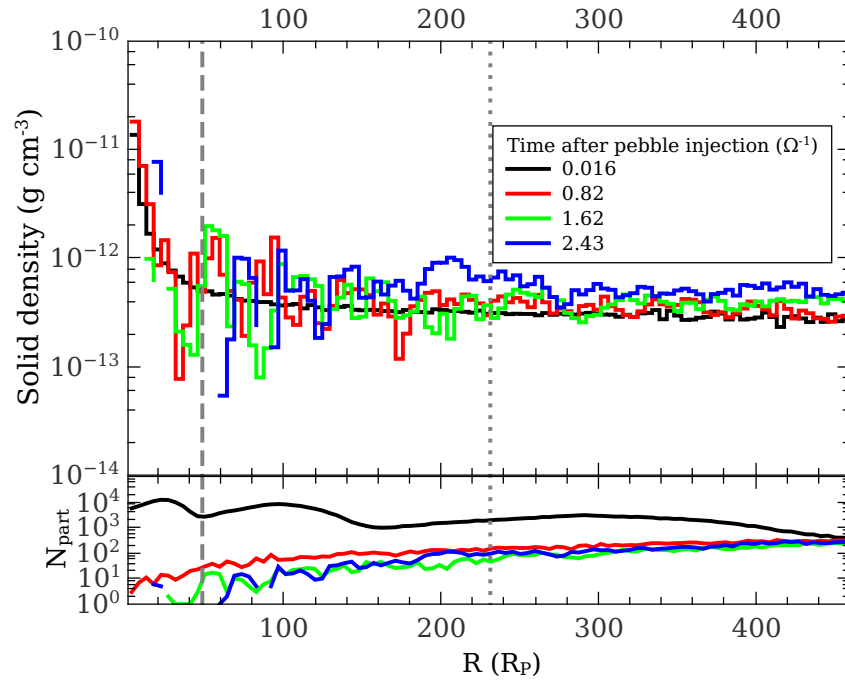


Figure 5.25: Same as Fig. 5.23, but for $s > 0.1$ cm size particle bin.

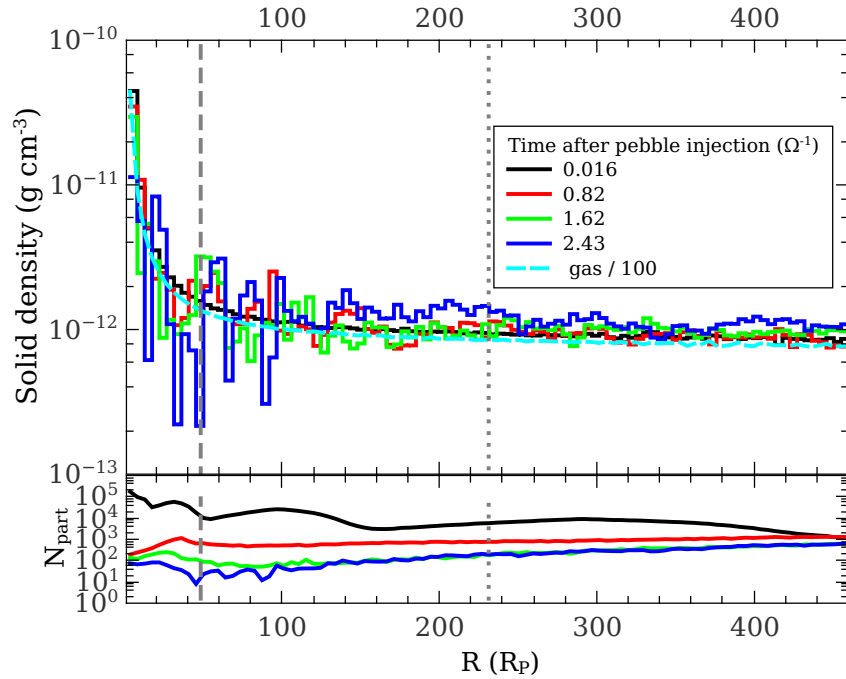
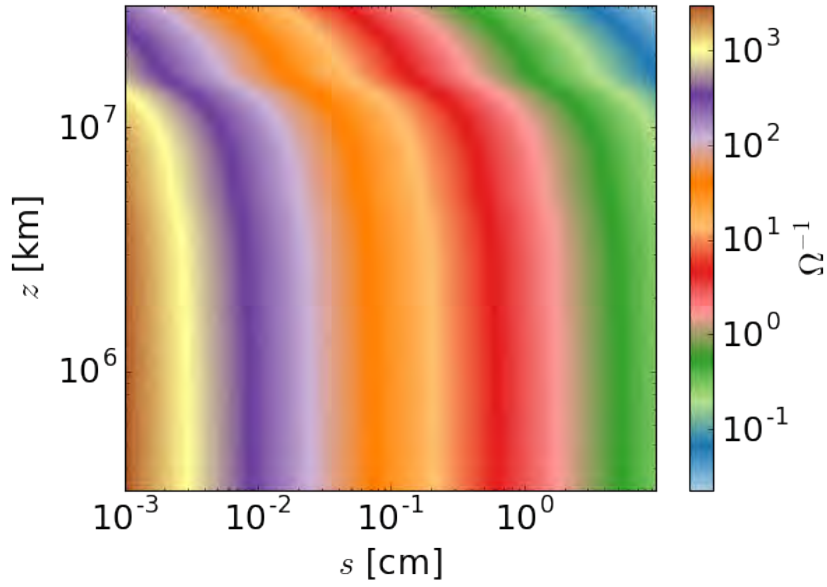
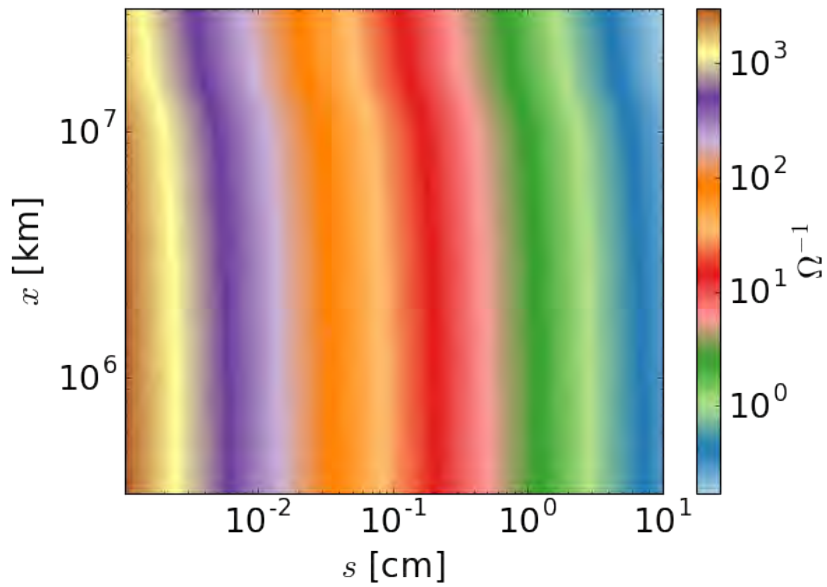


Figure 5.26: Solid mass distribution close to the embryo at different times for the m095t10 run without binning. The vertical dashed and dotted lines show the Bondi and Hill radii, respectively. The lower panel shows the number of macro-particles as a function of radius. As initially local macro-particles with low weights are replaced by macro-particles with larger weights from larger distances, the statistical noise increases.



(a) Vertical settling.



(b) Radial settling.

Figure 5.27: Local e-folding time for particle settling at 1 AU orbital distance. Panel (a) shows the vertical settling, panel (b) the radial settling (at the mid-plane) towards the pressure maximum at 1 AU.

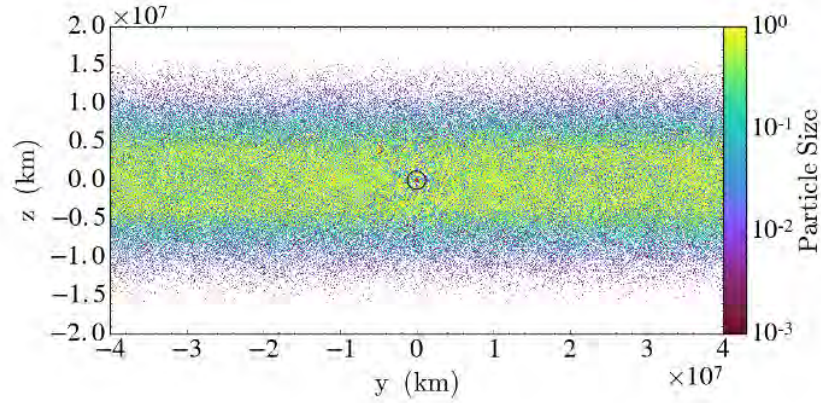


Figure 5.28: Vertical distribution of pebble sizes in the m095t00 run 1.6 orbits after the injection of macro-particles.

Therefore, instead of working with ill-defined and unknown equilibrium populations, we choose instead well-defined, localized sub-populations with initially constant dust-to-gas ratios for our measurements of accretion rates. Tests have shown that it takes only ~ 0.5 orbits after the injection of particles for the measured accretion rates to stabilize. The hydrodynamic flow patterns are established quickly as well, taking approximately the same amount of time. This shows that our initial relaxation of the flow patterns, which was allowed to continue for ~ 6 orbital periods, was certainly sufficient and allows for accurate measurements of accretion rates.

Fig. 5.28 shows the vertical distribution of pebbles in the m095t00 run, 1.6 orbits after the injection of macro-particles. The smallest particles ($s \leq 0.01$ cm; dark colours) continue to show essentially the vertical distribution of the gas, while larger particles ($s > 0.1$ cm; green to yellow) have begun to settle. This figure also nicely illustrates how small a perturbation the Hill sphere is relative to the size of our computational domain.

Figures 5.29 to 5.31 shows the distribution of particles and their sizes at the midplane, two orbits after the injection of particles. This time, the particles are split into 3 size bins: $s \leq 0.01$ cm (yellow), $0.01 \leq s < 0.1$ (red) and $s > 0.1$ cm (green). The vertical extent we collect particles from is limited to $1R_H$ in Fig. 5.29 and $2R_B$ in Figures 5.30 and 5.31, above and below the midplane. One instantly notices the two leading and trailing arms, stretching away from the embryo. The large concentration of particles there indicates that these particles are moving away from the embryo very slowly. The wakes are located just inside the separatrix sheets of the horseshoe orbit, with the smallest particles mostly concentrating in the outermost regions and the larger ones having orbits closer to the inside of the horseshoe. These particles carry a relatively small weight (they originate at the patches of higher level of refinement), so the features are somewhat artificially enhanced in the figure (which shows macro-particles), but the figure therefore also nicely illustrates the preferred ‘leaving’ paths of the particles. A large fraction of these particles have

actually entered and later left the Hill sphere, and the features are therefore concentrated in the midplane.

A zoom-in to R_B (Fig. 5.31) reveals that there is a concentration of small particles ($s < 0.1$ cm) inside the Bondi sphere. Larger particles do not linger there for long since they are effectively accreted. The Figure 5.32 shows particle paths based on high-cadence positions of tracer-particles, sub-divided into 3 size bins. The green colour represents $0.001 \leq s < 0.01$ cm, blue $0.01 \leq s < 0.1$ cm and black $0.1 \leq s < 1$ cm size particles. The smallest particles spend around $0.1\Omega^{-1}$ inside the Bondi sphere before they reach the embryo. In contrast, particles with $s \geq 0.01$ cm, are accreted on average 10 times faster, after they reach the Bondi sphere. Alternatively, some of the smallest particles, if they linger far enough from the embryo, are later carried out by the horseshoe gas flows.

In these runs we do not consider convection driven by the accretion heating (but see below), particle growth and evaporation. Sufficiently strong convection could possibly prevent the smallest particles from reaching the core. Also, as the gas temperature close to the embryo (≈ 4500 K near the $M = 0.95 M_\oplus$ embryo) greatly exceeds the melting point of any solid, evaporation of solids and the resulting enrichment of the atmosphere with heavy elements (e.g. Alibert 2017; Brouwers et al. 2017), is bound to play an important role in models with a realistic treatment of evaporation. As shown by Fig. 5.1, a more realistic equation of state leads to lower temperatures at the base of the atmospheres, but still large enough to cause evaporation.

Fig. 5.33 similarly shows the distribution of pebbles close to the midplane (inside $2R_B$) in the m01t00 run. It shows a very similar picture — escaping particles are trapped in the leading/inner and trailing/outer horseshoe orbit parts. The zoom-in of the figure (panel (b)) reveals an interesting, but expected difference — there is no accumulation of particles inside the Bondi sphere. There are two reasons that could contribute to that: the gas flows may be strong enough to readily carry small and intermediate size particles away, and larger particles are rapidly accreted. Panel (c) in Fig. 5.32 reveals the right answer: the stopping time, even of the smallest size particles we consider in our runs, is short enough that the gravitation of the embryo is not damped by the gas drag enough to prohibit particles from being accreted. The smallest particles in our simulation take merely a $0.04 \Omega^{-1}$ to be accreted. And the number of these smallest particles crossing the Bondi sphere is much larger, compared to the $M = 0.95 M_\oplus$ embryo. Here we remind the reader that we do not trace all the particles with this high cadence, therefore only a fraction of all the accreted particles are shown in Fig. 5.32 (we also, for greater clarity, limit the number of traces shown in these figures to 150).

Fig. 5.32 shows evidence for a variation of hydrodynamical deflection (e.g. Sellentin et al. 2013) - higher mass embryos are accompanied by much denser primordial atmospheres, in which the stopping time becomes smaller for larger particles. Whereas the majority of the particles in the size distribution we consider here have nearly ballistic orbits when being accreted by the lowest mass embryo (Fig. 5.32, panel (c)), they become significantly affected

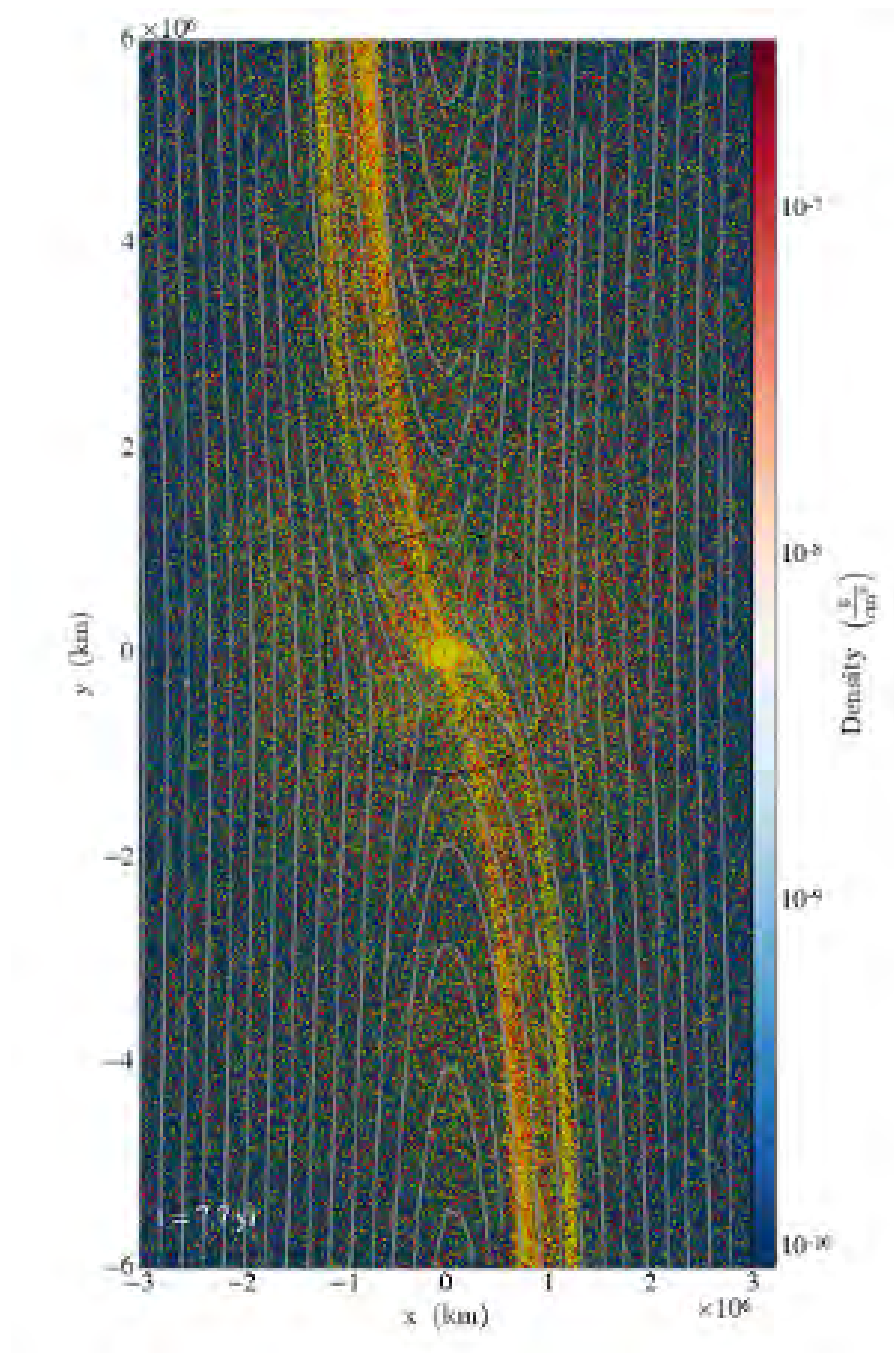


Figure 5.29: Gas density and Particle distribution over a $2R_H$ vertical extent above/below the midplane in the m095t00 run. The pebbles here are split into 3 size bins: $0.001 < s \leq 0.01$ cm (yellow), $0.01 < s \leq 0.1$ cm (red), and $0.1 < s \leq 1$ cm (green).

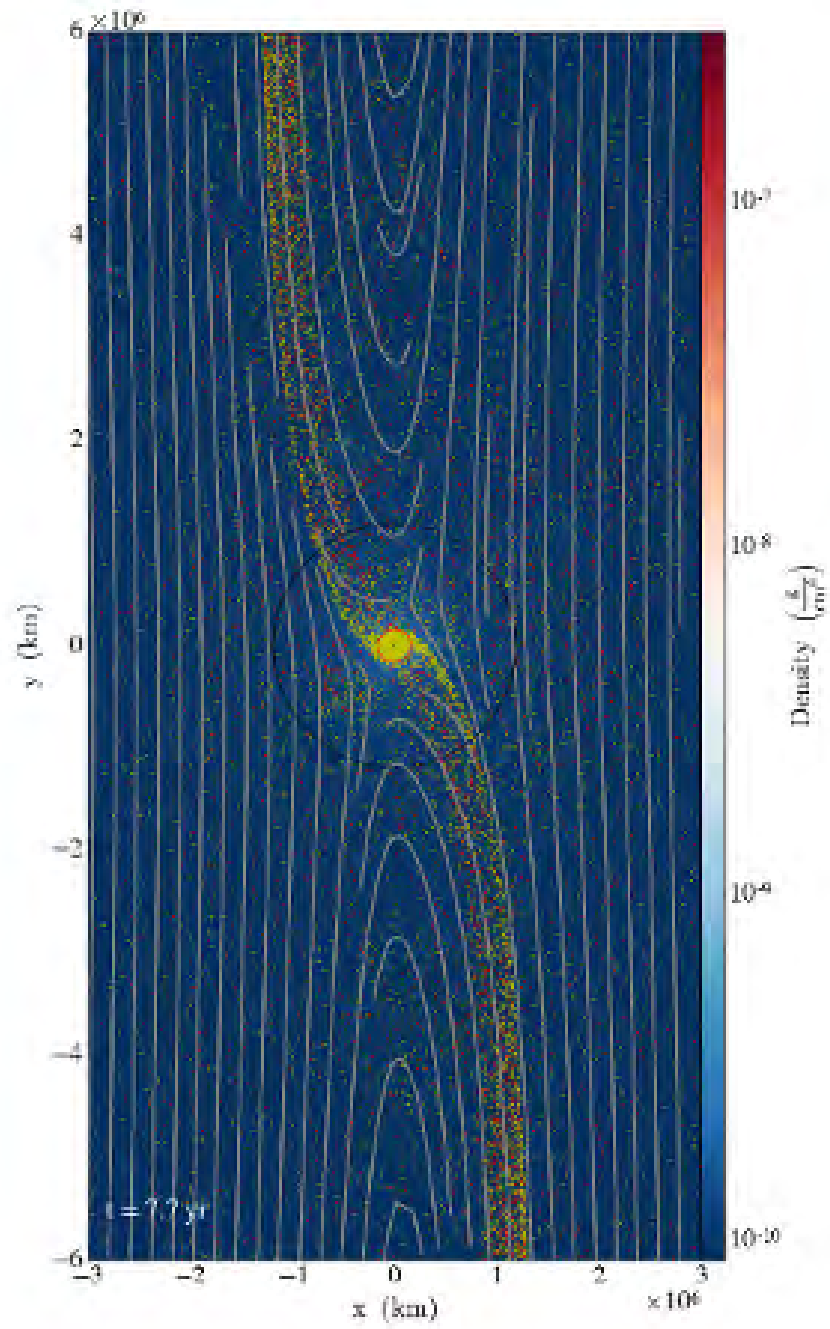


Figure 5.30: Same as Fig. 5.29, but with a $2R_B$ vertical extent.

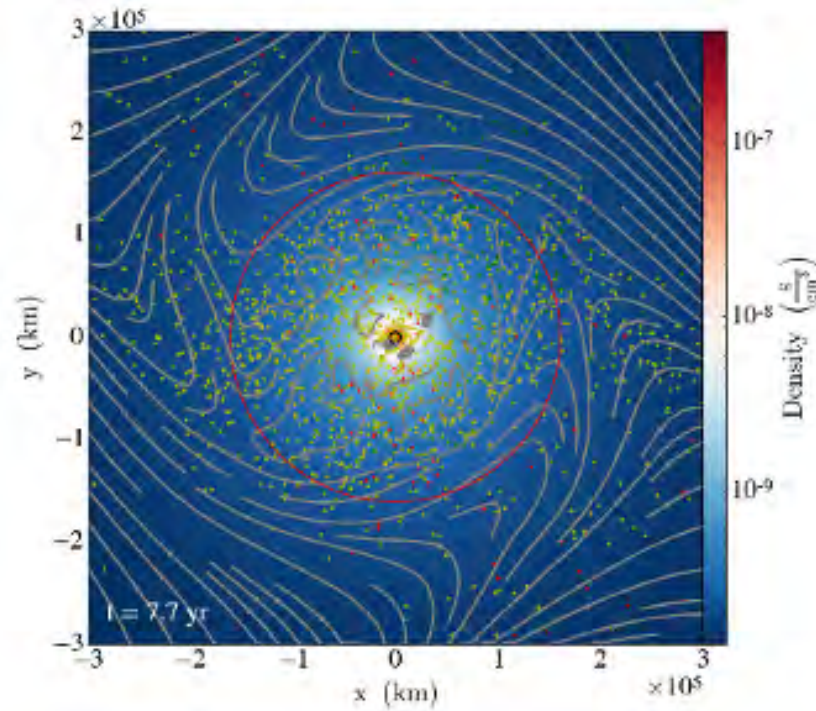


Figure 5.31: A zoom-in of Fig. 5.30

by the higher gas density envelopes in panels (b) and (a). In the latter, the highest-mass embryo case, the motion of the gas almost completely controls the motion of particles with size $s < 0.01$ cm.

5.5.2 Pressure traps

Having a pressure bump instead of a flat density distribution, whilst having no headwind, provides twofold advantages:

1. It creates a more self-contained region in the x -direction around the embryo's orbital radius, which retains the density wake produced by the embryo, preventing it from causing a forceful numerical bounce at the boundaries. This is also mitigated by the sponge-boundaries that we use, but a less forceful wake means a smaller area at the boundaries needs to be artificially damped.
2. High resolution observations (e.g. [ALMA Partnership et al. 2015](#); [Andrews et al. 2016](#)) show disks with rings and gaps, which affect the distribution of solids in the disk. Having the pressure bump allows particles to drift into the pressure maximum, thus mimicking the observed behaviour.

Since small particles are well coupled to the gas, at our densities and time scales only the largest particles can drift significantly towards the pressure maximum. Panel (b) in Fig. 5.27 shows the local e-folding time of radial

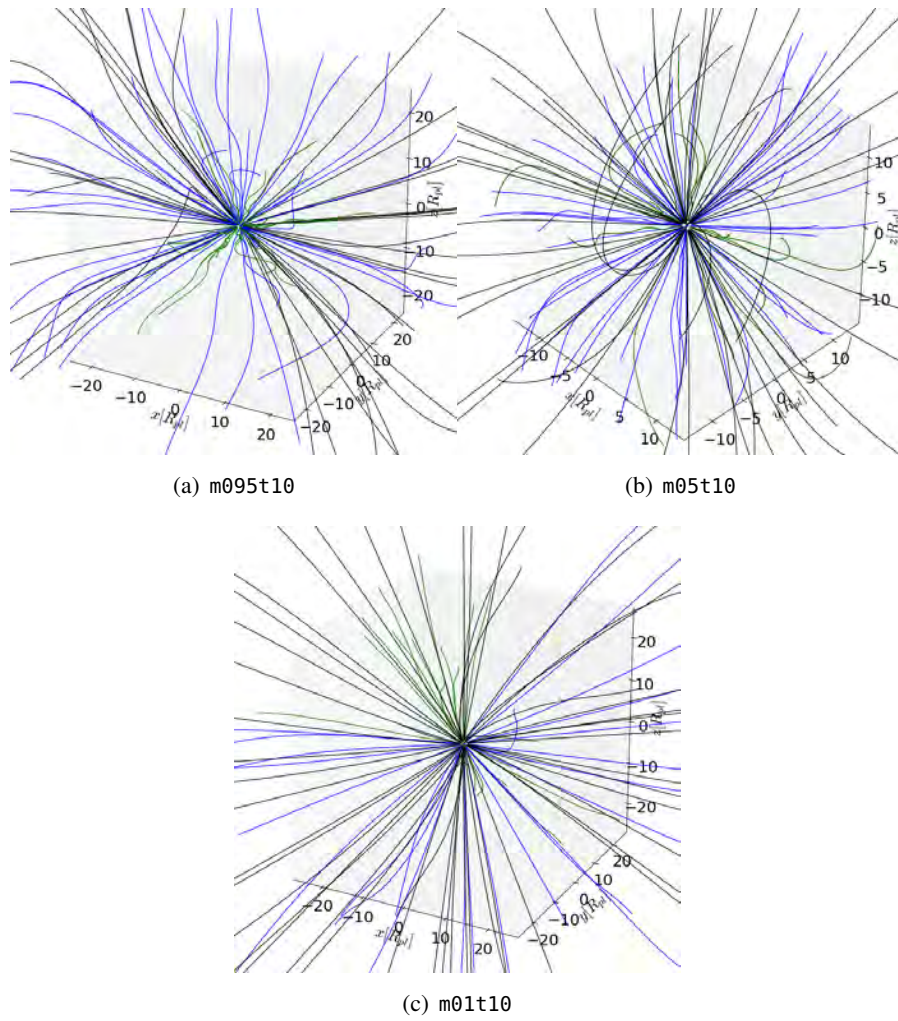
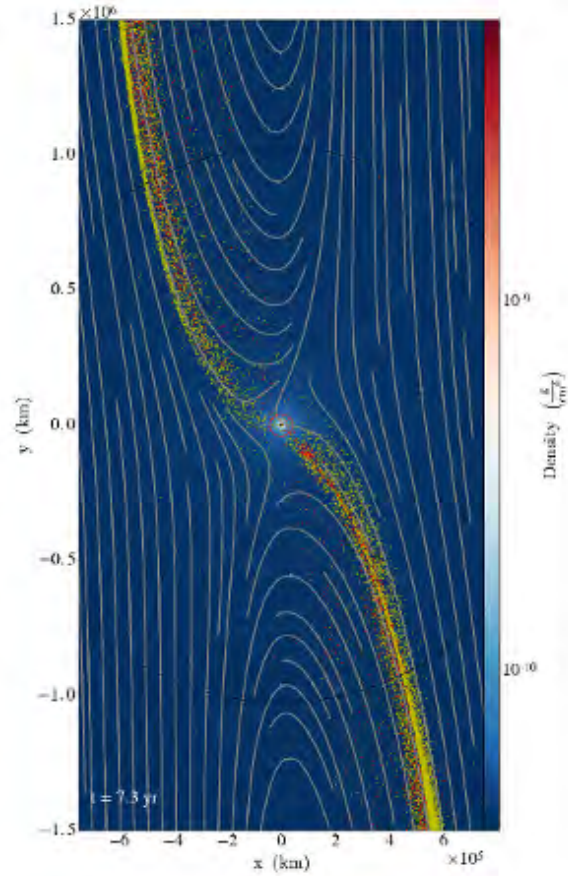
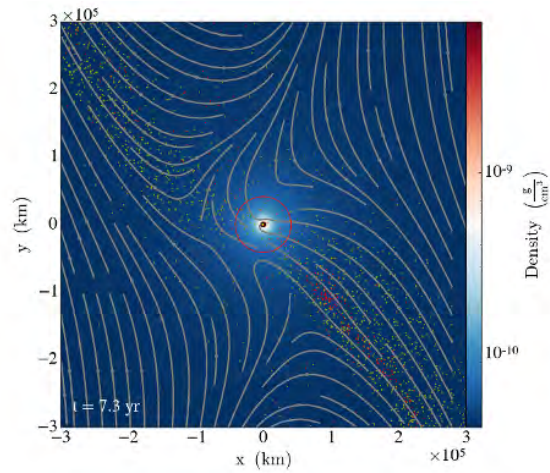


Figure 5.32: Trajectories of accreted particles. The axes are given in units of embryo radii. Green, blue and black paths are for particle sizes $0.001 \leq s < 0.01$ cm, $0.01 \leq s < 0.1$ cm, and $0.1 \leq s < 1$ cm, respectively.



(a) Particle distribution over a $2R_B$ vertical extent above/below the midplane. The black circle denotes the Hill sphere.



(b) A zoom-in of panel (a) to the Bondi sphere. The red circle denotes the Bondi sphere.

Figure 5.33: Gas density and pebble distribution close to the midplane in the `m01t00` run. The pebbles here are split into 3 size bins: yellow $s \leq 0.01$ cm, red $0.01 < s \leq 0.1$ cm and $s > 0.1$ cm are green.

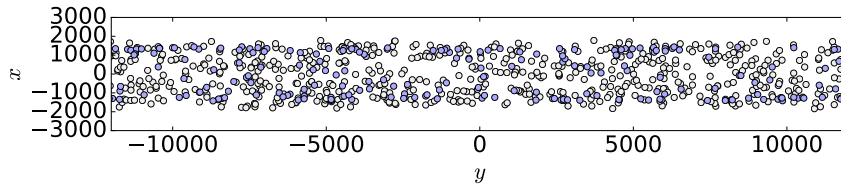
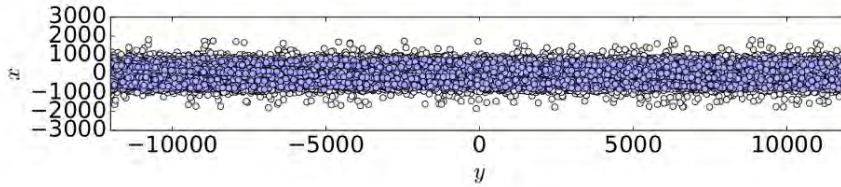
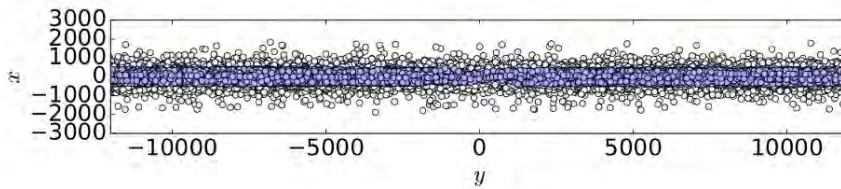
(a) $\Omega^{-1}=0.404$ (b) $\Omega^{-1}=1.21$ (c) $\Omega^{-1}=2.42$

Figure 5.34: Radial settling (in the x -direction) of particles at the midplane towards the pressure maximum at 1 AU. Grey particles have sizes < 8 cm, and blue particles have sizes ≥ 8 cm. $\Omega^{-1} = 0$ corresponds to the time of pebble injection.

settling of particles towards the pressure maximum at 1 AU. Since all the particles in the size distribution we consider have settling time scales longer than several orbits, to validate the radial settling behaviour, we additionally consider up to 10 cm size particles. Fig. 5.34 shows the radial settling of such particles. The grey colour-coded particles represent particles < 8 cm and the blue ones represent particles ≥ 8 cm. As can be seen, the largest particles settle towards the pressure maximum within several orbits, on a time scale consistent with Fig. 5.27.

5.5.3 Accretion of pebbles

When pebbles approach an embryo they are subject to an increasing two-body force and start to veer towards the embryo. Although from Fig. 5.32 it might seem that they come from all over the place, the figure greatly under-represents the particles (150 traces selected out of 15 000, again randomly selected from ≈ 2.6 million macro-particles), and the scales are concentrated to the closest 10-20 planetary radii around the embryos. The full ensemble of trace-particles (best visualised interactively) show distinct inflows and outflows through the Hill sphere.

Figures 5.35 to 5.37 shows the mass accretion rates across the Hill sphere, Bondi sphere and the embryo surface over the course of the m095t10 run, displayed as a set of Hammer projections. The macro-particles are sub-divided into 3 representative size-bins ($0.0 \leq s \leq 0.01$ cm, Fig. 5.35; $0.01 < s \leq 0.1$ cm, Fig. 5.36; and $0.1 < s \leq 1.0$ cm, Fig. 5.37). The figures show that the bulk of the net accretion comes from near the midplane, and predominantly from the large size particles. As they do not feel much gas drag, some of the largest particles can and do cross the Hill sphere from arbitrary directions. The dominating inflow regions are associated with the inner/trailing and outer/leading horseshoe orbits, and corresponding outflows in the outer/trailing and inner/leading horseshoe orbits. The accretion rates at distances R_B are much more isotropic, without clearly preferred trajectories. The modest outflows are mainly close to the polar regions and the inflows are slightly stronger closer to the midplane. Not all the mass accreted through the R_B sphere reaches the embryo surface during the time scales we consider here. The missing mass is contained in the smallest particles, which trace the gas flows very closely. Having even the slightest turbulence in the primordial atmosphere (which is always the case, as discussed earlier) traps these particles and prohibits them from reaching the surface over sufficiently small time scales. The Fig. 5.35 and Fig. 5.36 also show how inefficiently the subsets of smaller particles are accreted. Very similar trends are present in the other two embryo mass cases we consider in this work, therefore, the figures for $M = 0.5 M_\oplus$ and $M = 0.096 M_\oplus$ embryos are in the appendix 5.8.

Figures 5.53 to 5.55 similarly shows the mass accretion rates over the course of the m05t10 run. The accretion rates are about a factor of two lower than in the m095t10 case, and the preferred accretion paths through the Hill

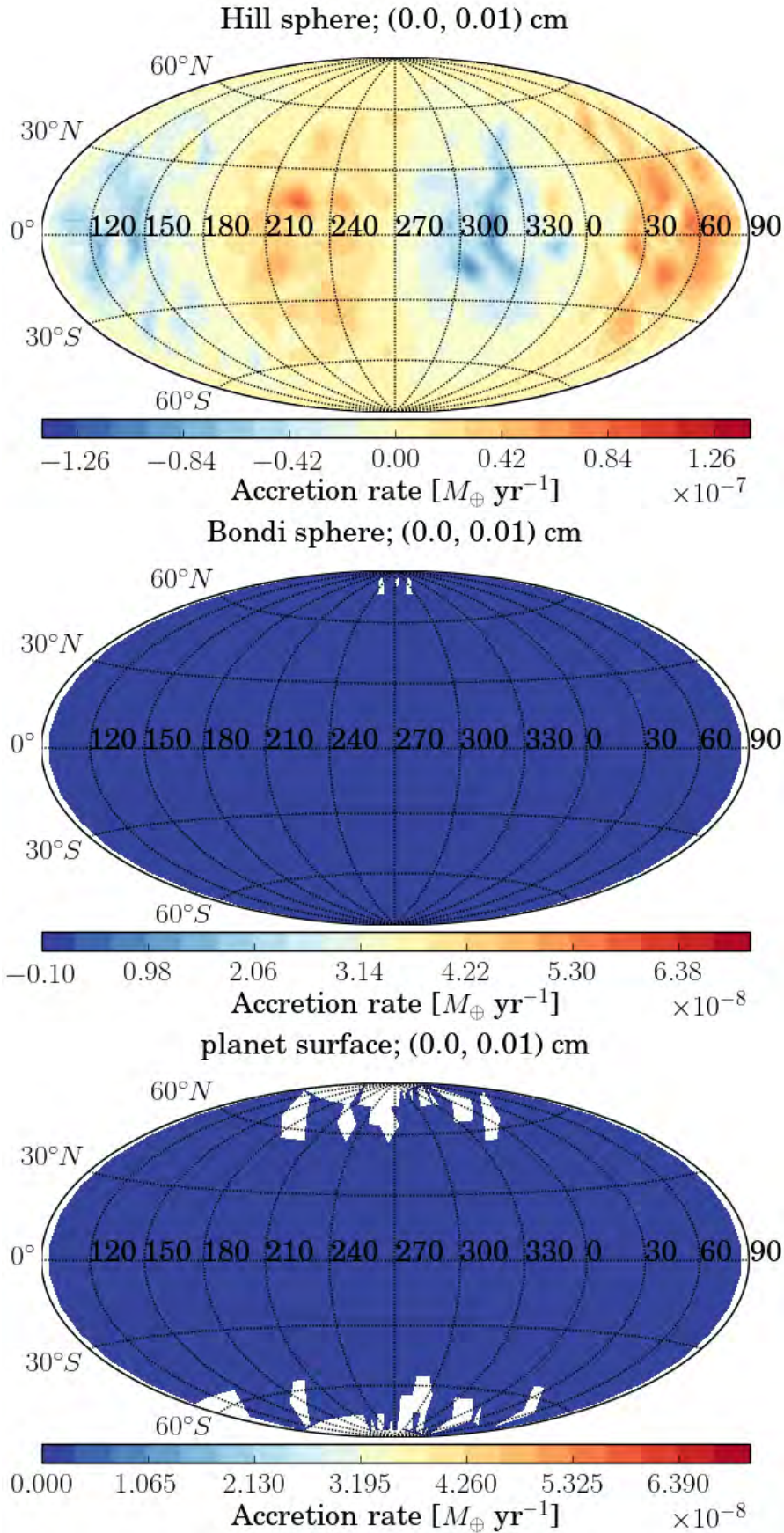


Figure 5.35: From top to bottom, the mass accretion rate of $0.0 \leq s \leq 0.01$ cm size particles across the Hill sphere, Bondi sphere and embryo surface, respectively, over the course of the m095t10 run, displayed as a Hammer projection. White regions indicates zero accretion; a longitude of 270° corresponds to the $-y$ -direction and a latitude of 0° corresponds to the disc midplane.

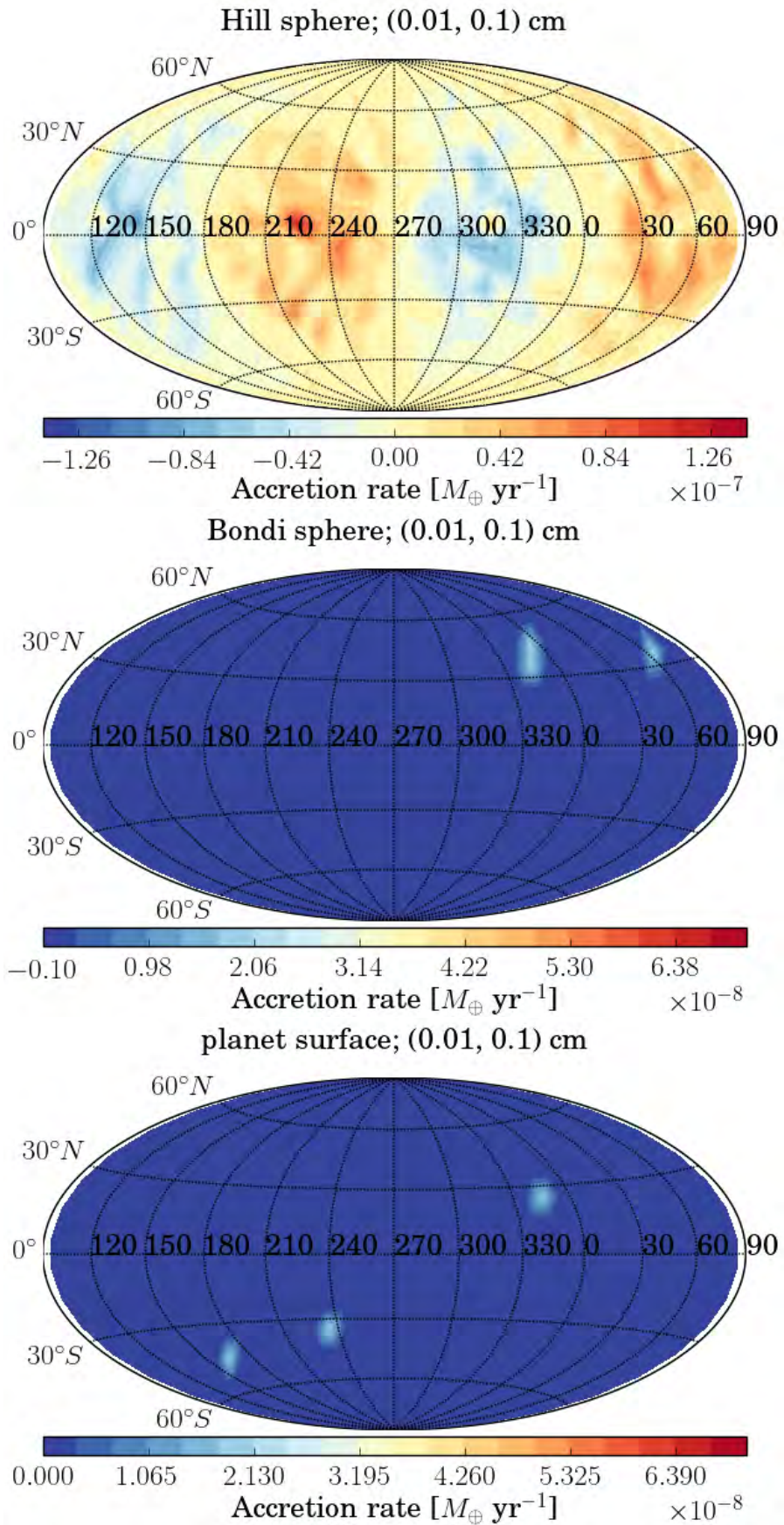


Figure 5.36: Same as Fig. 5.35, but of $0.01 < s \leq 0.1$ cm size particles.

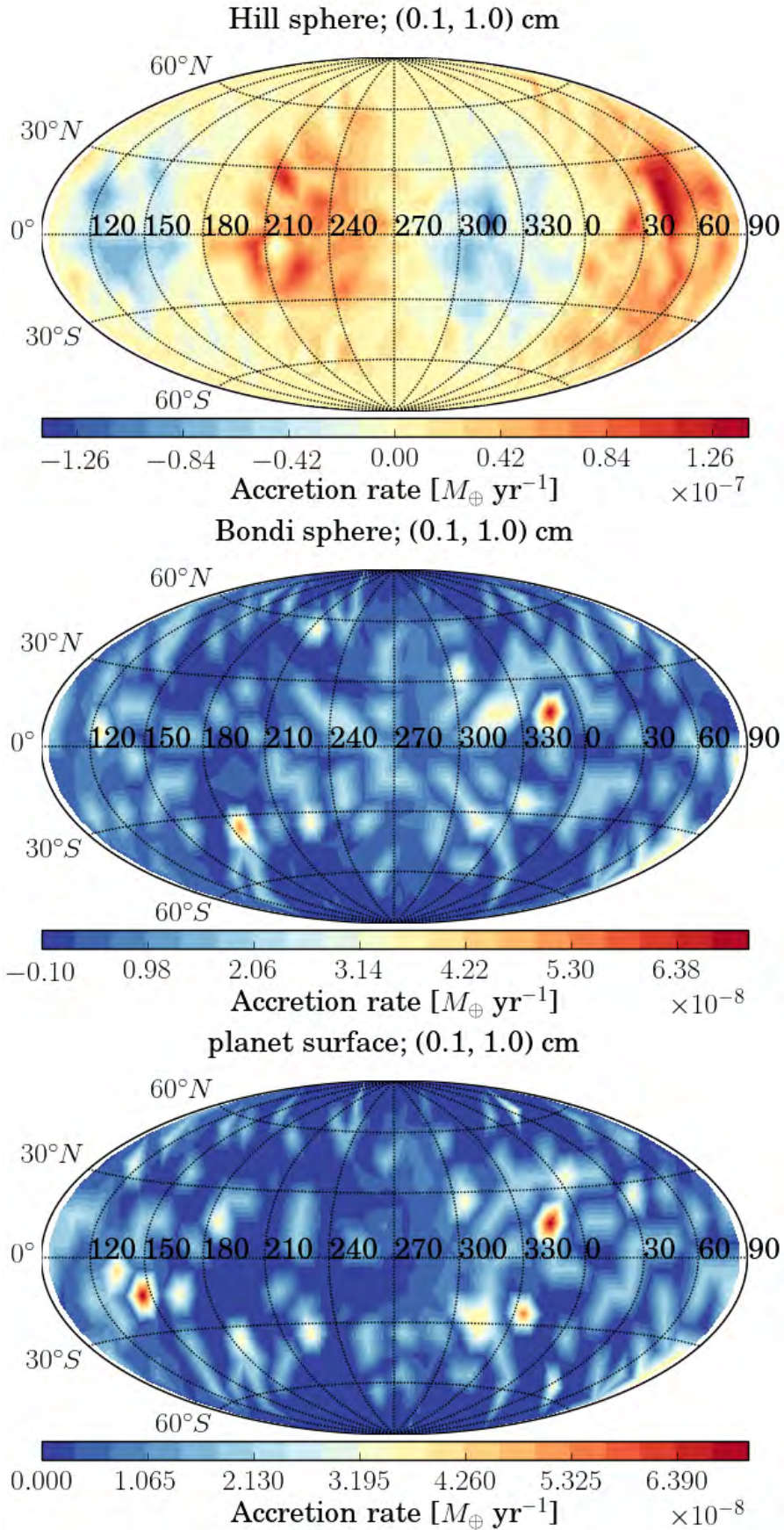


Figure 5.37: Same as Fig. 5.35, but of $0.0 \leq s \leq 0.01$ cm, $0.01 < s \leq 0.1$ cm and $0.1 < s \leq 1.0$ cm size particles.

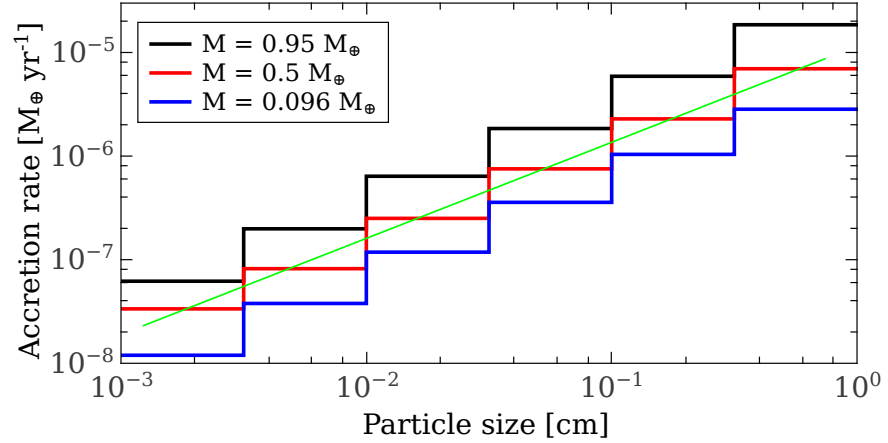


Figure 5.38: Pebble accretion rates, for particle sizes within each size bin, drawn from an initial distribution consisting of particles within $\pm R_H$ from the midplane, for the three embryo masses, $0.95 M_\oplus$ (black), $0.5 M_\oplus$ (red), and $0.096 M_\oplus$ (blue). The green line shows a mass accretion rate proportional to particle size, s .

sphere are once again closer to the midplane and the stagnation points (separators).

Lastly, Figures 5.56 to 5.58 shows the mass accretion rates over the course of the m01t10 run. Note that the contour levels are modified, in order to enhance the features. The simulation show a similar scenario to the cases with higher mass embryos, except the mass accretion rates are once again smaller. Also, there is nearly no mass flux leaving from the radius R_B . This is both because the R_B for such a small mass embryo is just 12.3 embryo radii, and because the atmosphere is too tenuous to stop the incoming particles.

5.5.4 Quantitative measurements of accretion rates

To allow selection of arbitrary sub-populations, our initial particle population is distributed all over space, with weights proportional to the local cell gas mass. To obtain accretion rates pertaining to a disk where particles have settled towards the midplane, we select the sub-population that initially resides within one Hill radius from the midplane, and subsequently measure accretion rates based on only those particles, renormalising their macro-particle weights w so they correspond to a total mass equal to the assumed dust-to-gas ratio (0.01) times the total gas mass in the experiment.

By sub-dividing the particle distribution into 6 size bins, we can study the dependency of the accretion rates on size. Fig. 5.38 shows that the net accretion rate onto the embryo scales linearly with the size s , as opposed to the $s^{2/3}$ scaling predicted by Lambrechts & Johansen (2012). The linear scaling is valid even for larger particles, all the way to dm-sized particles, as illustrated in Fig. 5.39. The accretion rate saturates (no longer increases with particle size) for particles larger than about 1 meter.

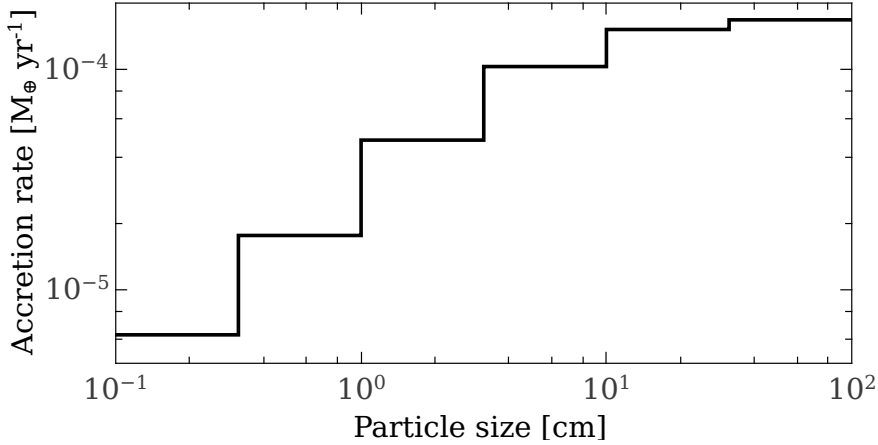


Figure 5.39: Pebble and boulder accretion rates, for particle sizes between 0.1 - 100 cm, subdivided into 6 size bins, drawn from an initial distribution consisting of particles within $\pm R_H$ of the midplane for the $0.95 M_{\oplus}$ embryo mass.

The runs with 56 million macro-particles gives similar results as the corresponding runs with 2.6 million particles, with less than 10% difference in the accretion rates through the Hill sphere and less than 1% difference at the Bondi sphere. Thus the results are rather robust, even when using only 2.6 million macro-particles. However, the larger the particle population, the smaller a fraction of it one can use, while still retaining statistical significance. The $M = 0.95 M_{\oplus}$ case, for example, initially has only about 20% of the macro-particles within one Hill radius of the midplane. Thus, to study midplane accretion rates it is useful to have a large particle population available.

An estimate of the maximum accretion rate may be obtained by taking the dust-to-gas ratio times the average gas mass flux through the Hill sphere. For our $M = 0.95 M_{\oplus}$ embryo immersed in our 1/10 MMSN disk this flux is $\approx 4 \cdot 10^{-3} M_{\oplus} \text{ yr}^{-1}$. With a dust-to-gas ratios of 0.01, we thus estimate a maximum accretion rate of about $4 \cdot 10^{-5} M_{\oplus} \text{ yr}^{-1}$. This rate is exceeded by about a factor of five in the 0.3 – 1 m size bin in Fig. 5.39. By comparison, the ‘Hill rate’ $\Sigma_p \Omega R_H^2$ is $3.9 \cdot 10^{-3} M_{\oplus} \text{ yr}^{-1}$, nearly identical to the actual, 3-D gas mass flux. Fig. 5.40 illustrates the efficiency of accretion of particles across a particular sphere (net accretion through a sphere normalised by the inward solid mass flux through the same sphere) in the m095t10 simulation. Evidently, a large fraction of all the particles, entering the Hill sphere leaves again without being accreted. The efficiency rapidly grows for smaller radial distances, and at $\sim 30R_p$ the efficiency is nearly perfect, except for particle sizes below 0.003 cm, which are still very well coupled to the gas there.

We do not see significant systematic differences when different pressure bump parameters ζ_p are used for the same mass embryo. This is to be expected, since the results will only change when the radial settling has become significant. One would expect on the one hand a tendency for reduction of the accretion rates, because of the smaller y -velocities closer to the orbital radius of the embryo, and on the other hand a tendency for increase, due to

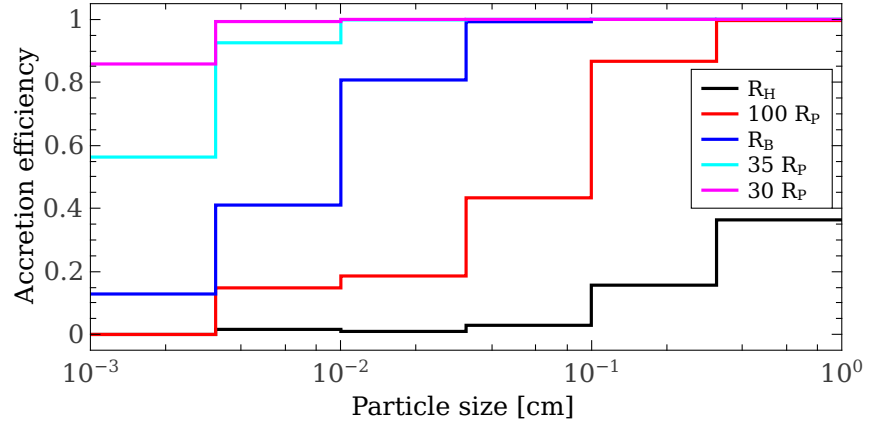


Figure 5.40: Pebble accretion efficiency (net accretion rate divided by total mass flux across a sphere of a particular radius) as a function of particle size, drawn from an initial distribution of particles within $\pm R_H$ of the mid-plane for the m095t10 run.

the accumulation of large size particles. Ultimately, the accretion rates would be constrained by the radial influx of particles from larger orbital radii into the pressure trap.

5.6 ACCRETION DRIVEN CONVECTION

The high resolution close to the embryo surfaces enables us to resolve convection driven by accretion heating. Accretion of solids onto the embryo releases a lot of potential energy, which is converted to heat via the friction force. To simulate the effects of the heating due to the accretion, we added an extra heating term Q_{accr} to one of our simulations, m095t10-conv. Considering a shell of extent dr at some distance r from the embryo, the volume $dV = A dr$, where $A = 4\pi r^2$, then has a potential energy difference (which is per unit mass) given by $\Phi(r + dr) - \Phi(r)$. To get an energy per unit volume we need to multiply with the mass accreted per unit time:

$$Q_{\text{accr}} = \frac{\dot{M} G M_p}{4\pi r^4}, \quad (5.31)$$

where Q_{accr} is the heating rate per unit volume and \dot{M} is the mass accretion rate (which we set to $10^{-6} M_{\oplus} \text{ yr}^{-1}$). The heating rate, Q_{accr} , is then added to the entropy equation (Eq. 5.4) via:

$$\frac{\partial s}{\partial t} = \dots + \frac{\rho Q_{\text{accr}}}{P_{\text{gas}}}. \quad (5.32)$$

Figures 5.41 and 5.42 illustrates the consequences of the addition of the accretion heating term in the m095t10-conv run. It shows extensive convective patterns, which considerably modify the gas flows around the embryo (Fig. 5.41). The horseshoe orbits have somewhat receded, and the weak random flows that appear in non-convective runs are effectively overwhelmed by the

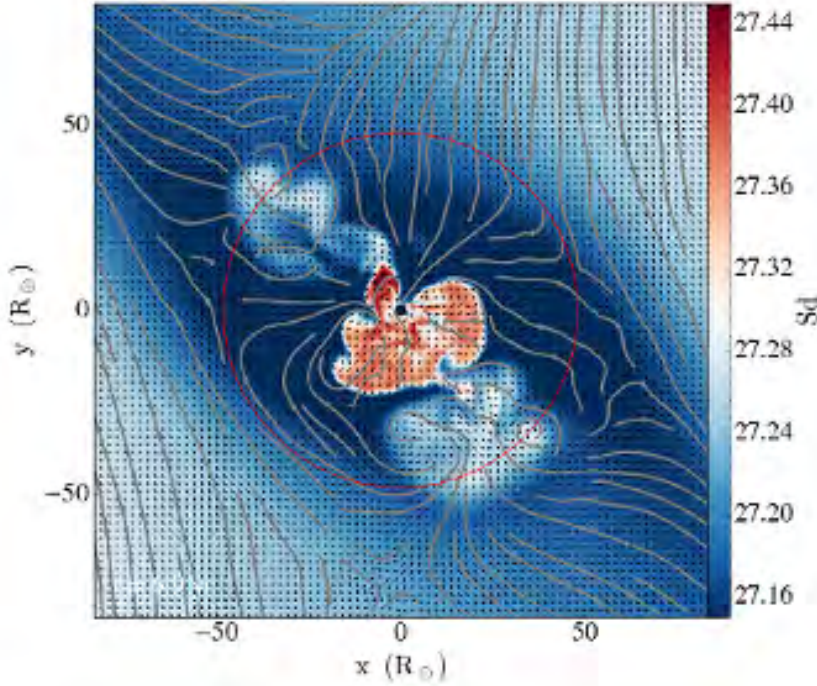


Figure 5.41: xy slice in the midplane of the entropy per unit mass in the vicinity of the core in a single snapshot of accretion driven convection in the m095t10-conv run.

much stronger convective flow patterns. The Fig. 5.42 shows a vertical projection of the convective motions, which extend out to nearly 40 embryo radii. The vicinity of the embryo is no longer in a quasi steady state - the gas flow patterns constantly change, and the interconnection between the primordial atmosphere and the disk is thus strengthened; i.e., no parts of the atmosphere are effectively isolated. The convection is very dynamic, with local velocities reaching $\sim 1 \text{ km s}^{-1}$, inducing sound waves when the convective cells reach the outskirts of the atmosphere. The direction of the outflows are constantly changing and now lack any significant constant patterns, but do have an approximately isotropic distribution of the velocity dispersion.

When we see or model convection at a stellar surface (e.g. in the form of ‘granulation’ on the Sun), the cellular patterns that develop are very much constrained by conservation of mass. In a stratification where mass density drops very rapidly with height, mass conservation forces the flows to “turn over”, from up to down, which again forces the horizontal size to be limited (lest the ratio of horizontal to vertical speed become very large). Here, we have a situation that is quite different, with a “small” body at the centre of a large spherical volume. This situation allows the flows much greater freedom, with a possibility of expansion in all directions.

The heating driving the convection in this study, computed assuming $\dot{M} = 10^{-6} M_{\oplus} \text{ yr}^{-1}$, is not consistent with the actual, about 20 times larger measured accretion rates (e.g. Fig. 5.38). Moreover, radiative energy transfer and

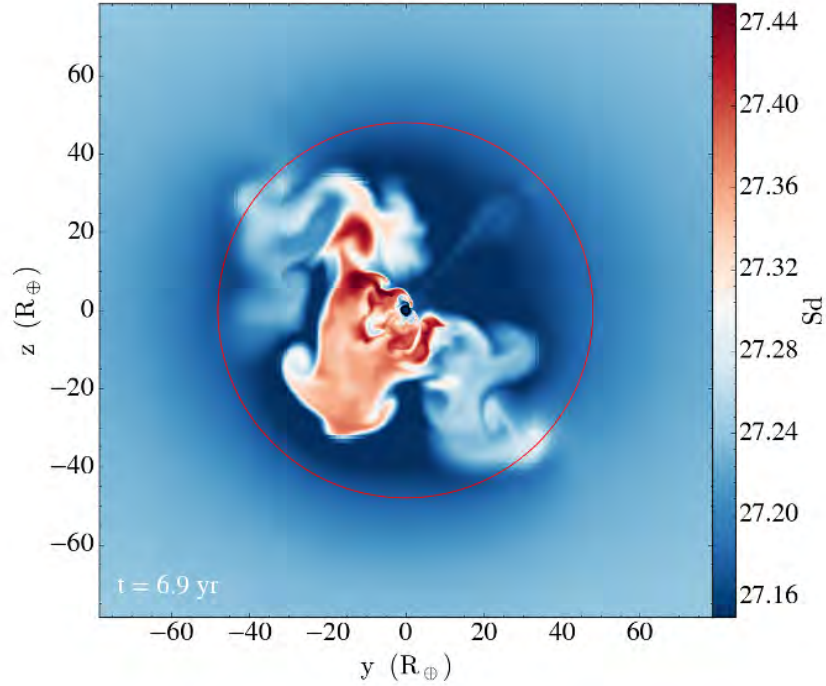


Figure 5.42: yz slice at $x = 0$ of the entropy per unit mass in the vicinity of the core in a single snapshot of accretion driven convection in the $m095t10$ -conv run. For clarity, the gas streamlines are omitted.

a more realistic EOS would tend to change the properties of convection, so to reach true consistency, improvements are necessary. Nevertheless, it is possible to learn already from the current experiment, which can illustrate to what extent the convective motions are able to affect accretion rates relative to an analogous non-convective case.

The Fig. 5.43 shows a small subset of high cadence paths for accreted particles, colour coded by size. Although their paths are affected, the largest particles are not significantly stirred up by the convective motions. The smaller the particles are, however, the more they are affected by the convective motions. Quantitative measurements show that the average of the unsigned mass fluxes through spherical surfaces where convection is active is much larger than in the non-convective case.

However, as illustrated in Fig. 5.44, we find that convection in the current case does not significantly reduce the net accretion rates. Formally, the accretion efficiency (the net accretion rate as a fraction of the unsigned solid mass flux) is reduced significantly for the smallest subset of particles, but this only reflects larger fluctuations in the solid mass flux (Fig. 5.45). The convective velocities in this case are generally on the order of the free fall drift velocities of the particles, as illustrated in Fig. 5.46, but the systematic drift of particles relative to the gas continues, and since the convective motions do not result in a net transport of mass, their effect on the particle drift is a second-order

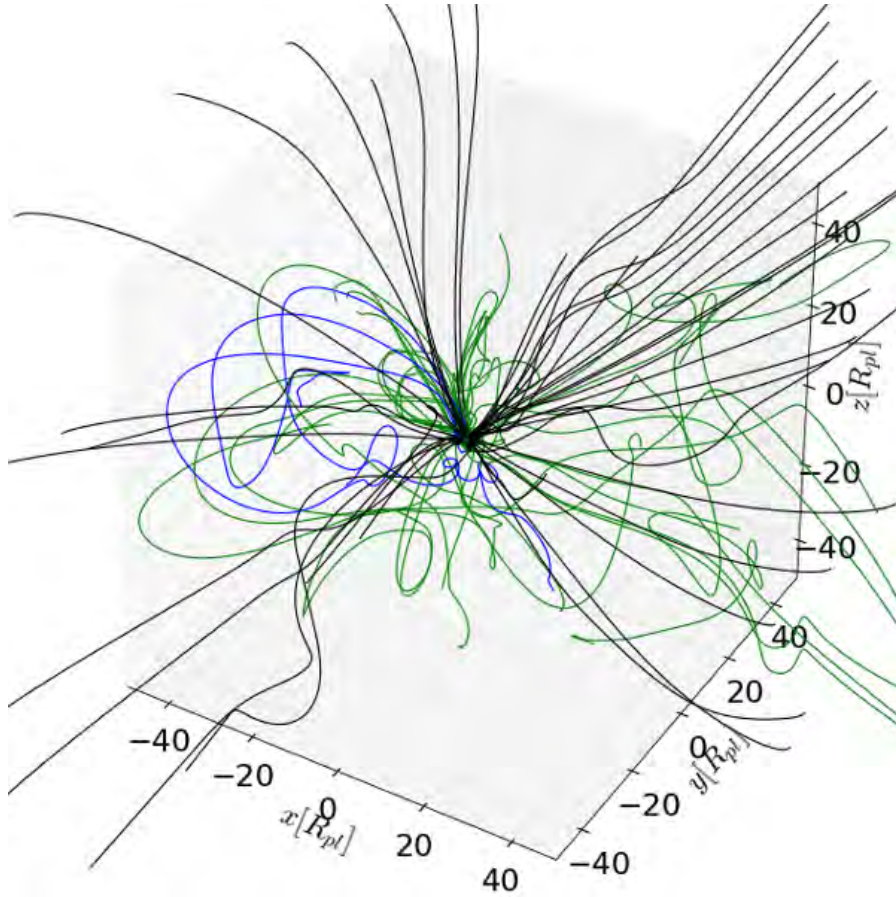


Figure 5.43: Particle paths in the vicinity of the core. Black curves show traces for particles of size $0.1 < s \leq 1$ cm, blue $0.01 < s \leq 0.1$ and green $0.001 < s \leq 0.01$ cm, respectively.

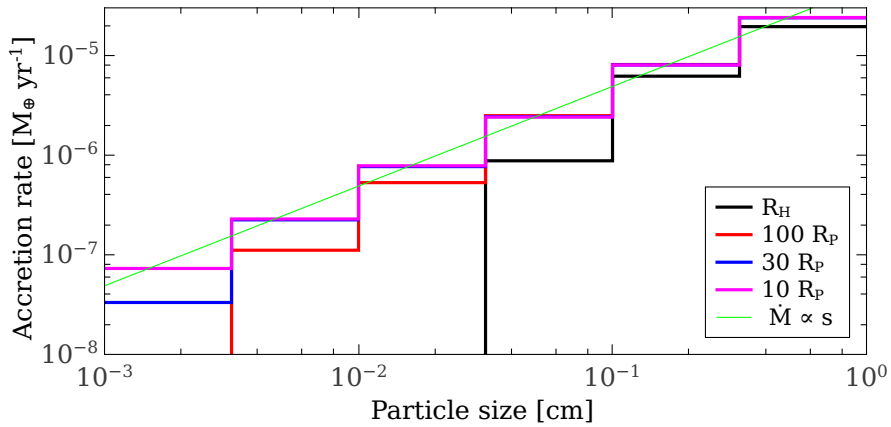


Figure 5.44: Pebble accretion rates when accretion driven convection (m095t10-conv run) is considered. Particle sizes are split into 6 representative logarithmic size bins. The green line shows a mass accretion rate proportional to particle size, s .

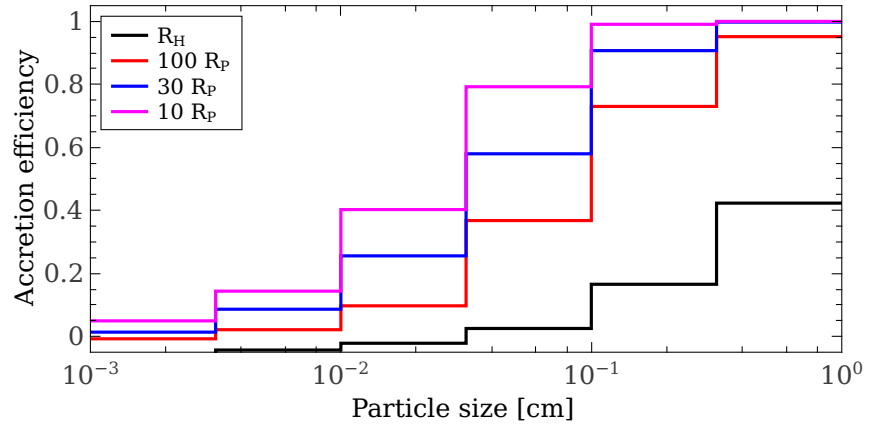


Figure 5.45: Pebble accretion efficiency when accretion driven convection is considered (m095t10-conv). Particle sizes are split into 6 representative logarithmic size bins.

effect. It is possible, however, that this could change if the convective motions were sufficiently resolved and included more turbulent, small-scale motions.

The effect on the particle accretion rate is also likely to increase, and possibly become quite significant, when accretion heating is included self-consistently by including radiative energy transfer and a realistic EOS. The resulting, self-consistent accretion rates are likely to be lower than the current values, but the convective motions are likely to be stronger than in our current, nominal case.

5.7 SUMMARY AND CONCLUSIONS

In this paper, we have reported the results from high resolution, nested, 3D hydrodynamic and particle simulations which focus on solid accretion onto Mars- to Earth-mass planetary embryos. The primary goals of this work were to establish realistic three-dimensional flow patterns inside and outside the Hill sphere, to use these to determine accurate accretion rates, and to investigate how the accretion rates depend on embryo mass, pebble size, and other factors.

Our excellent spatial resolution and efficient time integration, using locally determined time steps, made it possible—using only a single, 20-core compute node per run—to perform the first-ever simulations of pebble accretion covering scales from several disk scale heights to a few percent of a planet radius, including atmospheres that self-consistently connect to a surrounding accretion disk. It is also the first time that accretion heating driven convection has been modelled in a domain with such a large dynamic range.

We conducted a series of simulations with different planetary embryo masses and strengths of a pressure trap. To be able to accurately measure accretion rates, and to study how they are affected by convection, we injected millions of macro-particles with representative sizes ranging from 10 micron to 1 m. The motion of the particles were followed, taking into account drag forces

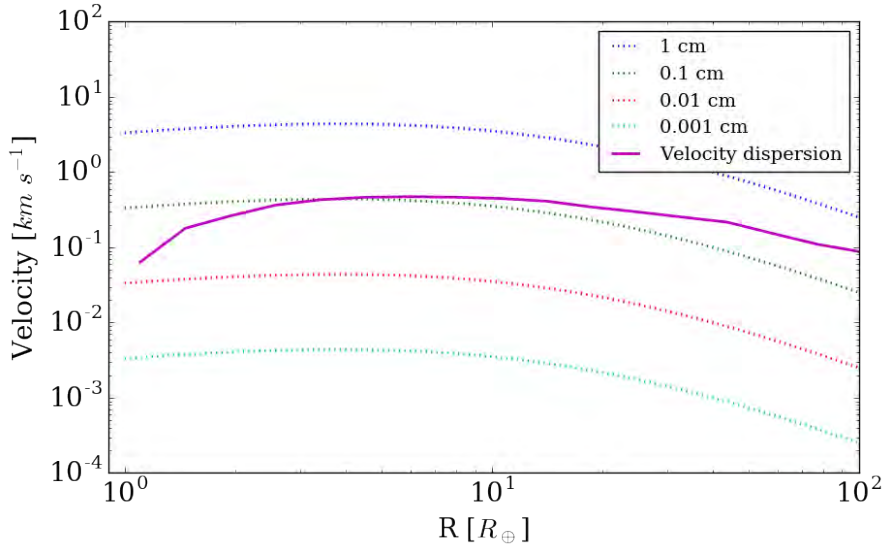


Figure 5.46: Free fall drag velocities of particles of size 1 cm (blue), 0.1 cm (green), 0.01 cm (red) and 0.001 cm (cyan). The velocity dispersion of the m095t10-conv run is shown in magenta.

relative to the gas, while feedback from the particle ensemble on the gas was neglected—consistent with the modest dust-to-gas ratios occurring in the models. The motions of a subset of particles were recorded in great detail, allowing 3D visualisations of particle paths.

Our main results may be summarized as follows:

1. Starting from approximately hydrostatic initial conditions, relaxation periods on the order of one orbit are sufficient to establish near quasi-stationary conditions in the vicinity of the Hill sphere.
2. The relaxed atmospheric structures do not differ dramatically from spherically symmetric hydrostatic atmospheres matched to surrounding disk conditions at the Hill radius.
3. Adiabatic and hydrostatic atmospheres with an ideal gas and $\gamma = 1.4$ do not differ substantially from atmospheres computed with a more realistic, tabular EOS (Tomida & Hori, 2016).
4. The presence of convection changes conditions well inside the Hill sphere from near-steady flows to dynamically evolving flows, albeit stationary statistics (e.g. velocity dispersion as a function of radius) develop in less than an orbital period.
5. The convective motions result in an enhanced mass exchange between different layers inside the Hill sphere, but do not significantly affect the mass exchange through the Hill sphere with the surroundings, nor do they affect the net accretion rates significantly.
6. In our fiducial 1/10 MMSN model, the (unsigned) gas mass flux through the Hill sphere for our 3D horseshoe flows is about $4 \cdot 10^{-3} M_{\oplus} \text{yr}^{-1}$, and

thus agrees closely with the canonical ‘‘Hill rate’’, $\Sigma\Omega R_H^2 = 3.9 \cdot 10^{-3} M_\oplus \text{yr}^{-1}$ (obtained assuming $\Sigma = 170 \text{ g cm}^{-2}$ and $R_H/R_\oplus = 231$).

7. The gas mass flux, scaled with the dust-to-gas ratio, is reflected in similar rates of particles passing both in and out of the Hill sphere, with inflow increasingly dominate for increasing particle size.
8. As illustrated by Figs. 5.33 and 5.35 to 5.37, the particles that are not accreted and leave the Hill sphere have preferred paths along the separators of the horseshoe flow and are concentrated towards the midplane.
9. In contrast, at the canonical Bondi sphere, the particle fluxes are mainly inward (except for the smallest particle sizes), and hence changes in the detailed structure of the layers close to the embryo (e.g. due to the EOS, including from evaporation of pebbles) are not important for the final accretion rates.
10. The accretion rates for different size particles scale linearly with particle size, in contrast to the 2/3 power scaling argued for by Lambrechts & Johansen (2012) and adopted in Lambrechts & Johansen (2014).
11. We find that the accretion rate of 0.3 – 1 cm particles for an $0.95 M_\oplus$ embryo immersed in a 1/10 MMSN disk, assuming a dust-to-gas ratio of 0.01 and assuming that the dust has settled to a midplane layer with height $H < R_H$, is about $2 \cdot 10^{-5} M_\oplus \text{yr}^{-1}$. Since the accretion rates scale essentially linearly with particle size and inversely with gas density, the accretion rate for the same size particles would be essentially the same in higher density disks; the larger supply of solids in a denser disk will tend to be cancelled by a correspondingly slower accretion speed.
12. For our 1/10 MMSN solar mass disk, the accretion rate saturates (no longer increases with particles size) for particles larger than about 1 m, while for denser disks the particles can be even larger. Thus, only for such large particle sizes will the accretion rates onto an embryo increase with the disk surface density. Conversely, if mm-size pebbles dominate the mass budget, the accretion rates depend only weakly on the disk surface density.

Having such a high spatial resolution means that we could only cover a limited parameter space and run the simulations for a relatively small number of orbital periods. We have also relied on an ideal gas EOS, while in reality the high temperatures near the embryo surface would lead to the dissociation of molecular hydrogen (e.g. D’Angelo & Bodenheimer 2013), and therefore result in a much denser and somewhat cooler inner atmosphere. This would not significantly alter the accretion efficiency of the larger particles, however, as these effects occur at small radii from which these particles are not able to escape.

Given the accretion rates we have determined above, we can estimate the growth time scales from low mass seeds to full planets, under the specified

conditions (i.e. a gas surface density of 170 g cm^{-3} , a dust-to-gas ratio of 0.01, and solids from within $H < R_H$). As per the results discussed above, to lowest order, the effects of disk density on mass supply and accretion speed cancel. The remaining dominant scaling is the dependence on embryo mass, which is approximately $M^{2/3}$, corresponding to a mass that grows approximately as t^3 . This implies that, as long as this approximate scaling persists, growth from a small seed takes on the order of three times the instantaneous mass divided by the instantaneous accretion rate.

We conclude that if growth from low mass embryos to full size planets is dominated by accretion of 0.3 – 1 cm size particles, the accretion from a low mass seed would have taken of the order of 0.15 million years in the case of Earth, and of the order of 0.1 million years in the case of Mars. With chondrule size particles—if we take them to be 0.3-1 mm—the growth times are 10 times longer. These estimates assume a local ratio of dust-to-gas surface densities of 0.01. Increased dust-to-gas ratios, e.g., due to radial accumulation of solids in a pressure trap, would lead to correspondingly reduced accretion times.

During the growth phase, embryos would inevitably be surrounded by hot, primordial atmospheres of much larger mass than the current day atmospheres of the rocky Solar System planets. The decrease in disk densities required to stop pebble accretion would also result in removal of much of the primordial atmosphere as it expanded to match the decreasing pressure at its outer boundary (Nordlund, 2011; Schlichting et al., 2015; Ginzburg et al., 2016). The isotopic signatures present in noble gases in the Earth’s atmosphere may provide indirect evidence related to this (Pepin, 1991, 1992a,b).

A decrease in gas and dust densities will lead to increased rates of radiative cooling, at first dominated by cooling in the vertical direction. The consequential, gradual flattening of the hydrostatic structure inside the Hill sphere could lead to the formation of a circumplanetary disk with prograde rotation (cf. Johansen & Lacerda, 2010). In order to model such an evolution, it is crucial to realistically include the major sources of heating, energy transport, and cooling: Accretion heating, the resulting convection, and radiative cooling while also using a realistic EOS (e.g. Tomida et al. 2013; cf. Fig. 5.1) and opacities.

To this end, we are currently conducting simulations that include these effects. In the future, we will also model the accretion heating in a manner consistent with the solid accretion rate (cf. Sect. 5.6) and include pebble destruction via ablation (e.g. Brouwers et al. 2017; Alibert 2017).

ACKNOWLEDGEMENTS

The work of AP and ÅN was supported by grant 1323-00199B from the Danish Council for Independent Research (DFF). CWO is supported by the Netherlands Organization for Scientific Research (NWO; VIDI project 639.042.422). The Centre for Star and Planet Formation is funded by the Danish National Research Foundation (DNRF97). Storage and computing resources at the University of Copenhagen HPC centre, funded in part by Villum Fonden

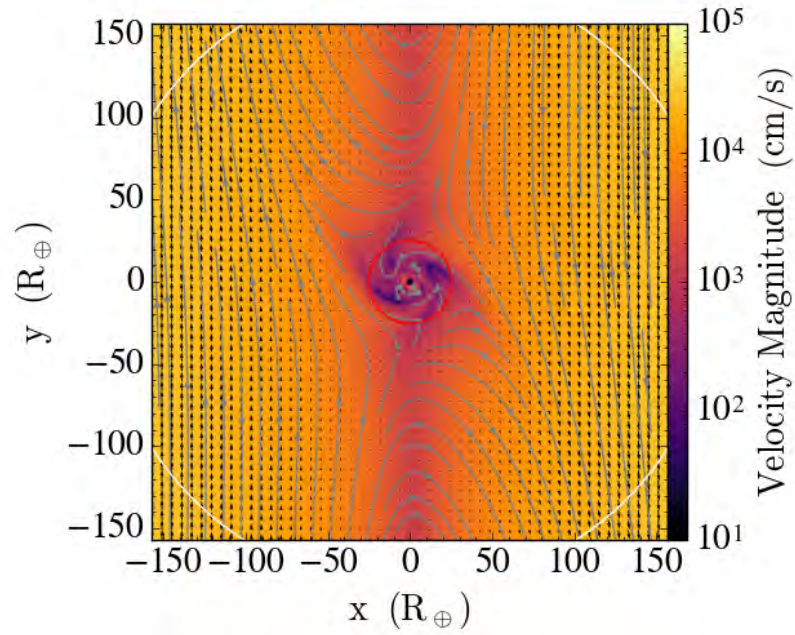


Figure 5.47: Same as in Fig. 5.6, but for the $M=0.5 M_{\oplus}$ embryo from the m05t00 run.

(VKR023406), were used to carry out the simulations presented here. The authors are grateful to Kengo Tomida and Yasunori Hori, who kindly provided the tabular EOS. AP is grateful to the Anton Pannekoek Institute at the University of Amsterdam for a three month stay during which part of this work was carried out. This research made use of the YT project for analysis and visualisation (Turk et al., 2011).

5.8 ADDITIONAL FIGURES

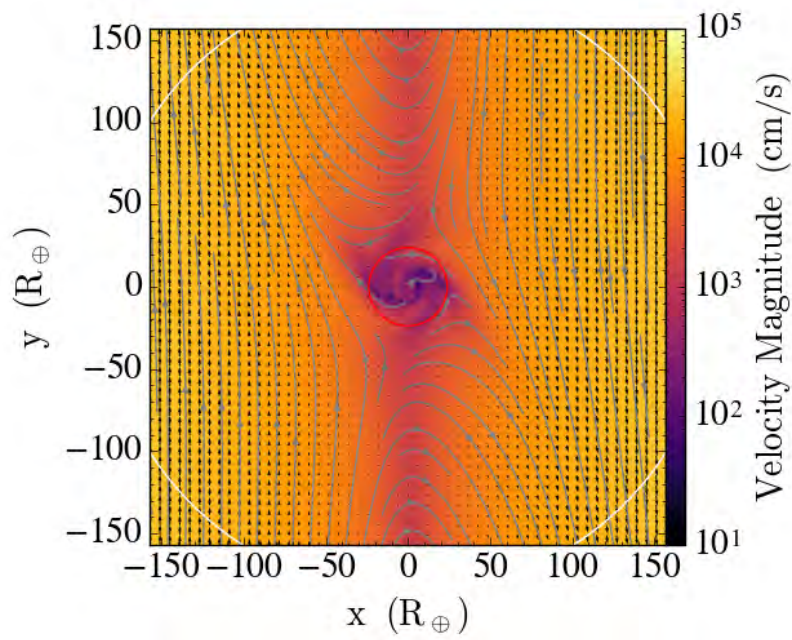


Figure 5.48: Same as in Fig. 5.7, but for the $M=0.5 M_{\oplus}$ embryo from the m05t00 run.

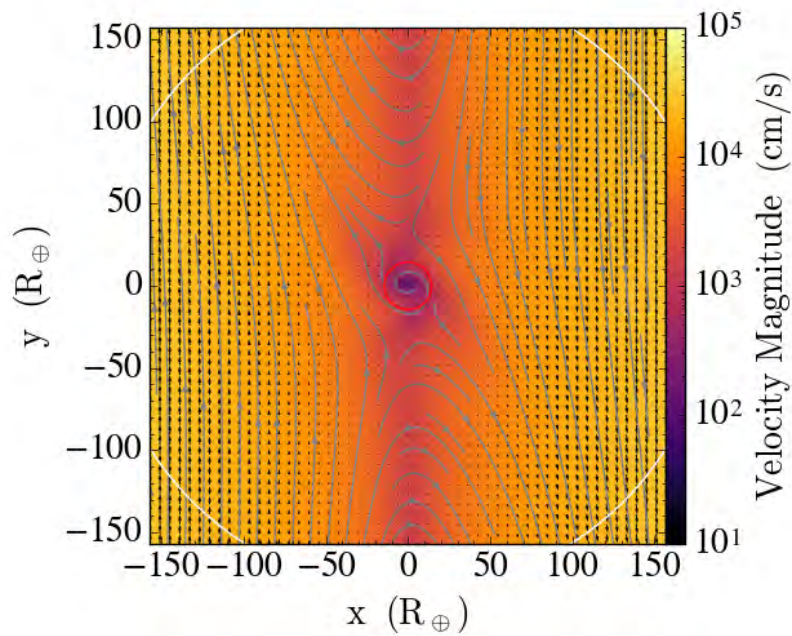


Figure 5.49: Same as in Fig. 5.8, but for the $M=0.5 M_{\oplus}$ embryo from the m05t00 run.

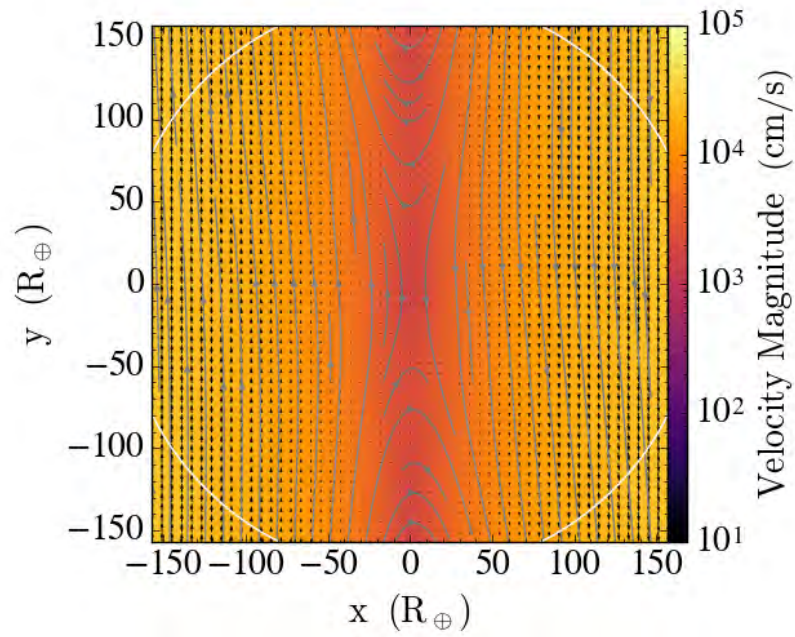


Figure 5.50: Same as in Fig. 5.9, but for the $M=0.5 M_{\oplus}$ embryo from the m05t00 run.

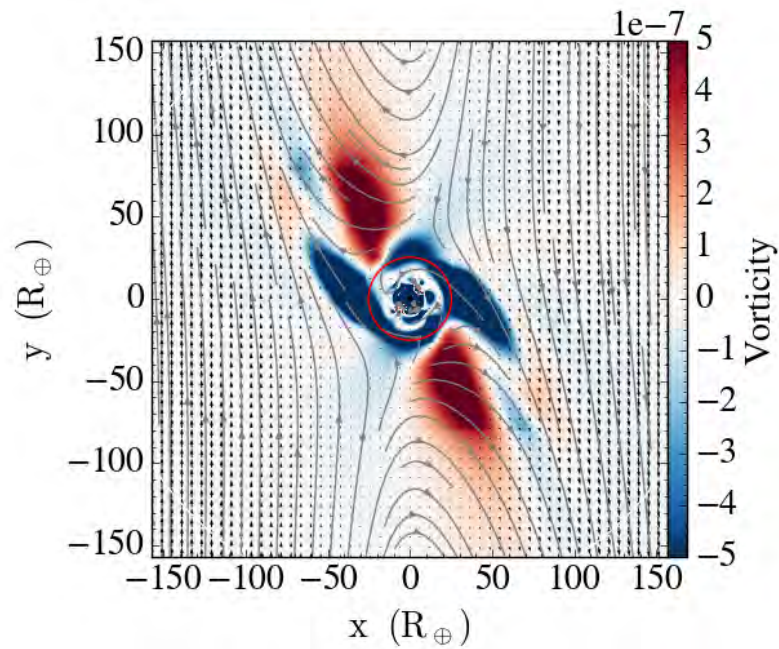


Figure 5.51: Same as in Fig. 5.10, but for the $M=0.5 M_{\oplus}$ embryo from the m05t00 run.

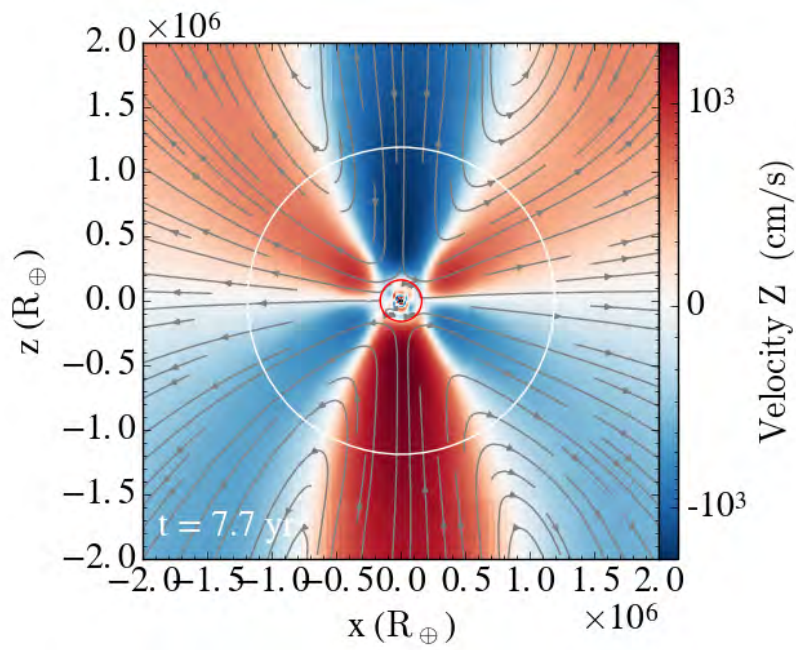


Figure 5.52: Same as in Fig. 5.11, but for the $M=0.5 M_{\oplus}$ embryo from the m05t00 run.

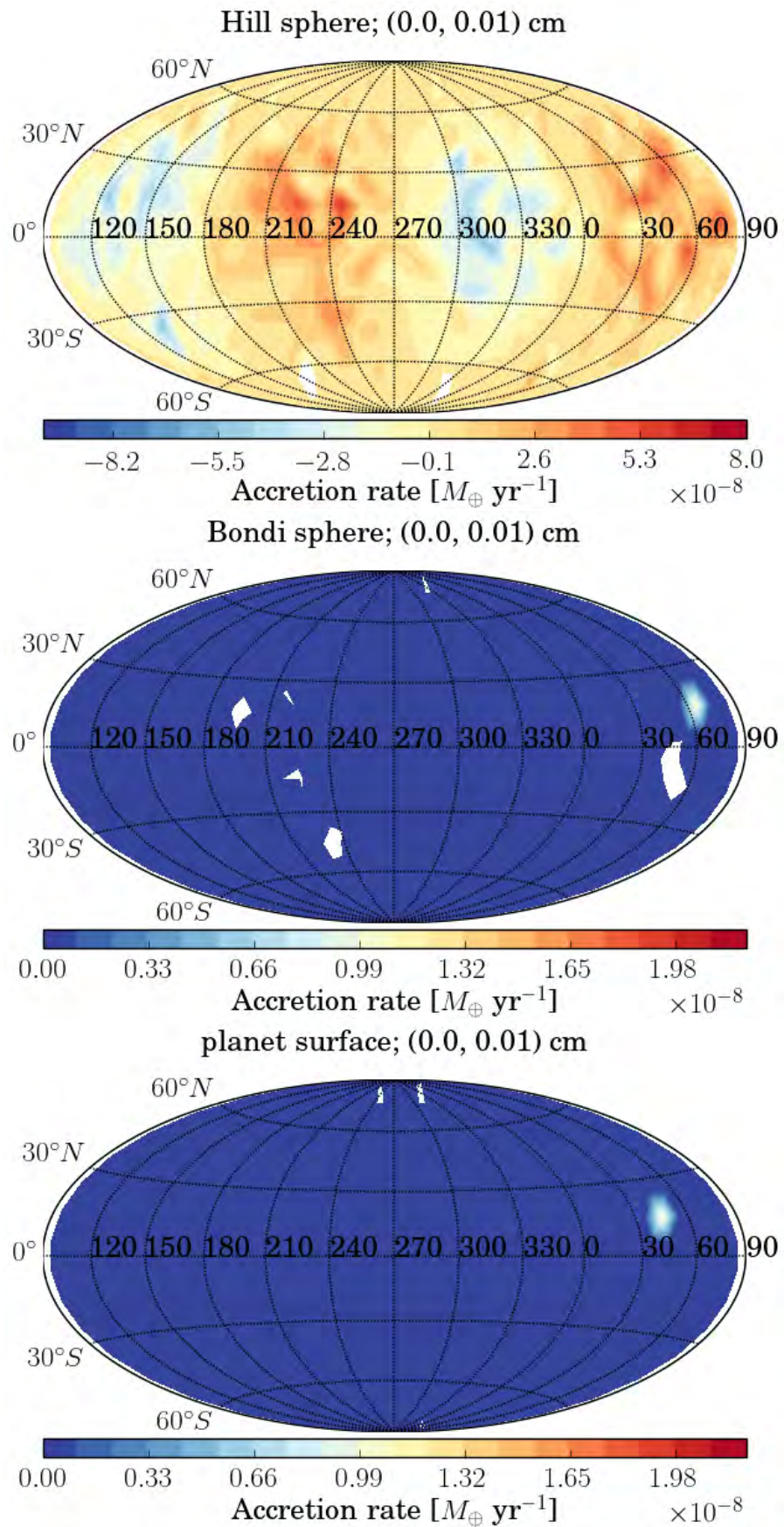


Figure 5.53: Same as Fig. 5.35, but for the m05t10 run.

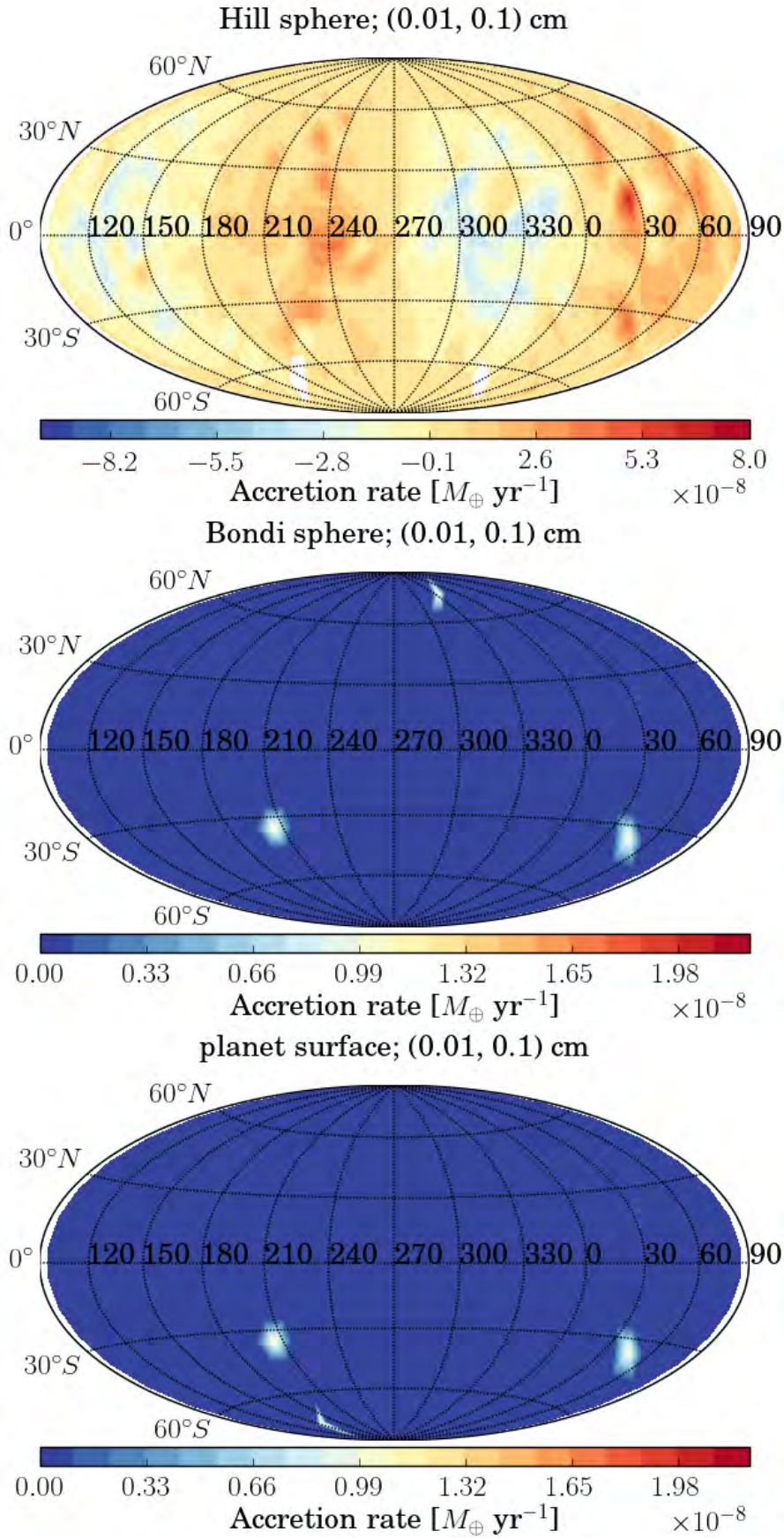


Figure 5.54: Same as Fig. 5.36, but for the m05t10 run.

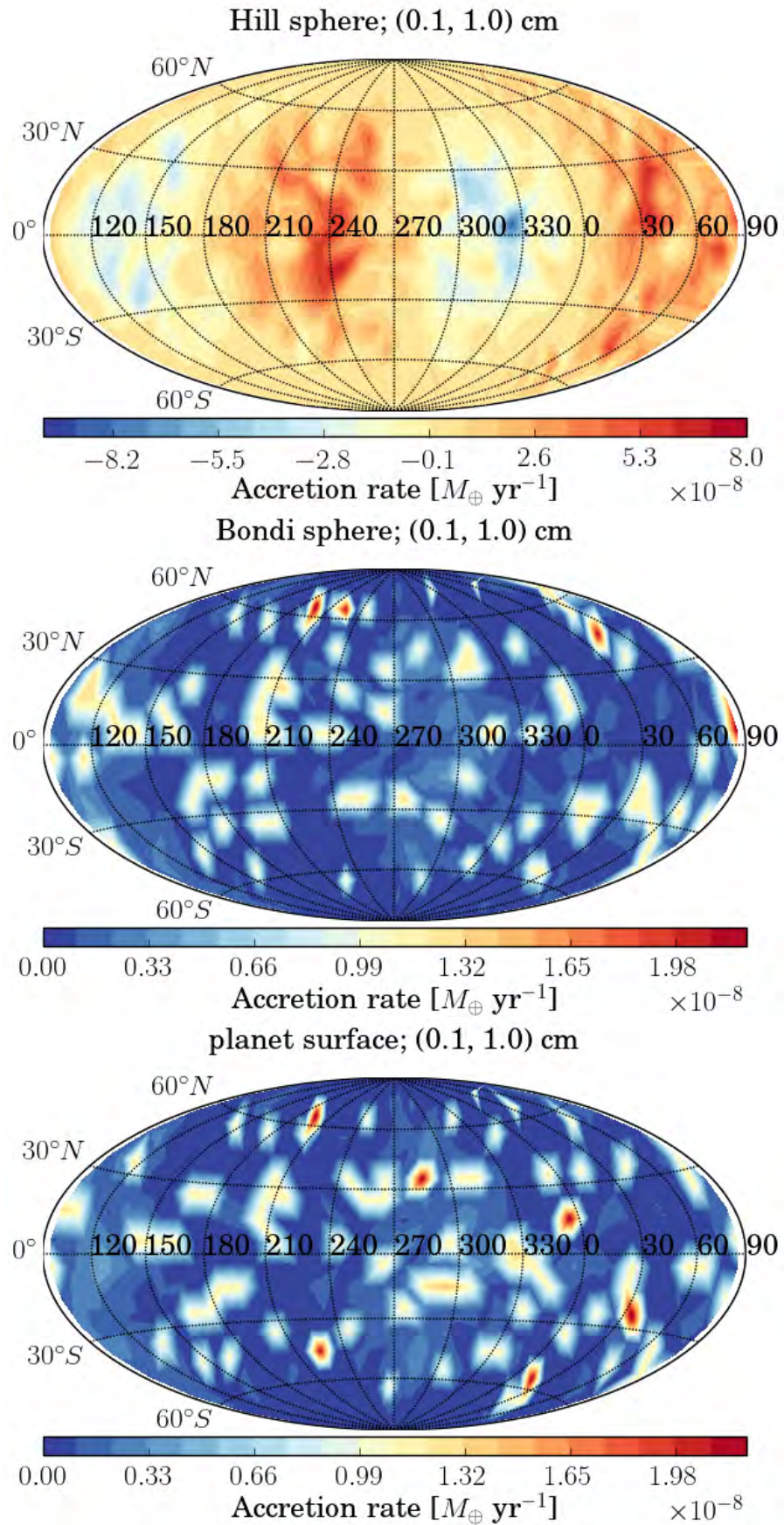


Figure 5.55: Same as Fig. 5.37, but for the m05t10 run.

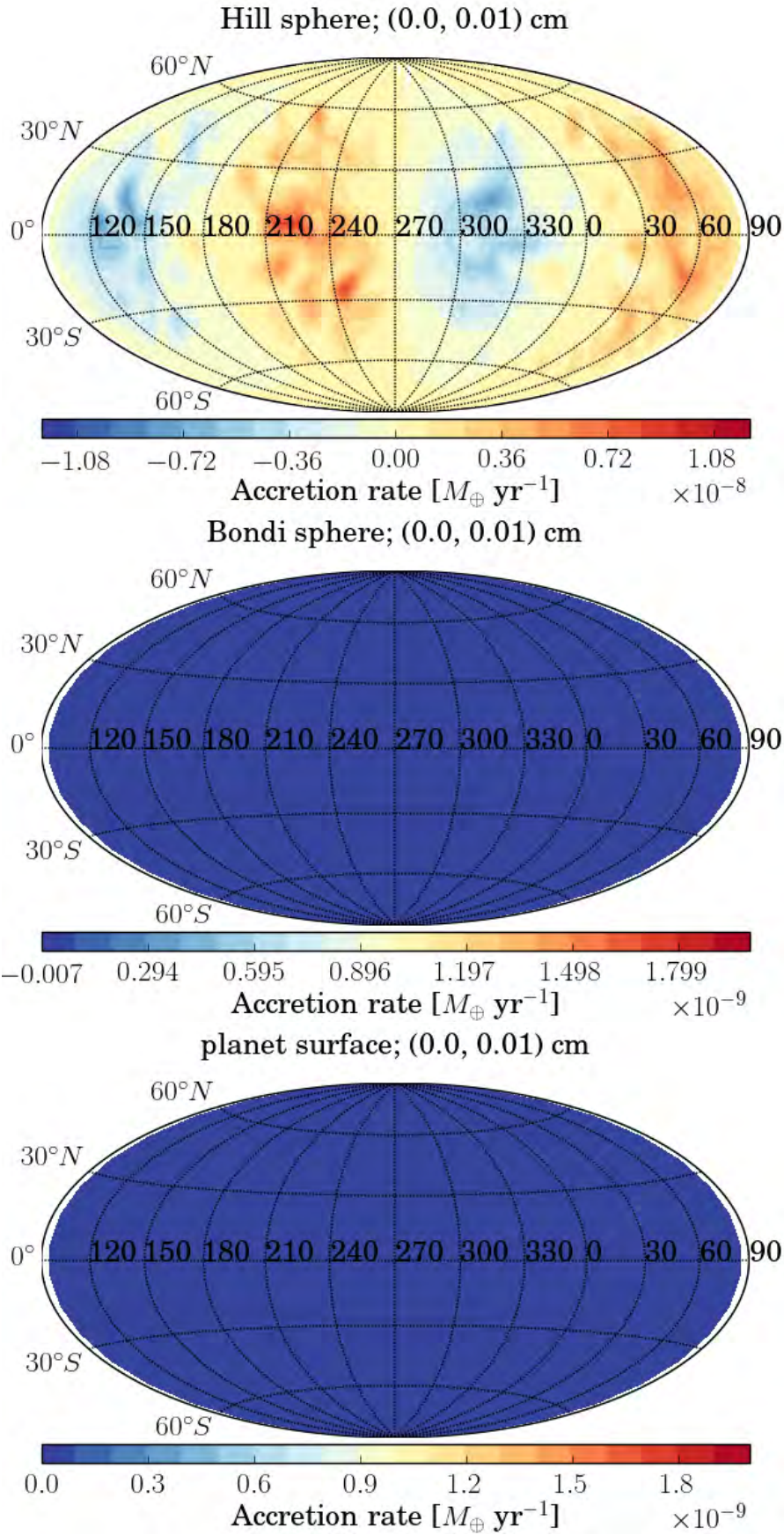


Figure 5.56: Same as Fig. 5.35, but for the m01t10 run.

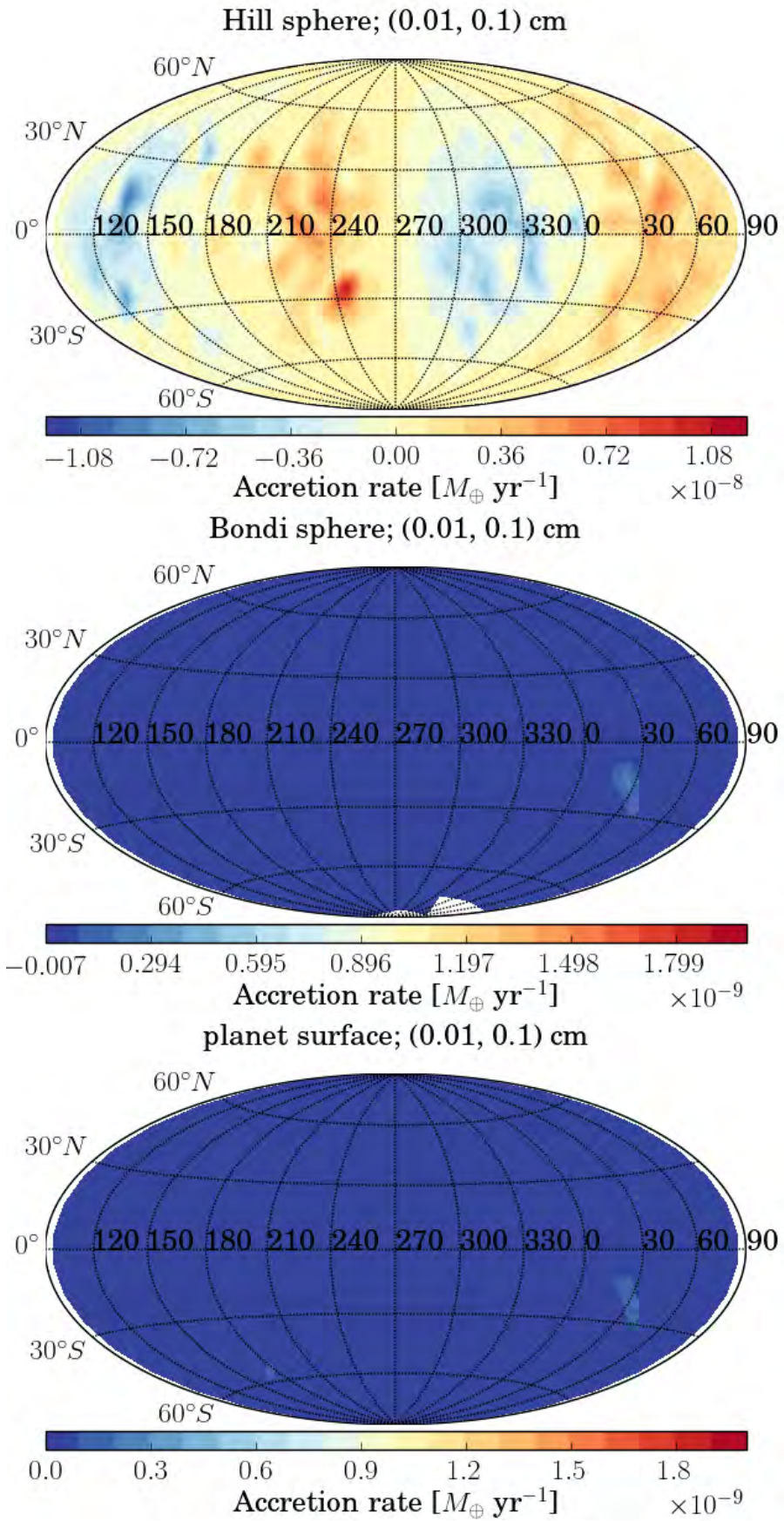


Figure 5.57: Same as Fig. 5.36, but for the m01t10 run.

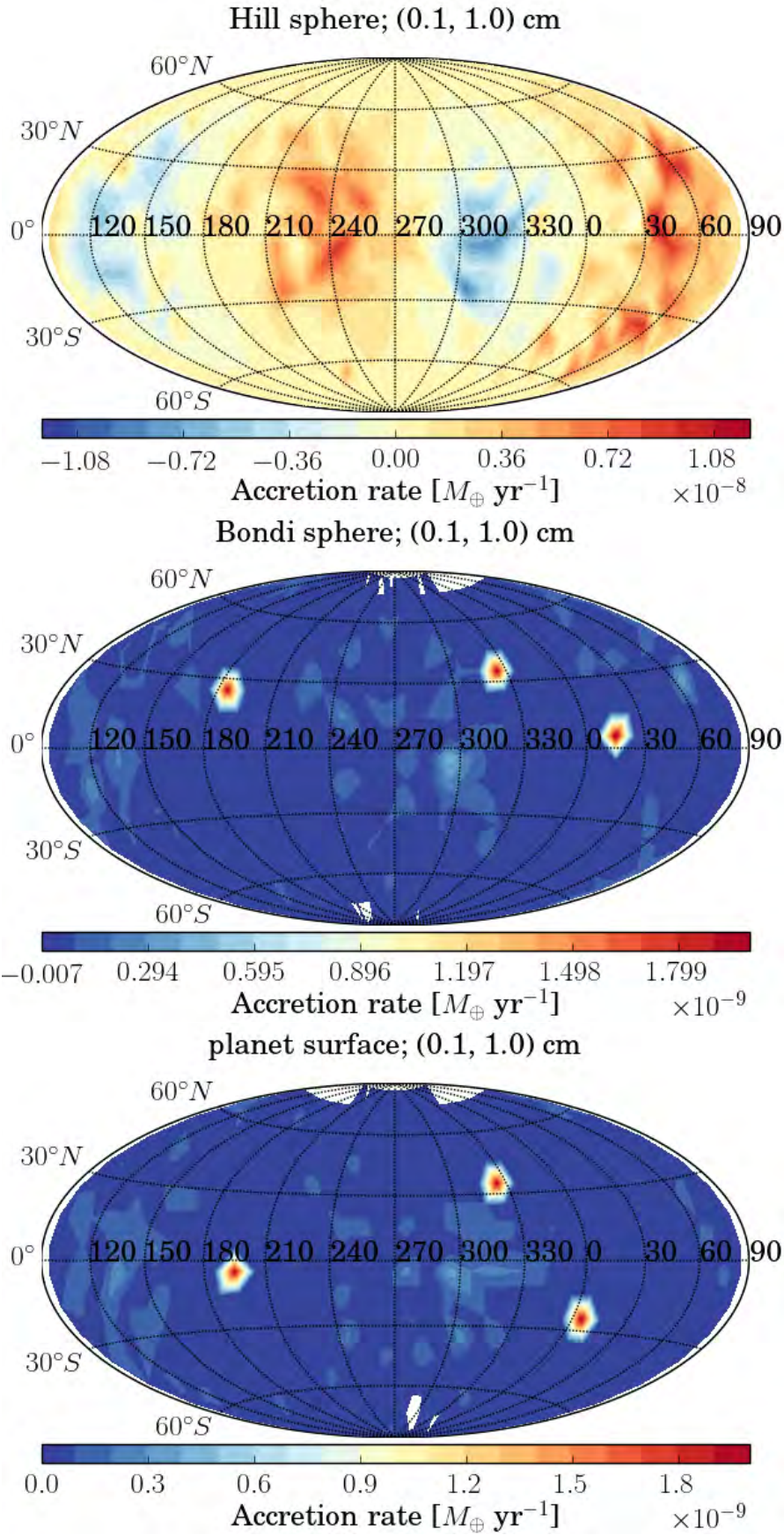


Figure 5.58: Same as Fig. 5.37, but for the m01t10 run.

PAPER IV: PEBBLE DYNAMICS AND ACCRETION
ONTO ROCKY PLANETS. II. RADIATIVE MODELS

Andrius Popovas, Åke Nordlund and Jon P. Ramsey

¹ Centre for Star and Planet Formation, Niels Bohr Institute and Natural History Museum of Denmark, University of Copenhagen, Øster Voldgade 5-7, DK-1350 Copenhagen K, Denmark

In preparation for *Monthly Notices of the Royal Astronomical Society Letters (MNRASL)*

We conduct a series of nested-grid, high-resolution hydrodynamic simulations of gas and particle dynamics in the vicinity of an Earth-mass embryo. We include radiative energy transport as well as heating resulting from the accretion of solids. Our results affirm the robustness of the previously determined linear scaling of solid accretion rates with the size of the particles. Keeping the embryo surface temperature constant, we show that radiative energy transport results in a tendency to reduce the entropy in the primordial atmosphere, but this tendency is, to a large extent, cancelled by an increase in the strength of convective energy transport, triggered by a correspondingly increased super-adiabatic temperature gradient. In the cases investigated here, where the optical depth to the disk surface is larger than unity, the reduction of the temperature in the outer parts of the Hill sphere relative to cases without radiative energy transport is only $\sim 100\text{K}$, but the accumulated effect on the mass density is on the order of a factor of two in the inner parts of the Hill sphere.

6.1 INTRODUCTION

Planetary embryos of sufficient mass embedded in optically thick protoplanetary accretion disks are necessarily accompanied by extended primordial atmospheres in near hydrostatic equilibrium, merging smoothly with the disk background at distances on the order of the Hill radius, $R_H = a \sqrt[3]{\frac{M_p}{3M_*}}$, where a is the semi-major axis of the embryo's orbit, and M_p and M_* are the masses of the embryo and the central star, respectively (Perri & Cameron, 1974; Bodenheimer & Pollack, 1986; Pollack et al., 1996; ?; Alibert, 2017).

The existence of dust and solid particles in the protoplanetary disk leads to accretion of solids onto such embryos, resulting in growth of the embryo and frictional heating of the surrounding primordial atmosphere. As long as the embryo atmosphere and surrounding disk is optically thick, convective motions are the most effective means of transporting heat through the atmosphere, with efficient convective transport leading to near-adiabatic stratification of the atmosphere (Stevenson, 1982; Wuchterl, 1993). The near-adiabaticity implies that the inner parts of the atmosphere are relatively hot, which, when combined with the reduction of the planet's gravity as the square of the distance, results in relatively low masses of atmospheres (e.g. Venturini et al., 2015).

If, on the other hand, the optical depth of the primordial atmosphere is not very large, radiative energy transport may be important, resulting in possibly significant changes in the stratification of the atmosphere. Radiative cooling tends to reduce the temperatures, which leads to lower pressures and density scale heights, thus increasing the mass of the atmosphere. A significant temperature drop could potentially lead to a situation where hydrostatic equilibrium is no longer possible, resulting in gravitational collapse and the formation of gas giants (e.g. Mizuno et al., 1978; Bodenheimer & Pollack, 1986; Hori & Ikoma, 2011).

In cases where catastrophic collapse of the atmosphere does not occur, the ultimate outcome depends crucially on the balance between removal of gas caused by the reduction of the density and pressure of the surrounding disk, and the tendency of increased radiative cooling—occurring for essentially the same reason—to lead to relatively light or more heavy atmospheres. As shown by Ginzburg et al. (2016), that balance may in the end decide if the final outcome is a gas dwarf, or a rocky planet with only a thin remaining atmosphere.

Properly accounting for radiative transfer of energy and the corresponding effects on the near-hydrostatic equilibrium of the primordial atmospheres is thus crucial for realistic and accurate modelling of early planet formation. Such efforts are additionally complicated by effects of *scattering*, which are known to be important at the wavelengths and temperatures of relevance (e.g. Pinte et al., 2009).

In this Letter, we therefore investigate the effects of radiative energy transfer on the primordial atmospheres of planetary embryos embedded in protoplanetary disks and the resulting, secondary effects on the particle dynamics

and pebble accretion onto rocky embryos. In Section 6.2 we briefly describe the simulation set up and the methods used to treat radiative energy transfer. We present and discuss the results in Section 6.3, and draw conclusions in Section 6.4.

6.2 METHODS

As in previous work (Popovas et al., submitted, hereafter PNRO), the current study is carried out using the new DISPATCH framework (Nordlund et al., 2018) in a three-dimensional, Cartesian (shearing box) domain, with a set of static, nested patches. We continue to use an ideal gas equation of state (EOS) with adiabatic index $\gamma = 1.4$ and molecular weight $\mu = 2$, and a disk with surface mass density 170 g cm^{-2} , corresponding to 1/10 of a minimum-mass-solar-nebula (MMSN). The grid set up is the same as in PNRO for a $M=0.95 M_{\oplus}$ planet at 1AU distance from the central star. We conduct a series of radiative-convective simulations, for which the basic radiative transfer and accretion heating parameters are summarized in Table 6.1.

The optical properties of the dust-gas mix in a hot, primordial atmospheres are quite uncertain, mainly due to factors related to dust coagulation and thermal processes. We choose here a combination of disk surface density and opacity specifically aimed at investigating a situation where optical depth effects start to become significant. To this end, we choose a total opacity (weighted with 80% scattering and 20% absorption) of $0.1 \text{ cm}^2 \text{ g}^{-1}$. Given a surface density of 170 g cm^{-2} , we thus obtain a midplane optical depth in the unperturbed disk of $\frac{1}{2} \times 0.1 \times 170 = 8.5$. The additional optical depth of the initial, adiabatic atmosphere is ≈ 6.0 , and hence the optical depth is indeed such that we may expect to begin to see the effects of radiative cooling.

6.2.1 Initial and boundary conditions

As initial conditions, we take a fiducial, fully relaxed MMSN/10 run with adiabatic stratification (i.e. run m095t10 in PNRO). The external and spherical boundary conditions for density ρ , entropy per unit mass and mass flux are the same as in PNRO. However, as we now also consider the radiative energy transport, appropriate boundary conditions must be considered. The disk is optically thick in the radial and azimuthal directions and is initially in radiative equilibrium in those directions, i.e., no heat exchange is happening radially and azimuthally. However, protoplanetary disks can and do cool radiatively in the vertical direction. Therefore the external boundaries for the radiative transfer of energy are as follows:

- $Q = I - S = 0$ at external x - and y -boundaries;
- $I^{\text{incoming}} = 0 \rightarrow Q^{\text{incoming}} = -S$ at external z -boundaries, where I is the radiation intensity in a specific direction, and S is the local source function.

Table 6.1: Parameters for the simulation runs. κ is the total opacity (absorption plus scattering). ε is the fraction of absorption. \dot{M} is the solid accretion rate.

Run	κ [$\text{cm}^2 \text{g}^{-1}$]	ε	\dot{M} [$M_{\oplus} \text{yr}^{-1}$]
m095	–	–	–
m095-conv-2e-6	–	–	$2 \cdot 10^{-6}$
m095-conv-2e-6-rt	0.1	0.2	$2 \cdot 10^{-6}$
m095-conv-2e-5-rt	0.1	0.2	$2 \cdot 10^{-5}$
m095-conv-2e-6-rt- $\kappa 1$	1.0	0.2	$2 \cdot 10^{-6}$

6.2.1.1 Heating from the embryo

As the envelope surrounding the embryo is optically thick during most of the disk evolution, the embryo and its atmosphere cannot radiate the heat away effectively when solids are accreted. The atmosphere is thus expected to remain nearly adiabatic through most of the build-up of the embryo mass, and the embryo must be correspondingly hot—above *solidus*—especially towards the end of the build-up period. Detailed predictions of temperatures and temperature histories require using realistic equations of state for the primordial atmosphere as well as for the planet itself, in combination with modelling of the thermal evolution over disk evolution time scales. This is a formidable task by itself, where sequences of simulations such as the ones reported here may be used to provide the required estimates of instantaneous cooling rates.

In any case, since the heat capacity of a planet is large the planet is expected to remain hot for a considerable time, even after the envelope becomes optically thin (Ginzburg et al., 2016). For the relatively brief periods of time covered by the current simulations it is thus certainly appropriate to consider the surface temperature of the embryo to be fixed, and we therefore adopt the surface temperature predicted from the adiabatic atmosphere model as a fixed lower boundary condition on the temperature of all models.

6.2.2 Radiative energy transport

We use a hybrid-characteristics ray tracing scheme (Nordlund et al., 2018) with 26 ray-directions (forward and reverse directions along 3 axes, 6 face diagonals, and 4 space diagonals) and a single frequency bin (constant opacity κ , measured in $\text{cm}^2 \text{g}^{-1}$). Since scattering is an important effect at the temperatures and wavelengths of relevance here, we split the opacity into an absorption part $\varepsilon\kappa$ and a scattering part $(1 - \varepsilon)\kappa$. At the levels of scattering albedos typically assumed—from 50% to 80%—and with the relatively slow time evolution dictated by convective motions, scattering can be handled with what essentially boils down to "lambda iteration"; i.e., iteratively feeding back the mean intensity from previous time steps into the source function of the next time step (Hubeny, 2003). Here, the time slices used in the DIS-

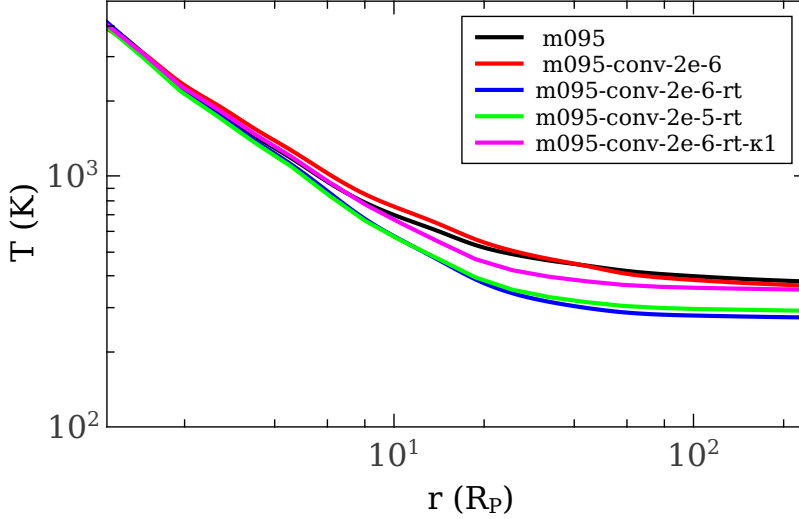


Figure 6.1: Temperature profiles, integrated over radial shells.

PATCH code framework may be used to *predict* the mean intensity in the next time step, thus efficiently reducing the time lag otherwise resulting from the use of the previous mean intensity.

In order to avoid that the intense radiation from the embryo surface results in narrow, parallel beams of strong radiation in the 26 angular direction used in the diffuse radiation solver, we replace the ray-based solver with a diffusion approximation in a region near the embryo. In the optically thick limit, the integral solution of the radiative transfer equation along any direction may be approximated by

$$Q = \frac{1}{2}(I^+ + I^-) - S \approx \frac{d^2S}{d\tau^2}, \quad (6.1)$$

where I^+ and I^- are the specific radiation intensities in the forward and reverse directions, and $S(\tau)$ is the source function, with τ the optical depth along the ray direction. A term proportional to the first derivative of the source function is omitted, since it cancels out when averaging the forward and reverse solutions along a given ray direction. Given the availability of the source function and opacity values on the Cartesian mesh, it is trivial to evaluate this expression in the three axis directions, and estimate the full space angle integrated heat exchange rate per unit mass

$$q \approx \kappa \frac{4\pi}{3} \left(\frac{d^2S}{d\tau_x^2} + \frac{d^2S}{d\tau_y^2} + \frac{d^2S}{d\tau_z^2} \right). \quad (6.2)$$

The ray-based diffuse radiation solver is used in all other parts of the model, tapering over with weights $w = e^{-(r/r_0)^6}$ and $(1-w)$ from Eq. 6.2 to a value of q based on averaging over the 26 forward and reverse ray directions used in the diffuse solver,

$$q \approx \kappa \frac{4\pi}{26} \sum_{j=1}^{13} (Q_j^+ + Q_j^-). \quad (6.3)$$

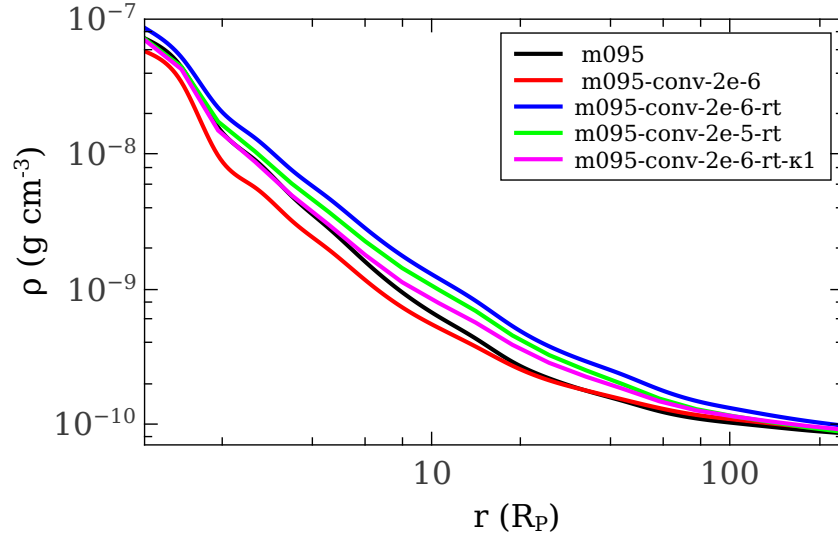


Figure 6.2: Density profiles, integrated over radial shells.

6.2.3 Particles

We use ~ 12 million macro-particles, each representing a swarm of identical particles. The initial spatial distribution of macro-particles is proportional to the local gas density, with particle sizes ranging from $10 \mu\text{m}$ to 1cm , using a flat distribution in logarithmic size. Rather than having to make assumptions about the settling and actual size distribution, we instead analyse sub-populations of our initial distribution. Specifically, to measure accretion rate as a function of particle size, we tag and follow only the particles in a narrow size range that initially reside within one Hill radius from the midplane. For more details about the particle distribution, their motion and selection, cf. PNRO.

6.3 RESULTS AND DISCUSSION

6.3.1 Gas dynamics

Figures 6.1 and 6.2 show thermal and density structure of the envelope, when no accretion heating and RT is considered (m095, black curves), when accretion heating, $\dot{M} = 2 \cdot 10^{-6} M_{\oplus} \text{yr}^{-1}$, driven convection is present (m095-conv-2e-6, red curves), when the same accretion heating and radiative cooling ($\kappa = 0.1 \text{cm}^2 \text{g}^{-1}$) is considered (m095-conv-2e-6-rt, blue curves), when the same accretion heating and radiative cooling is considered, but $\kappa = 1.0 \text{cm}^2 \text{g}^{-1}$ (m095-conv-2e-6-rt- $\kappa 1$, magenta curves) and when the accretion heating is increased to rates consistent with pebble-size particle accretion, $\dot{M} = 2 \cdot 10^{-5} M_{\oplus} \text{yr}^{-1}$ and radiative cooling ($\kappa = 0.1 \text{cm}^2 \text{g}^{-1}$) is considered (m095-conv-2e-5-rt, green curves). The values are shell-averaged over radii and over extended periods of time. Convective motions effectively transport the excess heating

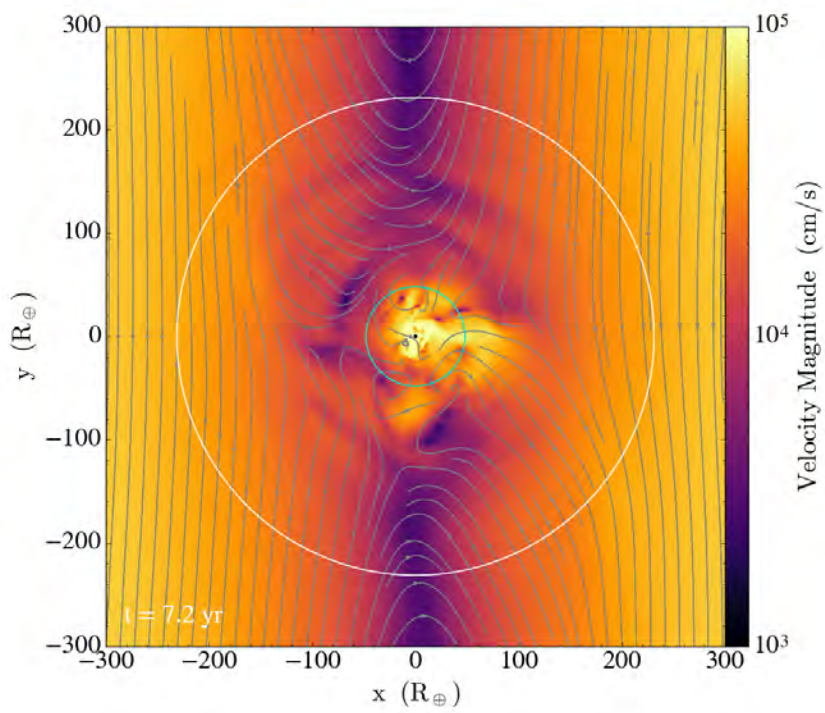


Figure 6.3: Velocity magnitude in the midplane in m095-conv-2e-6-rt simulation. The white circle shows the Hill sphere and the cyan circle shows the canonical Bondi sphere. Gray streamlines indicate gas flow patterns (of velocities projected onto the 2D plane).

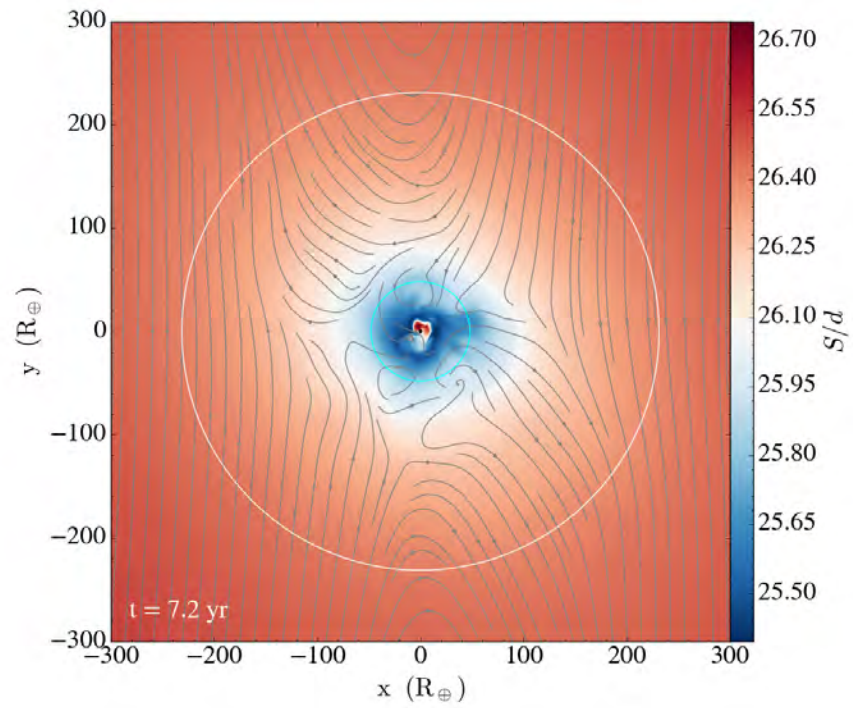


Figure 6.4: Entropy per unit mass in the midplane in `m095-conv-2e-6-rt` simulation. The white circle shows the Hill sphere and the cyan circle shows the canonical Bondi sphere. Gray streamlines indicate gas flow patterns (of velocities projected onto the 2D plane).

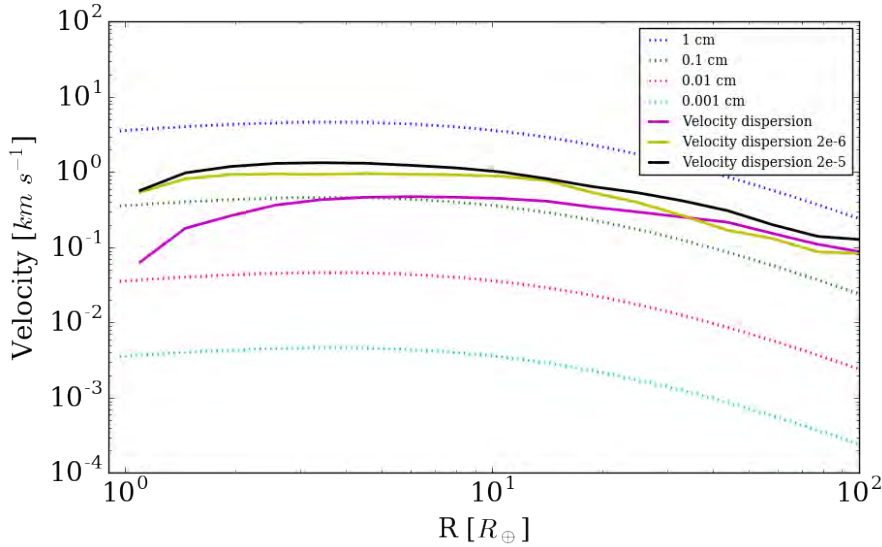


Figure 6.5: Time-averaged velocity dispersion profiles for convective simulations, in magenta for the `m095-conv-2e-6`, in yellow for `m095-conv-2e-6-rt`, and in black for `m095-conv-1e-5-rt`, shown against a background of free fall drag velocities of particles of size 1 cm (blue), 0.1 cm (green), 0.01 cm (red) and 0.001 cm (cyan).

from accretion of solids even when the `RT` is not considered (or κ is sufficiently high), thus there is no significant difference in thermal structure in the purely convective case. The fluctuations of temperature and density associated with the convection locally and temporarily modify the gas density, but on average the convective motions do not result in any net transport of gas mass. When radiative energy transport is turned on, the thermal structure near the embryo remains close to the adiabatic one, while further out the temperature is reduced. As the envelope adjusts its near-hydrostatic equilibrium to the lower temperature, it becomes on average denser. Since this is an effect that accumulates over depth—with pressure scale height proportional to the local temperature—the effect on the density is much larger than that on the temperature.

Figure 6.3 shows an example of the convective velocity flow for a simulation where radiative energy transfer is included (`m095-conv-2e-6-rt`). The motion patterns are similar in the case with pure convection (cf. Fig 20 in PNRO), but the velocity amplitudes are larger—especially at small radii—when radiative energy transfer is included. The reason for the increased velocity amplitudes is illustrated in Fig. 6.4. The radiative cooling tends to lower the entropy in the neighbourhood of the embryo, while simultaneously accretion heating keeps adding entropy, and the temperature of the embryo surface is held fixed. The net effect is a tendency to increase the temperature gradient, thus making it more super-adiabatic than in the case with only accretion heating, resulting in stronger driving of the convection. Near the embryo, the increase of the convective energy transport is largely able to compensate for the increased radiative cooling. Further out, where the convection motions are

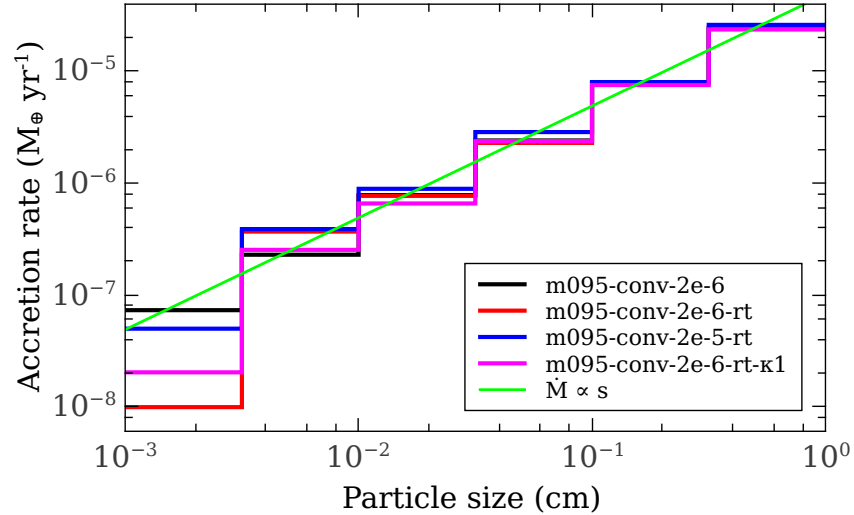


Figure 6.6: Pebble accretion rates, for particle sizes within each size bin, drawn from an initial distribution consisting of particles within $\pm R_H$ from the mid-plane, for the three different simulations. The green line shows a mass accretion rate proportional to particle size, s .

weaker and the optical depths to the vertical surfaces are smaller the effects of radiative cooling become more visible.

The increase of convective velocity amplitudes is illustrated quantitatively in Figure 6.5, against a background of vertical particle drift speeds. The figure shows that the velocity amplitudes near the embryo are increased with nearly an order of magnitude, becoming comparable to the vertical drift speed of 2-3 mm particles. Further out, where the horseshoe and shear flow patterns start to also contribute to the velocity dispersion, the effects of radiative cooling on the velocity dispersions diminish.

6.3.2 Solid accretion rates

In the previous paper of the series (Popovas et al., submitted, PNRO) we determined the accretion rates of solids, and showed that they scale linearly with the particle size. Here, we affirm that the previously determined accretion rates are robust. Figure 6.6 shows the pebble accretion rates for different simulation runs. Both with convective motions and radiative cooling these rates do not vary much from previously determined ones; the deviations are mainly due to increased noise as the motions of the gas stir the solids.

6.4 CONCLUSIONS AND OUTLOOK

In these first-of-a-kind, three-dimensional, radiative-convective models of hot and extended primordial atmospheres of Earth-mass embryos, with realistic, albeit schematic, scattering included, we find that radiative cooling is beginning to be significant, leading to local increases of the shell averaged mass

density on the order of a factor of two. For the conditions modelled here, the cooling effects do not penetrate down to the bottom of the atmosphere, where convection is still the dominant mechanism of energy transport. In response to the tendency from cooling to increase the radial temperature gradient, however, the amplitude of convective motions increase by nearly an order of magnitude near the embryo surface. In the radiatively cooled models, relative to the adiabatic and purely convective models, the total mass of the atmosphere is increased by a factor of about 4% and 27%, with $\kappa = 0.1$, $\dot{M} = 2 \cdot 10^{-5}$ and $\dot{M} = 2 \cdot 10^{-6} M_{\oplus} \text{ yr}^{-1}$, respectively.

We find that, even though radiative cooling begins to be significant, the accretion heating and the resulting convective energy transport are still dominating near the planet embryo, where the atmosphere temperature also remains "anchored" to the surface temperature of the planet embryo. This is encouraging, since it implies that planetary embryos embedded in protoplanetary disk can retain hot and hence relatively light atmospheres throughout much of the evolution of the disk.

When the disk and primordial atmosphere finally becomes genuinely optically thin, the atmosphere that remains around low mass planetary embryos are therefore relatively light, with their future fate depending on the relative balance between the slow cooling of the still hot embryo, and the secular loss of the remaining atmosphere. As argued by [Ginzburg et al. \(2016\)](#), it is the outcome of this balance that ultimately determines if a planet ends up as a gas dwarf, with a significant H+He atmosphere still remaining, or becomes a rocky planet, with an atmosphere consisting of only heavier gas molecules, possibly even dominated by out-gassing.

The current modelling should be seen as a pilot effort, exploring effects and probing what is currently possible. Obvious factors that need improvement are the ideal equation of state, the constant and grey opacity, and the spatial resolution, which even if larger than in comparable published simulations (e.g. [?](#)), still needs to be increased in order to better resolve the convective motions. Improving all these factors is certainly possible: The current results were obtained with only moderate computational effort, with each model requiring of the order of a few thousand core hours on a cluster with Intel Ivy Bridge cores.

The DISPATCH code framework ([?](#)) can handle arbitrary equations of state and opacities, using optimized table lookup, without significantly increasing the computational cost. The radiative transfer solvers are also prepared for multi-frequency experiments, using either representative frequencies or opacity distribution functions. The cost scales linearly with the number of opacity bins. The spatial resolution cost, as always, scales with the inverse fourth order power of the smallest resolution element. Although this can be partly mitigated by the use of local time steps (the same spatial region being split into a larger number of local patches), the main scaling of the computing time will remain essentially $N_{\text{bin}} N_{\text{cell}}^{4/3}$. Taking advantage of the essentially linear weak scaling of the DISPATCH code framework (c.f. Fig. 5, [Nordlund et al., 2018](#)) it is thus possible to perform simulations with tabular equation-of-state and

opacities, several opacity bins, and resolutions increased with a factor of 8, at costs per model of the order 10-20 million core hours. Alternatively one could run, using similar amounts of computing resources, a dozen or more models with a factor of 4 better resolution than the current one.

ACKNOWLEDGEMENTS

The work of AP and ÅN was supported by grant 1323-00199B from the Danish Council for Independent Research (DFF). The Centre for Star and Planet Formation is funded by the Danish National Research Foundation (DNRF97). Storage and computing resources at the University of Copenhagen HPC centre, funded in part by the Villum Foundation (VKR023406), were used to carry out the simulations presented here.

SUMMARY AND OUTLOOK

In my thesis work, together with my collaborators, I have performed computer simulations of the motion of gas and solids in the vicinity of Mars- to Earth-mass planetary embryos which are embedded in a protoplanetary disk. The goal of this work was to reduce the uncertainties, and uncertainties about uncertainties, involved in understanding early growth of planets. It was previously already predicted that pebble accretion is a very effective mechanism for planet formation (e.g. Ormel & Klahr 2010; Lambrechts & Johansen 2012; Morbidelli & Nesvorný 2012; Lambrechts & Johansen 2014) and the simulations presented in this thesis demonstrate the robustness of pebble accretion rates. To lowest order, the effects of disk density on mass supply of solids and accretion speed cancel each other out. The remaining dominant scaling is the dependence on embryo mass, which I find is approximately $M^{2/3}$, corresponding to an embryo mass that grows approximately as t^3 . This implies that, as long as this scaling persists, and assuming a constant dust-to-gas ratio, growth of an embryo from a small seed takes on the order of three times the instantaneous mass divided by the instantaneous accretion rate. If the dominant mass fraction of solids lies in chondrule size particles, this corresponds to ~ 1.5 million years to grow from a small seed to an Earth-mass planet at 1 AU and ~ 1 million years to grow a Mars-mass planet at 1.5 AU.

The state-of-the-art simulations presented in this thesis indicate that, in hot and extended primordial atmospheres, radiative cooling is significant. It leads to local shell-averaged increases of mass density on the order of a factor of two. The cooling effects do not, however, penetrate down to the bottom of the atmosphere, where convection is the dominant mechanism of energy transport. In response to the tendency of cooling to increase the radial temperature gradient, the amplitude of convective motions increases by nearly an order of magnitude near the embryo surface. Despite radiative cooling being significant, the accretion heating and the resulting convective energy transport still dominates over the radiative cooling near the planetary embryo. The atmosphere temperature also remains “anchored” to the surface temperature of the embryo. This implies that planetary embryos embedded in protoplanetary disks can retain hot, and hence relatively light, atmospheres throughout much of the evolution of the disk without becoming gas dwarf planets. Eventually, when the disk and primordial atmosphere become genuinely optically thin, the atmosphere that remains around low-mass planetary embryos is therefore relatively light, with its fate depending on the relative balance between the slow cooling of the still hot embryo, and the secular loss of the remaining gas. As argued by Ginzburg et al. (2016), it is the outcome of this balance that ultimately determines if a planet ends up as a gas dwarf, with a significant hydrogen and helium atmosphere still remaining, or becomes a rocky planet, with an atmosphere consisting of only heavier molecules.

The simulations presented in this thesis are based on an ideal gas equation of state. However, high temperatures close to the embryo (up to $\sim 4500\text{K}$ close to the surface of a $0.95M_{\oplus}$ core) have several important consequences. First, molecular hydrogen (H_2) dissociates and, since it is a highly endothermic process, the temperature will decrease. As the gas is in hydrostatic equilibrium, the density unavoidably increases. Second, these temperatures are much higher than the melting point of solids. Accreted particles can then evaporate before reaching the surface of the planet (e.g. [Alibert 2017](#); [Brouwers et al. 2017](#)). The resulting vapour contains a high fraction of metals (in the astrophysical periodic table of elements, everything heavier than helium is dubbed a metal), which in turn affects the local equation of state. Naturally, the ideal gas equation of state does not account for these consequences and therefore a realistic equation of state, which includes the effects from molecular hydrogen dissociation and potentially the enrichment with metals (e.g. [Venturini et al. 2016](#)), should be used in future work. This thesis contains calculations of highly accurate total internal partition functions for molecular hydrogen of different flavours, which can be used to calculate the dissociation equilibrium of hydrogen. I have also already compiled the raw data (experimental and *ab initio* calculations) for other molecules and their isotopologues of astrophysical interest, e.g., AlH , CN , CO , MgH , Na_2 , NaCl , SiO , SO , SiS , TiO , etc., and will produce the partition functions for these elements using a similar approach as used for H_2 (publication planned for late 2018). These total internal partition functions are also useful for calculating accurate gas opacities for radiative energy transfer. Given the known discrepancies and errors in the calculations of total internal partition functions in the existing literature (cf. [Popovas & Jørgensen, 2016](#)), in future work, the new, accurate total internal partition functions that I have produced (and will produce) should be used to compute the equation of state for computer simulations of star and planet formation.

The fundamental motivation behind this thesis was to account for environmental effects on the process of pebble accretion in a more realistic manner. Achieving it is therefore a significant stepping stone and it now becomes possible to investigate the stochastic nature of planet formation. The upcoming era of exa-scale HPC will permit astrophysicists to conduct multi-scale, multi-fluid simulations of protoplanetary disks with multiple embedded planets at high resolution. The disk itself could be a zoom-in taken from a global star formation environment (e.g. [Kuffmeier et al., 2017](#)), which would provide a more realistic environment in which to simulate protoplanetary disk evolution and planet formation. Furthermore, by understanding the intrinsic interplay between the stochastic effects, like sub-structure in the disk, magnetic fields, metallicities, chemistry, etc., we will eventually be able to directly relate the observed properties of exoplanets and their host stars to their early histories and formation environments.

One might consider this to be wishful thinking, but there is no reason why it should not come to pass. It will certainly require a lot of effort by many scientists across several disciplines, but with the current public and scientific

interest in exoplanets, and the thirst to understand their origins only increasing, I believe it is simply a matter of time.

BIBLIOGRAPHY

- Abgrall, H., Roueff, E., Launay, F., & Roncin, J.-Y. 1994, *Canadian Journal of Physics*, 72, 856
- Abgrall, H., Roueff, E., Launay, F., Roncin, J. Y., & Subtil, J. L. 1993, *Journal of Molecular Spectroscopy*, 157, 512
- Adams, M., Colella, P., Graves, D., et al. 2015, *Chombo Software Package for AMR Applications - Design Document*
- Alexiades, V., Amiez, G., & Gremaud, P.-A. 1996, *Communications in Numerical Methods in Engineering*, 12, 31
- Alibert, Y. 2017, *Astronomy and Astrophysics*, 606, A69
- ALMA Partnership, Brogan, C. L., Pérez, L. M., et al. 2015, *ApJ*, 808, L3
- Almgren, A. S., Beckner, V. E., Bell, J. B., et al. 2010, *ApJ*, 715, 1221
- Andrews, S. M., Rosenfeld, K. A., Kraus, A. L., & Wilner, D. J. 2013, *ApJ*, 771, 129
- Andrews, S. M., Wilner, D. J., Zhu, Z., et al. 2016, *ApJ*, 820, L40
- Armitage, P. J. 2013, *Astrophysics of Planet Formation*
- Bailly, D., Salumbides, E. J., Vervloet, M., & Ubachs, W. 2010, *Molecular Physics*, 108, 827
- Bally, J., Langer, W. D., Stark, A. A., & Wilson, R. W. 1987, *ApJ*, 312, L45
- Barge, P., Richard, S., & Le Dizès, S. 2016, *A&A*, 592, A136
- Barranco, J. A. & Marcus, P. S. 2005, *ApJ*, 623, 1157
- Baruteau, C. & Masset, F. 2013, in *Lecture Notes in Physics*, Berlin Springer Verlag, Vol. 861, *Lecture Notes in Physics*, Berlin Springer Verlag, ed. J. Souchay, S. Mathis, & T. Tokieda, 201
- Baumann, G., Haugbølle, T., & Nordlund, Å. 2013, *ApJ*, 771, 93
- Bell, C. P. M., Naylor, T., Mayne, N. J., Jeffries, R. D., & Littlefair, S. P. 2013, *MNRAS*, 434, 806
- Benítez-Llambay, P., Masset, F., Koenigsberger, G., & Szulágyi, J. 2015, *Nature*, 520, 63
- Benítez-Llambay, P. & Masset, F. S. 2016, *ApJS*, 223, 11
- Berger, M. J. & Colella, P. 1989, *Journal of Computational Physics*, 82, 64

- Berger, M. J. & Olinger, J. 1984, *Journal of Computational Physics*, 53, 484
- Berzins, M., Luitjens, J., Meng, Q., et al. 2010, in *Proceedings of the 2010 TeraGrid Conference*, TG '10 (New York, NY, USA: ACM), 3:1–3:8
- Beust, H., Augereau, J.-C., Bonsor, A., et al. 2014, *A&A*, 561, A43
- Bitsch, B., Johansen, A., Lambrechts, M., & Morbidelli, A. 2015a, *A&A*, 575, A28
- Bitsch, B., Lambrechts, M., & Johansen, A. 2015b, *A&A*, 582, A112
- Bizzarro, M., Connelly, J. N., & Krot, A. N. 2017a, in *Astrophysics and Space Science Library*, Vol. 445, *Astrophysics and Space Science Library*, ed. M. Pessah & O. Gressel, 161
- Bizzarro, M., Wielandt, D., Haugbølle, T., & Nordlund, A. 2017b, *LPI Contributions*, 1975, 2008
- Blum, J. & Wurm, G. 2000, *Icarus*, 143, 138
- Blum, J. & Wurm, G. 2008, *ARA&A*, 46, 21
- Bodenheimer, P. & Pollack, J. B. 1986, *Icarus*, 67, 391
- Bohn, H. U. & Wolf, B. E. 1984, *A&A*, 130, 202
- Boley, A. C. 2009, *ApJ*, 695, L53
- Boley, A. C., Hartquist, T. W., Durisen, R. H., & Michael, S. 2007, *ApJ*, 656, L89
- Bollard, J., Connelly, J. N., Whitehouse, M. J., et al. 2017, *Science Advances*, 3, e1700407
- Bonnor, W. B. 1956, *MNRAS*, 116, 351
- Born, M. & Oppenheimer, R. 1927, *Annalen der Physik*, 389, 457
- Borucki, W. J., Koch, D., Basri, G., et al. 2010, *Science*, 327, 977
- Boss, A. P. 1997, *Science*, 276, 1836
- Brandenburg, A. & Dobler, W. 2002, *Computer Physics Communications*, 147, 471
- Brouwers, M. G., Vazan, A., & Ormel, C. W. 2017, *ArXiv e-prints*, 1708, arXiv:1708.05392
- Brown, D. L., Henshaw, W. D., & Quinlan, D. J. 1997, *Overture: An object-oriented framework for solving partial differential equations*, ed. Y. Ishikawa, R. R. Oldehoeft, J. V. W. Reynders, & M. Tholburn (Berlin, Heidelberg: Springer Berlin Heidelberg), 177–184
- Bryan, G. L., Norman, M. L., O’Shea, B. W., et al. 2014, *ApJS*, 211, 19

- Cardona, O. & Corona-Galindo, M. G. 2013, *Rev. Mexicana Astron. Astrofis.*, 49, 209
- Cardona, O., Simonneau, E., & Crivellari, L. 2005, *Revista Mexicana de Fisica*, 51, 476
- Casassus, S., van der Plas, G., M, S. P., et al. 2013, *Nature*, 493, 191
- Cassan, A., Kubas, D., Beaulieu, J.-P., et al. 2012, *Nature*, 481, 167
- Cen, R. 2002, *ApJS*, 141, 211
- Charpinet, S., Fontaine, G., Brassard, P., et al. 2011, *Nature*, 480, 496
- Chatterjee, S. & Tan, J. C. 2014, *ApJ*, 780, 53
- Cimerman, N. P., Kuiper, R., & Ormel, C. W. 2017, *MNRAS*, 471, 4662
- Clarke, D. A. 1996, *ApJ*, 457, 291
- Clarke, D. A. 2010, *ApJS*, 187, 119
- Colonna, G., D'Angola, A., & Capitelli, M. 2012, *International Journal of Hydrogen Energy*, 37, 9656
- Cunningham, A. J., Frank, A., Varnière, P., Mitran, S., & Jones, T. W. 2009, *ApJS*, 182, 519
- Dabrowski, I. 1984, *Canadian Journal of Physics*, 62, 1639
- D'Angelo, G. & Bodenheimer, P. 2013, *ApJ*, 778, 77
- de Val-Borro, M., Edgar, R. G., Artymowicz, P., et al. 2006, *MNRAS*, 370, 529
- Dehnen, W. & Read, J. I. 2011, *European Physical Journal Plus*, 126, 55
- Dubey, A., Almgren, A., Bell, J., et al. 2014, *Journal of Parallel and Distributed Computing*, 74, 3217, domain-Specific Languages and High-Level Frameworks for High-Performance Computing
- Duffell, P. C. & MacFadyen, A. I. 2011, *ApJS*, 197, 15
- Duffin, D. F. & Pudritz, R. E. 2008, *MNRAS*, 391, 1659
- Dullemond, C. P. & Turolla, R. 2000, *A&A*, 360, 1187
- Dunham, J. L. 1932, *Physical Review*, 41, 721
- Ebert, R. 1955, *ZAp*, 37, 217
- Ebisuzaki, T. & Imaeda, Y. 2017, *New A*, 54, 7
- Evans, C. R. & Hawley, J. F. 1988, *ApJ*, 332, 659
- Fabrycky, D. C., Lissauer, J. J., Ragozzine, D., et al. 2014, *ApJ*, 790, 146

- Fischer, J., Gamache, R. R., Goldman, A., Rothman, L. S., & Perrin, A. 2003, *J. Quant. Spec. Radiat. Transf.*, 82, 401
- Fitzgerald, T. 2010, *Discourse on Civility and Barbarity* (Oxford University Press, USA)
- Friedrich, J. M., Weisberg, M. K., Ebel, D. S., et al. 2015, *Chemie der Erde / Geochemistry*, 75, 419
- Frimann, S., Jørgensen, J. K., Dunham, M. M., et al. 2017, *A&A*, 602, A120
- Frimann, S., Jørgensen, J. K., & Haugbølle, T. 2016, *A&A*, 587, A59
- Fromang, S., Hennebelle, P., & Teyssier, R. 2006, *A&A*, 457, 371
- Fryxell, B., Olson, K., Ricker, P., et al. 2000, *ApJS*, 131, 273
- Fuente, A., Baruteau, C., Neri, R., et al. 2017, *ApJ*, 846, L3
- Fung, J., Artymowicz, P., & Wu, Y. 2015, *ApJ*, 811, 101
- Galvagni, M., Hayfield, T., Boley, A., et al. 2012, *MNRAS*, 427, 1725
- Gamache, R. R., Hawkins, R. L., & Rothman, L. S. 1990, *Journal of Molecular Spectroscopy*, 142, 205
- Gamache, R. R., Kennedy, S., Hawkins, R. L., & Rothman, L. S. 2000, *Journal of Molecular Structure*, 517, 407
- Gillon, M., Triaud, A. H. M. J., Demory, B.-O., et al. 2017, *Nature*, 542, 456
- Ginzburg, S., Schlichting, H. E., & Sari, R. 2016, *ApJ*, 825, 29
- Glass-Maujean, M. & Jungen, C. 2009, *The Journal of Physical Chemistry A*, 113, 13124, pMID: 19548643
- Glass-Maujean, M., Jungen, C., Schmoranzer, H., et al. 2013a, *Journal of Molecular Spectroscopy*, 293, 11
- Glass-Maujean, M., Jungen, C., Spielfiedel, A., et al. 2013b, *Journal of Molecular Spectroscopy*, 293, 1
- Glass-Maujean, M., Jungen, C., Spielfiedel, A., et al. 2013c, *Journal of Molecular Spectroscopy*, 293, 1
- Glass-Maujean, M., Klumpp, S., Werner, L., Ehresmann, A., & Schmoranzer, H. 2007, *J. Chem. Phys.*, 126, 144303
- Goldbaum, N. J., Krumholz, M. R., & Forbes, J. C. 2016, *ApJ*, 827, 28
- Goldreich, P. & Schlichting, H. E. 2014, *AJ*, 147, 32
- Goldreich, P. & Tremaine, S. 1979, *ApJ*, 233, 857
- Goldreich, P. & Ward, W. R. 1973, *ApJ*, 183, 1051

- Goodman, A. A., Benson, P. J., Fuller, G. A., & Myers, P. C. 1993, *ApJ*, 406, 528
- Goorvitch, D. 1994, *ApJS*, 95, 535
- Greenberg, R., Hartmann, W. K., Chapman, C. R., & Wacker, J. F. 1978, *Icarus*, 35, 1
- Gudiksen, B. V., Carlsson, M., Hansteen, V. H., et al. 2011, *A&A*, 531, A154
- Güttler, C., Blum, J., Zsom, A., Ormel, C. W., & Dullemond, C. P. 2010, *A&A*, 513, A56
- Haugboelle, T., Grassi, T., Frostholm Mogensen, T., et al. 2017, *LPI Contributions*, 1975, 2025
- Haugbølle, T., Frederiksen, J. T., & Nordlund, A. 2013, *Physics of Plasmas*, 20, 062904
- Hayashi, C. 1981, in *IAU Symposium, Vol. 93, Fundamental Problems in the Theory of Stellar Evolution*, ed. D. Sugimoto, D. Q. Lamb, & D. N. Schramm, 113–126
- Hayek, W., Asplund, M., Carlsson, M., et al. 2010, *A&A*, 517, A49
- Hayes, J. C. & Norman, M. L. 2003, *ApJS*, 147, 197
- Heinemann, T., Dobler, W., Nordlund, Å., & Brandenburg, A. 2006, *A&A*, 448, 731
- Hernández, J., Hartmann, L., Calvet, N., et al. 2008, *ApJ*, 686, 1195
- Herzberg, G. 1945, *Molecular spectra and molecular structure. Vol.2: Infrared and Raman spectra of polyatomic molecules*
- Herzberg, G. 1950, *Molecular spectra and molecular structure. Vol.1: Spectra of diatomic molecules*
- Hopkins, P. F. 2015, *MNRAS*, 450, 53
- Hopkins, P. F. & Christiansen, J. L. 2013, *ApJ*, 776, 48
- Hori, Y. & Ikoma, M. 2011, *MNRAS*, 416, 1419
- Hubber, D. A., Rosotti, G. P., & Booth, R. A. 2018, *MNRAS*, 473, 1603
- Hubeny, I. 2003, in *Astronomical Society of the Pacific Conference Series, Vol. 288, Stellar Atmosphere Modeling*, ed. I. Hubeny, D. Mihalas, & K. Werner, 17
- Huber, K. & Herzberg, G. 1979, *Molecular Spectra and Molecular Structure: Constants of diatomic molecules, Molecular Spectra and Molecular Structure (Van Nostrand Reinhold)*

- Hubickyj, O., Bodenheimer, P., & Lissauer, J. J. 2005, *Icarus*, 179, 415
- Ida, S. & Makino, J. 1993, *Icarus*, 106, 210
- Inaba, S. & Ikoma, M. 2003, *A&A*, 410, 711
- Irwin, A. W. 1981, *ApJS*, 45, 621
- Irwin, A. W. 1987, *A&A*, 182, 348
- Isella, A., Pérez, L. M., Carpenter, J. M., et al. 2013, *ApJ*, 775, 30
- Jensen, E. L. N. & Akeson, R. 2014, *Nature*, 511, 567
- Jiang, Y.-F., Stone, J. M., & Davis, S. W. 2012, *ApJS*, 199, 14
- Johansen, A., Klahr, H., & Henning, T. 2006, *ApJ*, 636, 1121
- Johansen, A. & Lacerda, P. 2010, *MNRAS*, 404, 475
- Johansen, A., Mac Low, M.-M., Lacerda, P., & Bizzarro, M. 2015, *Science Advances*, 1, 1500109
- Johansen, A., Oishi, J. S., Mac Low, M.-M., et al. 2007, *Nature*, 448, 1022
- Jontof-Hutter, D., Rowe, J. F., Lissauer, J. J., Fabrycky, D. C., & Ford, E. B. 2015, *Nature*, 522, 321
- Jorgensen, U. G., Almlöf, J., Gustafsson, B., Larsson, M., & Siegbahn, P. 1985, *J. Chem. Phys.*, 83, 3034
- Kale, L. V., Böhm, E., Mendes, C. L., Wilmarth, T., & Zheng, G. 2008, in *Petascale Computing: Algorithms and Applications*, ed. D. Bader (Chapman & Hall / CRC Press), 421–441
- Kim, C.-G. & Ostriker, E. C. 2015, *ApJ*, 802, 99
- Klein, R. I. 1999, *Journal of Computational and Applied Mathematics*, 109, 123
- Klessen, R. S. & Hennebelle, P. 2010, *A&A*, 520, A17
- Kley, W. 1998, *A&A*, 338, L37
- Kley, W., Bitsch, B., & Klahr, H. 2009, *A&A*, 506, 971
- Kley, W. & Crida, A. 2008, *A&A*, 487, L9
- Kley, W. & Nelson, R. P. 2012, *ARA&A*, 50, 211
- Kokubo, E. & Ida, S. 1998, *Icarus*, 131, 171
- Konopacky, Q. M., Rameau, J., Duchêne, G., et al. 2016, *ApJ*, 829, L4
- Kravtsov, A. V., Klypin, A. A., & Khokhlov, A. M. 1997, *ApJS*, 111, 73

- Kritsuk, A. G., Nordlund, Å., Collins, D., et al. 2011, *ApJ*, 737, 13
- Kuffmeier, M., Frostholm Mogensen, T., Haugbølle, T., Bizzarro, M., & Nordlund, Å. 2016, *ApJ*, 826, 22
- Kuffmeier, M., Haugbølle, T., & Nordlund, Å. 2017, *ApJ*, 846, 7
- Kurucz, R. L. 1987, personal communication
- Lambrechts, M. & Johansen, A. 2012, *A&A*, 544, A32
- Lambrechts, M. & Johansen, A. 2014, *A&A*, 572, A107
- Lambrechts, M. & Lega, E. 2017, *Astronomy and Astrophysics*, 606, A146
- Laraia, A. L., Gamache, R. R., Lamouroux, J., Gordon, I. E., & Rothman, L. S. 2011, *Icarus*, 215, 391
- Le Roy, R. J., Chapman, S. G., & McCourt, F. R. W. 1990, *The Journal of Physical Chemistry*, 94, 923
- Levermore, C. D. & Pomraning, G. C. 1981, *ApJ*, 248, 321
- Levison, H. F., Thommes, E., & Duncan, M. J. 2010, *AJ*, 139, 1297
- Li, Z.-Y., Wang, P., Abel, T., & Nakamura, F. 2010, *ApJ*, 720, L26
- Lin, D. N. C. & Papaloizou, J. 1979, *MNRAS*, 186, 799
- Liu, B., Ormel, C. W., & Lin, D. N. C. 2017, *A&A*, 601, A15
- Lodato, G. & Price, D. J. 2010, *MNRAS*, 405, 1212
- Lommen, D., Maddison, S. T., Wright, C. M., et al. 2009, *A&A*, 495, 869
- Lynden-Bell, D. & Pringle, J. E. 1974, *MNRAS*, 168, 603
- Mac Low, M.-M., Norman, M. L., Konigl, A., & Wardle, M. 1995, *ApJ*, 442, 726
- Masset, F. S. & Benítez-Llambay, P. 2016, *ApJ*, 817, 19
- Masson, J., Teyssier, R., Mulet-Marquis, C., Hennebelle, P., & Chabrier, G. 2012, *ApJS*, 201, 24
- Mayor, M. & Queloz, D. 1995, *Nature*, 378, 355
- McBride, B. J., Heimel, S., Ehlers, J. G., & Gordon, S. 1963, *NASA Special Publication*, 3001
- McDowell, R. S. 1988, *J. Chem. Phys.*, 88, 356
- McDowell, R. S. 1990, *J. Chem. Phys.*, 93, 2801
- Mendygral, P. J., Radcliffe, N., Kandalla, K., et al. 2017, *ApJS*, 228, 23

- Men'shchikov, A., André, P., Didelon, P., et al. 2010, *A&A*, 518, L103
- Meru, F., Juhász, A., Ilee, J. D., et al. 2017, *ApJ*, 839, L24
- Meyer, C. D., Balsara, D. S., & Aslam, T. D. 2014, *Journal of Computational Physics*, 257, 594
- Mignone, A., Bodo, G., Massaglia, S., et al. 2007, *ApJS*, 170, 228
- Mizuno, A., Onishi, T., Yonekura, Y., et al. 1995, *ApJ*, 445, L161
- Mizuno, H., Nakazawa, K., & Hayashi, C. 1978, *Progress of Theoretical Physics*, 60, 699
- Morbidelli, A. & Nesvorný, D. 2012, *A&A*, 546, A18
- Mordasini, C., Mollière, P., Dittkrist, K.-M., Jin, S., & Alibert, Y. 2015, *International Journal of Astrobiology*, 14, 201
- Nordlund, A. 1982, *A&A*, 107, 1
- Nordlund, A. 1984, Iterative solution of radiative transfer problems with spherical symmetry using a single-ray approximation, ed. W. Kalkofen (Cambridge University Press), 211–233
- Nordlund, Å. 2011, in *IAU Symposium*, Vol. 276, *The Astrophysics of Planetary Systems: Formation, Structure, and Dynamical Evolution*, ed. A. Sozzetti, M. G. Lattanzi, & A. P. Boss, 105–112
- Nordlund, Å., Galsgaard, K., & Stein, R. F. 1994, in *NATO Advanced Science Institutes (ASI) Series C*, Vol. 433, *NATO Advanced Science Institutes (ASI) Series C*, ed. R. J. Rutten & C. J. Schrijver, 471
- Nordlund, Å., Haugbølle, T., Küffmeier, M., Padoan, P., & Vasileiades, A. 2014, in *IAU Symposium*, Vol. 299, *Exploring the Formation and Evolution of Planetary Systems*, ed. M. Booth, B. C. Matthews, & J. R. Graham, 131–135
- Nordlund, Å., Ramsey, J. P., Popovas, A., & Küffmeier, M. 2018, *ArXiv e-prints*
- Ormel, C. W. 2014, *ApJ*, 789, L18
- Ormel, C. W. & Klahr, H. H. 2010, *A&A*, 520, A43
- Ormel, C. W., Kuiper, R., & Shi, J.-M. 2015a, *MNRAS*, 446, 1026
- Ormel, C. W., Liu, B., & Schoonenberg, D. 2017, *A&A*, 604, A1
- Ormel, C. W., Shi, J.-M., & Kuiper, R. 2015b, *MNRAS*, 447, 3512
- Ormel, C. W., Spaans, M., & Tielens, A. G. G. M. 2007, *A&A*, 461, 215
- Paardekooper, S.-J., Baruteau, C., Crida, A., & Kley, W. 2010, *MNRAS*, 401, 1950

- Paardekooper, S.-J., Baruteau, C., & Kley, W. 2011, *MNRAS*, 410, 293
- Paardekooper, S.-J. & Mellema, G. 2006, *A&A*, 453, 1129
- Padoan, P., Haugbølle, T., & Nordlund, Å. 2012, *ApJ*, 759, L27
- Padoan, P., Haugbølle, T., & Nordlund, Å. 2014, *ApJ*, 797, 32
- Padoan, P., Juvela, M., Goodman, A. A., & Nordlund, Å. 2001, *ApJ*, 553, 227
- Padoan, P., Juvela, M., Pan, L., Haugbølle, T., & Nordlund, Å. 2016a, *ApJ*, 826, 140
- Padoan, P., Pan, L., Haugbølle, T., & Nordlund, Å. 2016b, *ApJ*, 822, 11
- Padoan, P., Zweibel, E., & Nordlund, Å. 2000, *ApJ*, 540, 332
- Pagano, D., Casavola, A., Pietanza, L. D., et al. 2009, *ESA Scientific Technical Review*, 257
- Papaloizou, J. C. B. & Pringle, J. E. 1984, *MNRAS*, 208, 721
- Paxton, B., Bildsten, L., Dotter, A., et al. 2010, *MESA: Modules for Experiments in Stellar Astrophysics*, *Astrophysics Source Code Library*
- Pepin, R. O. 1991, *Icarus*, 92, 2
- Pepin, R. O. 1992a, *Annual Review of Earth and Planetary Sciences*, 20, 389
- Pepin, R. O. 1992b, in *LPI Contributions*, Vol. 787, *Evolution of the Martian Atmosphere*, ed. J. G. Luhmann & B. M. Jakosky
- Perri, F. & Cameron, A. G. W. 1974, *Icarus*, 22, 416
- Pinte, C., Harries, T. J., Min, M., et al. 2009, *A&A*, 498, 967
- Piso, A.-M. A., Youdin, A. N., & Murray-Clay, R. A. 2015, *ApJ*, 800, 82
- Piszczatowski, K., Wach, G., Przybytek, M., et al. 2009, *Journal of Chemical Theory and Computation*, 5, 3039, PMID: 26609983
- Pollack, J. B., Hubickyj, O., Bodenheimer, P., et al. 1996, *Icarus*, 124, 62
- Popovas, A. & Jørgensen, U. G. 2016, *A&A*, 595, A130
- Popovas, A., Nordlund, Å., Ramsey, J. P., & Ormel, C. W. submitted, *ArXiv e-prints*
- Porth, O., Xia, C., Hendrix, T., Moschou, S. P., & Keppens, R. 2014, *ApJS*, 214, 4
- Pringle, J. E. 1981, *ARA&A*, 19, 137
- Ramsey, J. P., Clarke, D. A., & Men'shchikov, A. B. 2012, *ApJS*, 199, 13
- Ramsey, J. P. & Dullemond, C. P. 2015, *A&A*, 574, A81

- Ramsey, J. P., Haugbølle, T., & Nordlund, Å. submitted, in AS-TRONUM2017 Proceedings, Journal of Physics Conference Series
- Rein, H., Lesur, G., & Leinhardt, Z. M. 2010, *A&A*, 511, A69
- Ribas, Á., Bouy, H., & Merín, B. 2015, *A&A*, 576, A52
- Rijkhorst, E.-J., Plewa, T., Dubey, A., & Mellema, G. 2006, *A&A*, 452, 907
- Robitaille, T. P. 2011, *A&A*, 536, A79
- Ross, S. C. & Jungen, C. 1994, *Phys. Rev. A*, 50, 4618
- Rossi, S. C. F., Maciel, W. J., & Benevides-Soares, P. 1985, *A&A*, 148, 93
- Rubanenko, L., Steinberg, E., Schlichting, H., & Paige, D. A. 2017, in AAS/Division for Planetary Sciences Meeting Abstracts, Vol. 49, AAS/Division for Planetary Sciences Meeting Abstracts #49, 413.01
- Sadavoy, S. I. & Stahler, S. W. 2017, *MNRAS*, 469, 3881
- Safronov, V. S. 1960, *Annales d'Astrophysique*, 23, 979
- Safronov, V. S. 1966, *AZh*, 43, 817
- Sahlmann, J., Lazorenko, P. F., Ségransan, D., et al. 2013, *A&A*, 556, A133
- Sauval, A. J. & Tatum, J. B. 1984, *ApJS*, 56, 193
- Schlichting, H. E., Sari, R., & Yalinewich, A. 2015, *Icarus*, 247, 81
- Schoonenberg, D. & Ormel, C. W. 2017, *A&A*, 602, A21
- Sellentini, E., Ramsey, J. P., Windmark, F., & Dullemond, C. P. 2013, *A&A*, 560, A96
- Senn, P. & Dressler, K. 1987, *J. Chem. Phys.*, 87, 6908
- Shakura, N. I. & Sunyaev, R. A. 1973, *A&A*, 24, 337
- Shiokawa, H., Cheng, R. M., Noble, S. C., & Krolik, J. H. 2017, *ArXiv e-prints*
- Smith, A. M. S., Cabrera, J., Csizmadia, S., et al. 2018, *MNRAS*, 474, 5523
- Sørensen, G. O. & Jørgensen, U. G. 1993, *J. Chem. Phys.*, 99, 3153
- Springel, V. 2005, *MNRAS*, 364, 1105
- Springel, V. 2010, *MNRAS*, 401, 791
- Stein, R. F. & Nordlund, Å. 2012, *ApJ*, 753, L13
- Stevenson, D. J. 1982, *Planet. Space Sci.*, 30, 755
- Stoll, M. H. R. & Kley, W. 2016, *A&A*, 594, A57

- Stone, J. M., Gardiner, T. A., Teuben, P., Hawley, J. F., & Simon, J. B. 2008, *ApJS*, 178, 137
- Stone, J. M., Mihalas, D., & Norman, M. L. 1992, *ApJS*, 80, 819
- Stone, J. M. & Norman, M. L. 1992, *ApJS*, 80, 753
- Struve, O. 1952, *The Observatory*, 72, 199
- Stull, D. R., Prophet, H., & States, U. 1971, JANAF thermochemical tables [electronic resource] / D.R. Stull and H. Prophet, project directors, 2nd edn. (U.S. Dept. of Commerce, National Bureau of Standards Washington, D.C), 1 v. (unpaged) ;
- Szulágyi, J., Masset, F., Lega, E., et al. 2016, *MNRAS*, 460, 2853
- Takezawa, S. 1970, *J. Chem. Phys.*, 52, 2575
- Tan, J. C., Chatterjee, S., Hu, X., Zhu, Z., & Mohanty, S. 2016, *IAU Focus Meeting*, 29, 6
- Tatum, J. B. 1966, *Publications of the Dominion Astrophysical Observatory Victoria*, 13, 1
- Testi, L., Birnstiel, T., Ricci, L., et al. 2014, *Protostars and Planets VI*, 339
- Testi, L., Natta, A., Shepherd, D. S., & Wilner, D. J. 2003, *A&A*, 403, 323
- Teyssier, R. 2002, *A&A*, 385, 337
- Tobin, J. J., Looney, L. W., Wilner, D. J., et al. 2015, *ApJ*, 805, 125
- Tomida, K. & Hori, Y. 2016, personal communication
- Tomida, K., Tomisaka, K., Matsumoto, T., et al. 2013, *ApJ*, 763, 6
- Toomre, A. 1964, *ApJ*, 139, 1217
- Transtrum, M. K. & Sethna, J. P. 2012, *ArXiv e-prints*
- Tuomi, M. 2012, *A&A*, 543, A52
- Tuomi, M., Jones, H. R. A., Barnes, J. R., Anglada-Escudé, G., & Jenkins, J. S. 2014, *MNRAS*, 441, 1545
- Turk, M. J., Smith, B. D., Oishi, J. S., et al. 2011, *The Astrophysical Journal Supplement Series*, 192, 9
- van der Holst, B., Tóth, G., Sokolov, I. V., et al. 2011, *ApJS*, 194, 23
- van der Marel, N., van Dishoeck, E. F., Bruderer, S., et al. 2013, *Science*, 340, 1199
- Vardya, M. S. 1965, *MNRAS*, 129, 345

- Venturini, J., Alibert, Y., & Benz, W. 2016, *Astronomy and Astrophysics*, 596, A90
- Venturini, J., Alibert, Y., Benz, W., & Ikoma, M. 2015, *A&A*, 576, A114
- Visser, R. G. & Ormel, C. W. 2016, *A&A*, 586, A66
- Vogt, S. S., Burt, J., Meschiari, S., et al. 2015, *ApJ*, 814, 12
- Walch, S. K., Whitworth, A. P., Bisbas, T., Wunsch, R., & Hubber, D. 2012, *MNRAS*, 427, 625
- Weidenschilling, S. J. 1977, *MNRAS*, 180, 57
- Whipple, F. L. 1972, in *From Plasma to Planet*, ed. A. Elvius, 211
- Wolniewicz, L., Orlikowski, T., & Staszewska, G. 2006, *Journal of Molecular Spectroscopy*, 238, 118
- Wolszczan, A. & Frail, D. A. 1992, *Nature*, 355, 145
- Wuchterl, G. 1993, *Icarus*, 106, 323
- Xu, Z., Bai, X.-N., & Murray-Clay, R. A. 2017, *The Astrophysical Journal*, 847, 52
- Youdin, A. N. & Goodman, J. 2005, *ApJ*, 620, 459
- Yu, S. & Dressler, K. 1994, *J. Chem. Phys.*, 101, 7692
- Zanazzi, J. J. & Lai, D. 2017, *ArXiv e-prints*
- Zeng, L., Sasselov, D. D., & Jacobsen, S. B. 2016, *ApJ*, 819, 127
- Ziegler, U. 1998, *Computer Physics Communications*, 109, 111